Effects of Extracellular Surface Interactions on Mass Transport across Epithelial Cells

by

Kyoung Ah Min

A dissertation submitted in partial fulfillment
of the requirements for the degree of
Doctor of Philosophy
(Pharmaceutical Sciences)
in the University of Michigan
2013

Doctoral Committee:

Associate Professor Gustavo R. Rosania, Chair
Professor Kyung-Dall Lee
Professor Kathleen A. Stringer
Associate Professor Duxin Sun

To my family and friends

: With my love and respects

Acknowledgements

I would like to express my sincere gratitude to Dr. Gus Rosania for his support and insightful guidance throughout my Ph.D. training years. He taught me the attitude to keep discover science in every single experiment. I deeply respect his perseverance and enthusiasm in his research as a scientist. I also would like to thank my committee members, Dr. Kyung-Dall Lee, Dr. Duxin Sun, and Dr. Kathleen A. Stringer for their suggestions and guidance in my project.

I am also grateful to the Department of Pharmaceutical Sciences and the Rackham Graduate School for supporting me during my Ph.D. I appreciate the funding sources, Upjohn Fellowship, Warner Lambert & Parke Davis Fellowship, and Rackham Predoctoral Fellowship.

I greatly appreciate Dr. David E. Smith and Dr. Victor C. Yang for their sincere advice and suggestions in my project. I thank all my wonderful friends. They were always there for me to make this long journey for a Ph.D. possible; my classmates, Meong Cheol Shin, Bei Yang, Kefeng Sun, Deanna Mudie, Maria M. Posada, and Lilly Roy for their friendship and good memories through all the years; my previous lab members, Dr. Xinyuan Zhang, Dr. Jing-yu Yu, Dr. Nan Zheng, and Dr. Jason Baik for their valuable advice and support, and my present lab members, Arjang Talattof and Leo Arzu for their help and friendship.

I would like to dedicate my work to my parents who supported me with love and belief throughout my life. Lastly, I greatly thank my husband, Meong Cheol and my two lovely sons for being beside me all the time.

Table of Contents

List of Tables

List of Figures

List of Appendices

Abstract

Transport of molecules across cells is an important determinant of the absorption, distribution, and elimination properties of therapeutic agents in the body. While the ability to predict and control the absorption, distribution and elimination properties of therapeutic agents has been a long-standing goal in pharmaceutical sciences, cells are structurally and functionally complex, and in many cases transport phenomena have proved difficult to accurately model and predict, purely based on the internal organization of the cell. To address why this may be the case, this thesis combined microscopic imaging, mass transport measurements, and computational modeling, to investigate two complex cellular transport phenomena: i) uptake and permeation of magnetic nanoparticles across a canine kidney epithelial cell line, in the presence of a magnetic field; and, ii) uptake and permeation of small drug-like molecules across airway epithelial cells of different origins. For experiments, four kinds of transport probes were used: 1) superparamagnetic iron oxide nanoparticles that exhibited variations in transport kinetics under a pulsed *vs.* constant magnetic field; 2) two fluorescent probes (MitoTracker® Red or Hoechst® 33342) that exhibited differences in distribution in the airway and alveoli; 3) a passively diffusing small molecule drug (propranolol) that exhibited differences in transport behavior across different airway epithelial cells; and, 4) a highly insoluble compound (curcumin) that exhibited differences in transport across airway epithelial cells

in the presence of a complexing agent. Effects of spatiotemporal variations in a magnetic field on the extent of particle aggregation on the extracellular cell surface should be considered to optimize particle formulations and magnetic field applications for magnetically-guided targeting. For local lung delivery, absorption and distribution of inhaled formulations should be screened in the biorelevant cell model, by considering effects of local extracellular interactions. Altogether, the results of experiments and analyses show innovative approaches to interpret cell-based transport data in a more accurate manner by analyzing local molecular interactions and diffusion phenomena occurring at the extracellular surface of cells for a variety of transported materials ranging from small molecules to nanoparticles. Based on cell-based transport studies, quantitative microscopic imaging and *in situ* cellular pharmacokinetic modeling can potentially predict transport phenomena of drug-like molecules *in vivo* by dissecting variables resulting from extracellular surface properties.

Chapter 1

Introduction

1.1 Background

1.1.1 Cell permeability as a determinant of drug transport and distribution in the body (Pharmacokinetics)

In our body, there are physiological barriers composed of cells and interstitium. Xenobiotics must overcome those cell barriers to go into action sites such as the blood stream or deep tissues. Essential organs have well-differentiated epithelial and endothelial cells to control the absorption and distribution of xenobiotics as well as nutrients. After administration, drug molecules are to be distributed from the aqueous environment (*e.g.*, gastric fluid, blood, or extracellular fluid) into the tissue compartments and target cells. Measurements of cell permeability with drug-like molecules in the representative cell-types of the target tissues or organs can provide knowledge about how the drug molecules can be absorbed and distributed in the target sites. Cell Permeability is a key concept in terms of being able to understand the distribution of drugs in different compartments of the body. There have been enormous efforts to develop cell culture models for the purpose of drug screenings in the context of absorption, distribution, metabolism, excretion and toxicity (ADME/Tox) and drug efficacy/acting mechanism.

Drug permeability measurements using various cell models have facilitated high throughput screenings of drug candidates with appropriate physicochemical properties to ensure the distribution of drugs from the site of administration into the target tissue or organ. Cell permeability measurements are important tools for the early stages of drug discovery and development process. Permeability measurements of oral drugs in the Caco-2 cells as the cell model for intestinal absorption studies were well-correlated with drug absorption and distribution *in vivo* (1, 2). Blood-brain barrier (BBB) cultures are useful to study permeation of brain-targeting drugs for central nervous system (CNS) drug discovery/development (3). In addition to oral or brain delivery, there are a variety of useful cell models for permeability assays in the field of drug delivery (*i.e.,* transdermal, nasal, ophthalmic, buccal, or lung delivery, and so on).

1.1.2 Structural (anatomical) role of cell monolayers in separating different body compartments

Organs and tissues in our body are separated from each other by specialized surrounding cell structures called epithelial cell monolayers. This anatomical barrier is the site of transport, barrier, and secretory processes and plays a role in maintaining different body compartments. For example, intestinal epithelial mucosa layers separate the gut lumen from the body, endothelial cells in the capillaries of BBB separate the blood stream from the brain, and the airway epithelial cells separate the airway lumen from the blood circulation. Plasma membranes of the epithelial cells act as permeability barriers for the substances in the cell surface. The plasma membrane composed of lipid bilayers, proteins, carbohydrates, or cholesterol, *etc* controls the structures as well as absorptions dynamically. Epithelial cells directly contact with neighboring cells *via*

junctional complexes (4) such as tight junctions, gap junctions, and desmosomes, which are essential for more effective chemical and physical barriers as intact cell monolayers. These junctions can help prevent diffusion of solutes around the cells.

1.1.3 Functional (physiological) role of cell monolayers determining the rate of drug transport between adjacent body compartments

Lipid compositions in plasma membranes of the epithelial cell monolayers mainly determine the fate of drug molecules in terms of absorption/distributions according to the lipophilicy of the molecules. Passive diffusion is a main pathway of drug transport through the epithelial cells. However, for some types of drug molecules, there are other ways for absorptions by active transporters expressed on the cell membrane. These functional protein complexes can affect the absorption of their substrates (*e.g.*., nutrients (glucose or peptides) or chemicals) and contribute to the polarization of the epithelial cells. G. L. Amidon *et al.* showed that the permeability properties of cells that line the intestinal mucosa determine the rate of absorption of orally-administered drugs from the intestinal lumen (5, 6). Peptide transporters expressed on the epithelial cells in the gastrointestinal (GI) tract are key determinants of peptide-like drugs' uptake in the body as shown in D. E. Smith *et al.*'s work with PEPT1 and PEPT2 proton-coupled oligopeptide transporters (7). Efflux transporters play roles to remove drug molecules from cells, which have been reported as multidrug-resistance transporters (8). As a representative efflux pump, P-glycoprotein (P-gp) expressed in epithelial cells lining the gut is regarded as important to keep certain drugs (P-gp substrates) from entering the body (9, 10).

1.1.4 The concept of cell permeability as applied to whole body, systemic (PBPK) modeling

Now, it is evident that cell permeability may be important for capturing the transport kinetics of drug molecules in the different organ compartments. In the mathematical models for predicting molecular transport/distributions, the concept of permeability has been used in various perspectives. From the mid 1970s, all the way through the 1990s and then eventually in P. Poulin's and M. Rowland's predictive PBPK models (11-13), permeability across compartment boundaries of the cells was incorporated into physiologically-based pharmacokinetic (PBPK) modeling. Permeability was used as an essential parameter in the compartmental, non cell-based mechanistic organ models, such as G. L. Amidon *et al.*'s basic gastrointestinal theoretical model (1995-1997) (6), which was the beginning of the mechanistic ACAT (advanced compartmental absorption and transit) model (GastroPlus™) for capturing drug absorption from the GI tract into the body. Lastly, in the pioneering works related to mechanistic cell-based pharmacokinetic models, cell permeability has been useful for capturing molecular transport and distribution in the cells and subcellular organelles (kinetic models by S. Balaz *et al.*, S. Trapp *et al.*, and K. S. Pang *et al.* (1985-2008) (14-19), leading to predictive 1CellPK transport models by X. Zhang *et al.* and N. Zheng *et al.* (2006-2010) (20-23) which allow calculation of cell permeability). Cell permeability is also a major component to be considered in the context of the integration of 1CellPK models with the predictive compartmental organ model (24). This allows understanding local differences in drug absorption and distribution at the cellular and tissue level in the context of local differences in cell architecture and local variations in permeability.

1.2 Rationale and Significance

1.2.1 Paradigm shift in drug development process

Today, the burden on research and development budget of pharmaceutical companies is increasing by escalating costs for drug development and drug attritions. A recent report has mentioned that the final price to get a successful drug on the market might be more than a billion dollars with research time running into more than 10 years (25). However, FDA drug approvals have declined or remained flat through these years. It has been estimated that about 40–60% of such failure are caused by the deficiencies of ADME/Tox (26, 27). The significant failure rates of drug candidates in the late stages of drug development process have evoked the need for development of new *in vitro, in vivo,* and *in silico* tools that can eliminate inappropriate compounds before wasting substantial resources. Accordingly, a paradigm shift has occurred in the initial phases of the field of drug discovery and development. In the traditional drug design paradigm, the central stage focused on the activity and the specificity of a drug candidate, while some other properties, especially those related to ADME/Tox, are only considered at a later stage. The *in vitro* screening in the traditional paradigm usually failed to lead to good drug candidates because compounds with high molecular weight and lipophilicity tend to have high potency but poor absorption/distribution behaviors.

Therefore, in addition to the screening of pharmacological activity, ADME/Tox properties of a drug are now considered at an early stage to select drug candidates. Now, it is widely believed that the commercial success of a new chemical entity (NCE) depends on ADME properties with pharmacological activity. However, even though

combinatorial chemistry, automation, and high throughput screening (HTS) have contributed to test numerous compounds in a comparatively short time, success rate of clinical testing to final approval has remained low. Greater than 90% of the compounds entering phase I clinical trial failed to go on market and so did 50% going into phase III (27). Thus, the task of screening discovery compounds for biopharmaceutical properties (*e.g.*, solubility, intestinal permeability, metabolic stability and recently drug-drug interaction) is now a major challenge facing the industry. It is highly demanding to develop the mechanism-based pharmacokinetic model to define physicochemical properties of drug-like molecules which can exhibit optimal pharmacokinetics in clinics with high efficacy, low clearance, and low toxicity.

1.2.2 *In Silico* model development to predict pharmacokinetic properties

In the early- to mid-1990s, assaying numerous compounds was enabled by the advances in automation technology and experimental ADME/Tox techniques such as the *in vitro* permeability screening, the metabolic stability screening using hepatocytes or microsomes and the cytochrome P450 inhibition assays (28). In addition to the development of high throughput screening experimental assays, it was also urgently needed to develop effective computational methods for predicting ADME/Tox-related properties. Until now, many computational approaches have been developed for the ADME/Tox properties, such as bioavailability, aqueous solubility, intestinal absorption, blood-brain barrier penetration, drug-drug interactions, enzyme, transporter, plasma-protein binding and toxicity (29). Substantial progress has been made in developing a broad spectrum of models for estimation of drug absorption/disposition.

For the compounds to be developed with drug-like properties, the Lipinski's 'rule-of-five' has been considered as a general principle to distinguish drug-like molecules from nondrug-like molecules. This rule, the most popular filter for ADME predictions, was proposed by Lipinski and coworkers in 1997 from analysis of 2,245 drugs from the World Drug Index (30, 31). They found that poor absorption and permeation are more likely to occur when molecules have properties such as: 1) molecular weight >500, 2) calculated logP >5 (CLOGP), 3) number of hydrogen-bond donors (OH and NH groups) >5, or 4) numbers of hydrogen-bond acceptors (N and O atoms) >10. However, this rule should be regarded as a minimum criterion of a molecule to be drug-like. In fact, most compounds that fall within the 'rule–of-five' were found to have no potential to lead to a drug. Therefore, a lot of *in silico* models have been developed to predict drug-likeness in specific manners. Predicting the ADME properties were performed in two different ways: molecular modeling and data modeling. For molecular modeling, pharmacophore modeling or molecular docking has been used to explore the potential interactions between the small molecules and proteins known to be involved in ADME processes, such as cytochrome P450s, receptors or transporters (32). For data modeling, quantitative structure-activity relationship (QSAR) approaches have been applied using statistical methods (multiple linear regression (MLR), modern multivariate analysis techniques or machine-learning methods), based on appropriate descriptors. Currently, there have been many trials to establish QSAR model or statistical fitting model for drug absorptions or drug interactions with the metabolic enzymes or efflux transporters in the liver, intestine, blood-brain barrier. The QSAR model needs large datasets of molecules for the model

training, which may not be feasible for model development for inhaled drugs due to a lack of data with lung-targeting small molecules.

In contrast to these empirical models, mechanistic physiologically-based models predict more relevant kinetic parameters to physiological conditions without needs of large training sets of molecules and statistical fitting. Mechanistic models consider physiological, biophysical parameters and physicochemical properties of small molecules and input parameters should be based on scientific knowledge. As representative, pioneering studies in this area, S. Trapp and his coworkers have developed non-polarized suspension cell model to explain the cellular transport and intracellular accumulations of the small molecules in tumor cells, based on their prior plant cell model (16, 33). Basic principles in their models include: mass balance, Fick's law of passive diffusion, Nernst-Planck equation, Henderson-Hasselbalch equation, pH-partitioning theory, and ion-trapping mechanism. Using these principles, they explained molecular uptake and accumulations in each compartment, including cytosol, mitochondria and lysosomes as subcellular compartments. Suborganelles were defined as compartments based on morphology and physiology. In comparison, S. Balaz *et al.* divided cellular compartments into N compartments, which were composed of alternating aqueous and lipid phases as a catenary chain to describe kinetics of drug disposition and subcellular distribution (15, 34). In addition to the suborganellar distribution, drug metabolism has been studied as an important component for the cell-based pharmacokinetic models. Various catenary models to predict ADME profiles of small molecules in liver or intestine have been developed to include passive diffusion, protein binding, drug carriers, and efflux transporters and metabolic enzymes by K. S. Pang *et al*. (18, 19).

On the basis of these pioneering works, the state-of-art cellular pharmacokinetic model (1CellPK) was established by X. Zhang *et al.* to capture drug transport across membranes and also intracellular distribution into suborganelles such as mitochondria or lysosomes of the polarized epithelial cell in the presence of the apical to basolateral concentration gradient of monobasic molecules (20). The model was constructed with the coupled differential equations describing the mass balances in the multi-compartments by the Fick-Nernst-Planck equation. Passive diffusion was modeled by the Fick's law of diffusion for neutral molecules, and by combination of the Fick's law of diffusion and the Nernst-Planck equation for ionized molecules. This model considered both the physiological properties of the cells and physicochemical properties of the small molecules, and gave quantitative predictions of drug transport as well as concentration-time profiles in the functional subcellular organelles (mitochondria or lysosomes). 1CellPK showed good prediction of permeability in Caco-2 cell monolayer for monobasic drugs, and also for lysosomotropic drug molecules (20, 21, 23). Further, 1CellPK was utilized to develop the *in silico* lung model and also PBPK model for inhaled drug molecules (24).

1.2.3 *In vitro* cell-based assays for optimizing inhaled drug formulations

As the most convenient method for medication, oral administration has been widely studied with various models for different drug molecules ranging from small molecular compounds to large molecules such as proteins. For accurate and effective prediction of intestinal absorption, several *in vitro* methods have been developed. Among them, the most popular cell-based models for intestinal permeability were Caco-2 or MDCK (Madin-Darby canine kidney) cell culture systems (2, 35, 36). As another

important route of drug delivery, inhalation to airway in the lung is a well-established means for treating respiratory diseases with rapid onset of drug action, low systemic exposure, and reduced adverse effects (37, 38). The immediate onset of drug action is absolutely necessary to relieve acute asthmatic symptoms. By this route, pharmaceutical aerosols delivering the bronchodilators or glucocorticoids can obtain the high local concentrations of drug molecules in the target cell to treat asthma, chronic obstructive pulmonary disease (COPD) or pulmonary hypertension. On the other hand, the inhalation has been utilized for systemic drug delivery of the drugs with poor oral absorption such as peptides, proteins, or oligonucleotides into the deep lung regions due to the advantage of large absorptive area and comparatively low metabolism (39). As the global importance and rising prevalence of chronic respiratory diseases have been recognized, research for upper respiratory treatment is increasing in industry and academia (40). Even though inhalation has been used for delivering the drugs with diverse physicochemical properties, there has been little study about the relationship between the physicochemical properties of drug molecules and their pharmacokinetics in the respiratory system.

While most research has been focused on drug pharmacokinetics in the intestine, liver, or blood-brain barrier, few studies have been done about the drug transport and metabolism in the lung. Assessing the fate of the inhaled drugs is difficult due to the inaccessibility, delicate nature or complex structure of lung. In order to increase local drug concentration and decrease systemic bioavailability, transport mechanism and metabolism of the inhaled or oral drugs for pulmonary diseases have to be investigated. The interpretation of results in the animal or tissue studies (41, 42) can be complicated by inter-species variation and imprecise drug delivery into the lung. Commonly used *ex in*

vivo experiments for lung absorption studies, isolated perfused lung (IPL) (43) requires specialized techniques to maintain structural and functional integrity of the lung. Compared to complex experimental system, the use of airway epithelial cell cultures such as Calu-3, 16HBE14o-, or NHBE has advantages in mechanistic analysis about drug transport and metabolism in lung (44-46). The culture conditions on the transwell inserts have been well characterized for these cells under air-liquid interface (ALI) or liquid-liquid interface (LLI) culture conditions (46, 47). These *in vitro* cell-based assays have been used to study drug absorption, distribution or toxicity in airway (48-50). The *in vitro-in vivo* correlations in drug permeability have been reported with these cell cultures (51). Especially, Calu-3 has been widely utilized for drug permeability screening as well as studied for dissolution kinetics of particles (52, 53). It has been recognized as a promising airway cell model for optimizing the inhaled drug formulations (*i.e.*, size, shape, or charges of drug particles).

For *in vitro* respiratory epithelial cell model, various immortalized cell lines (*e.g.*, A549, L-2, H441, and MLE-15) have been characterized for the drug absorption including paracellular markers (54). However, significant variations in transepithelial resistance measurements from these cells among different laboratories make it very difficult to interpret drug transport data. In contrast to the lack of functional tight junctions in these immortalized cell monolayers (55), primary cultured pneumocyte monolayers appeared to show reliable tight junctions as useful *in vitro* cell culture models for drug absorption assays (56). As an *in vitro* biological microfluidic system of 2 cm-polymer chip, lung-on-a-chip was developed to study efficacy or toxicity of the inhaled drug formulations by reproducing the conditions of alveolar capillary interface in the lung

and mechanical environment of breathing (57). This biomimetic microsystem could reproduce organ-level response to different cell stimuli such as cytokines in microenvironment of the physiological lung and be utilized to investigate the interactions between particles from the inhaled formulations and the respiratory system.

1.2.4 *In vitro* cell-based assays for optimizing nanoparticle formulations

Nanobiotechnology plays an important role in the paradigm of drug discovery/development process. Nanoparticles made from biocompatible materials have contributed to improving the ADME properties of drug molecules ranging from small molecules to large molecules (*e.g.*, DNA, Protein, siRNA) and also utilized to facilitate drug targeting and enhancing drug efficacy with lessened side effects (58-60). In a parallel of advances in nanotechnology with nanofabrication, nanofluidics and nanoarrays, there have been various types of cell-based assay developments for different purposes (61). Various cancer or normal cell-types were used for testing the efficacy, toxicity, or targeting efficiency of nanoparticles for cancer diagnostic or therapeutic purposes (62-64). Advanced imaging techniques have been used in the process from characterization after synthesis, mechanistic studies (*i.e.*, endocytosis), to application of the nanoparticles (*i.e.*, transmission electron microscopy (TEM), confocal microscopy, magnetic resonance imaging (MRI)) (65-68).

Recent significant advances in nanoparticle technology have made it possible to integrate drug delivery, targeting and imaging into a single nanoparticle (62). This nanotheranostics combines drug therapy and diagnostic imaging using nanoparticle carriers, exhibiting significant clinical benefits. Superparamagnetic iron oxide nanoparticles (MNPs) have been recognized as feasible, biocompatible, stable

nanotheranostics for tumor imaging and drug delivery. MNPs can be used for MRI contrast agents (69) and easily modified on their surface with other biocompatible materials for the purpose of targeting or increasing stability in the blood stream (70). The surface coating can prevent particle precipitation and also protect the particles from being taken up by the reticular endothelial system (RES) such as macrophages in the circulation *in vivo* (71, 72). Modifications on surface charge or size of MNPs can enhance the interactions with the target cells and accordingly, cellular uptake (73-75). By the applied magnetic field, more amounts of MNPs locally or systemically administered can be detected in the target sites than in the neighboring cells (76-78).

Magnetofection is to enhance drug or gene delivery with MNPs into the cells by the externally applied magnetic field (79). MNP formulations for hyperthermia treatment can be tested *in vitro* tumor cell cultures. This assay utilizes the characteristics of tumor cells being more thermosensitive than the normal cells. The hyperthermia can be obtained by applying alternating magnetic fields of suitable frequencies that produce heat dissipation through the oscillation of MNPs' internal magnetic moment to kill the tumor cells with MNPs. With the *in vitro* cell-based system, the field strength or frequency of the magnetic field have been adjusted to optimize the MNP formulations to achieve better efficiency of magnetofection (80) or hyperthermia (81). For the cell/tissue engineering, cell micropatterning with the magnetic field applications could be used to generate microengineered platforms. External magnetic field can enhance cell-seeding into three-dimensional scaffolds using MNPs (82).

For the ADME/Tox studies, Caco-2, MDCK, Calu-3 cells, blood brain barrier (BBB) *in vitro* assays or primary cell cultures have been used to characterize the

functionalized nanoparticles (*e.g.*, polymer or lipid-based nanoparticles) in the context of transport/absorption as drug carriers (83-87). The *in vitro* BBB cultures were used for optimizing MNP formulations for brain targeting and MRI (88, 89). For inner ear diseases, the round window membrane (RWM) cultures composed of MDCK cells and fibroblasts (90-92) have been used to test transport efficiency and cellular uptake of MNPs. The *in vitro* studies about MNP transport across the cellular barriers under the magnetic field application should be more investigated for various batches of MNP formulations because it is hard to disseminate the effects of magnetic field on the interaction of MNPs with the cells from other physiological factors in the *in vivo* settings. It is meaningful to examine how MNPs interact with the cell surface under different magnetic field conditions in various initial doses of MNPs because administered doses of particles should be adjusted according to the magnetic field application and different MNP formulations for better ADME behaviors. With this initiative, my thesis work examining the transport/uptake of MNPs in MDCK cells on transwell inserts under different magnetic field application is expected to have an impact on the field of magnetic targeting and MRI.

1.2.5 Considerations in cell-based assay system for pharmacokinetic profiles

Due to the flexibility and low costs, *in vitro* cell-based model using the epithelial cells cultured on transwell inserts is useful for high throughput screenings of new chemical entities (NCE) or drug compounds with modified physicochemical properties. Epithelial cells are the main barrier for drug absorption when drug molecules are administered. Absorption of a drug molecule across cell barriers includes two stages: dissolution and membrane transfer. After administration, the drug molecule is dissolved

in the aqueous phases of the cell surface. The dissolved molecule is then transferred across the actual barrier composed of lipid bilayer membranes to reach the blood circulation. Then, the dissolved molecule crosses the biological membranes of the epithelial cells by two pathways of passive diffusion processes, transcellular (through the lipid bilayer membrane) and paracellular (*via* the pores of tight junctions), driven by a concentration gradient (93). The balance between the two pathways can be controlled by lipophilicity of the compound, which can be estimated by logP values (logarithm of octanol/water partition coefficient). At present, most of pharmaceutical research in industry or academia is focused on enhancing transcellular transport and increasing bioavailability in target sites with less toxicity or side-effects by reducing unnecessary accumulations of drug molecules.

The *in vitro* models with the respiratory cells (Calu-3 or 16HBE14o- cells) or other epithelial cells such as Caco-2, MDCK cells have been proven to be reliable models for the drug transport, so far (2, 36, 45). Yet, the experimental results found in various research sources show discrepancies caused by the different experimental settings or variations in the experimental system, even with the same drug molecules. The most reproducible and robust method should be established for measuring drug permeation and bioavailability by taking account of all the key factors determining drug transport measurements in order to guide more accurate data interpretation for reliable information. Transcellular transport of drug across cells could be affected by not only the physicochemical properties of drug molecules, but also cell surface properties - effective cellular penetrations could be determined by extracellular interactions between drug molecules and the cell surface. So far, few studies have been done to investigate

interactions between drug molecules and the cell surface, which is important to optimize drug absorption and distributions for better behaviors after drug administration. Different cell surface properties of different cells from various origins may influence the drug absorption, distribution and affect plasma concentrations, drug concentrations in target sites, and pharmacokinetic profiles (drug bioavailability, clearance, volume of distributions, eliminations).

Permeability and solubility are important pharmacokinetic properties as they are the main determinants of cellular penetration and bioavailability (increasing drug concentrations in plasma or target sites). There are several strategies to enhance drug permeability or solubility. Various co-solvents (*e.g.,* DMSO, ethanol, *etc*) have been used to resolve solubility issues, but those had disadvantages related to toxicity with the using doses (94, 95). Biocompatible reagents such as cyclodextrins, lipids or polymers have been utilized to increase solubility of poorly soluble drug molecules and also enhance transcellular permeability of drug compounds (96-99). Nanoparticle technologies have been also widely used to improve those properties of drug compounds in the market (100, 101). Moreover, the nanoparticles fabricated with active moieties such as antibodies or ligands have been used for active targeting to specific sites with less drug accumulation in unwanted sites (102, 103). The strategies using magnetic nanoparticles with externally applied magnetic field have been studied as a tool for active targeting or imaging as diagnosis or therapeutic purposes (*e.g.,* MRI) (104, 105). Different cell types may produce different extracellular environment under the physiological or diseased conditions; pH conditions, compositions of ions, membrane surface area/microvilli, development of mucins/proteoglycans, hydration properties, ciliary motility, diffusion

boundary layers. These factors determining the cell surface microenvironment can influence the extracellular interactions between the cells and drug molecules or the moieties of drug complexation agents or drug carriers and, in further, affect drug permeation and distribution.

The significance of my work shown herein is that the integration of permeability measurements using a cell-based model with microscopic imaging and mathematical modeling can help interpret drug transport assay data in a more accurate way to provide the pharmacokinetic profiles of drug-like candidates (ranging from small molecules to nanoparticles). This can be used as a rational guide for drug discovery through chemical modification for the purpose of drug targeting to overcome biological barriers.

1.2.6 Significance of cell microenvironment

Cell microenvironment refers to local surroundings with which cells interact through various chemical and physical signals and therefore has a profound influence on the behavior, growth and survival of cells (106). Biochemical components of cell microenvironment include molecules and compounds such as nutrients, hormones or growth factors in the fluid surrounding cells in organisms and play important roles in determining the characteristics of cells (cell heterogeneity). A physical component of a cell microenvironment includes the extracellular matrix (ECM) which provides not only mechanical and structural support to cells (107, 108), but also spatial coordination of signaling processes *via* soluble ligands or transmembrane receptors (109, 110). The ability of cells to sense the chemical, mechanical and topographical features of the ECM is important to maintain homeostasis including host defense immunity. Consequently, dysregulation or mutation of ECM components and fluid compositions may result in a

broad range of pathological conditions (106, 111-113). For instance, lung carcinoma was reported to express fewer integrins than did the normal bronchial epithelium (114). Thus, the cell microenvironment defines the physical and chemical interactions that control cellular physiology and fate. Cell microenvironment is known to play key roles in cancer progression and metastasis (115). Development of tight junctions in most cell barriers (*e.g.*, blood-brain barrier, intestine, lung) is crucial for transport control of xenobiotics (116, 117) and cells with intact tight junctions have been utilized for drug transport/absorption studies in various fields.

Major ECM components in epithelial cells/tissues are various types of collagens, elastin, microfibrillar proteins, non-collagenous glycoproteins, basement membrane proteoglycans, hyalectans, or small leucin-rich proteoglycans, and so on (118-122). Topographical, structural characteristics of ECM such as surface profile, shape (tortuosity), or porosity can affect the cell organization and also molecular transport (123). Porous membranes in the transwell inserts used for drug transport assays mimic the basemembrane beneath the cells in the physiological condition. Compositions or amount of coated materials (*e.g.*, collagen) (124-126) as well as pore sizes or densities in membranes (127, 128) affect drug transport/absorption across cells. In addition to the topography of the membrane, unstirred (or diffusion) water layer on the cell surface has been made data interpretation difficult. This physical barrier without defined boundary is affected by mixing conditions and also by heterogeneous cellular characteristics (*e.g.*, mucus secretion in intestinal or bronchial cells) in the *in vitro* or *in vivo* drug absorption studies (129-131).

In our body, various epithelial cells secrete different types of mucins which are heavily glycosylated, high-molecular weight proteins onto the cell surface. For example, tracheobronchial epithelial cells secrete mucins composed of epithelial mucins (MUC1, MUC4 and MUC16) and gel-forming mucins (MUC5B and MUC5AC) under air-liquid interfaced conditions (132). Airway surface liquid (ASL), the thin layer of fluid coating the airway epithelium, is composed of mucin, glycans, and macromolecules in water. Its composition and thickness are controlled by ion or water channels, providing hydration of cell surface and facilitating mucociliary clearance (133, 134). Mucociliary clearance is an important mechanism in the airway for innate lung defense and comprised of three components that influence drug transport/absorption in the lung: mucin secretion, and ciliary activity, ion transport activities controlling ASL. Pulmonary surfactants can also affect dissolution and permeability of particles from inhaled drug formulations (135, 136).

The amount, pH conditions, or composition (*e.g.*, ions, proteoglycans, other dissolved substances) of the fluidic phase in the cell microenvironment differ greatly depending on the origin of the cells (137). Many studies indicated that the tumor cell microenvironment has hypoxia (a reduction in oxygen tension) and an acidic interstitial fluid phase (138). Besides general ion channels, there are mechanosensitive ion channels (*e.g.*, K^+, Na^+, Ca^{2+} channels) expressed in the cells. In addition to integrin signaling in ECM, mechanosensitive ion channels can also regulate mechanoresponsiveness of cells and their fluidic phase environment through dynamic changes of ion substances (139, 140). Changes in ions in the cell surface could result in varied conditions in pH, hydrostatic and osmotic pressure, affecting transport of nutrients, signaling molecules, or drug molecules (141).

1.3 Questions and Hypotheses

As we discussed so far, cells have complex features in their structures and functions. Therefore, it is difficult to interpret drug transport phenomena solely based on intracellular organization and/or the properties of drug molecules. Many cases in drug transport system include multiple components besides drug molecules. In *in vitro* cell-based transport system, there could be chemical counterparts (solubilizing agents) or physical counterparts (external magnetic fields) of drug-like molecules in addition to biological cell barriers. It is important to consider the effects of multi-components on molecular interactions in the outer cell surface in the context of drug permeation across cell barriers. For the multi-component, cell-based transport assay system, we may ask the following questions and propose hypotheses according to these questions:

(1) Do interfacial phenomena at the cell surface play a major role in affecting the rate of cell barrier penetration under different conditions?

➔ Molecular interactions at the outer cell surface are the most critical determinants of transcellular transport.

(2) How does an external magnetic force affect the interactions between magnetic iron oxide nanoparticles (MNPs) and the cell surface?

➔ Externally applied magnetic fields may influence the MNPs' transport or cellular uptake by modulating extracellular interactions between particles and cells.

(3) Can the mechanistic cell-based pharmacokinetic model probe the effects of extracellular interactions on drug transport/accumulation in varied local regions of organs?

➔ Computational algorithms using the cellular pharmacokinetic model may help guide the data interpretations of molecular transport and cellular uptake.

(4) What are key parameters affecting drug transport/uptake in *in vitro* cell-based permeability assay system?

➔ Key parameters determining extracellular interactions of drug molecules might be predicted by the optimization algorithm in the mechanistic cellular pharmacokinetic model.

(5) Do solubilizing agents affect the local microenvironment on the cell surface?

➔ Solubilizing agents may affect permeation of drug molecules across the cell by controlling extracellular microenvironments.

1.4 Mechanisms of Extracellular Interactions

Mechanistically, we propose that cells vary greatly in surface properties and that this exerts the greatest influence on the pathway through which molecules are taken up by and make their way across cells. Multi-components in transport assays could interact with the cell surface properties, resulting in altered local microenvironments, and subsequently, passive transport of drug molecules. Depending on the assay system, various multi-components could co-exist with molecules or particles of interest.

By variations in the external magnetic force, magnetized particles could differentially interact with each other and exhibit varied particle distributions immediately on the cell surface, affecting the MNP's targeting. Quantitative transport assays with mass balance and microscopic imaging could exhibit how MNP transport/uptake is affected by extracellular interactions on the cell surface under spatiotemporal variations of magnetic field (pulsed *vs.* constant *vs.* no magnetic field).

Under physiological conditions, cell organization can lead to variations in the cell areas exposed to the drug molecules. Varied extracellular microenvironments along the airway to the alveoli in the lung exemplify the complex histology of the lung involving various factors including the secretion of substances on the cell surface, ion balance, hydration, pH conditions, ciliary motility, and physical structures of the ECM. In our system, we use physiologically-relevant cell models for *in vitro* cell-based permeability assays, together with collaborational works including an *in silico* model constructed with histological and physiological parameters of the lung and an *in vivo* animal model using local drug administration (intratracheal (IT) instillation). The integrated approach of *in vitro-in silico-in vivo* models could help to analyze the extracellular and/or intracellular components affecting local absorption/distribution of small molecules in airway *vs.* alveoli.

Unstirred water layers on the cell surface have been claimed to be absorption barriers for drug molecules in various *in vitro* and *in vivo* permeability studies. Effective diffusion aqueous layers could be measured according to varied stirring conditions in the experimental setup. However, the diffusion aqueous barriers could apparently reflect the combined variations of extracellular microenvironment factors related to extracellular

matrix and surface fluid, which renders difficult measurement of the barrier's thicknesses with bulk experimental methods. In our studies, the static aqueous layer components are incorporated into the mathematical cell-based pharmacokinetic model with the ranges of thicknesses based on the literature to reveal the effects of extracellular interactions of drug molecules on passive transport in the representative airway epithelial cell models.

Drug complexing agents such as cyclodextrins (CDs) are utilized in various pharmaceuticals due to the benefits of increasing drug solubility. The mechanism of the role of CDs to promote drug penetration into the cell membranes has been investigated in various scopes. A CD is a hydrophilic compound with a large molecular weight, making the drug-CD complex difficult to permeate across the cell membrane. However, the rapid equilibrium between the drugs in complex and the free drugs in the aqueous exterior could enable free drug permeations across the lipid membrane. Physiologically, diffusion aqueous barriers on the cell surface also impact drug transport in addition to the lipid membrane. Previous studies have shown that CDs can promote drug penetration with low toxicity by modulating the thicknesses of unstirred water layers. In our studies, the role of CDs would be investigated in the context of permeation and cell-association of a poorly water-soluble drug, curcumin, in the airway epithelial cell model, Calu-3, and airway tissues. Enhanced efficacy of curcumin advantaged by complexation with CDs would be confirmed by *in vivo* experiments with inflammatory conditions conducted by the collaborators.

1.5 Specific Aims

Accordingly, our studies presented herein evidence of the importance of molecular interactions at the outer cell surface in order to better understand cell barrier penetration, based on these specific aims to identify:

1) The effect of cell surface interactions on MNP aggregate formation leading to reduced cell barrier penetration in response to magnetic fields *in vitro*.
2) The effect of differences in cell surface area on the differential targeting of lipophilic cations to upper *vs.* lower airways *in vitro* (and *in silico, in vivo*).
3) The influence of differences in cell surface microenvironment as a likely explanation for the variation in transport rate in Calu-3 *vs.* NHBE cells *in vitro*.
4) The ability of cyclodextrin-curcumin complexes to promote curcumin transport across the Calu-3 cells *in vitro* (and *in vivo*).

The experiments that I performed were focused on probing the importance of the drug interactions on the cell surface using microscopic imaging, *in silico* modeling, and *in vitro* model systems with Transwell® inserts. Additionally, relevant *in vivo* studies and *in silico* modeling were performed by my collaborators.

1.6 References

1. Lennernäs H, Palm K, Fagerholm U, Artursson P. Comparison between active and passive drug transport in human intestinal epithelial (Caco-2) cells in vitro and human jejunum in vivo. Int J Pharmaceut. 1996;127(1):103-7.
2. Yamashita S, Tanaka Y, Endoh Y, Taki Y, Sakane T, Nadai T, et al. Analysis of drug permeation across Caco-2 monolayer: implication for predicting in vivo drug absorption. Pharm Res. 1997;14(4):486-91.
3. Reichel A. Addressing central nervous system (CNS) penetration in drug discovery: basics and implications of the evolving new concept. Chem Biodivers. 2009;6(11):2030-49.

4. Washington N, Washington C, Wilson C. Physiological pharmaceutics: barriers to drug absorption: CRC; 2000.
5. Amidon GL, Sinko PJ, Fleisher D. Estimating human oral fraction dose absorbed: a correlation using rat intestinal membrane permeability for passive and carrier-mediated compounds. Pharmaceut Res. 1988;5(10):651-4.
6. Amidon GL, Lennernäs H, Shah VP, Crison JR. A theoretical basis for a biopharmaceutic drug classification: the correlation of in vitro drug product dissolution and in vivo bioavailability. Pharmaceut Res. 1995;12(3):413-20.
7. Shen H, Smith DE, Yang T, Huang YG, Schnermann JB, Brosius III FC. Localization of PEPT1 and PEPT2 proton-coupled oligopeptide transporter mRNA and protein in rat kidney. American Journal of Physiology-Renal Physiology. 1999;276(5):F658-F65.
8. Borst P, Evers R, Kool M, Wijnholds J. A family of drug transporters: the multidrug resistance-associated proteins. Journal of the National Cancer Institute. 2000;92(16):1295-302.
9. Cao X, Gibbs ST, Fang L, Miller HA, Landowski CP, Shin H-C, et al. Why is it challenging to predict intestinal drug absorption and oral bioavailability in human using rat model. Pharmaceut Res. 2006;23(8):1675-86.
10. Battisti RF, Zhong Y, Fang L, Gibbs S, Shen J, Nadas J, et al. Modifying the sugar moieties of daunorubicin overcomes P-gp-mediated multidrug resistance. Molecular Pharmaceutics. 2007;4(1):140-53.
11. Theil FP, Guentert TW, Haddad S, Poulin P. Utility of physiologically based pharmacokinetic models to drug development and rational drug discovery candidate selection. Toxicol Lett. 2003;138(1-2):29-49.
12. Rowland M, Balant L, Peck C. Physiologically based pharmacokinetics in drug development and regulatory science: a workshop report (Georgetown University, Washington, DC, May 29-30, 2002). AAPS PharmSci. 2004;6(1):E6.
13. Rowland M, Peck C, Tucker G. Physiologically-based pharmacokinetics in drug development and regulatory science. Annu Rev Pharmacol Toxicol. 2011;51:45-73.
14. Baláž Š, Šturdík E. Kinetics of passive transport in water/membrane/water system. A mathematical description. General Physiology and Biophysics. 1985;4:105-8.
15. Baláž Š. Lipophilicity in trans-bilayer transport and subcellular pharmacokinetics. Perspectives in drug discovery and design. 2000;19(1):157-77.
16. Trapp S, Horobin RW. A predictive model for the selective accumulation of chemicals in tumor cells. Eur Biophys J. 2005;34(7):959-66.
17. Trapp S, Rosania GR, Horobin RW, Kornhuber J. Quantitative modeling of selective lysosomal targeting for drug design. European Biophysics Journal. 2008;37(8):1317-28.
18. Liu L, Pang KS. An integrated approach to model hepatic drug clearance. Eur J Pharm Sci. 2006;29(3-4):215-30.
19. Sun H, Zhang L, Chow EC, Lin G, Zuo Z, Pang KS. A catenary model to study transport and conjugation of baicalein, a bioactive flavonoid, in the Caco-2 cell

monolayer: demonstration of substrate inhibition. J Pharmacol Exp Ther. 2008;326(1):117-26.
20. Zhang X, Shedden K, Rosania GR. A cell-based molecular transport simulator for pharmacokinetic prediction and cheminformatic exploration. Mol Pharm. 2006;3(6):704-16.
21. Zhang X, Zheng N, Rosania GR. Simulation-based cheminformatic analysis of organelle-targeted molecules: lysosomotropic monobasic amines. J Comput Aided Mol Des. 2008;22(9):629-45.
22. Zhang X, Zheng N, Zou P, Zhu H, Hinestroza JP, Rosania GR. Cells on pores: a simulation-driven analysis of transcellular small molecule transport. Mol Pharm. 2010;7(2):456-67.
23. Zheng N, Zhang X, Rosania GR. Effect of phospholipidosis on the cellular pharmacokinetics of chloroquine. J Pharmacol Exp Ther. 2011;336(3):661-71.
24. Yu J-y, Rosania GR. Cell-based multiscale computational modeling of small molecule absorption and retention in the lungs. Pharmaceut Res. 2010;27(3):457-67.
25. FDA U. Challenge and opportunity on the critical path to new medical products. Rockville, MD: US Department of Health and Human Services US Food and Drug Administration Availabe at: http://www fda gov/downloads/Science Research/SpecialTopics/CriticalPathInitiative/CriticalPathOpportunitiesReports /ucm11411 pdf. 2004.
26. Hou T, Xu X. Recent development and application of virtual screening in drug discovery: an overview. Current pharmaceutical design. 2004;10(9):1011-33.
27. Kola I, Landis J. Can the pharmaceutical industry reduce attrition rates? Nature reviews Drug discovery. 2004;3(8):711-6.
28. Li AP. Screening for human ADME/Tox drug properties in drug discovery. Drug discovery today. 2001;6(7):357-66.
29. van de Waterbeemd H, Gifford E. ADMET in silico modelling: towards prediction paradise? Nature reviews Drug discovery. 2003;2(3):192-204.
30. Lipinski C, editor. Computational alerts for potential absorption problems: profiles of clinically tested drugs. Tools for Oral Absorption Part Two Predicting Human Absorption BIOTEC, PDD symposium, AAPS, Miami; 1995.
31. Lipinski CA, Lombardo F, Dominy BW, Feeney PJ. Experimental and computational approaches to estimate solubility and permeability in drug discovery and development settings. Adv Drug Deliver Rev. 2012.
32. Ekins S, de Groot MJ, Jones JP. Pharmacophore and three-dimensional quantitative structure activity relationship methods for modeling cytochrome P450 active sites. Drug metabolism and disposition. 2001;29(7):936-44.
33. Trapp S. Plant uptake and transport models for neutral and ionic chemicals. Environmental Science and Pollution Research. 2004;11(1):33-9.
34. Balaz S, Wiese M, Seydel JK. A kinetic description of the fate of chemicals in biosystems. Sci Total Environ. 1991;109-110:357-75.
35. Artursson P, Borchardt RT. Intestinal drug absorption and metabolism in cell cultures: Caco-2 and beyond. Pharmaceut Res. 1997;14(12):1655-8.

36. Irvine JD, Takahashi L, Lockhart K, Cheong J, Tolan JW, Selick HE, et al. MDCK (Madin-Darby canine kidney) cells: A tool for membrane permeability screening. J Pharm Sci. 1999;88(1):28-33.
37. Patton JS, Byron PR. Inhaling medicines: delivering drugs to the body through the lungs. Nat Rev Drug Discov. 2007;6(1):67-74.
38. Patton JS. Mechanisms of macromolecule absorption by the lungs. Adv Drug Deliver Rev. 1996;19(1):3-36.
39. Patton JS, Fishburn CS, Weers JG. The lungs as a portal of entry for systemic drug delivery. Proceedings of the American Thoracic Society. 2004;1(4):338-44.
40. Oversteegen L, Rovini H, Belsey MJ. Respiratory drug market dynamics. Nature reviews Drug discovery. 2007;6(9):695-6.
41. Schanker L, Mitchell E, Brown R. Species comparison of drug absorption from the lung after aerosol inhalation or intratracheal injection. Drug metabolism and disposition. 1986;14(1):79-88.
42. Sakagami M. In vivo, in vitro and ex vivo models to assess pulmonary absorption and disposition of inhaled therapeutics for systemic delivery. Adv Drug Deliver Rev. 2006;58(9):1030-60.
43. Tronde A, Bosquillon C, Forbes B. The isolated perfused lung for drug absorption studies. Drug Absorption Studies. 2008:135-63.
44. Forbes B. Human airway epithelial cell lines for< i> in vitro</i> drug transport and metabolism studies. Pharmaceutical science & technology today. 2000;3(1):18-27.
45. Steimer A, Haltner E, Lehr C-M. Cell culture models of the respiratory tract relevant to pulmonary drug delivery. Journal of aerosol medicine. 2005;18(2):137-82.
46. Lin H, Li H, Cho HJ, Bian S, Roh HJ, Lee MK, et al. Air-liquid interface (ALI) culture of human bronchial epithelial cell monolayers as an in vitro model for airway drug transport studies. J Pharm Sci. 2007;96(2):341-50.
47. Grainger CI, Greenwell LL, Lockley DJ, Martin GP, Forbes B. Culture of Calu-3 cells at the air interface provides a representative model of the airway epithelial barrier. Pharmaceut Res. 2006;23(7):1482-90.
48. Forbes II. Human airway epithelial cell lines for in vitro drug transport and metabolism studies. Pharm Sci Technolo Today. 2000;3(1):18-27.
49. Sporty JL, Horálková L, Ehrhardt C. In vitro cell culture models for the assessment of pulmonary drug disposition. 2008.
50. Rothen-Rutishauser B, Blank F, Mühlfeld C, Gehr P. In vitro models of the human epithelial airway barrier to study the toxic potential of particulate matter. 2008.
51. Mathias NR, Timoszyk J, Stetsko PI, Megill JR, Smith RL, Wall DA. Permeability characteristics of Calu-3 human bronchial epithelial cells: In vitro-in vivo correlation to predict lung absorption in rats. Journal of Drug Targeting. 2002;10(1):31-40.
52. Grainger C, Saunders M, Buttini F, Telford R, Merolla L, Martin G, et al. Critical Characteristics for Corticosteroid Solution Metered Dose Inhaler Bioequivalence. Molecular Pharmaceutics. 2012;9(3):563-9.

53. Patton JS, Brain JD, Davies LA, Fiegel J, Gumbleton M, Kim KJ, et al. The particle has landed--characterizing the fate of inhaled pharmaceuticals. J Aerosol Med Pulm Drug Deliv. 2010;23 Suppl 2:S71-87.
54. Kim K-J, Borok Z, Crandall ED. A useful in vitro model for transport studies of alveolar epithelial barrier. Pharmaceut Res. 2001;18(3):253-5.
55. Hermanns MI, Unger RE, Kehe K, Peters K, Kirkpatrick CJ. Lung epithelial cell lines in coculture with human pulmonary microvascular endothelial cells: development of an alveolo-capillary barrier in vitro. Lab Invest. 2004;84(6):736-52.
56. Elbert KJ, Schäfer UF, Schäfers H-J, Kim K-J, Lee VH, Lehr C-M. Monolayers of human alveolar epithelial cells in primary culture for pulmonary absorption and transport studies. Pharmaceut Res. 1999;16(5):601-8.
57. Huh D, Matthews BD, Mammoto A, Montoya-Zavala M, Hsin HY, Ingber DE. Reconstituting organ-level lung functions on a chip. Science. 2010;328(5986):1662-8.
58. Stella B, Arpicco S, Peracchia MT, Desmaële D, Hoebeke J, Renoir M, et al. Design of folic acid-conjugated nanoparticles for drug targeting. J Pharm Sci-Us. 2000;89(11):1452-64.
59. Panyam J, Labhasetwar V. Biodegradable nanoparticles for drug and gene delivery to cells and tissue. Adv Drug Deliver Rev. 2012.
60. Medarova Z, Pham W, Farrar C, Petkova V, Moore A. In vivo imaging of siRNA delivery and silencing in tumors. Nat Med. 2007;13(3):372-7.
61. Jain KK. The role of nanobiotechnology in drug discovery. Drug discovery today. 2005;10(21):1435-42.
62. Fernandez-Fernandez A, Manchanda R, McGoron AJ. Theranostic applications of nanomaterials in cancer: drug delivery, image-guided therapy, and multifunctional platforms. Appl Biochem Biotech. 2011;165(7):1628-51.
63. Brunner TJ, Wick P, Manser P, Spohn P, Robert N, Limbach LK, et al. In vitro cytotoxicity of oxide nanoparticles: comparison to asbestos, silica, and the effect of particle solubility. Environmental science & technology. 2006;40(14):4374-81.
64. Ferrari M. Cancer nanotechnology: opportunities and challenges. Nat Rev Cancer. 2005;5(3):161-71.
65. Chithrani BD, Ghazani AA, Chan WCW. Determining the size and shape dependence of gold nanoparticle uptake into mammalian cells. Nano Letters. 2006;6(4):662-8.
66. Gupta AK, Gupta M. Synthesis and surface engineering of iron oxide nanoparticles for biomedical applications. Biomaterials. 2005;26(18):3995-4021.
67. Slowing II, Trewyn BG, Giri S, Lin VY. Mesoporous silica nanoparticles for drug delivery and biosensing applications. Adv Funct Mater. 2007;17(8):1225-36.
68. Bulte JW. Magnetic nanoparticles as markers for cellular MR imaging. Journal of Magnetism and Magnetic Materials. 2005;289:423-7.
69. Hee Kim E, Sook Lee H, Kook Kwak B, Kim B-K. Synthesis of ferrofluid with magnetic nanoparticles by sonochemical method for MRI contrast agent. Journal of Magnetism and Magnetic Materials. 2005;289:328-30.

70. Lu AH, Salabas EL, Schuth F. Magnetic nanoparticles: synthesis, protection, functionalization, and application. Angew Chem Int Ed Engl. 2007;46(8):1222-44.
71. Cole AJ, David AE, Wang JX, Galban CJ, Yang VC. Magnetic brain tumor targeting and biodistribution of long-circulating PEG-modified, cross-linked starch-coated iron oxide nanoparticles. Biomaterials. 2011;32(26):6291-301.
72. Sun C, Lee JS, Zhang M. Magnetic nanoparticles in MR imaging and drug delivery. Adv Drug Deliver Rev. 2008;60(11):1252-65.
73. Chertok B, David AE, Yang VC. Polyethyleneimine-modified iron oxide nanoparticles for brain tumor drug delivery using magnetic targeting and intra-carotid administration. Biomaterials. 2010;31(24):6317-24.
74. Schwarz S, Wong JE, Bornemann J, Hodenius M, Himmelreich U, Richtering W, et al. Polyelectrolyte coating of iron oxide nanoparticles for MRI-based cell tracking. Nanomedicine: Nanotechnology, Biology and Medicine. 2012;8(5):682-91.
75. Chertok B, David AE, Moffat BA, Yang VC. Substantiating in vivo magnetic brain tumor targeting of cationic iron oxide nanocarriers via adsorptive surface masking. Biomaterials. 2009;30(35):6780-7.
76. Chertok B, David AE, Yang VC. Brain tumor targeting of magnetic nanoparticles for potential drug delivery: effect of administration route and magnetic field topography. J Control Release. 2011;155(3):393-9.
77. Chorny M, Fishbein I, Yellen BB, Alferiev IS, Bakay M, Ganta S, et al. Targeting stents with local delivery of paclitaxel-loaded magnetic nanoparticles using uniform fields. Proceedings of the National Academy of Sciences. 2010;107(18):8346-51.
78. Muthana M, Scott S, Farrow N, Morrow F, Murdoch C, Grubb S, et al. A novel magnetic approach to enhance the efficacy of cell-based gene therapies. Gene therapy. 2008;15(12):902-10.
79. Scherer F, Anton M, Schillinger U, Henke J, Bergemann C, Kruger A, et al. Magnetofection: enhancing and targeting gene delivery by magnetic force in vitro and in vivo. Gene therapy. 2002;9(2):102-9.
80. Kamau SW, Hassa PO, Steitz B, Petri-Fink A, Hofmann H, Hofmann-Amtenbrink M, et al. Enhancement of the efficiency of non-viral gene delivery by application of pulsed magnetic field. Nucleic Acids Research. 2006;34(5):e40-e.
81. Sonvico F, Mornet S, Vasseur S, Dubernet C, Jaillard D, Degrouard J, et al. Folate-conjugated iron oxide nanoparticles for solid tumor targeting as potential specific magnetic hyperthermia mediators: synthesis, physicochemical characterization, and in vitro experiments. Bioconjugate Chem. 2005;16(5):1181-8.
82. Kim D-H, Wong PK, Park J, Levchenko A, Sun Y. Microengineered platforms for cell mechanobiology. Annual review of biomedical engineering. 2009;11:203-33.
83. Yin Win K, Feng S-S. Effects of particle size and surface coating on cellular uptake of polymeric nanoparticles for oral delivery of anticancer drugs. Biomaterials. 2005;26(15):2713-22.

84. Lin Y-H, Chung C-K, Chen C-T, Liang H-F, Chen S-C, Sung H-W. Preparation of nanoparticles composed of chitosan/poly-γ-glutamic acid and evaluation of their permeability through Caco-2 cells. Biomacromolecules. 2005;6(2):1104-12.
85. Grenha A, Grainger CI, Dailey LA, Seijo B, Martin GP, Remuñán-López C, et al. Chitosan nanoparticles are compatible with respiratory epithelial cells< i> in vitro</i>. Eur J Pharm Sci. 2007;31(2):73-84.
86. Hu K, Li J, Shen Y, Lu W, Gao X, Zhang Q, et al. Lactoferrin-conjugated PEG–PLA nanoparticles with improved brain delivery:< i> In vitro</i> and< i> in vivo</i> evaluations. Journal of Controlled Release. 2009;134(1):55-61.
87. Kim HR, Gil S, Andrieux K, Nicolas V, Appel M, Chacun H, et al. Low-density lipoprotein receptor-mediated endocytosis of PEGylated nanoparticles in rat brain endothelial cells. Cellular and molecular life sciences. 2007;64(3):356-64.
88. Saiyed ZM, Gandhi NH, Nair MP. Magnetic nanoformulation of azidothymidine 5'-triphosphate for targeted delivery across the blood–brain barrier. Int J Nanomed. 2010;5:157.
89. Xie H, Zhu Y, Jiang W, Zhou Q, Yang H, Gu N, et al. Lactoferrin-conjugated superparamagnetic iron oxide nanoparticles as a specific MRI contrast agent for detection of brain glioma< i> in vivo</i>. Biomaterials. 2011;32(2):495-502.
90. Kopke RD, Wassel RA, Mondalek F, Grady B, Chen K, Liu J, et al. Magnetic nanoparticles: inner ear targeted molecule delivery and middle ear implant. Audiology and Neurotology. 2006;11(2):123-33.
91. Mondalek F, Zhang Y, Kropp B, Kopke R, Ge X, Jackson R, et al. The permeability of SPION over an artificial three-layer membrane is enhanced by external magnetic field. BioMed Central; 2006.
92. Barnes AL, Wassel RA, Mondalek F, Chen K, Dormer KJ, Kopke RD. Magnetic characterization of superparamagnetic nanoparticles pulled through model membranes. BioMagnetic Research and Technology. 2007;5(1):1.
93. Balimane PV, Chong S. Cell culture-based models for intestinal permeability: a critique. Drug discovery today. 2005;10(5):335-43.
94. Sharma A, Jain C. Techniques to enhance solubility of poorly soluble drugs: a review. Journal of Global Pharma Technology. 2010;2(2).
95. Hamid KA, Katsumi H, Sakane T, Yamamoto A. The effects of common solubilizing agents on the intestinal membrane barrier functions and membrane toxicity in rats. Int J Pharmaceut. 2009;379(1):100-8.
96. Davis ME, Brewster ME. Cyclodextrin-based pharmaceutics: past, present and future. Nature reviews Drug discovery. 2004;3(12):1023-35.
97. Zerrouk N, Corti G, Ancillotti S, Maestrelli F, Cirri M, Mura P. Influence of cyclodextrins and chitosan, separately or in combination, on glyburide solubility and permeability. European journal of pharmaceutics and biopharmaceutics. 2006;62(3):241-6.
98. O'driscoll C, Griffin B. Biopharmaceutical challenges associated with drugs with low aqueous solubility—The potential impact of lipid-based formulations. Adv Drug Deliver Rev. 2008;60(6):617-24.
99. Chen J, Ashton P, Smith TJ. Polymer-based, sustained release drug delivery system. Google Patents; 2002.

100. Hu J, Johnston KP, Williams III RO. Nanoparticle engineering processes for enhancing the dissolution rates of poorly water soluble drugs. Drug Dev Ind Pharm. 2004;30(3):233-45.
101. Shi J, Xiao Z, Kamaly N, Farokhzad OC. Self-assembled targeted nanoparticles: evolution of technologies and bench to bedside translation. Accounts of Chemical Research. 2011;44(10):1123-34.
102. Sanvicens N, Marco MP. Multifunctional nanoparticles–properties and prospects for their use in human medicine. Trends Biotechnol. 2008;26(8):425-33.
103. Byrne JD, Betancourt T, Brannon-Peppas L. Active targeting schemes for nanoparticle systems in cancer therapeutics. Adv Drug Deliver Rev. 2008;60(15):1615-26.
104. Bulte JWM. Magnetic nanoparticles as markers for cellular MR imaging. Journal of Magnetism and Magnetic Materials. 2005;289:423-7.
105. Ito A, Shinkai M, Honda H, Kobayashi T. Medical application of functionalized magnetic nanoparticles. Journal of bioscience and bioengineering. 2005;100(1):1-11.
106. Albelda SM, Buck CA. Integrins and other cell adhesion molecules. FASEB J. 1990;4(11):2868-80.
107. Buck CA, Horwitz AF. Cell surface receptors for extracellular matrix molecules. Annu Rev Cell Biol. 1987;3:179-205.
108. Akiyama SK, Nagata K, Yamada KM. Cell surface receptors for extracellular matrix components. Biochim Biophys Acta. 1990;1031(1):91-110.
109. Hynes RO, Naba A. Overview of the matrisome—an inventory of extracellular matrix constituents and functions. Cold Spring Harbor Perspectives in Biology. 2012;4(1).
110. Geiger B, Yamada KM. Molecular architecture and function of matrix adhesions. Cold Spring Harbor Perspectives in Biology. 2011;3(5).
111. Frantz C, Stewart KM, Weaver VM. The extracellular matrix at a glance. Journal of cell science. 2010;123(24):4195-200.
112. Juliano RL. Membrane receptors for extracellular matrix macromolecules: relationship to cell adhesion and tumor metastasis. Biochim Biophys Acta. 1987;907(3):261-78.
113. Ruoslahti E, Giancotti FG. Integrins and tumor cell dissemination. Cancer Cells. 1989;1(4):119-26.
114. Damjanovich L, Albelda S, Mette S, Buck C. Distribution of integrin cell adhesion receptors in normal and malignant lung tissue. Am J Resp Cell Mol. 1992;6(2):197.
115. Krishnan V, Stadick N, Clark R, Bainer R, Veneris JT, Khan S, et al. Using MKK4's metastasis suppressor function to identify and dissect cancer cell-microenvironment interactions during metastatic colonization. Cancer Metastasis Rev. 2012;31(3-4):605-13.
116. Tsukita S, Yamazaki Y, Katsuno T, Tamura A. Tight junction-based epithelial microenvironment and cell proliferation. Oncogene. 2008;27(55):6930-8.
117. Wolburg H, Lippoldt A. Tight junctions of the blood–brain barrier: development, composition and regulation. Vascular pharmacology. 2002;38(6):323-37.

118. Byron A, Humphries JD, Humphries MJ. Defining the extracellular matrix using proteomics. International Journal of Experimental Pathology. 2013.
119. Hynes RO. The extracellular matrix: not just pretty fibrils. Science. 2009;326(5957):1216-9.
120. Eerenstein W, Kalev L, Niesen L, Palstra TTM, Hibma T. Magneto-resistance and superparamagnetism in magnetite films on MgO and MgAl2O4. Journal of Magnetism and Magnetic Materials. 2003;258:73-6.
121. Ricard-Blum S. The collagen family. Cold Spring Harbor Perspectives in Biology. 2011;3(1).
122. Yurchenco PD. Basement membranes: cell scaffoldings and signaling platforms. Cold Spring Harbor Perspectives in Biology. 2011;3(2).
123. Keung AJ, Kumar S, Schaffer DV. Presentation counts: microenvironmental regulation of stem cells by biophysical and material cues. Annual review of cell and developmental biology. 2010;26:533-56.
124. Ho NF, Raub TJ, Burton PS, Barsuhn CL, Adson A, Audus KL, et al. Quantitative approaches to delineate passive transport mechanisms in cell culture monolayers. Transport Processes in Pharmaceutical Systems. 2000:219-316.
125. Bishop WP, Wen JT. Regulation of Caco-2 cell proliferation by basolateral membrane epidermal growth factor receptors. American Journal of Physiology-Gastrointestinal and Liver Physiology. 1994;267(5):G892-G900.
126. Sanders MA, Basson MD. Collagen IV regulates Caco-2 migration and ERK activation via α1β1-and α2β1-integrin-dependent Src kinase activation. American Journal of Physiology-Gastrointestinal and Liver Physiology. 2004;286(4):G547-G57.
127. Adson A, Raub TJ, Burton PS, Barsuhn CL, Hilgers AR, Ho NF, et al. Quantitative approaches to delineate paracellular diffusion in cultured epithelial cell monolayers. J Pharm Sci-Us. 1994;83(11):1529-36.
128. Zhang X, Zheng N, Zou P, Zhu H, Hinestroza JP, Rosania GR. Cells on pores: a simulation-driven analysis of transcellular small molecule transport. Molecular Pharmaceutics. 2010;7(2):456-67.
129. Adson A, Burton PS, Raub TJ, Barsuhn CL, Audus KL, Ho NF. Passive diffusion of weak organic electrolytes across Caco-2 cell monolayers: Uncoupling the contributions of hydrodynamic, transcellular, and paracellular barriers. J Pharm Sci-Us. 1995;84(10):1197-204.
130. Everitt C, Redwood W, Haydon D. Problem of boundary layers in the exchange diffusion of water across bimolecular lipid membranes. Journal of theoretical biology. 1969;22(1):20-32.
131. Khanvilkar K, Donovan MD, Flanagan DR. Drug transfer through mucus. Adv Drug Deliver Rev. 2001;48(2):173-93.
132. Kesimer M, Kirkham S, Pickles RJ, Henderson AG, Alexis NE, Demaria G, et al. Tracheobronchial air-liquid interface cell culture: a model for innate mucosal defense of the upper airways? Am J Physiol Lung Cell Mol Physiol. 2009;296(1):L92-L100.

133. Chambers LA, Rollins BM, Tarran R. Liquid movement across the surface epithelium of large airways. Respiratory physiology & neurobiology. 2007;159(3):256-70.
134. Davis CW, Lazarowski E. Coupling of airway ciliary activity and mucin secretion to mechanical stresses by purinergic signaling. Respiratory physiology & neurobiology. 2008;163(1):208-13.
135. Bur M, Huwer H, Muys L, Lehr C-M. Drug transport across pulmonary epithelial cell monolayers: effects of particle size, apical liquid volume, and deposition technique. Journal of aerosol medicine and pulmonary drug delivery. 2010;23(3):119-27.
136. Shah N, Shah V, Chivate N. Pulmonary Drug Delivery: A Promising Approach. Journal of Applied Pharmaceutical Science. 2012;2(06):33-7.
137. Haslene-Hox H, Tenstad O, Wiig H. Interstitial fluid–a reflection of the tumor cell microenvironment and secretome. Biochimica et Biophysica Acta (BBA)-Proteins and Proteomics. 2013.
138. Buscombe JR, Wong B. PET a tool for assessing the in vivo tumour cell and its microenvironment? Br Med Bull. 2013.
139. Martinac B. Mechanosensitive ion channels: molecules of mechanotransduction. Journal of cell science. 2004;117(12):2449-60.
140. Sun Y, Chen CS, Fu J. Forcing stem cells to behave: a biophysical perspective of the cellular microenvironment. Annu Rev Biophys. 2012;41:519-42.
141. Widdicombe J. Regulation of the depth and composition of airway surface liquid. J Anat. 2002;201(4):313-8.

Chapter 2

Transcellular Transport of Heparin-coated Magnetic Iron Oxide Nanoparticles (Hep-MION) Under the Influence of an Applied Magnetic Field

2.1 Background

Magnetic nanoparticles (MNPs) have been widely explored in biomedical applications, including drug/gene magnetofection, hyperthermia or cancer therapy and magnetic resonance imaging (MRI) (1). MNPs with iron cores (usually Fe_3O_4 or Fe_2O_3), also called magnetic iron oxide nanoparticles (MIONs), have superparamagnetic properties (2). Due to superparamagnetism, these particles generate significant susceptibility effects only in the presence of the external magnetic field. These properties are very useful to obtain MRI contrast enhancement, signal amplifications, and significant magnetic targeting efficiency. Due to the potential of "theranostics", many efforts have focused on modifying the sizes or surface coating materials of MNPs to stabilize the particles in suspension and increase efficiency for delivery (3). The surface coating of MNPs is critical for the stability as well as for the biodistribution and pharmacokinetics of MNPs. Without surface coating, the large hydrophobic surfaces of MNPs would induce interactions between the particles, resulting in aggregation and

precipitation. In addition, the surface coating of MNPs can protect them from the reticular endothelial system (RES) and therefore, prolong their systemic circulation *in vivo* (4, 5). Various coating materials have been used to minimize aggregation or precipitation under physiological conditions including both inorganic components (*e.g.*, silica, gold, gadolinium (Gd), carbon) and organic shells (*e.g.*, polymers, polysaccharides, proteins, lipids) (6-8).

Efficient magnetic targeting is highly dependent on physicochemical properties of MNPs, the strength of the applied magnetic force, and the particle pharmacokinetics. Efficient targeting occurs when the magnetic force is sufficient to overcome drag force. The magnetic force on a MNP is a function of the magnetic field gradient (flux density, ΔB), the core material's magnetic susceptibility (χ), and the core volume (V) as shown in equation 1.

$$F = \frac{\chi \cdot V}{\mu_0} B(\Delta B) \qquad (1)$$

where μ_0 is the magnetic permeability of free space. Volume is an adjustable property by particle size. Based on this equation, larger particles tend to be pulled toward the magnetic field. However, larger particles have the propensity for aggregating by themselves or as a result of magnetic field. Large number of particles captured by the magnetic field could block the blood vessel before the particle go into the target sites (9). It is quite challenging for the particles to go across the epithelial cell barriers into the systemic circulation or target tissues/organs under physiological conditions.

2.2 Rationale and Significance

To improve behavior of MNPs in pharmacokinetics, it is important to address the interactions between the MNPs and the magnetic field at the cell barriers. Cell permeability measurements could be useful to assess MNP transport and cellular uptake under various conditions (*i.e.* varying initial particle concentrations or magnetic field applications). Even though there have been many investigations in drug/gene delivery *in vitro* or *in vivo* and MRI, we have little knowledge about how extracellular interactions between particles and magnetic field could affect transcellular transport of MNPs.

Pharmacokinetic knowledge obtained from cell-based permeability assays has been an important basis for the high throughput screening of small molecular drugs (10, 11). In the simple, flexible *in vitro* cell-based permeability assays, various components contributing to drug transport could be analyzed more accurately, which could be difficult in the complex *in vivo* system. Herein, we use MDCK cells grown in the Transwell® inserts for the *in vitro*, proof-of-concept transport assays with MNPs. MDCK cells are known to be a generic epithelial cell model, and also used for round window membrane (RWM) model of the inner ear transport studies with MNPs (12-14). Based on this simple experimental design, we can investigate how MNPs are transported across the cellular barriers toward the magnetic field, which is important for improving various nanoparticle formulations using magnetic fields as promising pharmaceutical agents.

2.3 Abstract

In this study, magnetic iron oxide nanoparticles coated with heparin (Hep-MION) were synthesized and the transcellular transport of the nanoparticles across epithelial cell

monolayers on porous polyester membranes was investigated. An externally applied magnetic field facilitated the transport of the Hep-MION across cell monolayers. However, high Hep-MION concentrations led to an increased aggregation of nanoparticles on the cell monolayer after application of the magnetic field. Our results indicate that magnetic guidance of Hep-MION most effectively promotes transcellular transport under conditions that minimize formation of magnetically-induced nanoparticle aggregates. Across cell monolayers, the magnet's attraction led to the greatest increase in mass transport rate in dilute dispersions and in high serum concentrations, suggesting that magnetic guidance may be useful for in vivo targeting of Hep-MION.

2.4 Introduction

Magnetic iron oxide nanoparticles (MION) in colloidal dispersions have many different applications, including *in vitro* cell separation (15-17), drug delivery (18), gene delivery (i.e., magnetofection) (9, 19), tumor hyperthermia (20), and as magnetic resonance imaging (MRI) agents to enhance contrast of organs and tissues (21-23). Magnetic nanoparticles have raised a considerable amount of interest amongst pharmaceutical scientists, as vehicles to deliver genes or drug molecules to specific target sites. The transport of gene or drug molecules to specific target sites can be enhanced by the interaction of magnetic iron oxide nanoparticles with applied magnetic fields (14, 24). When therapeutics (drugs or genes) attached to the MION are injected at or near a target site and an external magnetic field applied, the therapeutic agents can be effectively concentrated in the target cells or tissues (25-27). Therefore, targeted drug or gene delivery with high efficacy and low side effects can be enhanced by using MION.

Mechanistically, various transport routes can be exploited for directing nanoparticles to specific sites of action within the living organism (28, 29). Epithelial cell monolayers are amongst the most important barriers limiting nanoparticle diffusion and distribution in the body. While lipophilic small molecules can easily diffuse across the plasma membranes of epithelial cells, molecules with larger size and less lipophilicity are not able to cross phospholipid bilayers (30, 31). Instead, they may be able to cross cell monolayers through gaps that may be present between cells, referred to as paracellular transport. We considered the possibility that transport of MION across cell monolayers may be facilitated by an external magnet field by attracting the particles and facilitating their passage between the cells. Transcellular transport of large hydrophilic molecules can be facilitated transporters, adsorptive or receptor-mediated transcytosis, which would be enhanced by high local concentrations of nanoparticles (32-34). Paracellular transport could also be facilitated simply by increasing the concentration of particles at the surface of the cells.

However, magnetic nanoparticle suspensions also have concentration-dependent stability issues, especially in the presence of a magnetic field. In the presence of a magnetic field, particles tend to attract to each other via strong magnetic dipole-dipole attractions between the particles (24, 35). Anisotropy of the forces between induced dipoles has been reported to cause the particles in dispersions to form linear chains (36). Moreover, the magnitude of the induced dipolar magnetic forces depends on the intensity of the applied magnetic field. When the magnetic nanoparticles orient in the direction created by the applied magnetic field, the induced dipole-dipole interactions become larger resulting in increased particle aggregation. To optimize these properties, various

synthetic methods have been developed to modulate the physicochemical properties of magnetic nanoparticles such as size, charge, and magnetic behavior (37-39). Surface coating methods have been developed to modify the nanoparticles with nontoxic and biocompatible stabilizers for practical biomedical applications of MION. Various polymeric coating materials such as dextran, carboxydextran, starch, and PEG (polyethylene glycol), etc. could be useful to prevent irreversible aggregation MION in aqueous or biological media.

In this study, the ferrite cores (maghemite (Fe_2O_3), magnetite (Fe_3O_4)) of MION coated with polymeric shells containing heparin were synthesized and evaluated in terms of the magnetization by applied magnetic field and transport across semipermeable membranes and epithelial cell monolayers. For testing, the Madin-Darby canine kidney (MDCK) epithelial cell line was used in the transport studies because they can differentiate into polarized columnar epithelium and form the cell monolayer with tight junctions when cultured on permeable membrane supports (40-42). MDCK cells are a common, model cell system to study passive and active, transcellular and paracellular transport mechanisms (41-43). We examined the superparamagnetic properties and stability of the Hep-MION suspensions. Then, we evaluated the transcellular transport of the Hep-MION in the presence and absence of an applied magnetic field. With the *in vitro* cell culture system, we studied how the applied magnetic field modulated the interactions of MIONs and cell monolayers. With microscopic observations, we monitored how the magnetic field affected the aggregation of particles in suspension and at the cell surface. We report that the ability of magnetic field to promote transport was

dependent on the concentration of nanoparticles, and was inhibited by the formation of particle aggregates at increasing particle concentrations.

2.5 Materials and Methods

Materials. Chemicals used to prepare the iron oxide nanoparticles were ferrous chloride tetrahydrate (Fluka), iron chloride hexahydrate (Sigma-Aldrich), and heparin sodium salt (Sigma, H4784). Lucifer Yellow (LY) was obtained from Sigma-Aldrich and DYNAL®-MPC-L magnet bar was purchased from Invitrogen (Carlsbad, CA). Transwell inserts with polyester membrane (pore size: 3 μm) were obtained from Corning Life Sciences (Lowell, MA). Dulbecco's Modified Eagle Medium (DMEM), Penicillin-Streptomycin, Dulbecco's phosphate buffered saline (DPBS), Fetal bovine serum (FBS), and Trypsin-EDTA solution were purchased from Gibco BRL (Invitrogen, Carlsbad, CA). All the chemicals used for preparation of Hank's balanced salt solution (HBSS) were purchased from Sigma-Aldrich (St. Louis, MO) and Fisher Scientific Co. (Pittsburgh, PA).

Synthesis of the Hep-MION. MION were synthesized according to the procedure previously reported by Kim *et al.* (44). The solution containing 0.76 mol/L ferric chloride and 0.4 mol/L of ferrous chloride (molar ratio of ferric to ferrous = 2:1) prepared at pH 1.7 under N_2 protection was added into a 1.5M NaOH solution under mechanical stirring. The mixture was gradually heated (1 ºC/min) to 78 ºC and held at this temperature for 1 h with stirring and N_2 protection. After the supernatant was removed by a permanent magnet, the wet sol was treated with 0.01 M HCl and sonicated for 1 h. The colloidal suspension of MION was filtered through a 0.45 μm and then a 0.22 μm membrane, followed by adjusting to a suspension containing 0.7 mg Fe/mL. Then, 200 mL of 0.7 mg

Fe/mL iron oxide nanoparticles were added to 200 mL of 1 mg/mL glycine under stirring condition, ultrasonicated for 20 min, and in further stirred for 2 hours. After free glycine was removed by ultrafiltration, the iron concentrations of the samples were measured by the inductively coupled plasma-optical emission spectroscopy (ICP-OES) analysis using the Perkin-Elmer Optima 2000 DV device (Perkin-Elmer, Inc., Boston, MA, USA), and then diluted to a concentration of 0.35 mg Fe/mL. As a final process, 100 mL of 0.35 mg Fe/mL of glycine-MION were added to 100 mL of 1 mg/mL heparin solution, under stirring condition and ultrasonication. The heparin-coated MION (Hep-MION) were obtained after free heparin was removed by ultrafiltration.

Physicochemical Characterization of the Hep-MION. Volume-weighted size and zeta potential of Hep-MION were measured with a NICOMP 380 ZLS dynamic light scattering (DLS) instrument (PSS, Santa Barbara, CA, USA), using the 632 nm line of a HeNe laser as the incident light. Transmission electron microscopy (TEM) using a JEOL 3011 high-resolution electron microscope (JEOL Tokyo, Japan) at an accelerated voltage of 300 kV. Samples were prepared by placing diluted particle suspensions on formvar film-coated copper grids (01813-F, Ted Pella, Inc, USA) and then dried at room temperature. Superparamagnetic properties of the Hep-MION were examined by using a superconducting quantum interference device (SQUID) (Quantum Design Inc., San Diego, CA, USA) at 25 ºC. The contents of irons in the magnetic nanoparticles were measured by the ICP-OES analysis and calibrated with an internal standard Yttrium and a work curve of iron standard samples from GFS Chemicals®. In order to test stability of the nanoparticles in the transport buffer, the sizes and distributions of nanoparticles in the various solutions such as water, HBSS with 1% FBS, or HBSS with 10% FBS were

measured after incubation at 37 ºC using NICOMP 380 ZLS DLS instrument. These nanoparticles solutions were also examined with a Nikon TE2000 inverted microscope (10 × objectives).

Transport of the Hep-MION across the polyester membrane. For the transport experiments using Hep-MION, the transport buffer, HBSS was prepared containing 137 mM NaCl, 5.4 mM KCl, 0.34 mM $Na_2HPO_4 \cdot 7H_2O$, 0.44 mM KH_2PO_4 (anhydrous), 1.3 mM $CaCl_2 \cdot 2H_2O$, 0.8mM $MgSO_4 \cdot 7H_2O$, 25 mM D-glucose in 1 L of Milli-Q water. As a buffering agent, 10 mM HEPES (4-(2-hydroxyethyl)-1-piperazine ethane sulfonic acid; $C_8H_{18}N_2O_4S$) was added to HBSS. The pH value of the HBSS with 10 mM HEPES was adjusted to be 7.4 by adding 1 N NaOH, and then used for the transport experiments after filtering through a 0.22 μm membrane. The transport experiments of Hep-MION were performed in 24-well culture plates with Transwell inserts of pore size 0.4 or 3 μm with sterile water or HBSS (pH 7.4) in the presence or absence of 1% or 10% FBS. Transport buffer (600 μL) at 37 ºC without the nanoparticles was added into the receiver chambers (basolateral compartments) in 24-well plates. The nanoparticle solution (100 μL of Hep-MION in transport buffer; 0.206, 0.2575, or 0.412 mg/mL) was added to the donor chamber (apical compartment) in Transwell insert with the polyester membrane. The insert containing the nanoparticle solution was transferred to the next well containing 600 μL of fresh transport buffer without the nanoparticles at each time point. After transport experiments were performed under stirring condition with VWR rocking platform shakers, the sample solutions were collected from the receiver (basolateral) sides at each time point and the donor (apical) side at the last time point. The solutions that might contain the remaining nanoparticles were also taken by washing the walls of

the donor sides and receiver sides with the transport buffer. Standard solutions for various concentration ranges (0.000515, 0.00103, 0.00206, 0.00412, 0.0103, 0.0206 mg/mL) were made by diluting the nanoparticle stock solution in sterile water (2.06 mg/mL) with the transport buffer. Two hundred μl of the standard solutions and all the samples were put into each well of Costar® 96-well cell culture plates (Corning Life Sciences), and the UV absorbance of the solutions in each well was measured at 364 nm by the UV plate reader (Powerwave 340, BioTEK, co.). The concentrations of the nanoparticles in all the samples were calculated based on this standard curve. The transcellular permeability coefficient, P_{eff} (cm/sec) was calculated by normalizing the mass transport rate (dM/dt) with the insert area, A_{insert} (0.33 cm^2) and apical concentration of nanoparticles, C_{ap} as shown in the following equation (2):

$$P_{eff} = \frac{\frac{dM}{dt}}{A_{insert} \cdot C_{ap}} \qquad (2)$$

With the magnet bar located beneath the plates, the transport experiments with shaking were also performed in order to assess the mass transport of nanoparticles in the presence of an applied magnetic field.

Transport of the Hep-MION across the cell monolayer. MDCK strain Ⅱ cells obtained from American Type Culture Collection (ATCC) (Manassas, VA) were maintained in 75-cm^2 flasks at 37 ºC in a 5% CO_2 containing humidified incubator. MDCK cells were cultured with media containing the DMEM with 2 mM L-glutamine, 4500 mg/l of D-glucose, and 110 mg/L of sodium pyruvate, 1× non-essential amino acids (Gibco 11140), 1% penicillin-Streptomycin (Gibco 10378), and 10% FBS. Culture media were changed every second day during the cultures. At confluency, MDCK cells were

trypsinized from the culture flasks and resuspended in the media. One hundred μL of the cell suspension with the density of 4×10^5 cells/cm^2 was added on the apical side of polyester membrane (0.33 cm^2, Transwell inserts, pore size: 3 μm) in 24-well culture plate containing 600 μL of media. After overnight incubation at 37 ºC in a 5% CO_2 atmosphere, the cell morphology and confluency were determined with the Nikon TE2000 microscope. Confluent cell monolayers seeded on transwell inserts in 24-well plates were rinsed twice by HBSS without the nanoparticles and incubated for 20 min in the HBSS with 10% FBS at 37 ºC in a 5% CO_2 atmosphere. After the incubation, transepithelial electrical resistance across the cell monolayer was measured at room temperature in each insert with the cells by Millipore Millicell® ERS electrodes. The inserts with the cells with TEER values higher than 150 Ω× cm^2 after 1 day's incubation was used for the transport experiments. All the transport experiments with or without the magnetic field were performed in the same way as described in the Experimental Section 2.4. The apical-to-basolateral transport experiments were conducted until 90 min with the magnetic bar (DYNAL®-MPC-L), while the experiments without the magnetic bar were performed until 120 min. Transcellular permeability coefficients, P_{eff} was calculated with the mass transport across the cell monolayer with equations (2). After the experiments, TEER was measured and the cell monolayer was examined with the microscope to verify the integrity of cell monolayer. Permeability of Lucifer Yellow (LY) was also measured with confluent cells on inserts to examine the intactness of the cell monolayer, using the Perkin-Elmer LS 55 fluorescence spectrometer (Ex 430 nm/Em 520 nm) to measure LY concentration changes in the basolateral compartment (with the aid of a standard curve). As a fluid phase marker, LY was used in order to examine endocytosis, in the presence or

absence of nanoparticles, with MDCK cells exposed to magnetic fields (45). Transport experiments were carried out by adding 80 μL of nanoparticle solution (0.322 mg/mL) and 20 μL of 10 mM Lucifer Yellow in the apical side with or without the magnetic field. After 90 min, the walls of apical side and basolateral side were rinsed twice with DPBS and the cells on the membrane in the insert were detached by trypsinization. The cells were examined in 96-well optical bottom plates on the Nikon TE2000S epifluorescence microscope using a standard FITC filter set acquisition channel (100 × objectives). Images were acquired with a CCD camera (Princeton Instruments). All the cell images were analyzed with Adobe photoshop and Metamorph® software.

2.6 Results and Discussion

2.6.1 Physicochemical Characterization of the Hep-MION Nanoparticles

Tissue targeting by magnetic nanoparticles depends on the magnetic susceptibility, size distribution and superparamagnetic properties of MION (35, 37-39). The magnetization/demagnetization curves of Hep-MION exhibited superparamagnetic behaviors without any hysteresis loop or remanence (Figure 1a). With increasing magnetic field (Gauss), the magnetization curves reached a plateau at high magnetic fields. As the applied magnetic field decreased, the Hep-MION became demagnetized and finally had negligible remnant field in the absence of an applied magnetic field. The remnant field of these nanoparticles was almost zero in the absence of an applied magnetic field. Our results were consistent with SQUID magnetization/demagnetization curves of different MION superparamagnetic nanoparticles (46). The lowered saturation magnetization (70 emu/g Fe) compared to bulk magnetite (92 emu/g Fe) is a phenomenon

that is commonly observed with magnetic nanoparticles (47). This has been typically attributed to the surface effects arising from a magnetically inactive layer covering the ferrite cores (maghemite (Fe_2O_3), magnetite (Fe_3O_4)). The saturation magnetization has also been shown to be dependent on synthesis methods and also particle size; decreasing as particle size is reduced (48, 49). The hydrodynamic size and zeta potential of the Hep-MION nanoparticles were 40.6 nm (±30 nm) and -51.2 mV, respectively. TEM images showed that these nanoparticles had small sizes around 10 nm which were smaller than the hydrodynamic size measured by light scattering in water (Figure 1b). According to previous studies, MION particles 6–15 nm in diameter can have a single magnetic domain with superparamagnetic properties, so they can be used for effective magnetic targeting or imaging (50).

2.6.2 Stability of the Hep-MION Nanoparticle Dispersions

The colloidal dispersions of Hep-MION were stable in water and maintained the hydrodynamic size distribution of the particles at room temperature even after the nanoparticles were stored at 4 ºC more than 1 year. To examine the stability of Hep-MION in physiological conditions, the nanoparticles were diluted in various buffers. Brown precipitates formed in PBS (phosphate buffered saline) without calcium and magnesium ions within 40 min at room temperature (data not shown). Larger precipitates formed in HBSS (cell culture medium containing calcium and magnesium ions). In the presence of 1% fetal bovine serum (FBS) added into HBSS, brown precipitates were visible after 5 h incubation at 37 ºC (data not shown). However, when FBS was added at higher concentrations (10%), the suspension of nanoparticles did not exhibit precipitates, even after 24 h incubation at 37 ºC. Therefore, serum components appeared to stabilize

these nanoparticle suspensions. To confirm these observations, hydrodynamic sizes of nanoparticles of different three batches in various solutions were measured after incubation at 37 ºC during different time period (Figure 2). Dynamic light scattering histograms (DLS plots) demonstrate the larger average values of particle size in HBSS containing 1 % FBS, compared to the samples in water or HBSS with 10 % FBS (Figure 2a, b, and c) after 24 h incubation at 37 ºC. After 5 h incubation, the average hydrodynamic sizes of the nanoparticles of three different batches in water, HBSS with 10% FBS, or 1% FBS were 57.93 nm (±9.10 nm), 76.70 nm (±7.33 nm), or 3515.53 nm (±260.23 nm), respectively (Figure 2d). The narrow size distribution of nanoparticle suspension in water or HBSS with 10% FBS was not changed during the incubation period, but the particle sizes in HBSS with 1% FBS showed an increase in size and size distribution during the incubation period up to 24 h (Figure 2d) consisting with the formation of aggregates of increasing size.

By visual inspection, we also determined how magnetic attraction patterns of Hep-MION varied in the presence of an applied external magnetic field (DYNAL®-MPC-L) in various buffer conditions. As time passed under the applied magnetic field, more iron oxide nanoparticles attracted to the magnet were visible as brown precipitates in HBSS with 10% FBS or water. In addition, the reversibility of magnetically-induced nanoparticle aggregates was examined in the capillary tubes in the presence of the applied magnetic field under various buffer conditions. In water or HBSS with 10% FBS, the particles attracted by the magnetic became dispersed again, after the applied magnetic field was removed (data not shown).

2.6.3 Transport of the Hep-MION across Porous Membranes

Aggregation of Hep-MION dispersions in HBSS with 1% FBS occurred gradually over a 24 h period (Figure 2c and d). Upon 24h incubation, the measured aggregate size appeared greater than the membrane pore size. To minimize buffer-induced aggregation and establish the effect of magnetic fields on Hep-MION permeability across porous membranes, transport experiments were performed with nucleopore polyester membranes with the pore size of 3 μm within 1 min upon dispersion in transport buffers. In the case of 0.206 mg/mL of nanoparticles in HBSS with 10% or 1% FBS, the P_{eff} approximately doubled in the presence of the magnetic field. At higher nanoparticle concentrations in the absence of a magnetic field, permeability of Hep-MION was greater in 10% FBS vs. 1% FBS (Table 1), suggesting that components in serum are affecting the diffusion behavior of nanoparticles across the membrane pores. With 0.412 mg/mL of nanoparticles in HBSS with 1% FBS, P_{eff} was 2.4-fold higher in the presence of a magnetic field. In HBSS with 10% FBS, the difference in P_{eff} in the presence or absence of the magnetic field became smaller with increasing nanoparticle concentrations. Therefore, the effect of the magnetic field on the transport of Hep-MION appears to be a complex function of both the concentration of the particles in the solution, as well as the effect of the medium on the stability of the dispersions and the diffusion of the particles across the membrane pores.

2.6.4 Transport of the Hep-MION across Cell Monolayers Promoted by a Magnetic Field

Next, transcellular transport experiments with Hep-MION were performed using MDCK cells grown on the polyester membrane (pore size: 3 μm). The experimental set

up consisted of the cells sitting on the porous membrane in the Transwell insert of 24-well plate, and buffer solutions in apical (donor chamber) and basolateral sides (receiver chamber) (Figure 3a). Applied magnetic field was provided by a permanent magnet at the bottom of the insert. As indicated, the upper boundary of buffer containing Hep-MION dispersions was separated from the surface of the magnet by 7 mm and the distance between the nucleopore membrane and magnet was 4 mm. As the magnetic field was applied from underneath the plate, Hep-MION dispersions were attracted towards the membranes. Based on magnetic field measurements (Figure 3b), the strength of the magnetic field at the level of the cell monolayer (4 mm-distance from magnet) was 100 millitesla while at the upper boundary of the nanoparticle dispersions (7 mm-distance from magnet) was about 65 millitesla. According to this experimental set up, in apical-to-basolateral transport experiments, the permeability coefficients (P_{eff}) of membranes covered by cell monolayers were about 3 orders of magnitude less than membranes without cells (Table 1 and Table 2). The rate of mass transport of nanoparticles across cell monolayer was greater in the presence than in the absence of the applied magnetic field (Figure 4a and 4b). The nanoparticles with high concentration (0.412 mg/mL) showed much lower mass transport at each time point than the nanoparticles of 0.2575 mg/mL under the applied magnetic field. The calculated permeability and mass transport rate across MDCK cell monolayers increased approximately ten-fold when the transport experiments were conducted in the presence of the applied magnetic field (Table 2). Based on t-test results, the permeability behaviors of iron oxide nanoparticles in the presence of an applied magnetic field were significantly different from those without the magnetic field. Nevertheless, the permeability enhancing effect of the magnetic field was

much greater in low concentrations (0.2575 mg/mL) of nanoparticles than higher concentrations (0.412 mg/mL; Table 2).

As a reference and internal control, we compared the permeability of Hep-MION at two different concentrations (0.2575 and 0.412 mg/mL) with the permeability of Lucifer Yellow (LY; 10 μM) in the same solution. LY is a soluble cell impermeant marker of paracellular transport. The permeability of 0.2575 mg/mL of nanoparticles without a magnetic field was slightly greater than the LY permeability (Figure 4c), while the permeability of 0.412 mg/mL of nanoparticles without magnetic field was similar to LY permeability ($p = 0.149$). Most remarkably, the permeability of Hep-MION under the applied magnetic field was much greater and statistically different from that of LY permeability (p-value $< 10^{-7}$ (0.2575 mg/mL) and $< 10^{-4}$ (0.412 mg/mL); Figure 4c), indicating that the permeability enhancement is due to a specific effect of the magnetic field on the particles. When the mass transport rates (*dM/dt*) were compared for different concentrations of Hep-MION under the same experimental conditions, *dM/dt* in low concentration (0.2575 mg/mL) of Hep-MION was higher than that of high concentration (0.412 mg/mL) of nanoparticles. Although we cannot explain the reason behind this difference it appeared to be statistically significance (Figure 4d; $p < 0.05$).

2.6.5 Accumulation of Hep-MION on Cell Monolayers Induced by a Magnetic Field

After the transport experiments, the cell monolayer on the inserts was examined with a microscope. There were dark regions on the cell monolayer exposed to a magnetic field even after various washing steps, suggesting nanoparticles were strongly bound or internalized by the cells (Figure 5). Without the magnet, the cell monolayer in the

treatment group (0.2575 or 0.412 mg/mL) was not different from the control cell monolayer without the nanoparticles (Figure 5a). However, after the transport experiments with the magnet, the cell monolayer in the treatment group became dark with nanoparticles. At high nanoparticle concentrations, nanoparticle aggregates were visible as opaque patches covering the cells (Figure 5b). From these observations (Figure 4 and 5), we cannot distinguish if Hep-MION are transported across the cell monolayer by transcellular or paracellular pathways. In either case, the transcellular transport of Hep-MION at low concentration (0.2575 mg/mL) could be facilitated by the increased concentration of particles at the cell surface. Transcellular transport of Hep-MION at high concentration (0.412 mg/mL) can be enhanced by the magnetic field to some degree, but the effect of the magnet at high concentration seems to be much smaller than at low concentration because particles can form large aggregates, upon interacting with the cells and with each other.

In order to determine whether the magnetically-induced particle associated with cells was specific to magnetized particles, the transport experiments were performed using LY as an internal, soluble reference marker. Cells were exposed to nanoparticles and LY, in the presence and absence of a magnetic field. After the experiments, cells were detached and examined by epifluorescence microscopy (Figure 6). LY served as a fluorescent fluid phase marker and showed endocytosed vesicles inside the cells (45). The overall size or distributions of LY positive vesicles inside the cells were relatively similar, in the presence and absence of the magnetic field. Therefore the ability of the magnetic field to promote the accumulation of Hep-MION on the cell monolayer is the result of a specific interaction between the magnetic field and the particles, as it does not

affect the interaction between the cells and LY, a soluble fluid phase marker of pinocytic uptake.

2.7 Conclusions

Hep-MION is a viable, candidate magnetic carrier for drug targeting or magnetic resonance imaging (MRI). In addition to the observed superparamagnetic properties, these magnetic nanoparticles have narrow size distribution and remain dispersed in physiological medium containing high serum concentrations so their physicochemical and stability properties are consistent with *in vivo* application. Hep-MION at high concentrations can form aggregates, especially in the presence of a magnetic field (51, 52). In the presence of a porous membrane or a cell monolayer, the diffusion of the particles at the membrane or cell monolayer surface becomes limited, leading to accumulation of particle aggregates at the cell or membrane surface. Accordingly, the effect of a magnetic field on the permeability of particles across porous membranes or cell monolayers is lower at high particle concentrations compared to lower particle concentrations. Low concentration of Hep-MION (0.2575 mg/mL) was less responsive to the magnetic field than higher concentration (0.412 mg/mL), but because the induced aggregates were smaller, the magnetically-induced increase in nanoparticle transport across nucleopore membranes or cell monolayers was relatively greater.

2.8 Acknowledgements

This work was supported by NIH Grant RO1-GM078200 to G.R.R. K.A.M. expresses thanks for the support from Upjohn Fellowship from the College of Pharmacy

at The University of Michigan. Authors would like to thank Yongzhuo Huang and Allan E. David for technical advice and critical reviews. We also thank Lei Zhang and Adam J. Cole for technical support.

2.9 Tables

Table 2-1. Comparing the transport behavior of Hep-MION in HBSS with 10% or 1% FBS, with or without the applied magnetic field.
Permeability coefficients (P_{eff}) were assessed with three different concentrations of nanoparticles (0.206, 0.2575 or 0.412 mg/mL) in triplicates. Average values of P_{eff} are displayed with standard deviations in the parenthesis.

Concentration of Hep-MION	**HBSS with 10% FBS**		**HBSS with 1% FBS**	
	Magnet (-)	**Magnet (+)**	**Magnet (-)**	**Magnet (+)**
	P_{eff} **(10^{-3} cm/sec)**		P_{eff} **(10^{-3} cm/sec)**	
0.206 mg/mL	3.19 (0.425)	7.21 (0.53)	3.04 (0.449)	6.77 (1.53)
0.2575 mg/mL	5.73 (0.272)	8.47 (0.408)	2.67 (0.544)	6.67 (0.679)
0.412 mg/mL	6.72 (0.17)	7.85 (0.849)	2.45 (0.425)	5.88 (0.736)

Table 2-2. Transport behavior of Hep-MION dispersions (0.2575 or 0.412 mg/mL) with or without an applied magnetic field.
The average and standard deviation (S.D.) of three different batches are displayed. The p-values (two-tails) were assessed with two sample t-test with equal variance (significance level: $p < 0.05$).

	P_{eff} (10^{-6} cm/sec)				dM/dt (10^{-7} mg/sec)			
Concentration (mg/mL)	**0.2575**		**0.412**		**0.2575**		**0.412**	
Magnet	-	+	-	+	-	+	-	+
Average	4.2	24	0.9	6.6	3.5	20	1.2	9
S.D.	0.8	3.7	0.5	0.7	0.7	3.2	0.7	1.0
p-value	5.81×10^{-3}		3.94×10^{-4}		5.81×10^{-3}		3.94×10^{-4}	

2.10 Figures

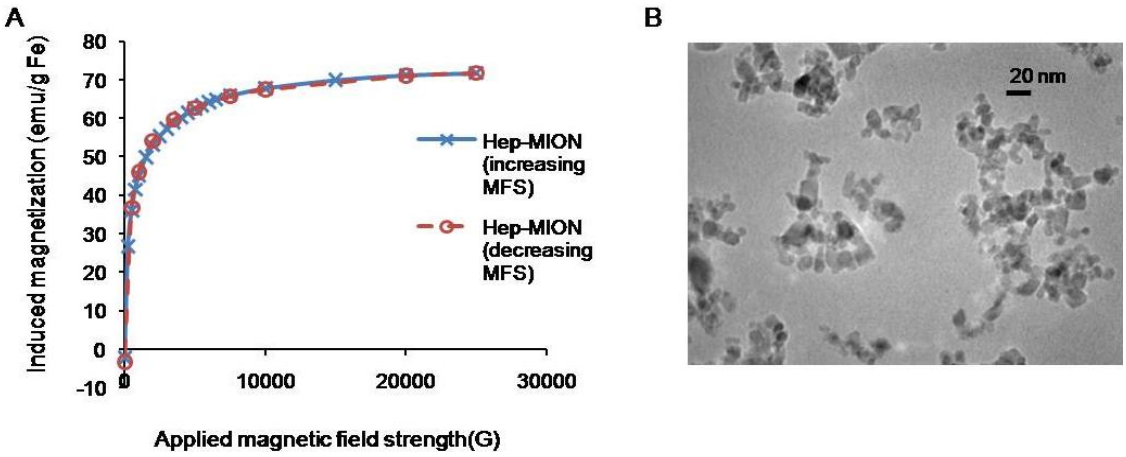

Figure 2-1. Physicochemical characterization of Hep-MION.

(**a**) Magnetization of the Hep-MION was displayed as a function of applied magnetic field (Gauss) in a range between 0 and 30,000 G by using the SQUID at 25 ºC. The magnetization data from SQUID analysis were normalized by Fe content with the unit of emu per gram of Fe. The magnetization curve of the Hep-MION under increasing magnetic field (MFS) overlapped with the demagnetization curve under decreasing magnetic field, consistent with the expected superparamagnetic properties of Hep-MION. (**b**) Transmission electron microscopic images were captured at an accelerated voltage of 300 kV. Scale bar on the image is 20 nm.

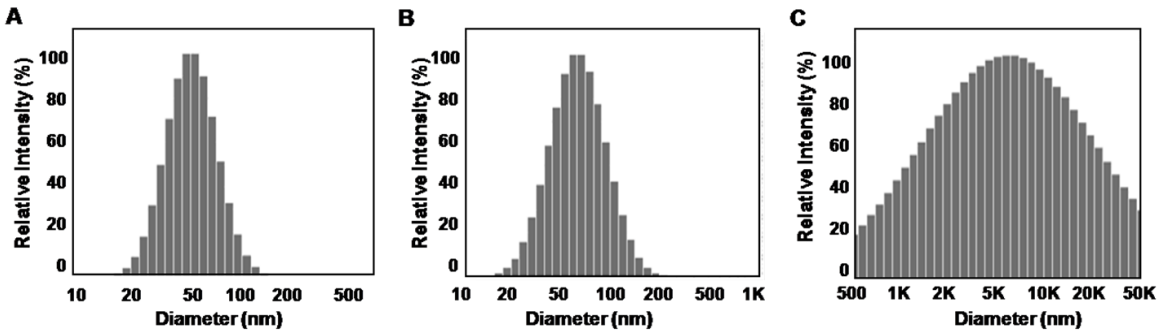

D

Buffer		Water			HBSS + 10 % FBS			HBSS + 1 % FBS		
Incubation (h)	**Time**	**0 h**	**5 h**	**24 h**	**0 h**	**5 h**	**24 h**	**0 h**	**5 h**	**24 h**
Average (nm)	**Size**	61.37	57.93	59.50	75.47	76.70	76.37	1053.27	3515.53	17659.43
S.D. (nm)		6.07	9.10	6.38	6.31	7.33	7.46	66.82	260.23	1243.76

Figure 2-2. Stability of Hep-MION dispersions in physiological buffers.

Dynamic light scattering histograms of Hep-MION in water (**a**), HBSS with 10% FBS (**b**), and HBSS with 1% FBS **(c)** after 24 h incubation at 37 ºC. Relative intensity values (%) are displayed with diameters (nm) in a log-scale. Particle size measurement of Hep MIONs (**d**) in three different batches in HBSS with 1% FBS, 10% FBS, or water after incubation at 37 ºC for 0, 5 and 24 h (n = 3). Sizes and distributions of nanoparticles in the various solutions (water, HBSS with 1% FBS, or HBSS with 10% FBS) were measured using NICOMP 380 ZLS DLS instrument after incubation at 37 ºC.

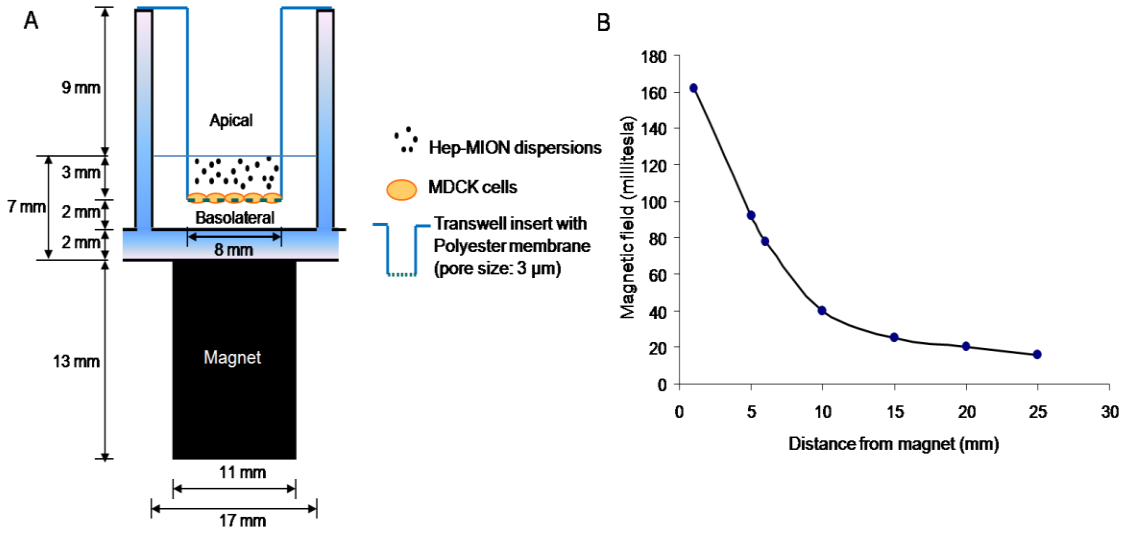

Figure 2-3. Diagram of the experimental set up.

(**a**) The cells were seeded on the polyester membrane (pore size: 3 µm) in Transwell inserts. One magnet (11 mm × 13mm) was placed beneath the well. Hep-MION dispersions were added into the apical compartment (donor chamber) to be transported through the porous membrane into the basolateral compartment (receiver chamber) containing transport buffer. Lengths and widths of the insert in the 24-well plate and magnet are displayed as millimeters. (**b**) Applied magnetic field of the magnet decreases with the increasing distance from the magnet. A 3-axis Hall Teslameter (THM 7025, GMW Associates, San Carlos, CA) was used to measure the magnetic field. X-axis of the graph represents the vertical distance from the magnet's surface.

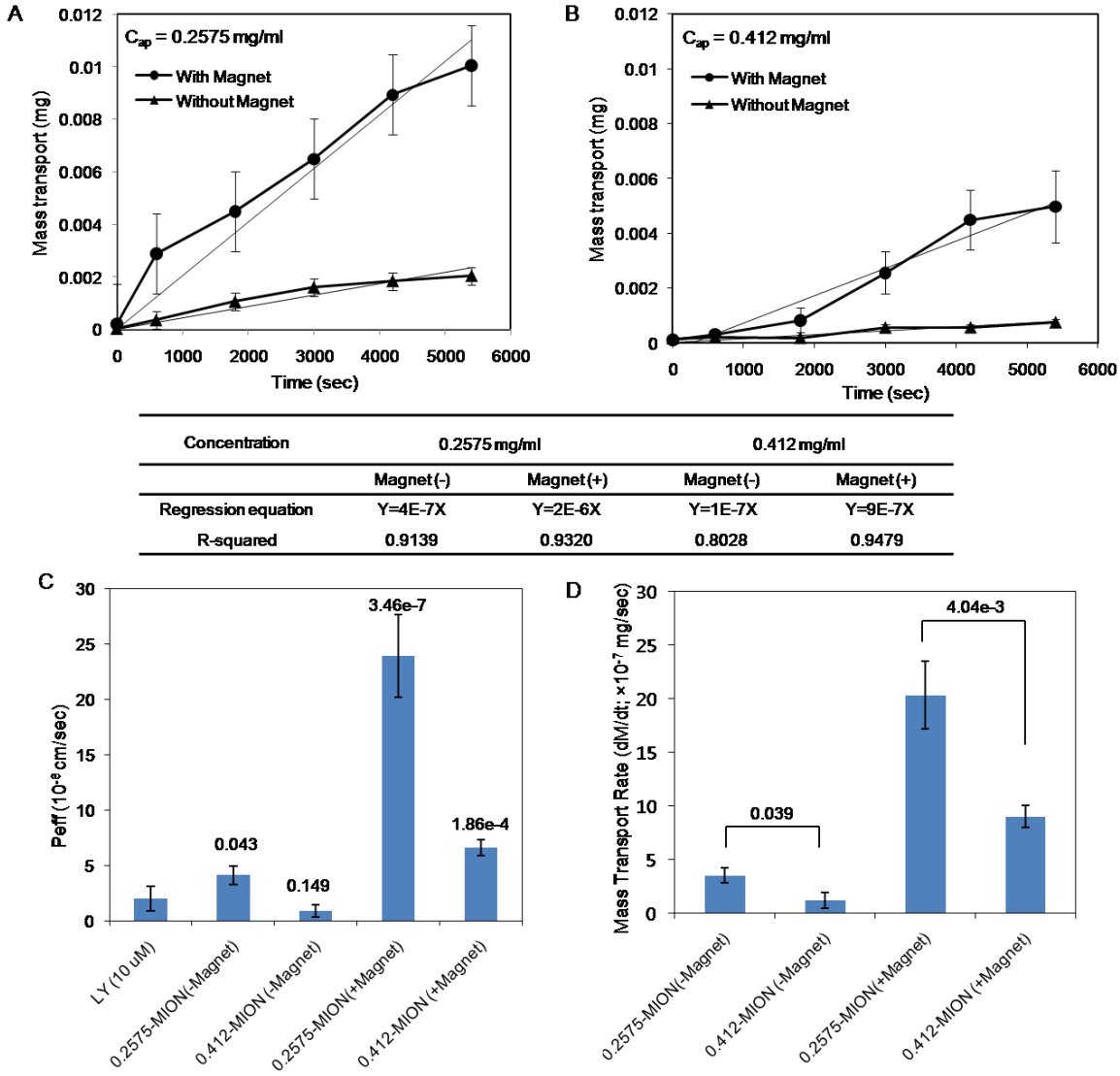

Concentration	0.2575 mg/ml		0.412 mg/ml	
	Magnet(-)	Magnet(+)	Magnet(-)	Magnet(+)
Regression equation	Y=4E-7X	Y=2E-6X	Y=1E-7X	Y=9E-7X
R-squared	0.9139	0.9320	0.8028	0.9479

Figure 2-4. Quantitative analysis of apical-to-basolateral (AP-to-BL) mass transport of Hep-MION across MDCK cell monolayers.

Transport experiments across confluent monolayers were performed with Hep-MION dispersions at 0.2575 (**a**) or 0.412 mg/mL (**b**) in HBSS with 10% FBS. Experiments were performed in triplicates and standard error bars are shown. Equations and R^2 values of the regression lines of mass transport as a function of time for the apical concentration (C_{ap}; 0.2575 and 0.412 mg/mL) are displayed in the table. (**c**) The permeability coefficient, P_{eff} values of the nanoparticles (C_{ap}; 0.2575 and 0.412 mg/mL) were compared with the permeability of Lucifer Yellow (LY). P-values of t-test results are indicated over the each bar. (**d**) The mass transport rates (*dM/dt*) of the nanoparticles (C_{ap}; 0.2575 and 0.412 mg/mL) were displayed with p-values of t-test results to show the different effects of

concentration of Hep-MION on the transcellular transport in the presence or absence of the applied magnetic field.

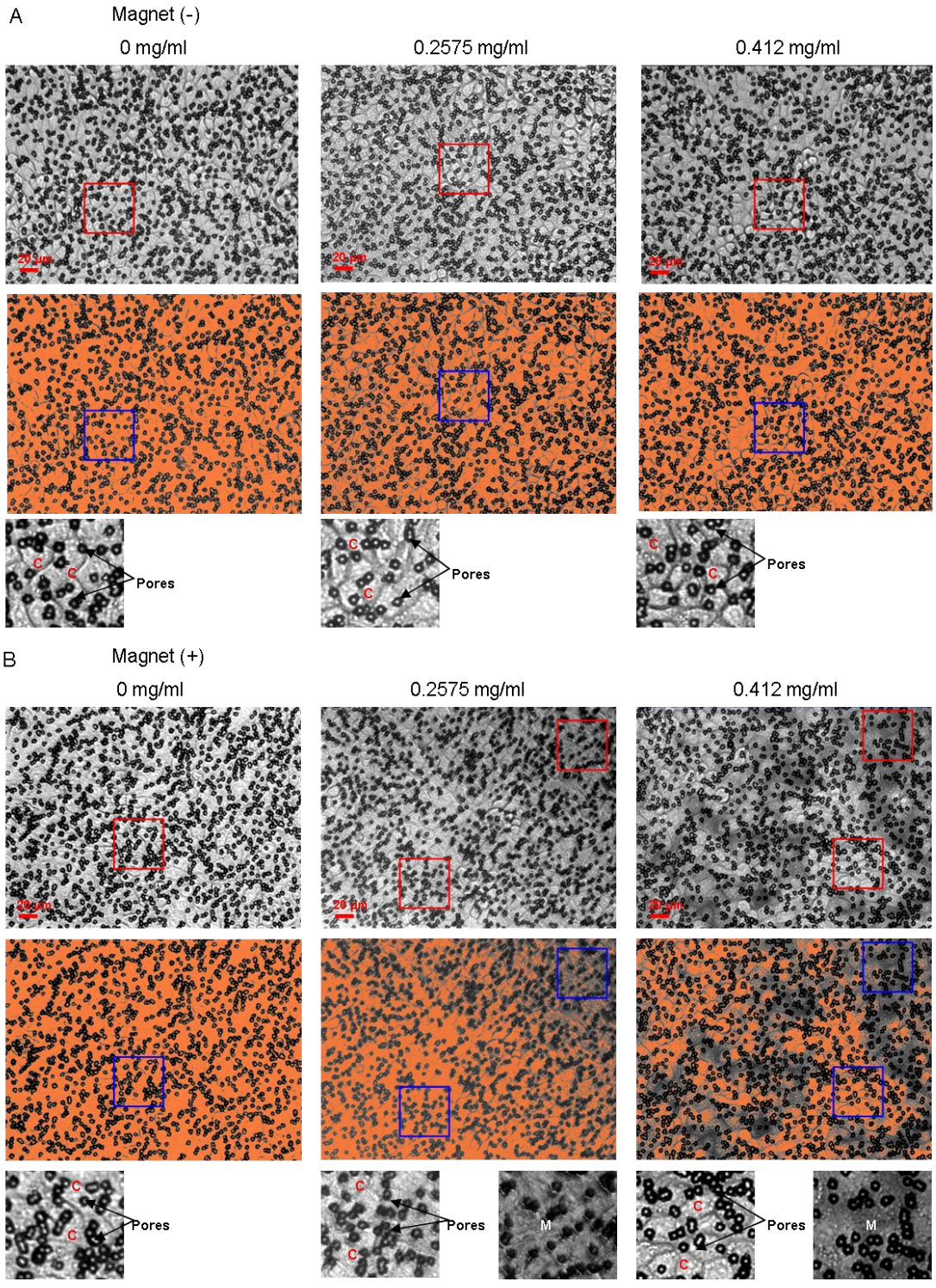

Figure 2-5. Bright field microscopy of MDCK cell monolayers on polyester membrane (pore size: 3 μm) after transport experiments with Hep-MION.

The cell monolayer without (**a**) or with the magnetic field (**b**) is shown (20 × magnifications). Beneath each image of the cell monolayers, the regions of the monolayer

that do not exhibit shading due to the dark nanoparticle aggregates are highlighted in orange. Zoom-in regions are indicated with red and blue boxes in the original and highlighted orange images. The dark pores (size: 3 μm) (indicated with arrows labeled "Pores") are randomly distributed on the membrane and pointed to in the zoom-in images with the cells (**c**). With an applied magnetic field, the darker regions (in zoom-in images) of the cell monolayer reflect accumulation of magnetic nanoparticles ("M") in association with the cell monolayer (0.2575 or 0.412 mg/mL). Scale bar corresponds to 20 μm in the bright field images.

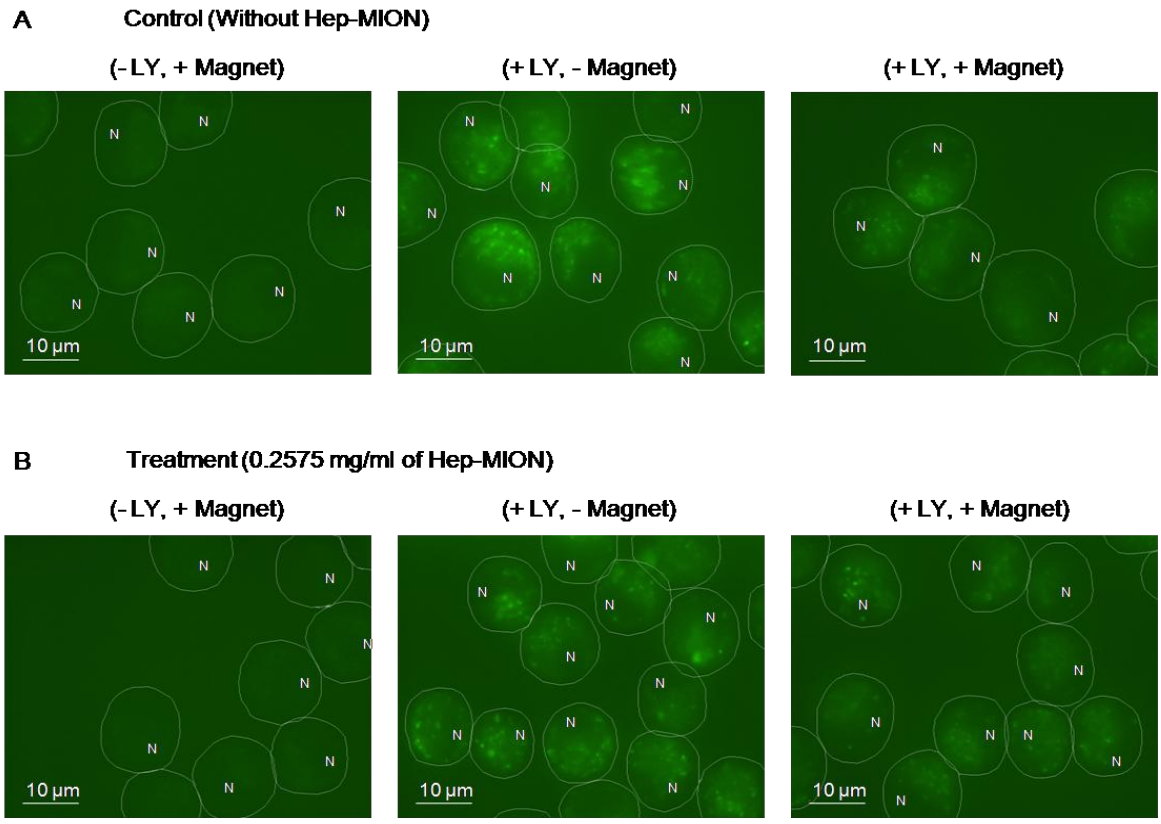

Figure 2-6. Lucifer Yellow (LY) uptake in the presence and absence of Hep-MION was investigated in transcellular transport experiments, with and without the magnetic field.

The vesicles inside the cells became labeled upon incubation with the fluorescent fluid phase marker, LY, visible using the FITC excitation/emission channel of the Nikon TE2000S epifluorescence microscope (100 × objective). (**a**) Control experiments without Hep-MION. (**b**) Experimental treatment group with Hep-MION (0.2575 mg/mL). Scale bar of 10 µm and nucleus of each cell as "N" are displayed in each image. For display, contrast was enhanced and the circumference of each cell (in white) was manually outlined with Adobe Photoshop.

2.11 References

1. Gupta AK, Naregalkar RR, Vaidya VD, Gupta M. Recent advances on surface engineering of magnetic iron oxide nanoparticles and their biomedical applications. Nanomedicine. 2007;2(1):23-39.
2. Thorek DL, Chen AK, Czupryna J, Tsourkas A. Superparamagnetic iron oxide nanoparticle probes for molecular imaging. Annals of biomedical engineering. 2006;34(1):23-38.
3. Gupta AK, Gupta M. Synthesis and surface engineering of iron oxide nanoparticles for biomedical applications. Biomaterials. 2005;26(18):3995-4021.
4. Cole AJ, David AE, Wang JX, Galban CJ, Hill HL, Yang VC. Polyethylene glycol modified, cross-linked starch-coated iron oxide nanoparticles for enhanced magnetic tumor targeting. Biomaterials. 2011;32(8):2183-93.
5. Cole AJ, David AE, Wang JX, Galban CJ, Yang VC. Magnetic brain tumor targeting and biodistribution of long-circulating PEG-modified, cross-linked starch-coated iron oxide nanoparticles. Biomaterials. 2011;32(26):6291-301.
6. Zhang C, Wängler B, Morgenstern B, Zentgraf H, Eisenhut M, Untenecker H, et al. Silica-and alkoxysilane-coated ultrasmall superparamagnetic iron oxide particles: a promising tool to label cells for magnetic resonance imaging. Langmuir. 2007;23(3):1427-34.
7. Ma Y, Manolache S, Denes FS, Thamm DH, Kurzman ID, Vail DM. Plasma synthesis of carbon magnetic nanoparticles and immobilization of doxorubicin for targeted drug delivery. Journal of Biomaterials Science, Polymer Edition. 2004;15(8):1033-49.
8. Lu AH, Salabas EeL, Schüth F. Magnetic nanoparticles: synthesis, protection, functionalization, and application. Angewandte Chemie International Edition. 2007;46(8):1222-44.
9. Dobson J. Gene therapy progress and prospects: magnetic nanoparticle-based gene delivery. Gene therapy. 2006;13(4):283-7.
10. White RE. High-throughput screening in drug metabolism and pharmacokinetic support of drug discovery. Annual review of pharmacology and toxicology. 2000;40(1):133-57.
11. Artursson P, Borchardt RT. Intestinal drug absorption and metabolism in cell cultures: Caco-2 and beyond. Pharmaceut Res. 1997;14(12):1655-8.
12. Kopke RD, Wassel RA, Mondalek F, Grady B, Chen K, Liu J, et al. Magnetic nanoparticles: inner ear targeted molecule delivery and middle ear implant. Audiology and Neurotology. 2006;11(2):123-33.
13. Mondalek F, Zhang Y, Kropp B, Kopke R, Ge X, Jackson R, et al. The permeability of SPION over an artificial three-layer membrane is enhanced by external magnetic field. BioMed Central; 2006.
14. Barnes AL, Wassel RA, Mondalek F, Chen K, Dormer KJ, Kopke RD. Magnetic characterization of superparamagnetic nanoparticles pulled through model membranes. BioMagnetic Research and Technology. 2007;5(1):1.
15. Bulte JWM, Douglas T, Witwer B, Zhang SC, Strable E, Lewis BK, et al. Magnetodendrimers allow endosomal magnetic labeling and in vivo tracking of

stem cells. Nat Biotechnol. 2001;19(12):1141-7.
16. Olsvik O, Popovic T, Skjerve E, Cudjoe KS, Hornes E, Ugelstad J, et al. Magnetic Separation Techniques in Diagnostic Microbiology. Clin Microbiol Rev. 1994;7(1):43-54.
17. Yakub GP, Stadterman-Knauer KL. Immunomagnetic separation of pathogenic organisms from environmental matrices. Methods Mol Biol. 2004;268:189-97.
18. Alexiou C, Arnold W, Klein RJ, Parak FG, Hulin P, Bergemann C, et al. Locoregional cancer treatment with magnetic drug targeting. Cancer Res. 2000;60(23):6641-8.
19. McBain SC, Griesenbach U, Xenariou S, Keramane A, Batich CD, Alton EWFW, et al. Magnetic nanoparticles as gene delivery agents: enhanced transfection in the presence of oscillating magnet arrays. Nanotechnology. 2008;19(40):405102-6.
20. Moroz P, Jones SK, Gray BN. The effect of tumour size on ferromagnetic embolization hyperthermia in a rabbit liver tumour model. Int J Hyperther. 2002;18(2):129-40.
21. Bulte JWM. Magnetic nanoparticles as markers for cellular MR imaging. J Magn Magn Mater. 2005;289:423-7.
22. Ferguson RM, Minard KR, Krishnan KM. Optimization of nanoparticle core size for magnetic particle imaging. J Magn Magn Mater. 2009;321(10):1548-51.
23. Wang YXJ, Hussain SM, Krestin GP. Superparamagnetic iron oxide contrast agents: physicochemical characteristics and applications in MR imaging. Eur Radiol. 2001;11(11):2319-31.
24. Pankhurst QA, Connolly J, Jones SK, Dobson J. Applications of magnetic nanoparticles in biomedicine. J Phys D Appl Phys. 2003;36(13):R167-R81.
25. Chertok B, Moffat BA, David AE, Yu FQ, Bergemann C, Ross BD, et al. Iron oxide nanoparticles as a drug delivery vehicle for MRI monitored magnetic targeting of brain tumors. Biomaterials. 2008;29(4):487-96.
26. Jain TK, Richey J, Strand M, Leslie-Pelecky DL, Flask CA, Labhasetwar V. Magnetic nanoparticles with dual functional properties: Drug delivery and magnetic resonance imaging. Biomaterials. 2008;29(29):4012-21.
27. Polyak B, Friedman G. Magnetic targeting for site-specific drug delivery: applications and clinical potential. Expert Opin Drug Del. 2009;6(1):53-70.
28. Balimane PV, Chong S. Cell culture-based models for intestinal permeability: a critique. Drug Discov Today. 2005;10(5):335-43.
29. Ward PD, Tippin TK, Thakker DR. Enhancing paracellular permeability by modulating epithelial tight junctions. Pharm Sci Technolo Today. 2000;3(10):346-58.
30. Kitchens KM, Kolhatkar RB, Swaan PW, Eddington ND, Ghandehari H. Transport of poly(amidoamine) dendrimers across Caco-2 cell monolayers: Influence of size, charge and fluorescent labeling. Pharm Res. 2006;23(12):2818-26.
31. Rojanasakul Y, Wang LY, Bhat M, Glover DD, Malanga CJ, Ma JK. The transport barrier of epithelia: a comparative study on membrane permeability and charge selectivity in the rabbit. Pharm Res. 1992;9(8):1029-34.

32. Berry CC, Curtis ASG. Functionalisation of magnetic nanoparticles for applications in biomedicine. J Phys D Appl Phys. 2003;36(13):R198-R206.
33. Ma YJ, Gu HC. Study on the endocytosis and the internalization mechanism of aminosilane-coated Fe3O4 nanoparticles in vitro. J Mater Sci Mater Med. 2007;18(11):2145-9.
34. Swaan PW. Recent advances in intestinal macromolecular drug delivery via receptor-mediated transport pathways. Pharm Res. 1998;15(6):826-34.
35. Tartaj P, Morales MD, Veintemillas-Verdaguer S, Gonzalez-Carreno T, Serna CJ. The preparation of magnetic nanoparticles for applications in biomedicine. J Phys D Appl Phys. 2003;36(13):R182-R97.
36. Calderon FL, Stora T, Mondain Monval O, Poulin P, Bibette J. Direct measurement of colloidal forces. Phys Rev Lett. 1994;72(18):2959-62.
37. Gupta AK, Gupta M. Synthesis and surface engineering of iron oxide nanoparticles for biomedical applications. Biomaterials. 2005;26(18):3995-4021.
38. Kuhn SJ, Hallahan DE, Giorgio TD. Characterization of superparamagnetic nanoparticle interactions with extracellular matrix in an in vitro system. Ann Biomed Eng. 2006;34(1):51-8.
39. Lemarchand C, Gref R, Couvreur P. Polysaccharide-decorated nanoparticles. Eur J Pharm Biopharm. 2004;58(2):327-41.
40. Gaush CR, Hard WL, Smith TF. Characterization of an Established Line of Canine Kidney Cells (Mdck). P Soc Exp Biol Med. 1966;122(3):931-5.
41. Hidalgo IJ, Raub TJ, Borchardt RT. Characterization of the Human-Colon Carcinoma Cell-Line (Caco-2) as a Model System for Intestinal Epithelial Permeability. Gastroenterology. 1989;96(3):736-49.
42. Irvine JD, Takahashi L, Lockhart K, Cheong J, Tolan JW, Selick HE, et al. MDCK (Madin-Darby canine kidney) cells: A tool for membrane permeability screening. J Pharm Sci. 1999;88(1):28-33.
43. Balimane PV, Chong SH, Morrison RA. Current methodologies used for evaluation of intestinal permeability and absorption. J Pharmacol Toxicol. 2000;44(1):301-12.
44. Kim DK, Zhang Y, Voit W, Rao KV, Muhammed M. Synthesis and characterization of surfactant-coated superparamagnetic monodispersed iron oxide nanoparticles. J Magn Magn Mater. 2001;225(1-2):30-6.
45. Bomsel M, Prydz K, Parton RG, Gruenberg J, Simons K. Endocytosis in filter-grown Madin-Darby canine kidney cells. J Cell Biol. 1989;109(6):3243-58.
46. Yu F, Huang Y, Cole AJ, Yang VC. The artificial peroxidase activity of magnetic iron oxide nanoparticles and its application to glucose detection. Biomaterials. 2009;30(27):4716-22.
47. Yamaura M, Camilo RL, Sampaio LC, Macedo MA, Nakamura M, Toma HE. Preparation and characterization of (3-aminopropyl) triethoxysilane-coated magnetite nanoparticles. J Magn Magn Mater. 2004;279(2-3):210-7.
48. Kim EHL, H.S.; Kwak, B.K.; Kim, B.K. Synthesis of ferrofluid with magnetic nanoparticles by sonochemical method for MRI contrast agent. J Magn Magn Mater. 2005;289:328-30.
49. Lee Y, Lee J, Bae CJ, Park J-G, Noh H-J, Park J-H, Hyeon T. Large-Scale Synthesis of Uniform and Crystalline Magnetite Nanoparticles Using Reverse

Micelles as Nanoreactors under Reflux Conditions. Adv Funct Mater. 2005;15:503-9.
50. Chatterjee J, Haik Y, Chen CJ. Size dependent magnetic properties of iron oxide nanoparticles. J Magn Magn Mater. 2003;257(1):113-8.
51. Caruso F, Susha AS, Giersig M, Mohwald H. Magnetic core-shell particles: Preparation of magnetite multilayers on polymer latex microspheres. Adv Mater. 1999;11(11):950-3.
52. Yu F, Yang VC. Size-tunable synthesis of stable superparamagnetic iron oxide nanoparticles for potential biomedical applications. J Biomed Mater Res A. 2010;92(4):1468–75.

Chapter 3

Pulsed Magnetic Field Improves the Transport of Iron Oxide Nanoparticles through Cell Barriers

3.1 Background

As one approach to overcome the biological barriers for the nanoparticle delivery, magnetic targeting has been widely studied for various applications (*e.g.* MRI, cancer research). Much research has been conducted to test various MNP formulations for targeting strategies *in vivo* using constant magnetic fields. Advanced studies with animal brain tumor models have shown that local administration of MNPs *via* intra-arterial injections enabled selective targeting of the tumor regions under the constant magnetic field (1-3). MNPs coated with the starch linked to polyethylene glycol (PEG) showed brain tumor targeting efficiency after systemic administration and better pharmacokinetics with longer circulations in plasma than starch-coated MNPs without PEG (4, 5). Most of animal studies with MNPs have been focused on efficacy or toxicity of MNPs by the applied magnetic field. Still, there is little knowledge about the rationale of administering doses of MNPs and strength or frequencies of applied magnetic field. The complex system with various physiological factors as *in vivo* often make it hard to analyze the variables substantially affecting the cell barrier penetration or distribution of

MNPs with various physicochemical properties. Cell-based permeability experiments could provide useful platforms to assess the pharmacokinetic behaviors of various MNP formulations according to the modulation of external magnetic field. There have been trials to use cell-based permeability assays using Transwell® inserts to optimize MNP formulations for inner ear disease (6, 7).

3.2 Rationale and Significance

Many physicochemical properties of MNP preparations (*i.e.*, size, surface chemistry) can influence their propensity to form aggregates and the particle aggregation could become severer when the particles are subjected to the external magnetic field (8-10). As shown in our previous studies in Chapter 2, MNPs can form severe particle aggregations on the cell surface proportionally, depending on the particle concentrations under the constant magnetic field. It was shown that these particle aggregations inhibit the transcellular targeting with particle retentions on the cell surface.

Clinical trials with magnetic targeting are hampered due to the concerns about the possibility of blockages of blood vessels by MNP aggregations under the strong magnetic field applied to human (3, 11-13). Magnetically induced particle aggregation can affect the performance of MNPs as targeting vehicles, accompanying the side effects of vascular thromboembolic events or unnecessary accumulation of MNPs (3, 14, 15). In addition, particle aggregations induced by magnetic field can affect MRI contrast effects by decreasing contrast enhancement (16, 17). The particle aggregations induced by magnetic fields could depend on the distance of the target or administration sites from the magnet as well as the duration or frequency of magnet application. Some *in vivo* studies

have shown that sub-maximal magnetic fields may be useful to avoid severe particle aggregation that often occurs during magnetic targeting experiments (3, 18). Our approach to characterize the MNP formulations under different magnetic field conditions in the presence of cell barriers could be important to establish rational guides for drug targeting using MNPs and magnetic field to overcome the biological barriers.

3.3 Abstract

Understanding how a magnetic field affects the interaction of magnetic nanoparticles (MNPs) with cells is fundamental to any potential downstream applications of MNPs as gene and drug delivery vehicles. Here, we present a quantitative analysis of how a pulsed magnetic field influences the manner in which MNPs interact with and penetrate across a cell monolayer. Relative to a constant magnetic field, the rate of MNP uptake and transport across cell monolayers was enhanced by a pulsed magnetic field. MNP transport across cells was significantly inhibited at low temperature under both constant and pulsed magnetic field conditions, consistent with an active mechanism (*i.e.,* endocytosis) mediating MNP transport. Microscopic observations and biochemical analysis indicated that, in a constant magnetic field, transport of MNPs across the cells was inhibited due to the formation of large (>2 μm) magnetically induced MNP aggregates, which exceeded the size of endocytic vesicles. Thus, a pulsed magnetic field enhances the cellular uptake and transport of MNPs across cell barriers relative to a constant magnetic field by promoting accumulation while minimizing magnetically induced MNP aggregation at the cell surface.

3.4 Introduction

Interest in magnetic nanoparticles (MNPs) has been considerably raised by their numerous biomedical applications, including cell labeling (19), *in vitro* cell separation (20, 21), drug/gene delivery (22, 23), and contrast agents in magnetic resonance imaging (MRI) (24, 25). Magnetic guiding of MNPs, for example, could be very useful in tissue engineering by facilitating delivery of attached cargoes in a precise, spatially controlled manner. These applications are enabled by the unique physicochemical properties of MNPs, including intrinsic magnetic susceptibility (10, 26), small particle sizes (27, 28), and multifunctional surface chemistry (9, 29). MNPs having an iron oxide core (magnetite (Fe_3O_4) or maghemite (Fe_2O_3)) and exhibiting superparamagnetic behavior, often referred to as superparamagnetic iron oxide nanoparticles (SPION) or magnetic iron oxide nanoparticles (MION), have attracted attention due to their relatively low toxicity profile. Their superparamagnetic property insures particle stability under storage and use, while their responsiveness to applied magnetic fields can be exploited for magnetically guided particle targeting (8) or imaging (30).

The cellular targeting or transcellular transport of MNPs under the influence of a magnetic force can be differentially enhanced through various pathways (31, 32). Previously, we observed that magnetic fields can promote apical-to-basolateral transport of heparin-coated MNPs across epithelial cell monolayers, but only at low particle concentrations (33). Interestingly, transport of MNPs was inhibited at higher particle concentrations. This may be due to the increased tendency of MNPs to form aggregates in suspension at higher concentrations (34). Nanoparticles composed of bare iron oxide cores are especially susceptible to aggregate formation by van der Waals attraction forces

(35). These attractive forces are often overcome through modification of the surface chemistry of MNPs (35-39). Surface modification can improve the stability of MNPs as drug carriers in physiological media (33, 40), increase drug/gene targeting efficiency *in vivo* (5), and facilitate the targeting of MNPs to tumor sites (41, 42).

For individual particles, size (27, 28, 43), surface chemistry (9, 29), and surface charge (31) are key factors that affect particle interactions with cells. Nevertheless, even surface-modified MNPs may agglomerate and form large clusters under the influence of a magnetic field due to the induced magnetic dipole-dipole attractions (44, 45). Effects of magnetic fields on the aggregation state of MNPs in the human body are largely unknown. However, animal studies indicate that magnetically induced MNP aggregation can affect the performance of MNPs in drug targeting and delivery applications (46). Furthermore, MNP aggregates can clog blood vessels and accumulate in off-target sites (47, 48). Because of these known complications, understanding how an applied magnetic field affects the aggregation state of MNPs interacting with cells could be important and relevant for optimizing the behavior of MNPs as MRI contrast agents and as magnetically guided drug or gene delivery vehicles.

Here, we studied the effects of MNP aggregate formation on targeting and transport across a cell barrier. Using a controlled *in vitro* assay system to enable quantitative measurement of particle transport kinetics (Figure 1), we assessed the differential effects of a pulsed magnetic field and constant magnetic field on the transport of particles across the cell monolayer and their intracellular uptake and retention on the cell surface. In our experimental setup, MNPs were added in suspension to the apical (donor) compartment on top of a confluent epithelial cell monolayer differentiated on a

porous membrane support. A magnetic field was applied from the opposite side of the membrane and was either kept constant or pulsed on and off. Transport experiments were performed under different temperature conditions to determine the influence of active cellular processes on particle targeting, uptake, and transport. Finally, effects of spatiotemporal changes of the external magnetic field on the particle transport kinetics were investigated by transmission electron microscopy and confocal microscopy and related to bulk quantitative measurements of particle mass distribution.

3.5 Materials and Methods

Materials. Chemicals used to prepare the Hep-MNPs or TRITC-labeled MNPs and quantify the iron contents (ferrozine assays) were obtained from the Sigma-Aldrich (St. Louis, MO). Chemicals used to prepare Hank's Balanced Salt Solution buffer (HBSS; pH 7.4, 10 mM HEPES, 25 mM D-glucose) were from Fisher Scientific, Inc. (Pittsburgh, PA). Cell culture reagents and DYNAL-MPC-L magnet bar were purchased from Invitrogen (Carlsbad, CA). Transwell inserts with polyester membrane were purchased from Corning Co. (Lowell, MA). UV/vis plate reader (BioTEK Synergy BioTEK, Co.) was used to measure absorbance values of the samples from the transport experiments after ferrozine assays. A Phillips CM-100 transmission electron microscope and a Zeiss LSM 510-META laser scanning confocal microscope were used for cell examinations after transport experiments.

Preparation of Heparin-Coated Iron Oxide Nanoparticles (Hep-MNPs). As previously reported (33), a solution containing 0.76 mol/L of ferric chloride and 0.4 mol/L of ferrous chloride (molar ratio of ferric (Fe^{3+}) to ferrous (Fe^{2+}) = 2:1) was

prepared at pH 1.7 under N_2 protection and then added into 1.5 M sodium hydroxide solution under stirring condition. The mixture was gradually heated (1 °C /min) to 78 °C and held at this temperature for 1 h with N_2 protection under stirring. After the supernatant was removed by a permanent magnet, the wet sol treated with 0.01 M HCl was sonicated for 1 h. The colloidal suspension of MNPs was filtered through a 0.45 μm and then a 0.22 μm membrane. Suspension was adjusted to contain 0.7 mg Fe/mL. Two hundred milliliters of 0.7 mg Fe/mL iron oxide nanoparticles were added to 200 mL of 1 mg/mL glycine with stirring. Next, the suspension was ultrasonicated for 20 min, followed by stirring for 2 h. After free glycine was removed by ultrafiltration, the iron content of the samples was measured by inductively coupled plasma-optical emission spectroscopy (ICP) analysis using a Perkin-Elmer Optima 2000 DV instrument (Perkin-Elmer, Inc., Boston, MA), calibrated with an internal Yttrium reference, and a standard curve of iron samples (GFS Chemicals). The MNP suspension was diluted to a concentration of 0.35 mg Fe/mL. As a final step, 100 mL of 0.35 mg Fe/mL of glycine-MNPs were added to 100 mL of 1 mg/mL heparin solution, under stirring condition and ultrasonication. Heparin-coated MNPs (Hep-MNPs) were obtained after free heparin was removed by ultrafiltration. Superparamagnetic properties of Hep-MNPs were confirmed with a superconducting quantum interference device (SQUID) (Quantum Design Inc., San Diego, CA, USA) (33). Physicochemical characterization of MNP preparations was conducted by measuring the size and zeta potential of MNPs in water or in the serum-containing buffer solution using Malvern Zetasizer (Malvern Instruments, Malvern, UK) (see Appendix A; Figure A1).

Cell culture. MDCK strain II cells obtained from American Type Culture Collection (ATCC) (Manassas, VA) were cultured in 75 cm^2 flasks at 37 °C, 5% CO_2 containing humidified incubator. MDCK cells were cultured with growth medium consisting of Dulbecco's Modified Eagle Medium (DMEM; Invitrogen, Carlsbad, CA) with 2 mM L-glutamine, 4500 mg/L of D-glucose, and 110 mg/L of sodium pyruvate, 1×non-essential amino acids (Gibco 11140), 1 % penicillin-Streptomycin (Gibco 10378), and 10% fetal bovine serum (FBS; Gibco 10082). After reaching 70-80% confluency, MDCK cells were detached from the culture flasks using trypsin, and subcultured at a split ratio of 1:10.

To prepare supported cell monolayers for transport experiments, cells in suspension (100 μL, 4×10^5 cells/cm^2) was added into the apical side of Transwell inserts with the polyester (PET) membrane (area = 0.33 cm^2, pore size = 3 μm) (Corning co., Lowell, MA) in 24-well culture plate containing 600 μL of growth media in the basolateral side. After overnight incubation at 37 °C, 5% CO_2 incubator, the confluent MDCK cell monolayers on Transwell inserts were rinsed twice with HBSS buffer (pH 7.4) and pre-incubated for 20 min in HBSS with 10% FBS (transport buffer) at 37 °C. Transepithelial electrical resistance of the cell monolayer was measured by Millipore Millicell ERS electrodes. TEER values were calculated after subtracting baseline TEER values measured with membrane inserts without cells. Only inserts with the confluent cells showing TEER values higher than 150 Ω×cm^2 were used for transport experiments.

Experimental setup. Transport buffer (600 μL) without MNPs was added into the basolateral (bottom) chamber and MNP suspension (100 μL of MNPs in transport buffer) at different initial concentrations was added to the apical (top) side of the Transwell insert.

Apical-to-basolateral transport experiments were conducted over 90 min with or without the magnetic bar (DYNAL-MPC-L (Invitrogen, Carlsbad, CA)), applied to the bottom of the plate (Figure 1a). Magnetic flux density along the vertical distance from the surface of magnetic bar was measured by 3-axis Hall Teslameter and depicted with color gradient map by the "TriScatteredInterp" function in MATLAB R2010b (Figure 1b).

Transport measurements and microscopic imaging. During transport experiments, plates were stirred using a VWR rocking platform shaker. Sample solutions (300 μL) were collected from the basolateral chambers at each time point. Fresh 300 μL of transport buffer without the particles was then added back into the basolateral chambers. At the final time point (90 min), the solutions from donor and receiver chambers were collected and both sides of the inserts were twice washed with cold Dulbecco's phosphate buffered saline (DPBS). For measurements, standard and sample solutions were put into the 96-well plates (Nalge Nunc International, Rochester, NY) for UV absorbance measurement at 364 nm using a plate reader (Synergy, BioTEK, Co.). Concentration of MNPs in the each well of the 96-well plate was determined with the aid of a standard curve.

To confirm monolayer integrity, TEER was measured after each experiment. Then, cell monolayers were washed with cold DPBS buffer, and the cells were examined using an Olympus BX-51 upright light microscope under bright field illumination. Images of cell monolayers after experiments were acquired with an Olympus DP-70 digital camera. In the brightfield images, the clusters of particle aggregates in five different images at each case were analyzed by the Integrated morphometric analysis (IMA) function of Metamorph (Molecular Devices, Inc) (N = 5). Total clustered area of

particle aggregates was normalized by overall cell monolayer and displayed as percentages for the comparisons at different initial MNP concentrations.

Effect of magnetic field variations on Hep-MNP transport. Transport studies under different conditions of the magnetic field were performed at 37 or 4 °C. For transport experiments in the presence of a constant magnetic field, the magnetic bar was fixed at the bottom of the plate and transport studies were performed for 90 min. For transport experiments under a pulsed magnetic field, cells were first incubated with MNPs but without the magnet during an initial 5 min period. Samples were taken out from basolateral side, after which the magnetic bar was placed at the bottom of the plate and the MNP suspensions was incubated for an additional 5 min, with shaking. At the end of the 5 min, the magnetic bar was removed and incubation was continued for 5 more minutes, with shaking. In this manner, the magnetic field was pulsed for 8 cycles. Transport samples in the basolateral side were collected at 5, 10, 30, 50 and 70 min. At the final time point (90 min), the total volume was removed from apical and basolateral sides. To measure the intracellular content of MNPs, cells in the inserts were washed with cold DPBS buffer twice and detached from the membranes with trypsin. Trypsinization also removed the MNPs from the cell surface. The isolated cells were counted and after centrifugation at 4,000 rpm, 5 min, the cell pellets were lysed with 1% Triton X-100 (Sigma-Aldrich, St. Louis, MO) for 30 min on ice. After centrifugation at 12,000 rpm, 5 min, supernatants of the cell lysates were analyzed for iron content.

Quantitative analysis of iron content. Iron content was measured using Ferrozine-based assay. The solution of the Fe oxidizing agent, ferrozine, was prepared by solubilizing 80 mg of Ferrozine, 68 mg of Nepcuproine, 9.635 g of Ammonium acetate (final

concentration: 5 M in solution), 8.806 g of Ascorbic acid (2 M in solution) in 25 mL Milli-Q water (Bedford, MA) while stirring. For measurements, samples collected from transport studies were diluted in HBSS buffer. Diluted sample solution (83.3 μL) was mixed with 16.7 μL of 6 N HCl (final concentration of HCl in 100 μL solution is 1 N) in 1.5 mL microcentrifuge tubes. To release Fe from MNPs into solution, a potassium permanganate ($KMnO_4$) solution in HCl was prepared by mixing 3.55 mL of 0.2 M $KMnO_4$ with 1.5 mL of 2 M HCl. The sample solution (100 μL) was mixed with 100 μL of the $KMnO_4$/HCl solution and then heated in a 60 °C water bath for 2 h. Next, 30 μL of ferrozine solution was added to the samples and vortexed. The solution was cooled down to room temperature (RT) and then, 200 μL samples were transferred to a 96-well plate. Absorbance values were measured at 550 nm with UV/VIS plate reader (BioTEK Synergy BioTEK, co.). Iron standards were also prepared using the same procedure and subject to ICP. A standard curve was generated by ICP analysis and ferrozine assay using the Fe standard solutions in the range of Fe content (0- 90 Fe nmoles).

Quantitative analysis of mass balance. For quantitative analysis of mass balance, transported fraction of MNPs (α, %), entrapped fraction of particles inside the cells (β, %), retained fraction of particles at apical suspension (γ, %), and retained fraction of particles at cell surface (δ, %) were calculated relative to the initial masses of MNPs (*Map_initial*) added to the cells at the start of each transport experiment, using equations (1-5).

$$\alpha = \frac{Mbl\_final}{Map\_initial} \times 100 \quad (1)$$

$$\beta = \frac{IM\_final}{Map\_initial} \times 100 \quad (2)$$

$$\gamma = \frac{Map\_final}{Map\_initial} \times 100 \quad (3)$$

$$\delta = \frac{Mcellsurface}{Map\_initial} \times 100 \quad (4)$$

$$Mcellsurface = Map\_initial - Mbl\_final - IM\_final - Map\_final - M\_rinsed \quad (5)$$

In these equations, *Mbl_final* or *Map_final* refer to the mass of MNPs in basolateral (target) side or apical side at 90 min. *IM_final* refers to the measured intracellular mass of MNPs from the Triton-X treated cells following removal of extracellular, cell-surface-associated MNPs by trypsin digestion. The masses of particles retained on the cell surface (*Mcellsurface*) were calculated by equation (5), corresponding to any residual particle masses that cannot be accounted for the masses in the intracellular, basolateral, or apical suspensions at 90 min and the masses in the solutions used to rinse the apical cell surface and basolateral side (*M_rinsed*). The ratio α/β was calculated from the fraction of targeted nanoparticles into the basolateral side over time (90 min) (α) normalized by the entrapped fraction of MNPs in the cells (β) at each case.

Transmission electron microscopy (TEM). Under different magnetic field conditions (no magnetic field, constant or pulsed magnetic field), transport experiments in MDCK cell monolayers with MNPs at high particle concentration (0.659 mg Fe/mL) were performed at 37 °C and then cells were prepared for TEM imagings. Cell monolayers on the inserts were washed twice with HBSS containing 10% FBS, and then washed twice with Sorensen's buffer. The washed cells on inserts were fixed for 30 min with 2.5%

glutaraldehyde in 0.1 M Sorensen's buffer (pH 7.4), followed by rinsing with 0.1 M Sorensen's buffer. Then, samples were incubated with 1% osmium tetroxide in 0.1 M Sorensen's buffer and rinsed twice with water. Next, samples were dehydrated for 5 min each in 50, 70, 90, and 100% ethanol, infiltrated in Epon and polymerized at 60 °C for 24 h. Embedded samples were sectioned with an ultramicrotome, and images were captured using a Phillips CM-100 transmission electron microscope at magnifications from 3,400 to 180,000 ×. Images of MNP aggregates on the apical cell surface and cytosol were displayed with the scale bars. For the quantitative analyses of the TEM images, the diameter of the major axis in the elliptical circle of the endosome and the size of MNP aggregates were measured by Metamorph from at least 10 images under different magnetic field conditions. The sizes of endosome and MNP aggregates inside the endosome were measured by Metamorph from at least 10 different TEM images at each case of the applied magnetic field condition. In the case of endosome, the diameter in major axis of endosome (assumed as an elliptical circle) were measured as the sizes of endosomes. The distance between the both ends of the aggregates was measured as the size of MNP aggregates.

Confocal microscopy. To examine the MNPs transported through the cells and pores in the membrane, Z-stack images were acquired using a Zeiss LSM 510-META laser scanning confocal microscope. For this purpose, Hep-MNPs labeled with TRITC were prepared. Rhodamine isothiocyanate (TRITC, Sigma-Aldrich) 1 mg dissolved in 200 μL of DMSO was slowly added to 5 mg Fe (200 μL of 25 mg Fe/mL stock solution) of Hep-MNPs. After incubation for 3 hours at 25 °C, the reaction mixture was dialyzed (Sigma, MWCO: 12 kDa) against 10% DMF solution for overnight with change of the dialyzing

solution at every 6 to 8 h. Next, the reaction mixture was dialyzed against Milli-Q water. After transport studies with TRITC-labeled Hep-MNPs for 90 min with the applied magnetic field or without the applied magnetic field, the cells in the inserts were incubated with LysoTracker Green DND-26 (Molecular Probes, Invitrogen) for 30 min and then, placed on the Lab-Tek I-chamber slide for live cell imaging. Particles were visualized in confocal scanning through Z-axis with Helium Neon 1 laser (543 nm).

Quantitative microscopic image analysis of magnet-induced MNP aggregates in suspension. Ten microliters of MNP suspension in HBSS with 10% FBS was placed on a slide and a No. 1 coverslip was placed on the drop of MNP suspension. The magnet was placed at the edge of the slide glass and the particle aggregation of MNPs in the presence of magnetic field was measured over time (0-3 h) at varying distances from the magnet (0.1-10 mm) using an Olympus BX-51 upright light microscope at 1000 × magnification. Using bright field optics, images were captured with an Olympus DP-70 high resolution digital camera at each time point (0, 5, 10, 30 min, and every 30 min until 3h). After background subtraction and thresholding, the images were analyzed with Metamorph software (Molecular Devices, Inc) using the IMA function to measure the area of clusters (particle aggregates). Total sizes (area, μm^2) of clusters of particle aggregates in the brightfield images of particle suspension within 2 mm (0.1, 0.5, 1, and 2 mm) from the magnet were measured by Metamorph for different initial MNP concentrations (0.258 or 0.412 mg Fe/mL).

Quantitative analysis of magnet-induced changes in MNP concentration in suspension. Over time, magnet-induced changes in MNP concentration were measured as a function of distance from the magnet, using a 1 mm diameter glass tube was filled

with MNP suspension (0.258 or 0.412 mg Fe/mL) up to 20 mm along the tube. The magnetic bar was placed at the edge of the tube, horizontally, so the particles in suspension were pulled towards the magnet. Movement of MNPs toward the magnet to the distance from the magnet was examined using an UVP transilluminator (Upland, CA). Images of the tube aligned with the magnetic bar on the brightfield illuminator were captured using a Sony DSC-W70 digital camera (0-3 h). Intensity of the solution in the tube was measured using the Line scan function in Metamorph from three different images. In the equation (6), I_0 or I_T indicates intensity of the solution in the tube at zero or each time point.

$$OD = \log \frac{I_0}{I_T} \tag{6}$$

Based on the optical density (OD), the mass of MNPs at each point along the tube was calculated with a standard curve generated with the same set up, using MNP suspensions of known dilutions. Concentrations of MNPs at each segment in the tube (0.1-0.5, 0.5-2, 2-4, and 4-7 mm from the magnet) were calculated by dividing the integrated mass of MNPs over a length of the tube by the calculated volume of that segment of the tube, assuming a cylinder. Concentrations of MNPs (mg Fe/mL) moving toward the magnet across the tube were tracked with the time under the external magnetic field.

Statistical analysis. GraphPad Prism 5.03 (GraphPad Software; LaJolla, CA) was used for data analyses. Unpaired Student's t-test was used with a significance level, 0.05. As a post test of one-way analysis of variance (one-way ANOVA), Tukey's multiple comparison test was performed with a significance level, $\alpha = 0.05$.

3.6 Results

3.6.1 Enhanced Cellular Uptake and Penetration under a Pulsed Magnetic Field

Visual inspection after transport studies under the constant magnetic field indicated a greater accumulation of microscopically visible MNP aggregates on the cell monolayers with increasing concentrations of MNP in the donor compartment (Figure A2 in the Appendix A). Under constant magnetic field conditions, the area of the cell surface visibly covered by MNP aggregates at high MNP concentration (0.412 mg Fe/mL) was 34% (±2.99), 3-fold larger than those at lower concentration (0.258 mg Fe/mL) (11% (±5.00)) (Unpaired t test, p value = 0.0022). Thus, we hypothesized that the decrease in the rate of particle transport under constant magnetic field conditions at higher initial MNP concentration might be due to the increased retention of large, magnetically induced MNP aggregates at the cell surface. To test this possibility, we decided to determine whether a pulsed magnetic field could be used to promote transport across a cell barrier relative to a constant magnetic field condition by minimizing the formation of large magnetized aggregates while pulling the MNPs toward the cell surface and across the cells. To test this, the transport of particles across MDCK cell monolayers was assessed under pulsed magnetic field, constant magnetic field, or no magnetic field conditions (Figure 2). Under pulsed magnetic field conditions, at high MNP concentrations (0.412 and 0.659 mg Fe/mL), the rate of particle transport across cells increased 8.5- and 13.6-fold compared to the rate of transport under no magnetic field conditions, respectively (Figure 2a). Compared with constant magnetic field conditions, a 2.5-fold greater rate of particle transport across cells was observed under pulsed magnetic

field conditions, at MNP concentration of 0.412 mg Fe/mL (Figure 2a). This enhancement in particle transport rate was even greater (4-fold) at the highest MNP concentration tested (0.659 mg Fe/mL; Figure 2a). A comparison of the mass of MNPs internalized by cells under various magnetic field conditions (Figure 2b) revealed the apparent intracellular mass was 1.5- to 1.8-fold higher under pulsed magnetic field than under constant magnetic field conditions, indicating that pulsing the magnet promoted both intracellular uptake and transport of MNPs.

3.6.2 Lowering Temperature Inhibited MNP Transport under a Magnetic Field

The rate of MNP transport across the cell monolayers and the intracellular accumulation of MNPs in the presence of a magnetic field were significantly lower at 4 °C relative to the corresponding rates measured in transport experiments done at 37 °C (Figure 2c). In fact, the intracellular uptake of MNPs was reduced to the point that intracellular MNP mass at 4 °C under pulsed or constant magnetic field conditions was similar to the intracellular accumulation of MNPs measured in no magnetic field at 37 °C. At 37 °C, the intracellular masses of MNPs under pulsed and constant magnetic field conditions were 3.7- to 5.5-fold and 2.5- to 3.1-fold greater, depending on MNP concentration, than that observed under no magnetic field conditions, respectively (Figure 2d). However, when the studies were repeated under 4 °C, no significant increase in intracellular mass accumulation was found under pulsed or constant magnetic field relative to no magnetic field conditions (Figure 2d). Therefore, it was realized that lowering the temperature dramatically inhibited both the cellular uptake and transport of MNPs, even in the presence of the external magnetic field.

3.6.3 Decreased MNP Transport Were Associated with Increased MNP Accumulations on Cells

On the basis of mass balance analysis using equations 1-5 in the Materials and Methods, the transported fraction of MNPs under a constant magnetic field condition (α) was decreased from 8% (±0.72) to 4% (±0.52) with increasing initial MNP concentrations (Figure 3a). However, the fraction of particles retained on the cell surface (δ) exhibited a corresponding increase with increasing starting MNP concentration from 25% (±1.42) at 0.412 mg Fe/mL to 36% (±6.31) at 0.659 mg Fe/mL (Figure 3b). Under pulsed magnetic field conditions, however, a significantly greater fraction of particles crossed the cell monolayer (α), while decreased particle masses were retained on the apical surface of the cells (δ), compared to results obtained with a constant magnetic field. Under a pulsed magnetic field condition, the fraction of intracellular particles (β) remained almost constant, from 1.59% (±0.15) at 0.412 mg Fe/mL to 1.62% (±0.06) at 0.659 mg Fe/mL, as the initial MNP concentration increased (Figure 3c). The differential effect of the magnet on the transport *versus* intracellular uptake of MNPs (α/β) was determined by calculating the ratio of the fraction of MNPs transported across the cells (α) divided by the fraction of particles trapped inside the cells (β). While there was no significant change of α/β under constant magnetic field compared to no magnetic field, notably, α/β increased about 2.5-fold under pulsed magnetic field relative to no magnetic field conditions (Figure 3d). Thus, while transport of MNPs across cellular barriers was enhanced over intracellular uptake under all conditions tested, the transport/uptake ratio was greatest under pulsed magnetic field conditions.

3.6.4 Cell Surface-Associated MNP Aggregates Formed Faster than Uptake under a Constant Magnetic Field

In order to assess whether the large, visible particle aggregates that accumulated on the cell surface under constant magnetic field conditions formed in suspension prior to contacting the cells, we measured the aggregation behavior of MNPs in the absence of the supported cell monolayers, as a function of distance from the magnet. Experiments were performed by subjecting MNP suspension in a transparent glass tube to the same magnetic field conditions used in our Transwell insert setup. A microscope was used to image the formation of MNP aggregates as a function of distance from the magnet over time, under 1000× magnification. At 0.412 mg Fe/mL (initial donor MNPs concentration), visible particle aggregates were detectable only at <0.5 mm from the magnet's surface (Figure A4a). After 30 min under the magnetic field, visible particle aggregates were observed between 1 and 2 mm from the magnet. However, at distances ≥3 mm from the magnet, no particle aggregates were visible microscopically, even after 3 h. For statistical analysis, the area of MNP clusters was measured in microscopic images (Figure 4a). Within the closest distance from the magnet (≤1 mm), massive aggregation was observed as early as 10 min in a constant magnetic field.

Nevertheless, as the distance from the magnet increased, the size of visible particle aggregates precipitously decreased. At distances ≥3 mm, there were no microscopically measurable particle aggregates. To determine the extent to which the magnetic field affected the concentration of MNPs at the level of the Transwell insert, we also measured the changes in MNP concentration in suspension over time as a function of distance from the magnet (Figure 4b). Rapid movement of MNPs close to the magnet

resulted in an increase in local concentration near the magnet. However, particles located >4 mm from the magnet (at the level of the Transwell insert) moved more slowly toward the magnet, leading to a small but insignificant change in MNP concentration at distances >4 mm from the magnet. Therefore, the results suggested that it was at the level of the cell monolayer that the magnetic force was sufficient to pull down the MNPs onto the cell surface. The microscopically visible aggregates most likely formed after particles interacted with the surface of the cells. Although it is possible that some magnetically induced aggregates may be formed in suspension, those aggregates would have to be smaller than the resolution limit of the imaging system (<250 nm).

3.6.5 Magnetically Induced MNP Aggregation Did Not Affect Cellular Transport/Uptake in the Absence of Magnet

Control experiments were performed to determine whether inducing formation of MNP aggregates before adding them to the cells affected cell barrier penetration, cellular uptake, or retention on the cell surface when the transport experiments were carried out in the absence of a magnetic field. Mass transport rate and apparent intracellular mass of MNPs were measured, and for mass balance analysis, α, β, and δ (%) were calculated. Under these conditions, there were no significant differences in MNP transport, cellular uptake, and particle retentions on the cell surface in the absence of a magnetic field when MNP suspensions were exposed to different magnetic field conditions prior to the transport experiments (Figure A5 and A6). Cell images captured after the transport experiments did not reveal obvious differences in the accumulation of MNPs on the cell surface. These control experiments are consistent with the applied magnetic field mostly

affecting the manner in which MNPs interact with the cells and with each other, at the moment they come in contact with the cell surface.

3.6.6 Pulsed Magnetic Field Enhanced Uptake/ Transport and Decreased Cell Surface MNP Aggregates

To further investigate the pathway through which a pulsed magnetic field enhances transport of MNPs across cell monolayers relative to a constant magnetic field, cell monolayers were examined by TEM after 90 min transport experiments at 37 °C. Under constant magnetic field conditions, large numbers of MNP aggregates were visible on the extracellular side of the apical cell surface at high MNP concentration (0.659 mg Fe/mL). The size of the particle aggregates on the cell surface was often >2 μm (Figure 5a and zoom-in image). Smaller MNP aggregates were visible inside cells and were always observed inside the lumen of membrane-bound vesicles (Figure 5c). The intracellular aggregates were much smaller than those present on the extracellular face of the apical membrane (Figure 5b,c). Remarkably, under pulsed magnetic fields, the size of particle aggregates on the extracellular face of the apical membrane was 206 ± 125 nm, which was significantly smaller than the size of the aggregates measured under constant magnetic field conditions (551 ± 519 nm) (ANOVA, p value <0.001) (Figure 5d and zoom-in). Nevertheless, the intracellular MNP aggregates found inside membrane-bound vesicles in constant and pulsed magnetic field conditions were of similar size: 155 ± 123 and 140 ± 80 nm, respectively (Figure 5c,e,f). In the absence of magnetic field, there were fewer aggregates on the cell surface (Figure 5g, zoom-in, and h) than under the applied magnetic field. In negative control experiments, no particles were observed, as expected (Figure 5i). Thus, while intracellular MNP aggregates were always of size

smaller than endosomes under various magnetic field conditions (Figure 5j), the size of MNP aggregates that formed under a constant magnetic field condition was greater than the size of the aggregates that fit in the endosomes, remaining on the extracellular, apical cell surface.

3.6.7 Large Particle Aggregates Formed at the Basolateral Side under a Constant Magnetic Field

Using optical microscopy, we also examined the transport of MNP suspension at high particle concentration (0.659 mg Fe/mL) across cell monolayers under different magnetic field conditions. Under bright-field illumination, there were visible differences in the accumulation of MNPs under various magnetic field conditions (Figure 6a). In the absence of magnetic field, no particle aggregates were detected by confocal epifluorescence microscopy (Figure 6b). Under constant magnetic field conditions, however, large MNP particle aggregates were observed not only on the apical side of the cells but also at the basolateral side of the cells, clogging the pores of the membrane. In contrast, under pulsed magnetic field conditions, although fluorescence of MNPs was observed in association with the cells, there were no large aggregates present on either the apical or basolateral sides of the cells.

3.7 Discussion

On the basis of this study, a pulsed magnetic field can be used to enhance the transport of MNPs into and across a cellular barrier (Figure 7). In contrast, when the magnetic field is held constant, large magnetized aggregates form at the cell surface, resulting in a greatly decreased fraction of particles being endocytosed by the cells or

actively transported across the cellular barrier. Microscopically visible MNP aggregates that formed at the cell surface in the presence of a constant magnetic field were too large to be taken up by endocytosis, and they accumulated on the cell surface at a faster rate than they were endocytosed by the cells. Based on the finding that all intracellular MNPs were found inside membrane-bound vesicles and that the size of MNP aggregates that can be accommodated by these vesicles is limited to the size of the vesicles, these results suggest that a constant magnetic field is less efficient at promoting MNP transport because large magnetized MNP clusters do not penetrate across the cellular barrier, due to steric constraints inhibiting their uptake. Supporting this notion, we did not observe any MNPs in the intercellular spaces at the level of the cell monolayer. We also observed a dramatic inhibitory effect of lowering temperature on the ability of magnetic fields to promote transport of MNPs across the cell monolayers, consistent with transport of MNPs across the cells occurring *via* temperature-sensitive endocytic uptake, followed by transcytosis. In control transport experiments carried out in the absence of a magnet, MNP suspensions pre-exposed to a magnetic field exhibited similar transport behaviors as MNP suspensions that had not been pre-exposed to a magnetic field (Figures A5 and A6).

Mechanistically, our results point to endocytic uptake as a key factor affecting the interaction between MNPs and cells, even in the presence of an external magnetic field. This is consistent with previous studies (28, 48). Inhibition of endocytosis by lowering the temperature reduced cellular uptake and transport of MNPs. Unfortunately, probing the role of endocytosis on the targeting and transport of MNPs is very difficult *in vivo*, and only a few such studies on middle ear epithelium have been conducted (7, 49).

Nevertheless, our observations suggest that TEM analyses could be performed to study how a magnetic field facilitates the targeting, transport, and cellular uptake of MNPs *in vivo*. In our experiments, TEM revealed the formation of sub-micrometer-sized cell surface aggregates that were endocytosed, as well as the formation of large, cell surface MNP aggregates that were not endocytosed. Functional differences in MNP performance could be correlated with the targeting and transport properties of MNPs, as well as size differences in MNP aggregates on the cell surface or basolateral membrane under the different magnetic field applications (constant *vs.* pulsed magnetic field). Similar TEM observations could be performed *in vivo*.

For *in vitro* magnetic labeling or magnetofection applications, the quantitative analysis developed in this study can be used to reveal how the cellular uptake and targeting of particles are affected by the manner in which the external magnetic field is modulated. For *in vivo* drug targeting and delivery experiments, similar quantitative analysis of MNP aggregation and transport pathways will be essential to guide the future development of magnetic targeting strategies and their downstream application in drug or gene delivery. For clinical MRI, quantitative analyses of magnetic field-induced MNP aggregation could also help improve the performance of MNPs as contrast agents and prevent possible side effects that may result from induced particle aggregates (*e.g.*, vascular thromboembolic events or unwanted accumulation of MNPs in off-target sites) (14, 15, 46). While many physicochemical properties of MNP preparations can influence their propensity to form aggregates (8-10), the performance of MNPs as contrast agents for MRI experiments can be affected by their magnetically induced aggregation state (16). While magnetically induced MNP aggregates show decreased contrast enhancement in

MRI (17), our experiments are specifically relevant to MNP targeting in the context of magnetically guided therapy. Related to this, magnetic field strengths in clinical MRI instruments are orders of magnitude greater than those used in our transport experiments (11, 12, 46). Therefore, field-induced particle aggregates can be expected to form even more readily in clinical MRI applications (13). Consistent with our experiments, continuous exposure to high strength magnetic fields does not necessarily lead to greater tissue targeting, as compared with lower strength magnetic fields (46).

Certainly, we expect that further quantitative analysis will be essential to identify MNP formulations with the most suitable physicochemical properties (*i.e.*, particle size, surface modifications, nanomaterial types, batch-to-batch variations) for *in vitro* and *in vivo* use and also clinical applications. Although our experiments did not test the performance of different MNP formulations, spatiotemporal variations in the magnetic field are expected to interact differently with MNP preparations possessing different physicochemical properties. Most likely, magnetic field strength, number, and frequency of pulses will need to be optimized in a formulation-specific manner, so as to achieve maximal uptake (or transfection efficiency). Perhaps, more importantly, our results clearly indicate importance of exploring the effects of spatiotemporal variations in magnetic fields in the context of *in vivo* drug/gene delivery applications. Indeed, the vast majority of *in vivo* targeting/delivery and MRI experiments involving MNPs have been done in the presence of a constant magnetic field. While all our experiments have been done *in vitro*, our results suggest that the interaction of a pulsed magnetic field with particle dosing, the distance from the magnet, and overall duration of applying magnetic field may also be exploited to obtain the most effective, selective, and reliable magnetic

applications. Previously, submaximal magnetic field strengths have been used *in vivo* to avoid severe particle aggregations that often occur during magnetic targeting experiments (18). However, a pulsed magnetic field may offer distinct advantages in terms of its ability to minimize cell surface aggregate formation while maximizing the force driving the cellular uptake and transport of particles.

3.8 Conclusions

To summarize, the retention of MNPs on the cell surface, as well as the cellular uptake and transcellular targeting of MNPs, has been quantitatively analyzed in relation to the initial MNP concentrations and their interaction with a constant *versus* pulsed magnetic field. At high particle concentrations, the propensity of forming large particle aggregates after interaction of MNPs with the cell surface was reduced by pulsing on and off the magnetic field. Because of steric hindrance, large particle aggregates cannot be endocytosed, resulting in an increased fraction of MNPs accumulating at the cell surface when the magnetic field is kept constant. By pulsing the magnetic field, the apical to basolateral transport of MNPs across the cell monolayers was maximized by effectively concentrating MNPs at the cell surface while avoiding the formation of large MNP aggregates. Ultimately, our results suggest that spatiotemporal variations in the magnetic field can be effectively used to optimize *in vitro* and *in vivo* magnetically guided drug or gene targeting strategies for many potential clinically relevant applications.

3.9 Acknowledgements

This work was made possible through grants from NIH (R01GM078200 to G. R. R. and R01CA114612, R01NS066945 to V. C. Y.); NSF (EPS-1158862 Subagreement 34-21530-200-76190 to A. E. D.); World Class University (WCU) project of the MEST and NRF of South Korea (R31-2008-000-10103-01 to V. C. Y.); Warner Lambert/Parke Davis Fellowship (to K. A. M.); and a Rackham Predoctoral Fellowship of the University of Michigan (to K. A. M.). Authors thank A. Talattof for technical supports, D. Sorenson (Microscopy and Image Analysis Laboratory, University of Michigan) for TEM analysis, and C. J. Galban (Department of Radiology, Center for Molecular Imaging, Medical School, University of Michigan) for helpful advice. V. C. Y. is also a Participating Faculty in the Department of Molecular Medicine and Biopharmaceutical Sciences, College of Medicine & College of Pharmacy, Seoul National University, South Korea.

3.10 Figures

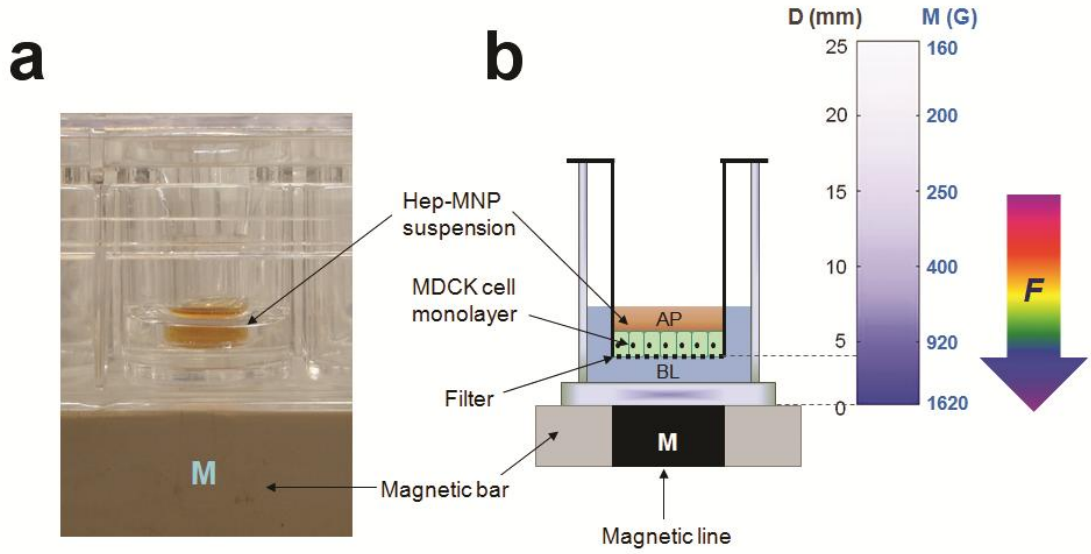

Figure 3-1. MNP transport experiments were carried out using Transwell inserts.

(**a**) Experimental setup with the transport system using Transwell inserts. Supported MDCK (Madin-Darby Canine Kidney) II cell monolayers were grown on porous polyester membrane and used for apical (AP)-to-basolateral (BL) transport studies with 24-well plate placed on a magnetic bar. Heparin-coated MNPs (Hep-MNPs) suspensions were loaded in the apical side. The transport of MNPs across cells was monitored by collecting samples from the basolateral side. (**b**) Schematic representation of the transport system with the magnetic flux density map. Dimensions of the experimental setting are depicted in mm units. Vertical color gradient bar represents the magnetic flux density (*M*, G) as a function of the distance from the surface of magnet (*D*, mm).

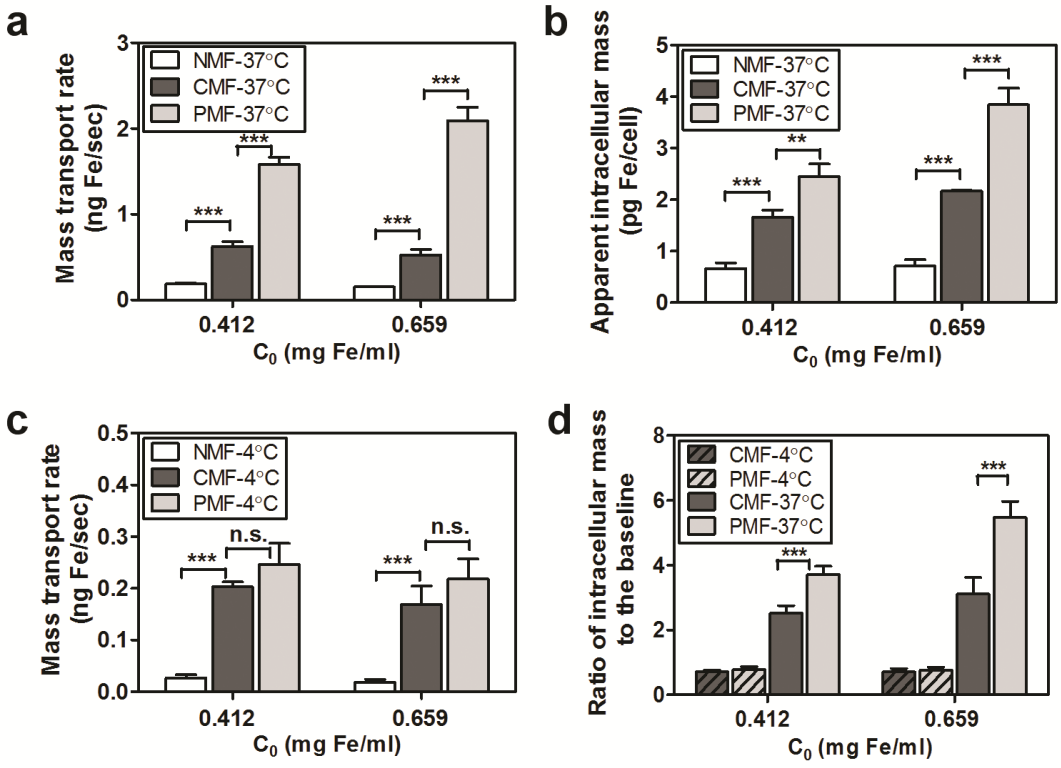

Figure 3-2. Mass transport of MNPs across MDCK cell monolayers was differentially affected by increasing MNP concentrations (0.412 or 0.659 mg Fe/mL) under various magnetic field conditions (NMF corresponds to "no magnetic field"; CMF means "constant magnetic field"; and, PMF is "pulsed magnetic field"; N = 3).

(**a**) Mass transport rates of MNPs and (**b**) apparent intracellular masses of MNPs per cell, after a 90 min transport experiment, for different initial MNP concentrations (C_0: 0.412 or 0.659 mg Fe/mL) under various magnetic field conditions (NMF, CMF, or PMF; 37 °C). (**c**) Rates of mass transport of MNPs across cells at 4 °C, at 0.412 or 0.659 mg Fe/mL under different magnetic field conditions (NMF, CMF, or PMF). (**d**) Ratio of intracellular masses of MNPs divided by the baseline, intracellular mass measured under NMF condition at 37 °C, as calculated after 90 min transport experiments under various experimental conditions (4 °C *vs.* 37 °C; CMF *vs.* PMF). For statistical analysis, one-way ANOVA test was followed by Tukey's multiple comparison tests ($\alpha = 0.05$) to determine significant differences between the means.

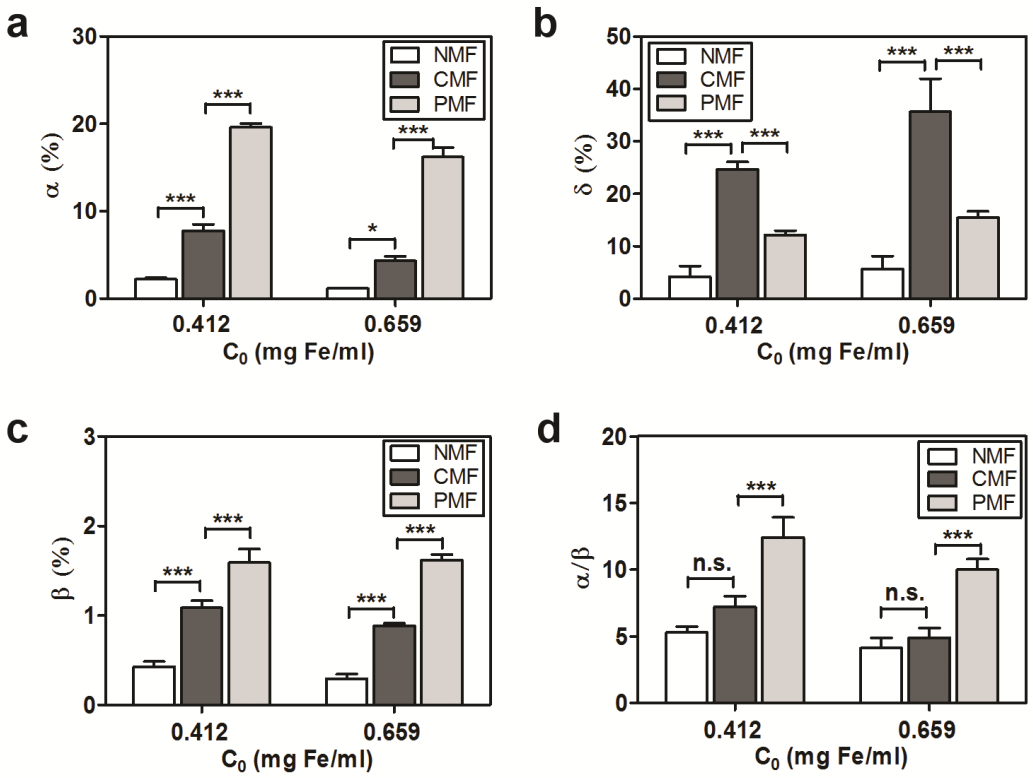

Figure 3-3. Mass balance analysis revealed different fractions of MNPs associated with different compartments, after transport experiments across cell monolayers under different magnetic field conditions.

Transport experiments were done at 0.412 or 0.659 mg Fe/mL (C_0) and data were subjected to mass balance analysis (eqs 1-5). (**a**) Apical-to-basolateral transported fraction of MNPs, α (%); (**b**) fraction of particles bound to the cell surface, δ (%); (**c**) fraction of particles inside the cells, β (%). (**d**) Ratio (α/β) is depicted at 0.412 or 0.659 mg Fe/mL under various magnetic field conditions (NMF, CMF, or PMF). Statistical analysis was performed using one-way ANOVA with Tukey's multiple comparison tests ($\alpha = 0.05$) to determine significant differences between the means.

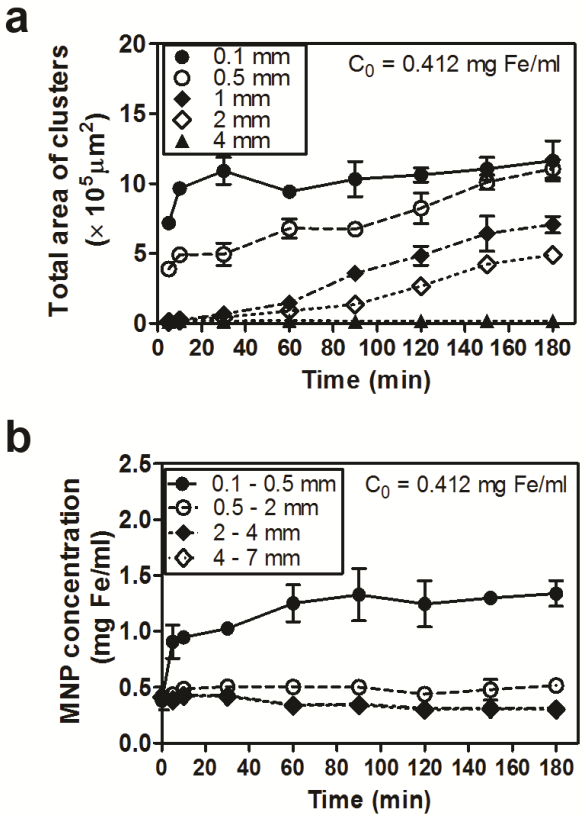

Figure 3-4. Visible, magnetically induced aggregation of MNPs in suspension decreased in size with increasing distance from the magnet.

(**a**) Total sizes (area, μm^2) of clusters of particle aggregates measured from the bright-field images of particle suspension within 4 mm (0.1, 0.5, 1, 2, and 4 mm) from the magnet are displayed as a function of time (5-180 min) under the magnetic field. (**b**) MNP concentration changes at each segment in the tube (0.1-0.5, 0.5-2, 2-4, and 4-7 mm from the magnet) are plotted as a function of time (5–180 min) under the external magnetic field (0.412 mg Fe/mL).

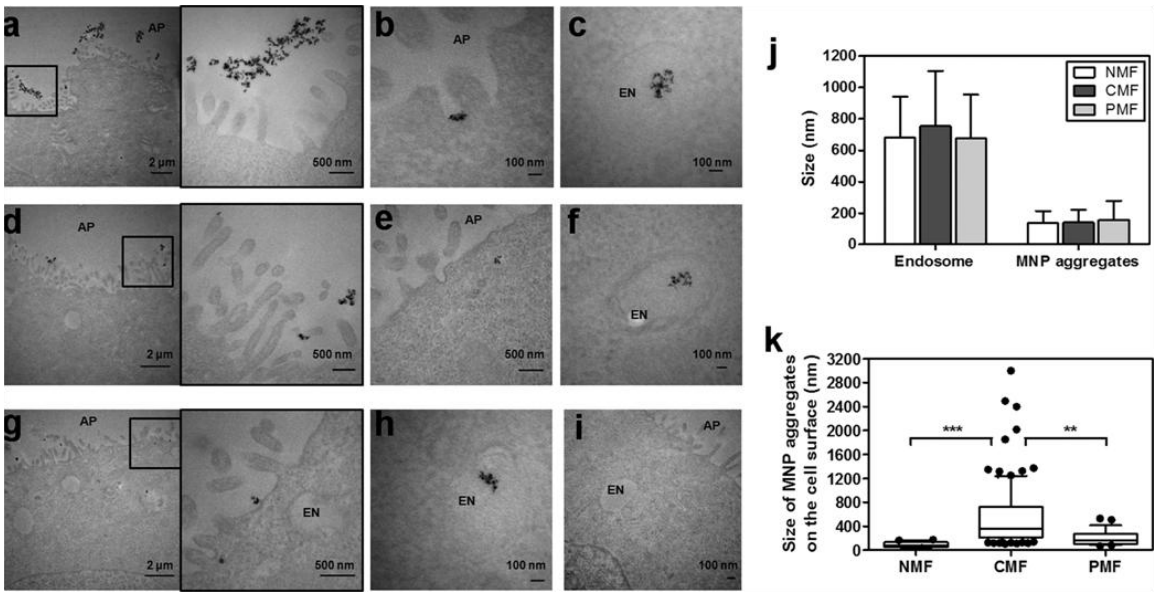

Figure 3-5. Transmission electron microscopy (TEM) revealed different sizes of MNP aggregates associated with cell monolayers after transport experiments under different magnetic field conditions.

"AP" and "EN" indicates apical side and endosome, respectively. Under CMF conditions, (**a**) large aggregates were visible on the extracellular face of the apical cell membrane (zoom-in image next to the original image); (**b**) smaller MNP aggregates were sometimes visible in the cell surface invaginations; (**c**) smaller MNP aggregates were observed inside endosomes. Under PMF conditions, (**d**) MNP aggregates on extracellular face of the apical cell membrane were smaller in size; (**e**) some MNPs were also observed in apical membrane invaginations; (**f**) intracellular MNPs were observed inside endosomes. Under NMF conditions, (**g**) only small MNP aggregates were visible on the extracellular face of the apical cell surface; (**h**) some small MNP aggregates were observed inside endosomes. (**i**) In the absence of MNPs, no MNPs were observed on the cell surface and inside the cells. (**j**) Sizes of endosome and MNP aggregates inside the endosome measured by Metamorph are depicted for different magnetic field conditions (NMF, CMF, or PMF). (**k**) Sizes of MNP aggregates retained on the apical cell surface are compared in different magnetic field conditions (NMF, CMF, or PMF). Whisker plots with 10-90% percentiles are depicted with the solid dots as outliers. For statistical analysis, one-way ANOVA test followed by Tukey's multiple comparison testing was used ($\alpha = 0.05$) to determine significant differences between the means.

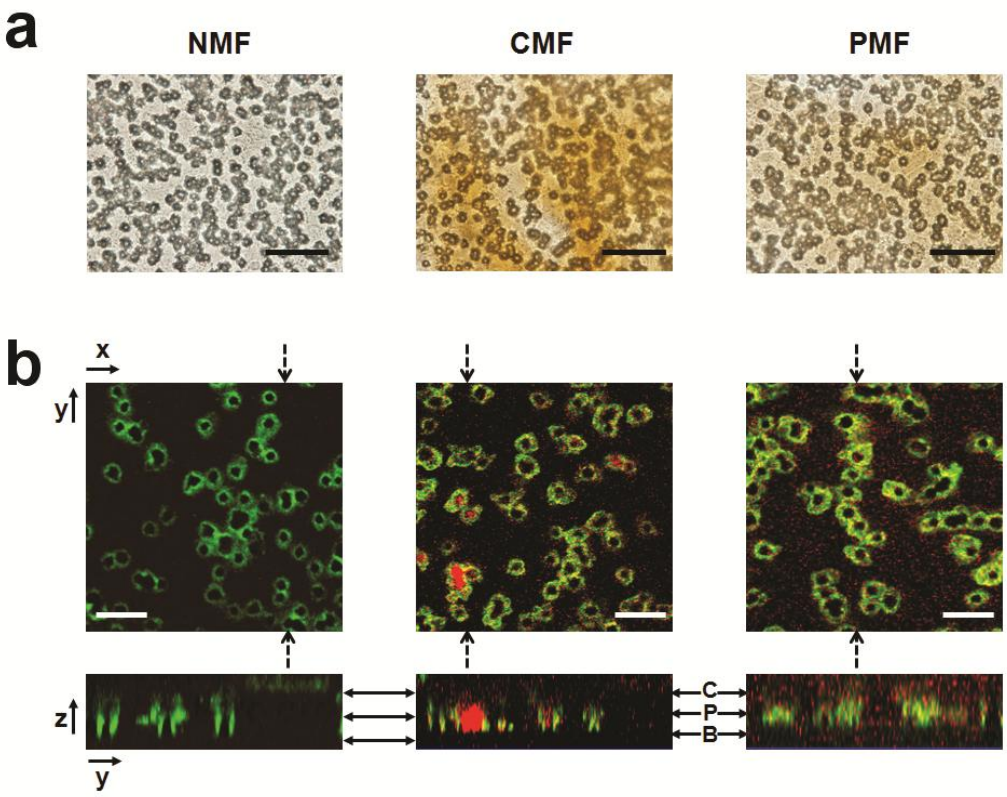

Figure 3-6. Transmitted light and confocal epifluorescence microscopy revealed MNP aggregates on cell monolayers and pores of the polyester membrane after 90 min transport studies with MNPs at high MNP concentration (0.659 mg Fe/mL).

MNPs showed different aggregation patterns, depending on the magnetic field conditions (NMF, CMF, or PMF). (**a**) Images of supported cell monolayers captured by Olympus BX-51 upright light microscope under bright-field illumination at 1000×magnifications (scale bar = 10 μm). (**b**) Images of TRITC-labeled MNPs acquired with a confocal fluorescence microscope, showing the pores of the membrane stained with LysoTracker Green dyes after 30 min incubation under NMF, CMF, or PMF conditions (scale bar = 10 μm). The top image corresponds to a confocal plane across the PET membrane of the Transwell insert, parallel to the plane of the cell monolayer. The bottom image corresponds to an orthogonal yz plane cutting across the cells and the membrane, perpendicularly to the plane of the cell monolayer. Solid bidirectional arrows indicate cytoplasm of the cells (C), pore (P), and basolateral (B) side at each yz plane.

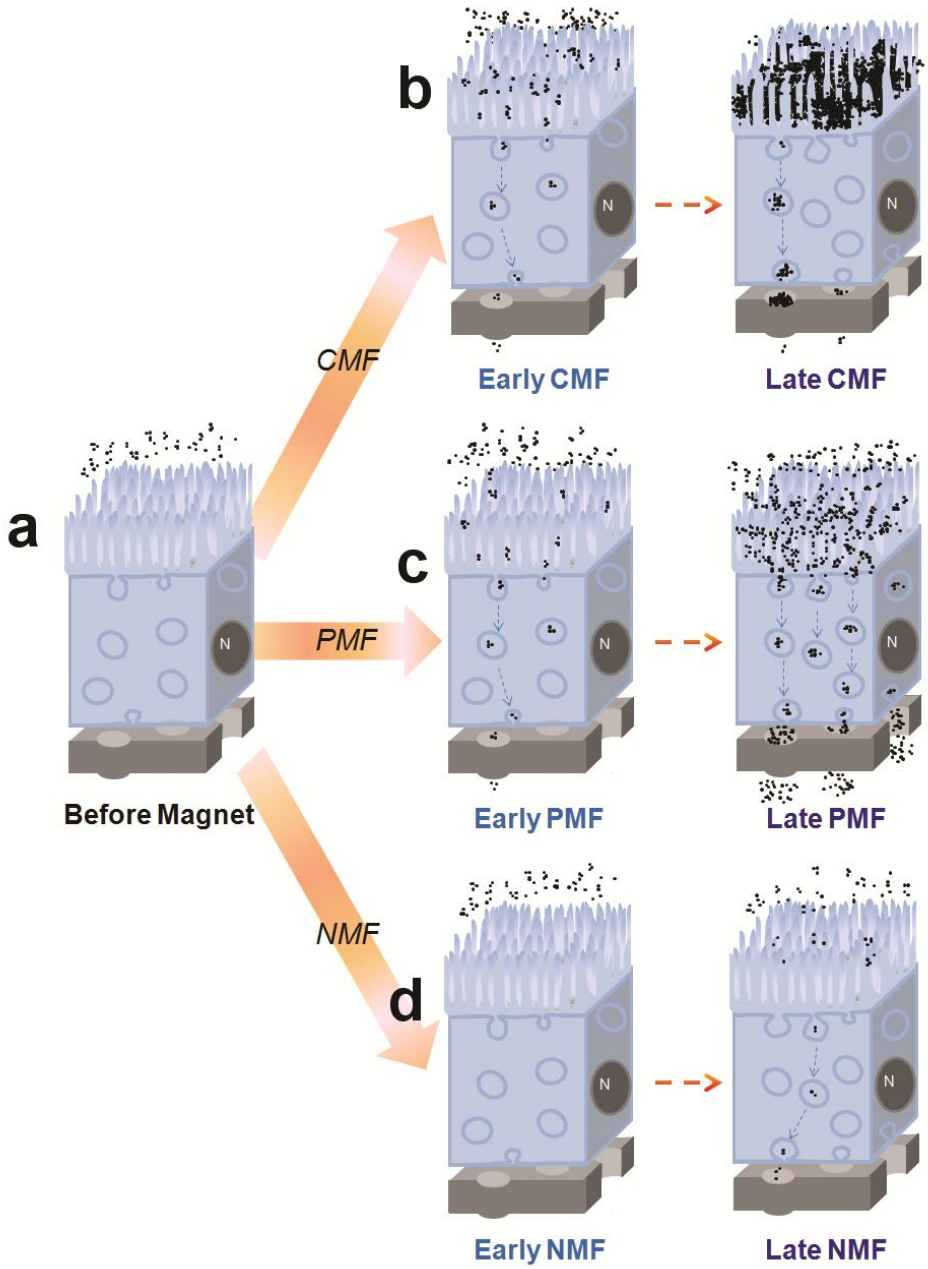

Figure 3-7. Descriptive diagram summarizing the different spatiotemporal behaviors of MNPs under various magnetic field conditions (NMF, CMF, or PMF) based on our quantitative and microscopic observations.

"N" means cell nuclei. (**a**) Before the magnetic field is applied, most of MNPs (random assemblies of black dots) are suspended in the apical compartment. (**b**) Under CMF conditions, the suspended particles are attracted by the magnetic field toward the cell surface, translocated into the cell *via* endocytosis, and to the basolateral side *via* transcytosis. At a later time point, accumulations of larger MNPs aggregates on the cell surface sterically inhibit endocytosis of MNPs, and large MNP aggregates form on the

basolateral side, clogging the pores on the membrane. (**c**) Under PMF conditions, translocations of the particles *via* endocytosis are facilitated by the pulsed magnetic field while the formation of particle aggregates on the cell surface is minimal. There is no clogging by MNP aggregates at the basolateral side of the cells. (**d**) In the absence of magnetic field (NMF), endocytic uptake of MNPs occurs slowly with much fewer MNP aggregates visible on the cell surface or in endocytic vesicles.

3.11 Supporting Information Available

This material is published in *ACS Nano* and supporting information (experimental methods and results with figures) is available in the Appendix A.

3.12 References

1. Chertok B, David AE, Yang VC. Polyethyleneimine-modified iron oxide nanoparticles for brain tumor drug delivery using magnetic targeting and intra-carotid administration. Biomaterials. 2010;31(24):6317-24.
2. Chertok B, Moffat BA, David AE, Yu FQ, Bergemann C, Ross BD, et al. Iron oxide nanoparticles as a drug delivery vehicle for MRI monitored magnetic targeting of brain tumors. Biomaterials. 2008;29(4):487-96.
3. Chertok B, David AE, Yang VC. Brain tumor targeting of magnetic nanoparticles for potential drug delivery: effect of administration route and magnetic field topography. J Control Release. 2011;155(3):393-9.
4. Cole AJ, David AE, Wang JX, Galban CJ, Hill HL, Yang VC. Polyethylene glycol modified, cross-linked starch-coated iron oxide nanoparticles for enhanced magnetic tumor targeting. Biomaterials. 2011;32(8):2183-93.
5. Cole AJ, David AE, Wang JX, Galban CJ, Yang VC. Magnetic brain tumor targeting and biodistribution of long-circulating PEG-modified, cross-linked starch-coated iron oxide nanoparticles. Biomaterials. 2011;32(26):6291-301.
6. Kopke RD, Wassel RA, Mondalek F, Grady B, Chen K, Liu J, et al. Magnetic nanoparticles: inner ear targeted molecule delivery and middle ear implant. Audiology and Neurotology. 2006;11(2):123-33.
7. Mondalek F, Zhang Y, Kropp B, Kopke R, Ge X, Jackson R, et al. The permeability of SPION over an artificial three-layer membrane is enhanced by external magnetic field. BioMed Central; 2006.
8. Sonvico F, Mornet S, Vasseur S, Dubernet C, Jaillard D, Degrouard J, et al. Folate-conjugated iron oxide nanoparticles for solid tumor targeting as potential specific magnetic hyperthermia mediators: Synthesis, physicochemical characterization, and in vitro experiments. Bioconjugate Chem. 2005;16(5):1181-8.
9. Yuan JJ, Armes SP, Takabayashi Y, Prassides K, Leite CAP, Galembeck F, et al. Synthesis of biocompatible poly[2-(methacryloyloxy)ethyl phosphorylcholine]-coated magnetite nanoparticles. Langmuir. 2006;22(26):10989-93.
10. Chatterjee J, Haik Y, Chen C-J. Size dependent magnetic properties of iron oxide nanoparticles. Journal of Magnetism and Magnetic Materials. 2003;257(1):113-8.
11. Hartwig V, Giovannetti G, Vanello N, Lombardi M, Landini L, Simi S. Biological effects and safety in magnetic resonance imaging: a review. Int J Environ Res Public Health. 2009;6(6):1778-98.
12. Riches SF, Collins DJ, Scuffham JW, Leach MO. EU Directive 2004/40: field measurements of a 1.5 T clinical MR scanner. Br J Radiol. 2007;80(954):483-7.
13. David AE, Cole AJ, Chertok B, Park YS, Yang VC. A combined theoretical and in vitro modeling approach for predicting the magnetic capture and retention of magnetic nanoparticles in vivo. J Control Release. 2011;152(1):67-75.
14. Duran JD, Arias JL, Gallardo V, Delgado AV. Magnetic colloids as drug vehicles. J Pharm Sci. 2008;97(8):2948-83.

15. Arruebo M, Fernández-Pacheco R, Ibarra MR, Santamaría J. Magnetic nanoparticles for drug delivery. Nano Today. 2007;2(3):22-32.
16. Tromsdorf UI, Bigall NC, Kaul MG, Bruns OT, Nikolic MS, Mollwitz B, et al. Size and surface effects on the MRI relaxivity of manganese ferrite nanoparticle contrast agents. Nano Lett. 2007;7(8):2422-7.
17. Muller RN, Gillis P, Moiny F, Roch A. Transverse relaxivity of particulate MRI contrast media: from theories to experiments. Magn Reson Med. 1991;22(2):178-82; discussion 95-6.
18. Gao X, Wang Y, Chen K, Grady BP, Dormer KJ, Kopke RD. Magnetic Assisted Transport of PLGA Nanoparticles Through a Human Round Window Membrane Model. Journal of Nanotechnology in Engineering and Medicine. 2010;1(3):031010.
19. Ferrari M. Cancer nanotechnology: opportunities and challenges. Nat Rev Cancer. 2005;5(3):161-71.
20. Medarova Z, Pham W, Farrar C, Petkova V, Moore A. In vivo imaging of siRNA delivery and silencing in tumors. Nat Med. 2007;13(3):372-7.
21. Liong M, Lu J, Kovochich M, Xia T, Ruehm SG, Nel AE, et al. Multifunctional inorganic nanoparticles for imaging, targeting, and drug delivery. ACS Nano. 2008;2(5):889-96.
22. Cheng J, Teply BA, Jeong SY, Yim CH, Ho D, Sherifi I, et al. Magnetically responsive polymeric microparticles for oral delivery of protein drugs. Pharm Res. 2006;23(3):557-64.
23. Dobson J. Gene therapy progress and prospects: magnetic nanoparticle-based gene delivery. Gene Ther. 2006;13(4):283-7.
24. Bulte JWM. Magnetic nanoparticles as markers for cellular MR imaging. Journal of Magnetism and Magnetic Materials. 2005;289:423-7.
25. Peng XH, Qian XM, Mao H, Wang AY, Chen Z, Nie SM, et al. Targeted magnetic iron oxide nanoparticles for tumor imaging and therapy. Int J Nanomed. 2008;3(3):311-21.
26. Lu AH, Salabas EL, Schuth F. Magnetic nanoparticles: synthesis, protection, functionalization, and application. Angew Chem Int Ed Engl. 2007;46(8):1222-44.
27. Muller K, Skepper JN, Posfai M, Trivedi R, Howarth S, Corot C, et al. Effect of ultrasmall superparamagnetic iron oxide nanoparticles (Ferumoxtran-10) on human monocyie-macrophages in vitro. Biomaterials. 2007;28(9):1629-42.
28. Chithrani BD, Ghazani AA, Chan WCW. Determining the size and shape dependence of gold nanoparticle uptake into mammalian cells. Nano Letters. 2006;6(4):662-8.
29. Eberbeck D, Kettering M, Bergemann C, Zirpel P, Hilger I, Trahms L. Quantification of the aggregation of magnetic nanoparticles with different polymeric coatings in cell culture medium. J Phys D Appl Phys. 2010;43(40).
30. Janib SM, Moses AS, MacKay JA. Imaging and drug delivery using theranostic nanoparticles. Adv Drug Deliver Rev. 2010;62(11):1052-63.
31. Win KY, Feng SS. Effects of particle size and surface coating on cellular uptake of polymeric nanoparticles for oral delivery of anticancer drugs. Biomaterials. 2005;26(15):2713-22.

32. Yamamoto H, Kuno Y, Sugimoto S, Takeuchi H, Kawashima Y. Surface-modified PLGA nanosphere with chitosan improved pulmonary delivery of calcitonin by mucoadhesion and opening of the intercellular tight junctions. Journal of Controlled Release. 2005;102(2):373-81.
33. Min KA, Yu F, Yang VC, Zhang X, Rosania GR. Transcellular Transport of Heparin-coated Magnetic Iron Oxide Nanoparticles (Hep-MION) Under the Influence of an Applied Magnetic Field. Pharmaceutics. 2010;2(2):119-35.
34. Koch AM, Reynolds F, Merkle HR, Weissleder R, Josephson L. Transport of surface-modified nanoparticles through cell monolayers. Chembiochem. 2005;6(2):337-45.
35. Petri-Fink A, Steitz B, Finka A, Salaklang J, Hofmann H. Effect of cell media on polymer coated superparamagnetic iron oxide nanoparticles (SPIONs): Colloidal stability, cytotoxicity, and cellular uptake studies. European Journal of Pharmaceutics and Biopharmaceutics. 2008;68(1):129-37.
36. Kim DK, Mikhaylova M, Zhang Y, Muhammed M. Protective coating of superparamagnetic iron oxide nanoparticles. Chem Mater. 2003;15(8):1617-27.
37. Zhang L, Yu FQ, Cole AJ, Chertok B, David AE, Wang JK, et al. Gum Arabic-Coated Magnetic Nanoparticles for Potential Application in Simultaneous Magnetic Targeting and Tumor Imaging. Aaps J. 2009;11(4):693-9.
38. Thunemann AF, Schutt D, Kaufner L, Pison U, Mohwald H. Maghemite nanoparticles protectively coated with poly(ethylene imine) and poly(ethylene oxide)-block-poly(glutamic acid). Langmuir. 2006;22(5):2351-7.
39. Dias AMGC, Hussain A, Marcos AS, Roque ACA. A biotechnological perspective on the application of iron oxide magnetic colloids modified with polysaccharides. Biotechnol Adv. 2011;29(1):142-55.
40. Wu W, He Q, Jiang C. Magnetic iron oxide nanoparticles: synthesis and surface functionalization strategies. Nanoscale Res Lett. 2008;3(11):397-415.
41. Chertok B, David AE, Moffat BA, Yang VC. Substantiating in vivo magnetic brain tumor targeting of cationic iron oxide nanocarriers via adsorptive surface masking. Biomaterials. 2009;30(35):6780-7.
42. Cole AJ, Yang VC, David AE. Cancer theranostics: the rise of targeted magnetic nanoparticles. Trends Biotechnol. 2011;29(7):323-32.
43. Huang J, Bu L, Xie J, Chen K, Cheng Z, Li X, et al. Effects of nanoparticle size on cellular uptake and liver MRI with polyvinylpyrrolidone-coated iron oxide nanoparticles. ACS Nano. 2010;4(12):7151-60.
44. Socoliuc V, Taculescu A, Podaru C, Dobra A, Daia C, Marinica O, et al. Clustering in Water Based Magnetic Nanofluids: Investigations by Light Scattering Methods. Aip Conf Proc. 2010;1311:89-95.
45. Espurz A, Alameda JM, Espurznieto A. Magnetically Induced Dielectric Anisotropy in Concentrated Ferrofluids. J Phys D Appl Phys. 1989;22(8):1174-8.
46. Chertok B, David AE, Yang VC. Brain tumor targeting of magnetic nanoparticles for potential drug delivery: effect of administration route and magnetic field topography. J Control Release. 2011;155(3):393-9.
47. Driscoll CF, Morris RM, Senyei AE, Widder KJ, Heller GS. Magnetic targeting of microspheres in blood flow. Microvasc Res. 1984;27(3):353-69.

48. Kim JS, Yoon TJ, Yu KN, Noh MS, Woo M, Kim BG, et al. Cellular uptake of magnetic nanoparticle is mediated through energy-dependent endocytosis in A549 cells. Journal of Veterinary Science. 2006;7(4):321-6.
49. Dormer K, Seeney C, Lewelling K, Lian G, Gibson D, Johnson M. Epithelial internalization of superparamagnetic nanoparticles and response to external magnetic field. Biomaterials. 2005;26(14):2061-72.

Chapter 4

Integrated Pharmacokinetic Approach for Developing Site-Directed Molecular Probes for Lung

The contents in this Chapter have been published in PLoS Computational Biology with titled as "A Cell-Based Computational Modeling Approach for Developing Site-Directed Molecular Probes" (Yu J-y, Zheng N, Mane G, Min KA, Hinestroza JP, Zhu H, Stringer KA, Rosania GR. A Cell-based Computational Modeling Approach for Developing Site-Directed Molecular Probes. *PLoS Comput Biol.* 2012;8(2):e1002378). My contribution to this paper was to elucidate how the different molecular probes are transported and accumulate in the human airway epithelial primary cells according to their physicochemical properties through *in vitro* cell-based permeability assays. My collaborators have performed *in vitro* assay with canine kidney cell lines to describe molecular transport with different directions (apical-to-basolateral; lateral transport), *in silico* computational modeling and *in vivo* studies to characterize the deposition/transport patterns of molecular probes in the airways *vs.* alveoli. My contribution illustrates the effects of cell areas exposed to molecules along the cell multilayers on local distribution of the molecules.

4.1 Background

Research about site-directed probes or biomarkers has been actively conducted with various perspectives, from discovery of disease targets to development of specific probes for site imaging or drug targeting. Enzymes or receptors expressed in the specific local regions have been utilized as special biomarkers for disease diagnosis or therapy (1, 2). Efforts to discover the site-directed molecules have been paralleled with the studies to synthesize specific activators or inhibitors for the targets to modulate the target molecules' functions and relevant mechanistic pathways in the pathologies. Especially, imaging with the site-directed probes locally retained in the specific tissues or organs can help to diagnose the diseased conditions ahead of the advanced stages. For intense tissue remodeling such as asthma and COPD, the pulmonary pathologic conditions involve different molecules in the process of regulations. Therefore, there have been many trials synthesizing chemical acting agents for the targets (3, 4). Because of therapeutic benefits of the inhaled drug delivery on the pulmonary diseases (rapid onsets, low systemic exposure and side effects), the inhaled drug market has been gradually growing worldwide. The global pulmonary drug delivery technology market, valued at $19.6 billion in 2010, is projected to reach nearly $44 billion by 2016 (5). Research and development (R&D) is actively engaged on new products in the inhaled drug delivery.

However, due to the complicated, delicate properties of the lung, it has been quite challenging to measure the local drug concentrations and develop locally acting, inhaled molecules deposited on the regions of interest along the upper to lower respiratory systems. Anatomically, lung is composed of two distinct regions, the central conducting airways and the peripheral respiratory alveolar region. Conducting airways are bifurcated

into smaller branches continuously starting from trachea (6). The airways are composed of the airway epithelial lining as a principal barrier with a secretory and ciliated epithelium and submucosal glands, and cartilaginous elements in the large bronchi. Alveoli regions are composed of a thin epithelial cell layer (Type I and II alveolar epithelial cells) and macrophage cells. The squamous type I cell in alveoli covers approximately 96% of the surface are, the rest 3% of the surface is covered by the cuboidal type II cells. The endothelial surface of the lung is large enough for the efficient gas exchange (7). The interstitium of the lung contains extracellular matrix with various cell components (*e.g.*, collagen, fibroblasts, monocytes, and lymphocytes), and interstitial fluid (8). The heterogeneous cellular composition across different regions of the lung along the upper and lower respiratory thus accounts for the difference in molecular transport behavior between airways and alveoli.

4.2 Rationale and Significance

Previously, the cellular pharmacokinetic model (1CellPK) showed good predictions for intestinal permeability of drug molecules and subcellular distributions of lysosomotropic molecules (9, 10). This model helped establish the lung model based on the anatomical features of the airway and alveoli to estimate the relationship between the physicochemical properties of the inhaled drug molecules and the regional absorption rates in the lung (11). The absorption rate constants calculated by the model based on the physicochemical properties of the drug molecules (pK_a, logP, and molecular radius) showed consistency with the experimental measurements of drug absorption in the lung.

So far, many studies have demonstrated that the regional lung deposition of drugs depends on the aerodynamic particle size by delivery devices (12-14). However, regional differences in local lung exposure to drug molecules have not been investigated based on the physicochemical properties of molecules for their delivery. Distribution of molecules in various regions of the lung could be affected by the route of administration as well as histological microenvironments in airway or alveoli (15, 16). Herein, on the basis of the anatomical and biophysical understandings of respiratory systems (upper or lower) and established lung model, we estimated local transport and retention of the molecular probes for airway or alveoli targeting with *in vitro-in silico-in vivo* model approach. Two small molecular probes, MitoTracker® Red and Hoechst® 33342 were investigated in the context of the appropriate properties as site-directed probes, by mechanism-based model predictions and *in vitro*, *in vivo* permeability experiments. Our approach is significant because it would enable us to understand how the inhaled drug molecules or bioimaging probes behave after local administration to the lung and thus, the effects of different regional cell microenvironment (airway *vs.* alveoli, different absorption areas) on drug transport. This strategy may help guide the development of lung regional-targeted drug formulations for clinical diagnosis or therapy.

4.3 Abstract

Modeling the local absorption and retention patterns of membrane-permeant molecules in a cellular context could facilitate development of site-directed chemical agents for bioimaging or therapeutic applications. Here, we present an integrative approach to this problem, combining *in silico* computational models, *in vitro* cell based

assays and *in vivo* biodistribution studies. To target small molecule probes to the epithelial cells of the upper airways, a multiscale computational model of the lung was first used as a screening tool, *in silico*. Following virtual screening, cell monolayers differentiated on microfabricated pore arrays and multilayer cultures of primary human bronchial epithelial cells differentiated in an air-liquid interface were used to test the local absorption and intracellular retention of selected probes, *in vitro*. Lastly, experiments involving visualization of bioimaging probe distribution in the lungs after local and systemic administration were used to test the relevance of computational models and cell-based assays, *in vivo*. The results of *in vivo* experiments were consistent with the results of *in silico* simulations, indicating that mitochondrial accumulation of membrane permeant, hydrophilic cations can be used to maximize local exposure and retention, specifically in the upper airways after intratracheal administration.

4.4 Introduction

Local administration of therapeutic agents or bioimaging probes is commonly used to maximize concentrations at a desired site of action and to minimize side effects or background signals associated with distribution in off-target sites. However, in the specific case of inhaled, small molecule therapeutic agents or bioimaging probes, cell impermeant molecules may rapidly disappear from the sites of deposition via mucociliary clearance (17, 18). Conversely, cell permeant small molecules can rapidly diffuse away and disappear from the site absorption, down their concentration gradient (19). Therefore, we decided to explore an integrative simulation approach (Figure 1) to study how the

physicochemical properties of small molecule probes may be optimized to maximize local targeting and retention in the upper respiratory tract.

Previously, we constructed multiscale, cell-based computational models of airways and alveoli to predict the relative absorption, accumulation and retention of inhaled chemical agents (11). In these models, the transport of small molecules from the airway surface lining to the blood or from the blood to the airway surface lining were modeled using ordinary differential equations (ODEs) (9, 20). These ODEs described the transport of drug molecules across a series of cellular compartments bounded by lipid bilayers (Figure 1A), which form the surface of each airway generation, modeled as a tube (Figure 1B). For a monoprotic base, the concentration of molecule in each subcellular compartment was divided into two components: neutral and ionized (10, 21). Accordingly, two drug specific properties were used as input to simulate the transport process across each lipid bilayer: the logarithms of the octanol:water partition coefficient of the neutral form of the molecule (i.e., $\log P_n$) and the pK_a of the molecule. The logarithm of the octanol:water partition coefficient of the ionized form of the molecule (i.e., $\log P_d$) can be derived from $\log P_n$ or it can be incorporated as an independent input parameter that can be measured or calculated with cheminformatics software. For different compartments with different pHs and lipid fractions, the free fraction of the neutral and ionized forms of molecules was calculated according to the molecule's pK_a, $\log P_n$, and $\log P_d$, using the Henderson-Hasselbalch equation and the laws of mass action.

Anatomically, the structure of the airways was modeled as a tree-like branching system of cylinders with progressively narrowing diameter (22) (Figure 1C). Starting with the trachea as the trunk of the tree and ending in the alveoli as the leaves, each

branching segment corresponded to an airway 'generation' characterized by a particular surface area, blood flow, and cellular organization (11, 23). Histologically, the walls of the airways or alveoli were modeled as multiple layers of epithelial, interstitial and endothelial cells separating the air from the blood. Several structural and functional differences between the airways and alveoli are noteworthy: 1) Cartilage and smooth muscle are present only in the interstitium of the airways; 2) The surface area of the alveoli is two orders of magnitude larger than airways; and 3) While the blood flow to the alveoli corresponds to 100% of cardiac output from the right ventricle, the blood flow of the airways is approximately 1% of the cardiac output from the left ventricle (24, 25).

To predict a molecule's absorption and retention in different airway generations, the transport properties of small molecules across cellular membranes, as well as the local partitioning of molecules into lipid in different subcellular compartments can be calculated with the Fick and Nernst-Planck equations to describe the transport of the neutral and charged species of the molecule (11). In simulations, combinations of logP and pK_a spanning a range of values were used as input to simulate the changes in concentration of molecules of varying chemical structure, as they are absorbed from the airway surface lining liquid into the blood or vice versa.

Here, we applied this cell-based transport model as a virtual screening tool, to identify compounds with differential distribution profiles in airways and alveoli, after intratracheal (IT) or intravenous (IV) administration. In addition, two innovative *in vitro* cell based assays were developed to assess the absorption and retention of molecules across multiple layers of cells along the lateral (Figure 1 D-F) and transversal planes of a cell monolayer (Figure 1G)). Finally, *in vivo* microscopic bioimaging experiments were

performed to visualize the distribution of fluorescent probes in the lung after either IT or IV administration (Figure. 1H). The results revealed that the mitochondrial sequestration of hydrophilic, cell-permeant cations can provide an effective mechanism for maximizing their local exposure and retention at the site of absorption. Accordingly, mitochondriotropic cations may be useful as fiduciary markers of local, inhaled drug deposition patterns in the upper respiratory tract.

4.5 Methods

General Methodology. All of the equations and default parameter values were based on our published model (11). The ODEs that describe this lung pharmacokinetic (PK) model were solved numerically in a Matlab® simulation environment (Version R2009b, The Mathworks Inc, Natick, MA). The ODE15S solver was used to address the issue of the stiffness in ODEs, and the relative and absolute error tolerance was set as 10^{-12} to minimize numerical errors. The Matlab scripts used for virtual screening and simulation purposes are provided, together with detailed instructions for running them, in the online supplemental materials (Text S1, S2, S3, S4, S5, S6). The results of detailed parameter sensitivity analysis are provided in the Appendix B.

Virtual Screening of Small Monobasic Molecules Targeting the Airways after IT Instillation. For virtual screening, the airway and alveoli were linked to a systemic pharmacokinetic model through their respective blood compartments using a single compartment PK elimination model (equation 1) (26):

$$V_b \frac{dC_b}{dt} = -C_b CL \qquad (1)$$

Where V_b is the volume of the blood compartment; C_b is the concentration in the blood; and CL is the clearance. The same initial dose (1 mg/kg) was used as an input parameter to simulate IT instillation experiments in the airways and alveoli, respectively. For virtual screening, clearance in the systemic circulation was set to zero. The logP_n (-2 to 4 with interval of 0.1 units) and the pK_a (5 to 14 with interval of 0.2 units) of monobasic compounds were independently varied and used as input parameters, in all possible combinations. For each set of physicochemical input parameters (logP_n and pK_a) two important pharmacokinetic indexes were calculated: 1) the percentage of mass deposited in the airways and alveoli (relative to the total mass in whole lung; and, 2) the concentration in the alveolar and airway regions, calculated as the sum of the masses in all the compartments in said regions of the lung divided by the sum of all the compartment volumes in that region. The area under the tissue concentration curve (AUC) for the airways and alveoli was calculated using the trapezoidal rule. The AUC ratio of airways to alveoli after inhalation was calculated by dividing the AUC of the airways by the AUC of the alveoli for every combination of logP_n and pK_a that were used as input.

For comparison, simulations were also run to simulate an intravenous (IV) bolus injection, with the initial concentration in venous blood as calculated with equation 2:

$$C_{0,vb} = Dose / V_{vb}, \qquad (2)$$

The volume of venous and artery blood was set to 13.6 and 6.8 ml, respectively (26, 27). The concentration in the blood was fixed (clearance set to 0) with the assumption of no significant plasma protein binding and a drug concentration blood to plasma ratio of 1.

Detailed Simulation Analysis of Fluorescent Probe Distribution in the Airways and Alveoli After Local and Systemic Administration. Based on the results of virtual screening, two fluorescent probes were selected for further testing: Hoechst® 33342 (Hoe, Molecular Probes, CA, USA) to represent a highly hydrophobic, weakly basic molecule that can serve as a reference marker for a readily absorbed probe with limited intracellular retention; and, Mitotracker® Red (MTR, Molecular Probes, CA, USA) to represent a more hydrophilic cation that could serve as a candidate fiduciary marker for local inhaled drug deposition and absorption patterns. MTR was modeled with a single, fixed positive charge and a $\log P_d$ = 0.16. Hoe was modeled as a lipophilic, monobasic molecule with a pKa = 7.8 and a $\log P_n$ = 4.49 (calculated with ChemAxon, www.chemaxon.com). These physicochemical properties were used as input parameters to calculate the time dependent changes of the probe concentrations in the airways and alveoli, respectively. For simulations of IT instillation, the same initial concentration (1 mM) of MTR and Hoe was assumed as the initial condition for the airways and alveoli. The same initial dose used for IT instillation was also used for IV administration. Blood clearance was fixed to 0 for simulations, unless otherwise noted.

Cell–Based Transport Assays on Microfabricated Pore Arrays. A customized transwell insert system was constructed using a polyester membrane with microfabricated pore arrays precisely machined using a focused ion beam (Hitachi FB-200A) (28) (Figure 1E). These membranes support cell growth and the pores serve as a point source for compound administration to single cells on a cell monolayer (Figure 1F). The pore arrays were comprised of 3 μm diameter cylindrical pores, arranged 20 μm apart in a 5-by-5 square array. Pores were also arranged 40, 80 and 160 μm apart in 3-by-3 symmetrical

arrays. The pores were individually machined using a high brightness Ga liquid metal ion source coupled with a double lens focusing system. The perforated membranes were glued (Krazy Glue®) to the bottom of hollow Transwell® holder (Costar 3462 or 3460), creating a permeable support for cell growth (Figure 1D). The integrity of the insert system was tested by adding 5 mM Trypan Blue (dissolved in Hank's balanced salt solution; HBSS) to the insert wells (28). The insert was considered intact if there was no evidence of Trypan Blue leakage from the edge of the insert membrane. For assessing lateral cell-cell transport, Madin-Darby canine kidney (MDCK) cells were purchased from ATCC (CCL-34^{TM}) and grown (37°C, 5% CO_2) in Dulbecco's modified Eagle's medium (DMEM, Gibco 11995) containing 10% FBS (Gibco 10082), 1 × non-essential amino acids (Gibco 11140) and 1% penicillin/streptomycin (Gibco 15140). MDCK cells were seeded on polyester membranes containing the pore arrays at a density between 1×10^5-2×10^5 cells/cm^2 and were grown until a confluent cell monolayer formed (Figure 1F). To evaluate the effect of pore arrays on cell monolayer intactness, MDCK cells were washed and incubated in transport buffer (HBSS buffer supplemented with 25 mM D-glucose, pH 7.4) for 30 min followed by transepithelial electrical resistance (TEER) measurement using Millipore Millicell® ERS. Cell monolayers were used for experiments only if the background subtracted TEER values were higher than 100 $\Omega\cdot$cm^2 and if the cells covering the pore arrays appeared as an intact monolayer.

Measurement of Lateral Cell-to-Cell Transport and Retention Using Microfabricated Pore Arrays. To assess cell-to-cell transport along the plane of the monolayer (Figure 1D-F), fluorescent dyes were added into the basolateral compartment of the transwell system (at time 0). The dynamic staining pattern in the cells was imaged

(Nikon TE2000S epifluorescence microscope equipped with a triple-pass DAPI/FITC/TRITC filter set (Chroma Technology Corp. 86013v2)). The 12-bit grayscale images were acquired using a CCD camera (Roper Scientific, Tucson, AZ). For measurements, individual cells or nuclei in these images were manually outlined using the region tool in MetaMorph® software (Molecular Devices Corporation, Sunnyvale, CA). The average and standard deviation of cellular or nucleus fluorescence intensity was measured using MetaMorph®, after subtracting the background fluorescence intensity estimated from the unstained regions of the monolayer distant to the pores. The rate of Hoe staining in the nucleus was measured as the slope of fluorescence increase normalized by the slope of increase in the first nucleus (closest to the pore).

Measurement of Intracellular Retention Using Normal Human Bronchial Epithelial Cell Multilayers Differentiated on Air-Liquid Interfaces. Normal human bronchial epithelial cells (NHBE, Clonetics™, passage 1; Lonza, Walkersville, MD) were cultured (37°C, 5% CO_2) and seeded (passage 2) at 2.5×10^5 cells/cm^2 on a Transwell® insert (Corning Inc., Lowell, MA; area: 0.33 cm^2, pore size: 0.4 μm) in NHBE differentiation media (Lonza, Walkersville, MD). The apical media was aspirated after 24 h of cell seeding and the cells on the polyester membrane were maintained in media only in the basolateral compartment of the air-liquid interface culture (ALC) (29, 30). On day 8 of ALC, the integrity of the cell layers on the membrane was assessed by light contrast microscope and by transepithelial electrical resistance (TEER) (31). After equilibration of the cell layers on the insert with pre-warmed HBSS buffer (10 mM HEPES, 25 mM D-glucose, pH 7.4) for 30 min (37°C, 5% CO_2), TEER values were obtained and cells with

TEER values of ~ 600 $\Omega \cdot cm^2$ were used for the transport and retention assays (29, 30, 32-34).

NHBE cell multilayers grown on the inserts were examined with a Zeiss LSM 510-META laser scanning confocal microscope (Carl Zeiss Inc., Thornwood, NJ) with a 60 × water immersion objective on day 8 of ALC culture. For the confocal analyses, three different cell-permeant dyes were prepared by dilution with HBSS buffer (10 μg/ml Hoe; 2.5 μM Lytotracker® Green (LTG, Molecular Probes, CA); and 1 μM MTR). After the cell multilayers were washed with HBSS, 240 μl of dye mixture (80 μl of each dye in HBSS) was added to the apical compartment and 600 μl of HBSS was added to the basolateral side. After 30 min, transport of the dyes across the cell layers was measured by placing the insert into a two-chambered slide (Lab-Tek®; Thermo Scientific Nunc co., Rochester, NY) and acquiring images along the Z-axis (interval, 1 μm) in three fluorescence channels (coherent enterprise laser (364 nm) for Hoe, Argon laser (488 nm) for LTG, and Helium neon 1 laser (543 nm) for MTR). The distribution of probes applied in the apical compartment of the NHBE cell multilayer cultures was assessed in 3D reconstructions of the acquired images of probe distribution, using MetaMorph® software (Figure 1G). The relative distributions of MTR, Hoe, and LTG dyes across the multilayers were assessed by imaging analyses through multiple Z-stacks. After background subtraction, the integrated intensity of each fluorescence channel per cell was summed in each cell layer and divided by the total integrated intensity in all the layers to calculate the percentage of relative distribution of the integrated fluorescence signal of each dye associated with inner cell layer or the exposed surface layer of the NHBE cell multilayer.

Visualizing Probe Distribution in Mice Lungs after IT Instillation or IV Administration. The distribution of MTR and Hoe in airways and alveoli after IT and IV injection in live mice were determined by microscopic imaging of cryopreserved lung tissue sections and confirmed by visual inspection followed by quantitative imaging of high resolution tiled mosaics assembled from fluorescence images of tissue sections (Figure 1H). For these experiments, male C57BL/6J mice (Jackson Laboratory, Bar Harbor, ME; 8 weeks, 20-30 g) were used and the protocol was approved by the University of Michigan's animal care and use committee in accordance with the National Institutes of Health Office of Laboratory Animal Welfare "Principles of Laboratory Animal Care." MTR (50 μg in 10 μl DMSO) and Hoe (90 μl of 10 mg/ml in ddH_2O) were mixed so that the final concentration of MTR and Hoe was 0.94 and 14.61 mM, respectively. Mice received either 50 μl of dye mixture or 50 μl saline (control) via IV tail vein injection or IT instillation (35). For IV administration, conscious mice were briefly restrained and for IT instillation mice were anesthetized with isoflurane gas, and the dose was delivered to the airway via the oral route as previously described.

In order to study the differential regional distribution of fluorescent dyes in the lung, mice were anesthetized with ketamine/xylazine 40 minutes after dosing. A thoracotomy was performed and a heparinized blood sample was acquired by cardiac puncture. The trachea was cannulated (20G luer stub) after which the lungs were inflated with ~1 mL of a 30% sucrose-optimal cutting temperature (OCT; Tissue-Tek, Sakura Finetek USA, Torrance, CA USA) mixture and removed *en bloc*. The lungs were immersed in OCT and were immediately frozen (at -80°C) (36).

For microscopy, coronal lung sections (7 μm) were imaged using an epifluorescence Olympus BX-51 microscope equipped with the standard DAPI, FITC and TRITC filter sets. A series of low-magnification (×4) left and right lung section images were electronically captured with an Olympus DP-70 high-resolution digital camera using Image J software (ImageJ 1.44b, National Institute of Health, USA; http://rsb.info.nih.gov/ij). In order to permit comparisons of image brightness and fluorescence, images for each lung section were acquired using the same illumination and image acquisition settings. Mosaics of the entire lung were tiled using Photoshop® (version 4; Adobe Systems Inc., San Jose, CA) and quantitative image analysis was carried out using the integrated morphometric analysis function of MetaMorph®. Background subtracted fluorescence intensity values over the airways and alveoli were measured, as the integrated value of all pixels per unit area of the manually selected airway and alveolar tissue regions, using the images acquired with the DAPI channel. In turn, the same airway and alveolar tissue regions were used to measure the MTR fluorescence signal using the images acquired with the TRITC channel.

4.6 Results

For virtual screening experiments, molecules with maximal tissue exposure (AUC) in the airways after inhalation were identified by using combinations of logP_n and pK_a as input parameters in a multiscale, cell-based lung transport model (Figure 2). For weak bases, lower lipophilicity and higher pK_a promoted intracellular retention and led to greater local exposure relative to the alveoli (Figure 2A, B). The calculated airway/alveoli exposure ratio (Figure 2C) ranged from 100 to 700 and increased with

lowered logP_n (increasing hydrophilicity) and higher pK_a (greater positively charged fraction at physiological pH). Essentially, cell-permeant, hydrophilic molecules harboring a fixed positive charge showed the greatest accumulation and retention in the cells of the upper airway relative to the alveoli, following IT administration.

To probe the role of the route of administration, simulations were also performed by independently varying logP_n and pK_a to calculate the mass deposition pattern in the airways and alveoli under steady state conditions after IV administration (Figure 2D-F). In this manner we established the relationship between the physicochemical properties of small molecules and absolute and relative mass distribution in the airways (Figure 2D) and alveoli (Figure 2E). Following IV administration, the majority of the mass was deposited in the alveoli irrespective of the physicochemical properties of the molecules (Figure 2F); the airways held less than 20% of total drug mass in the lungs. Compounds with low logP_n and high pK_a tended to exhibit the largest airway to alveoli mass ratios, which paralleled the results obtained after IT administration.

In order to validate the results of these virtual screening experiments, two fluorescent bioimaging probes, MTR and Hoe, were selected for more detailed analysis. MTR is cell-permeant, hydrophilic cation, and Hoe is a cell-permeant, hydrophobic weak base. Based on the screening results (Figure 3) and more detailed simulations (Figure 3), the concentration profiles of these two fluorescent molecules in the airways and alveoli were markedly different after IT (Figure 3A, B) and more similar after IV (Figure 3C, D) administration. When given IT, the predicted MTR concentration, 40 to 60 min after administration, was nearly 10-fold higher in the airways than in the alveoli (Figure 3A). Conversely, the predicted concentration of Hoe in the airways was two-fold higher in

alveoli than in airway (Figure 3B). When given IV, the predicted concentration of MTR in the airways was almost same as that in alveoli (Figure 3C). However, the predicted concentration of Hoe in the airways was higher in alveoli (Figure 3D). Thus, MTR should be retained in the airways specifically after IT administration, whereas Hoe should not be retained in airways relative to alveoli regardless of the route of administration.

Next, cell-based assays were used to establish the intracellular retention of MTR and Hoe at a site of absorption. For this purpose, a transwell insert system with micro-fabricated pores was constructed. After seeding MDCK epithelial cells on the patterned pore arrays and adding hydrophobic fluorescent compounds in the basolateral side of cell monolayer, the time course dye uptake in the cells sitting above the pores and the kinetics of lateral transport from the cells lying on top of the pore to the neighboring cells was visualized by fluorescence microscopy.

Three hours after the addition of Hoe to the basolateral compartment, only cells that were within close vicinity of pores were stained, indicating that the cells formed a tight seal with the pores such that each pore fed almost exclusively into cells that were in immediate contact with the pores (Figure 4). Monitoring of the cell-to-cell diffusion of Hoe over time, indicated that the pores served as point sources of sustained dye supply to the adjacent cells (Figure 4A-D) and for cells grown on membranes with pores spaced by 80 μm (Figure 4C) or 160 μm (Figure 4D), each pore could be considered as the single point source of dye molecules. Quantitative image analysis revealed that the rate of staining rapidly decreased as the distance of the cells from the pores increased (Figure 4E, F). Remarkably, only cells in the vicinity of each pore were labeled.

As controls, cells were stained with Hoe plus BCECF-AM from the basolateral compartment (Figure 4G-I). BCECF-AM is a nonfluorescent cell-permeant ester, which generates a cell-impermeant, fluorescent molecule upon intracellular hydrolysis. While the extent of Hoe diffusion was dependent on the distance from the pores (Figure 4G), the green fluorescence of the hydrophillic ester hydrolysis product (BCECF) was exclusively restricted to the first layer of cells that were in direct contact with pores (Figure 4H, I).

Similar to the Hoe staining pattern, MTR also exhibited a highly constrained diffusion pattern with most of the staining restricted to the vicinity of each pore (Figure 5). After two-hours of staining from the basolateral compartment with both Hoe (Figure 5A) and MTR (Figure 5B), only cells with 60 microns of the pore were stained with both probes (Figure 5C). The normalized fluorescence intensity of MTR and Hoe were similar in the first and second layers of cells, but MTR showed higher penetration into the third layer (Figure 5D).

In the transversal direction, the absorption and retention of MTR and Hoe across multiple layers of cells was also assessed in primary NHBE cells differentiated as multilayers in ALC (Figure 6). For the experiments, MTR and Hoe were simultaneously added in the apical side of the cells and intracellular accumulation was assessed using 3D reconstructions of the cell multilayers (Figure 6). As a positive control, LTG was also included in the apical HBSS buffer. Thirty minutes after the addition of probes to the apical compartment, both MTR and Hoe staining were constrained to the first, outer surface layer of cells (Figure 6, left). The cells beneath the surface layer of cells were stained with LTG (Figure 6, right), indicating that the limited penetration of both MTR and Hoe. Different transport patterns of MTR, Hoe and LTG across the cell multilayers

were verified by image quantitation using MetaMorph® software in the multiple Z-stack images of NHBE cell multilayers. Approximately 96% ±2.76% of MTR or 96% ±2.48% of Hoe was retained in the surface cell layer whereas 50% ±15.62% of LTG fluorescence was associated with the surface cell layer. Tukey's multiple comparison test following ANOVA (one-way analysis of variance) test showed statistically significant difference between MTR and LTG (p-value<0.0001) and also between Hoe and LTG (p-value<0.0001), but not between MTR and Hoe with p-value larger than 0.05 (α=0.05).

As an ultimate test of the results of *in silico* virtual screening experiments, mice were administered a mixture of MTR and Hoe by either IV tail vein or IT instillation and the distribution of the molecules in the lungs was assessed by fluorescent microscopy (Figure 7). Hoe distributed throughout the lungs regardless of route of administration (Figure 7A, B) with fluorescence in both alveoli and airways (Figure 7C, D). Following IV administration, MTR also distributed throughout the lung in both airways and alveoli (Figure 7E). Conversely, IT administered MTR resulted in highly uneven fluorescence distribution (Figure 7F). Most importantly, the airway regions showed comparable MTR fluorescence in airway vs. alveoli after IV (Figure 7G) but higher MTR fluorescence intensity in airways compared with the alveoli following IT delivery (Figure 7H).

To confirm these observations quantitative image analysis was performed to compute background subtracted integrated intensity of alveolar and airway regions, to quantify the relative, differential fluorescence intensity distribution of Hoe and MTR in airway and alveoli. The fluorescence MTR/Hoe ratio ranged from 2.42 to 3.27 for IT administration. For MTR and Hoe, the mean (±s.d.) percent airway delivery was 23.9% ±5.8% and 8.8% ±2.7%, respectively (based on 422 region measurements from a single

lung). For IV administration, the fluorescence MTR/Hoe ratio ranged from 0.95 to 1.45. The mean (±s.d.) percent airway delivery for MTR and Hoe were 7.5% ±2.5% and 7.1% ±1.8%, respectively (based on 383 region measurements from a single lung). The images and measurements were consistent with local intracellular retention of MTR in the airways compared with Hoe, following IT (but not IV) instillation. These *in vivo* results paralleled the *in silico* simulation results (Figure 3).

In order to identify the most important parameters that might explain the differences in local retention of MTR and Hoe, a parameter exchange analysis was performed using computational simulations. For this purpose, individual parameters of the airway were exchanged with those of the alveoli, one at a time, and the simulations were rerun to calculate the exposure (AUC) of MTR and Hoe. Based on the results of this simulation analysis (Table 1) the volume of interstitial smooth muscle cells together with the volume of mitochondria were the primary factors determining the retention of MTR in the upper airways relative to alveoli. Secondarily, the surface areas of epithelial and endothelial cell layers were important, affecting retention in opposite directions. Taken together, these results suggest that the mitochondrial density per unit absorption surface area is the key histological organization parameter responsible for the higher retention of MTR in upper airways after IT administration.

4.7 Discussion

In traditional pharmacokinetic studies, drug distribution in the lungs is analyzed in a homogeneous and well-stirred compartment (26, 37). Here, we have elaborated an integrated, cell-based approach to model local drug absorption and transport phenomena,

aimed at identifying cell-permeant molecules that are retained in the cells of the upper airway upon local pulmonary administration via the inhaled route. This integrated approach can be exploited for bioimaging probe development or for optimizing the local concentration of pulmonary medications (15, 16).

Locally acting, inhaled medications are of considerable interest for treating various pulmonary ailments, including asthma, chronic obstructive pulmonary disease (COPD) and pulmonary hypertension (12, 24, 38). The therapeutic benefits of inhaled medications include targeted drug delivery, rapid onset of action, low systemic exposure with a resultant reduction in systemic side effects (39, 40). Nevertheless, measuring local drug concentrations in the lungs is challenging. Previously, regional differences in local lung exposure have received little attention in the context of small molecule targeting and delivery. Inhaled drug development efforts ignore the possibility that local differences in drug exposure could influence regional differences in drug transport properties that are associated with structural and functional characteristics of the airways and alveoli (41-43). Accordingly, the approach presented here is significant because it furthers our understanding of how inhaled drug molecules and bioimaging probes behave after local administration to the lungs. These findings have important implications in pulmonary drug development.

Our simulations and experiments indicate that route of administration, histological organization and circulatory parameters can affect the retention and distribution of different molecular agents in various regions of the lung based on lipophilicity and ionization properties of molecules, and as such, may be of pivotal importance for the optimization of drug targeting (15, 16). Specifically, we considered two major and clearly

distinguishable regions of the lungs: the airways and the alveoli, which are histologically and physiologically distinct. Extensive studies have demonstrated that the regional lung deposition of drugs is largely dependent on the aerodynamic particle size generated by delivery devices (12-14, 41). Here, we introduce the concept that other parameters (e.g., the chemical properties of molecules) may be as important for predicting the behavior of pulmonary delivered of drugs. This is evidenced from our simulations which indicated that, after absorption into the blood, the majority of drug mass (>80% of total mass in lungs) is predicted to accumulate in the alveoli because of its larger volume and higher lipid content and compounds with high lipophilicity and low pK_a will accumulate to even a greater extent in the alveoli. Although inhaled drug targeting leads to most of the drug mass deposited in the upper airways, without significant intracellular retention, the molecules can be rapidly absorbed and circulate back to the lung to accumulate in the alveoli. In theory, only molecules that are retained in the cells of the upper airways at the local site of administration can be effectively targeted to the upper airways.

To study the transport properties of small molecules in airways and in alveoli, we conducted simulations concentrated on characterizing the behavior of two fluorescent compounds, MTR or Hoe, because they exhibited large differences in simulated transport behaviors. In addition, two *in vitro* cell based assays were developed to test the local cellular uptake and retention properties of small molecules: 1) Primary NHBE cell cultures comprised of cell multilayers differentiated on transwell insets in the presence of an air-liquid interface; and 2) MDCK cell monolayer cultures on microfabricated pore arrays to establish the lateral cell-to-cell transport kinetics of small molecules, along the plane of the cell monolayer. In the case of Hoe and MTR, both *in vitro* assays confirmed

that the probes were taken up and largely retained by cells in the immediate vicinity of site of absorption and that the extent of diffusion followed a dye concentration gradient from the pores. Our *in vitro* findings indicated that the lateral cell-to-cell diffusion of MTR and Hoe was highly constrained. These *in vitro* results confirmed that both Hoe and MTR were retained intracellularly at a significant level in the presence of a transcellular concentration gradient both in the apical-to-basolateral and lateral directions. These results were also informative in terms of the time scale of intracellular accumulation and the relative labeling intensity afforded by these two fluorescent probes in the presence of a transcellular gradient. However, the *in vitro* assays did not reveal a major difference in the local retention of MTR and Hoe. Based on this observation, the behavior of these probes in these *in vitro* assays appeared most consistent with the predicted behavior of the probes in the alveoli.

Nevertheless, the results of *in vivo* studies closely paralleled those obtained *in silico,* in that MTR was retained in airways upon local IT administration while Hoe distributed in both airways and alveoli irrespective of the route of administration. Although *in vitro* results were useful to confirm the high, local intracellular retention of the probes, the *in silico* model is a better representation of the three-dimensional organization and physiological parameters of the *in vivo* situation. Parameter sensitivity analysis indicates that mitochondrial uptake of hydrophilic cations, in relation to the surface area over which absorption occurs, is the critical histological component responsible for high exposure of MTR when given via IT instillation. This is because as MTR traverses from the lumen of the airway into the interstitium, it is rapidly taken up into the mitochondria, driven by the high negative membrane potential of the

mitochondrial inner membrane. Conversely, release of MTR from the mitochondria out into the circulation is very slow because the membrane potential slows the release. In the case of the alveoli, the alveolar epithelial cells have much higher apical and basolateral plasma membrane surface areas relative to the mitochondrial membrane surface area. The higher cell surface area facilitates mass transport of MTR across the cells and into the circulation, which reduces MTR accumulation in mitochondria.

In contrast to MTR, Hoe is a lipophilic weakly basic compound with a pKa of 7.5. Therefore, at physiological pH, half of the Hoechst molecules exist in a highly membrane-permeant, neutral form. Transmembrane diffusion of the neutral form of Hoe is orders of magnitude faster than that of a cationic form. So there is no significant accumulation or retention of Hoe in either the airways or the alveoli. When administered by IV injection, the direction of distribution is from blood to the tissue. The distribution between blood and tissue is mostly a function of the partitioning or binding of molecules from the circulation to the tissue, which is dependent on the cell density of the tissue, the membrane content of the tissue, and the affinity of the probes for membranes and intracellular components in the tissue. Thus, after IV administration, both Hoe and MTR tended to partition more into alveoli than into the airways.

In conclusion, we have elaborated an integrated *in silico*-to-*in vitro*-to-*in vivo*, modeling approach which has applicability toward the optimization of site-specific targeting of locally-administered molecules. In the process, we have found that MTR is a candidate fiduciary marker for local drug deposition and absorption patterns in the airways. Due to the compartmental nature of the lungs, computational simulations can be linked to upstream process, such as pulmonary particle deposition, dissolution and mucus

clearance, as well as to downstream processes that can be captured by pharmacodynamic models (44-46). With additional effort this approach can be expanded to include macromolecules, acidic, zwitterionic molecules as well as molecules possessing multiple ionization sites, to further development of probes of lung structure and function (47, 48).

4.8 Acknowledgements

This work was supported by funding from the National Institute of General Medical Sciences (grant R01GM078200 to G.R.R.) and the National Institute of Child Health and Human Development (grant R15HD065594 to K.A.S.).

4.9 Tables

Table 4-1. Results of parameter exchange analysis.

	Airways	Alveoli
Epithelium Surface Area	+	−
Smooth Muscle Volume	−−−	++
Endothelium Area	−	+
Macrophage Volume	unaffected	unaffected
Immune Cells Volume	unaffected	unaffected
Interstitium Volume	−−	−
Mitochondria Volume	−−	+
Blood Flow Rate	unaffected	unaffected
Clearance	unaffected	−

Table indicates the direction in which the exposure (AUC) of MTR changes after IT instillation, upon exchanging the indicated parameter values between airway and alveoli. A plus indicates an increase, while a minus indicates a decrease in AUC relative to the baseline lung model parameters. One plus or minus sign corresponds to a 1.1 to 1.5 fold change in AUC; two plus or minus signs to a 1.5 to 2 fold change; and three plus or minus signs to a $>$5 fold change. For clearance, the parameter value was increased 10-fold.
doi:10.1371/journal.pcbi.1002378.t001

4.10 Figures

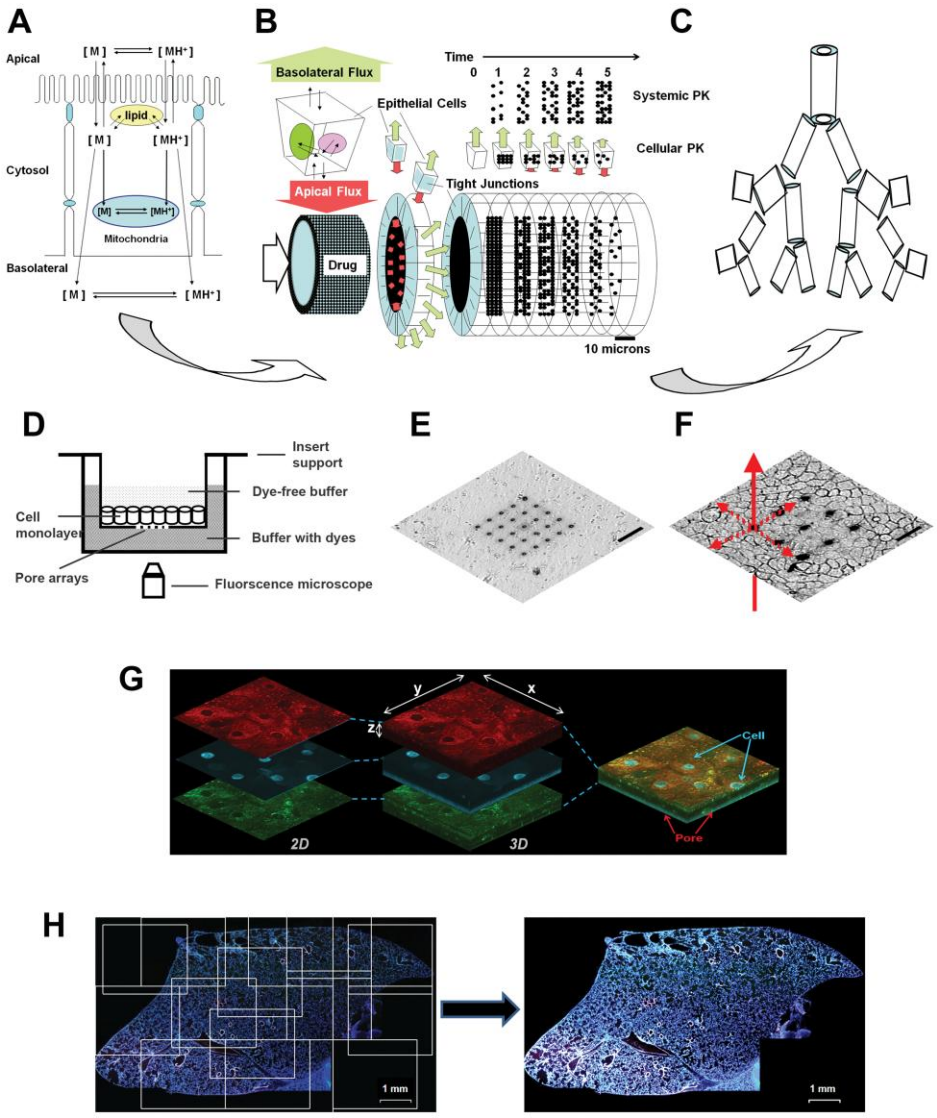

Figure 4-1. General methodology of integrative, cell based transport modeling.

A) For in silico simulations at the cellular level, a monobasic compound diffuses across a phospholipid bilayer and undergoes ionization and partition/binding in each compartment. The neutral form of the monobasic molecule is indicated as [M], and the protonated, cationic form of the molecule is indicated as [MH^+]. **B)** For in silico simulation at the histological level, each airway generation is modeled as a tube lined by epithelial cells; as molecules are absorbed over time, the drug concentration in the lumen decreases accompanied by an increase in drug concentration in the circulation. **C)** For in silico simulation at the organ level, the lung is modeled as a branching tree, with airway generation modeled as a cylinder, from the trachea to the alveoli. **D)** Experimental design of insert system with patterned pore arrays on membrane support for viewing lateral

transport of fluorescent molecules along the plane of a cell monolayer, away from a point source. **E)** Transmitted light image of a 5 × 5, 3 μm diameter pore array (20 μm spacings) on a polyester membrane. **F)** Transmitted light image of an MDCK cell monolayer above a membrane support with 3 × 3, 3 μm diameter pore array (40 μm spacings). Scale bar: 40 μm. **G)** 3D reconstruction of confocal images of the distribution of three fluorescent probes added to the uppermost surface of NHBE cell multilayers grown on air-liquid interface cultures on porous membrane support. Each 3D plane is composed of the image with the fluorescent channel; red (MTR), blue (Hoe), and green (LTG). **H)** Illustration of the tiling algorithm used to visualize and quantify the distribution of Hoe and MTR in lung cryosections, after IT and IV coadministration of the probes.

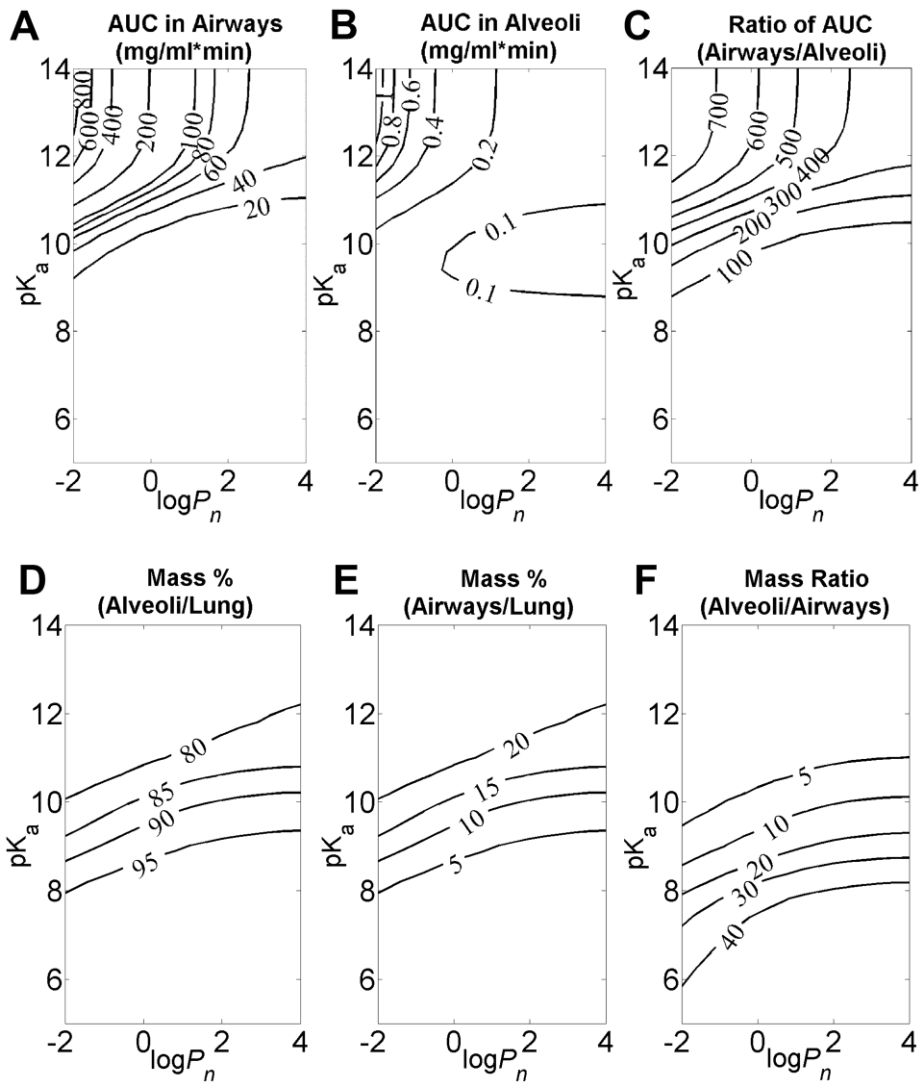

Figure 4-2. Virtual screening of monobasic compounds based differential tissue distribution in the airways and alveoli, using combinations of logP_n and pK_a as input.

For simulations, the initial dose was set to 1mg/kg for airways and alveoli. Contour lines indicate: **A)** The calculated AUC (unit: mg/ml*min) in airways; **B)** The AUC (unit: mg/ml*min) in alveoli; **C)** The AUC contrast ratio of airways to alveoli; **D)** The mass percentage (%) inalveoli relative to the total mass in lung; **E)** The mass percentage (%) in airways relative to the total mass in lung; **F)** The mass ratio of alveoli to airway.

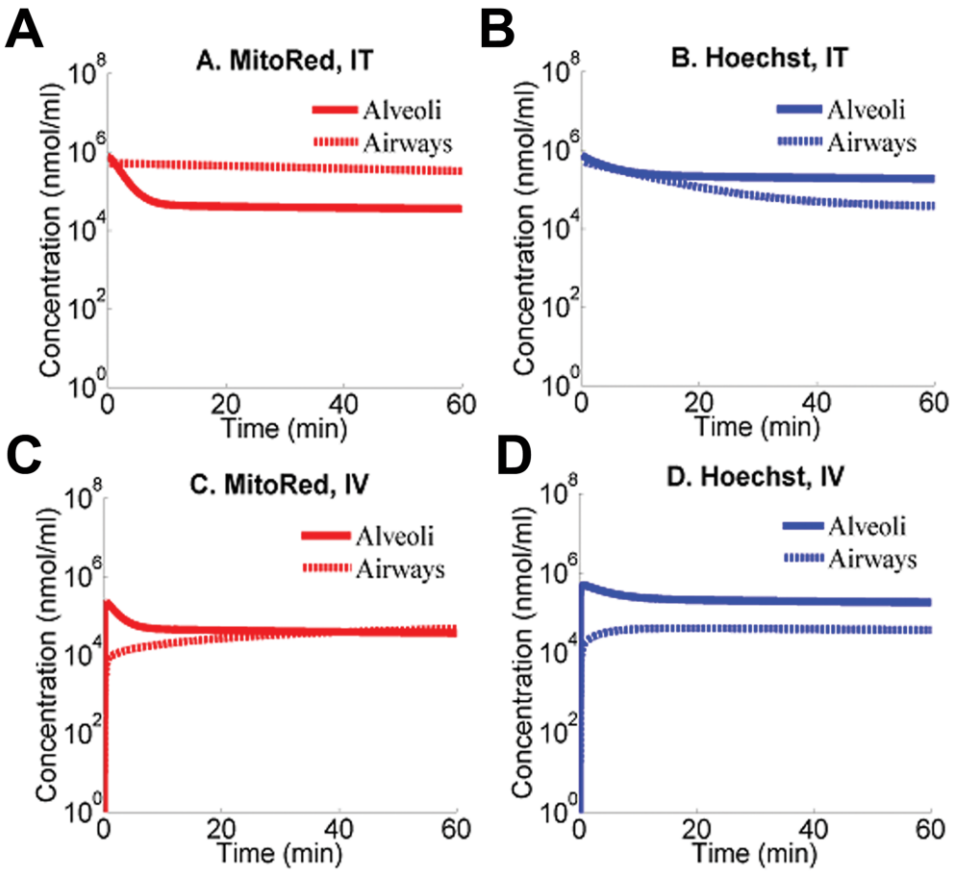

Figure 4-3. Simulations of local pharmacokinetics of MTR and Hoe after IV and IT administration.

A) The simulated tissue concentration in airways (dash line) and alveoli (solid line) of MTR administered by IT instillation; **B)** The simulated tissue concentration in airways (dash line) and alveoli (solid line) of Hoe administered by IT instillation; **C)** The simulated tissue concentration in airways (dash line) and alveoli (solid line) of MTR administered by IV injection; **D)** The simulated tissue concentration in airways (dash line) and alveoli (solid line) of Hoe administered by IV injection.

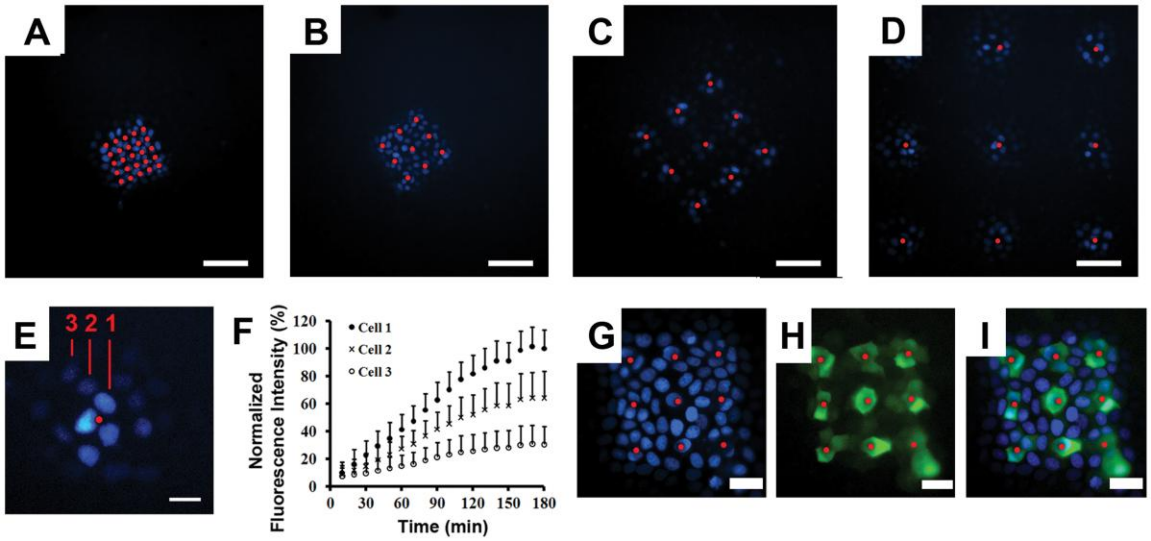

Figure 4-4. Probing the intracellular retention of Hoe along the plane of a cell monolayer.

For the experiments, Hoe was added to the basolateral compartment and incubated for 3 hrs, with cell monolayers sitting on top of patterned pore arrays. Red spots indicate the location of pores; Scale bar: 80 μm. Cells were imaged using the DAPI channel of an epifluorescence microscope. **A)** 5 × 5 array of 3 μm pores with 20 μm spacings; **B)** 3 × 3 array of 3 μm pores with 40 μm spacings; **C)** 3 × 3 array of 3 μm pores with 80 μm spacings; **D)** 3 × 3 array of 3 μm pore array with 160 μm spacings; **E)** Fluorescent images of a cell monolayer incubated for 3 hours in the presence of Hoe in the basolateral compartment; **F)** corresponding measurements of fluorescence intensity of cells in A), showing the average fluorescence of each nucleus normalized by the average fluorescence of the nucleus closest to the pore at the 3 hr time point, and plotted as mean ± s.d. (n = 6). **G)** Fluorescence image of cell monolayer on a 3×3 array of 3 μm pores with 40 μm spacings after 2 hr incubation with Hoe and BCECF-AM in the basolateral compartment; **H**) FITC channel corresponding to BCECF staining of the same cells as in ; **I**) Image overlays of C and D.

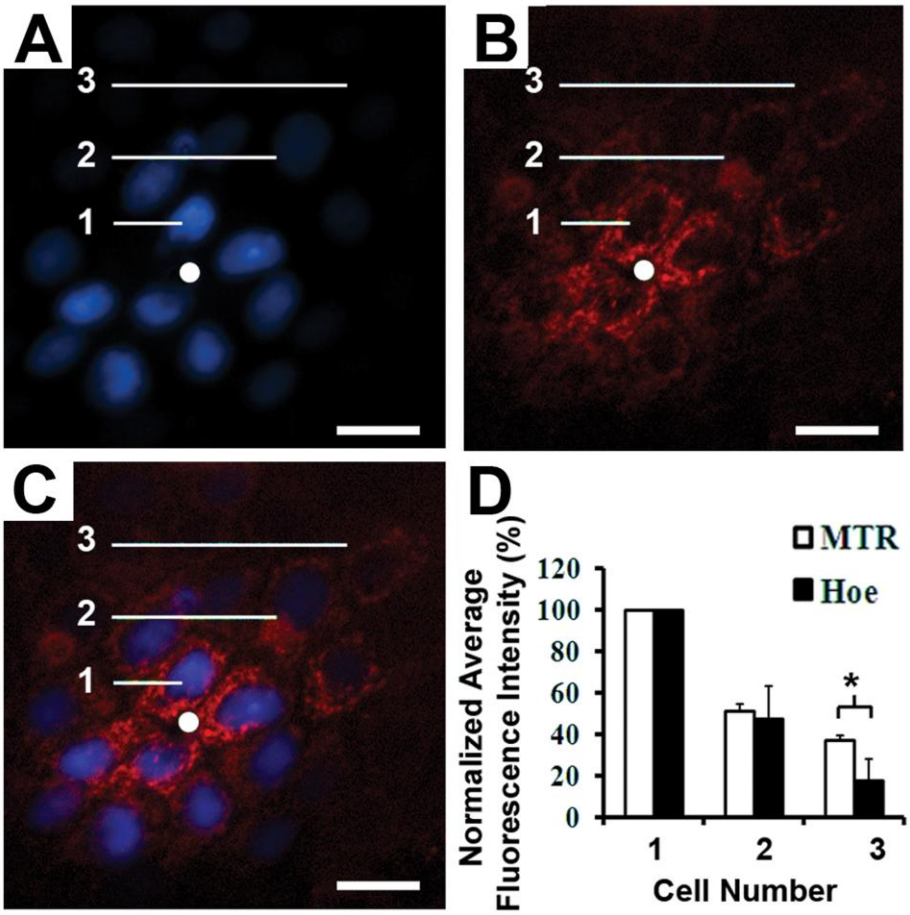

Figure 4-5. Probing the intracellular retention of MTR along the plane of a cell monolayer.

Cell monolayers on pore arrays were incubated for 2 hr with Hoe and MTR in the basolateral compartment. White spots indicate the location of pores; Scale bar: 20 μm. **A)** Fluorescent image acquired with the DAPI channel showing Hoe diffusing on a cell monolayer sitting on top of a single pore of a 3×3 array of 3 μm pores with 160 μm spacings; **B)** Same field as in A, visualized with the TRITC channel to show the staining of MTR; **C)** Overlay of A and B showing the overlapping Hoe (blue) and MTR (red) staining patterns. **D)** Plots of the fluorescence intensity of Hoe and MTR, separated by 0, 1, 2 or 3 layers of cells from a pore, and normalized by the fluorescence intensity of the cell closest to the pore; asterisk indicates a statistically significant difference using Student's T-test; $p<0.05$; $n= 6$).

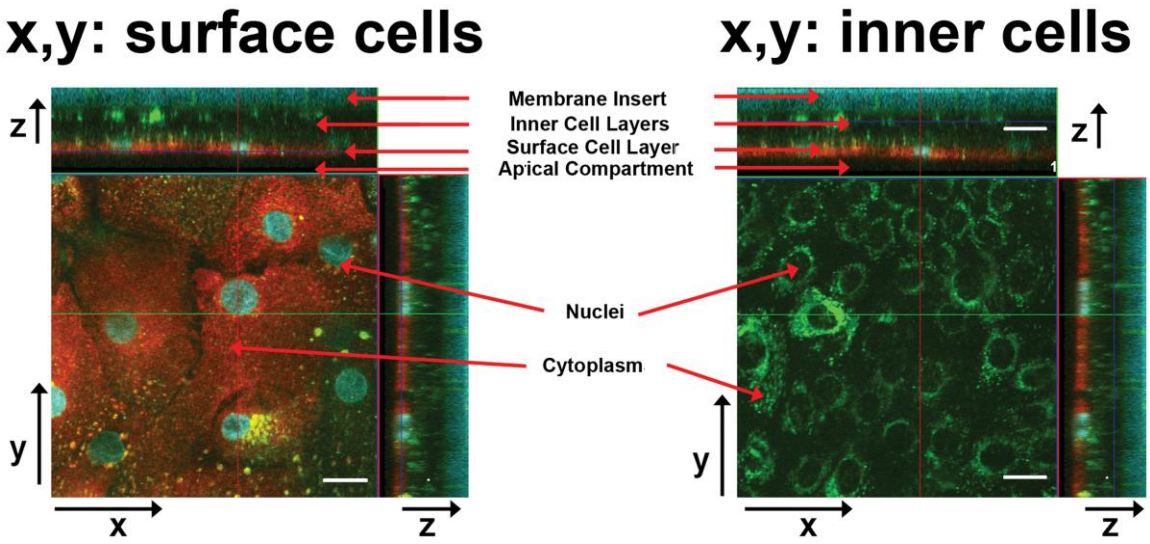

Figure 4-6. Fluorescent confocal images of NHBE cell multilayers on the porous membrane with Z-stacks stained with MTR, Hoe and LTG.

Each compartment (membrane inserts (bottom), inner cell layers, surface cell layer, and apical compartment (top)) through z-axis were indicated with the red arrows in xz planes while cell nuclei and cytoplasm in xy planes. The panel to the left shows an x, y cross section through the apical surface layer of the cell multilayer. The panel to the right shows an x, y cross section through the inner cell layer of the cell multilayer. Scale bar: 20 μm.

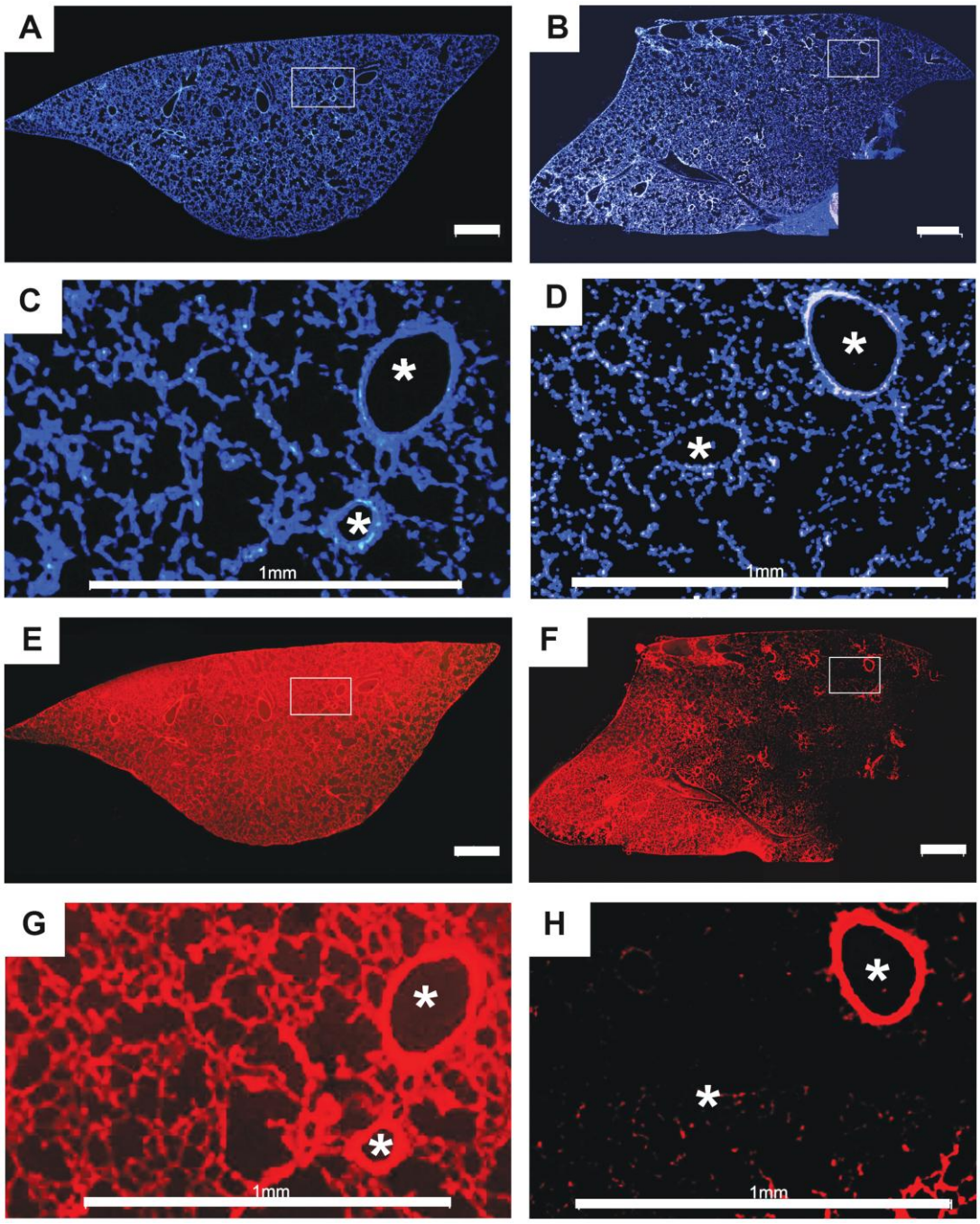

Figure 4-7. Tiled fluorescent micrographs of coronal cryosections obtained from the left lung of a mouse that received either an IV (**A, C, E, G**) or IT (**B, D, F, H**) dose of a mixture of Hoe and MTR.

A) DAPI channel fluorescence image showing Hoe distribution following IV administration; **B**) DAPI channel fluorescence image showing Hoe distribution following IT administration; **C**) High magnification view of the boxed region in A; **D**) High magnification view of the boxed region in B; **E**) TRITC channel fluorescence image showing MTR distribution following IV administration; **F**) TRITC channel fluorescence

image showing MTR distribution following IT administration; **G**) High magnification view of the boxed region in E; **H**) High magnification view of the boxed region in F. Scale bar = 1 mm.

4.11 Supporting Information Available

This material is published in *PLoS Computational Biology* and supporting information (Parameter sensitivity results) is available in the Appendix B.

4.12 References

1. Wiedl T, Arni S, Roschitzki B, Grossmann J, Collaud S, Soltermann A, et al. Activity-based proteomics: identification of ABHD11 and ESD activities as potential biomarkers for human lung adenocarcinoma. Journal of proteomics. 2011;74(10):1884-94.
2. Dekkers J, Wiegerinck C, de Jonge H, de Jong N, Bijvelds M, Nieuwenhuis E, et al., editors. WS14. 5 A functional CFTR assay using primary cystic fibrosis intestinal organoids. 35th European Cystic Fibrosis Conference Dublin, Ireland, 6–9 June 2012; 2012.
3. Barnes PJ. Chronic obstructive pulmonary disease: new opportunities for drug development. Trends in pharmacological sciences. 1998;19(10):415-23.
4. Cazzola M, Matera MG. The effective treatment of COPD: Anticholinergics and what else? Drug Discovery Today: Therapeutic Strategies. 2006;3(3):277-86.
5. Research B. Pulmonary Drug Delivery Systems: Technologies and Global Markets: BCC Research; 2011.
6. Weibel ER. Morphometry of the human lung. Anesthesiology. 1965;26(3):367.
7. Kim K-J, Ehrhardt C. Drug absorption studies: in situ, in vitro and in silico models: Springer; 2008.
8. Harding R, Pinkerton KE, Plopper CG. The lung: Development, aging and the environment: Academic Press; 2004.
9. Zhang X, Shedden K, Rosania GR. A cell-based molecular transport simulator for pharmacokinetic prediction and cheminformatic exploration. Mol Pharm. 2006;3(6):704-16.
10. Zhang X, Zheng N, Rosania GR. Simulation-based cheminformatic analysis of organelle-targeted molecules: lysosomotropic monobasic amines. J Comput Aided Mol Des. 2008;22(9):629-45.
11. Yu J-y, Rosania GR. Cell-based multiscale computational modeling of small molecule absorption and retention in the lungs. Pharmaceut Res. 2010;27(3):457-67.
12. Gumbleton M, Taylor G. Challenges and innovations in effective pulmonary systemic and macromolecular drug delivery. Adv Drug Deliv Rev. 2006;58(9-10):993-5.
13. Usmani OS, Biddiscombe MF, Barnes PJ. Regional lung deposition and bronchodilator response as a function of beta(2)-agonist particle size. Am J Resp Crit Care. 2005;172(12):1497-504.
14. Shoyele SA, Cawthome S. Particle engineering techniques for inhaled biopharmaceuticals. Adv Drug Deliver Rev. 2006;58(9-10):1009-29.
15. Krondahl E, Tronde A, Eirefelt S, Forsmo-Bruce H, Ekstrom G, Bengtsson UH, et al. Regional differences in bioavailability of an opioid tetrapeptide in vivo in rats after administration to the respiratory tract. Peptides. 2002;23(3):479-88.
16. Miller LA, Hurst SD, Coffman RL, Tyler NK, Stovall MY, Chou DL, et al. Airway generation-specific differences in the spatial distribution of immune cells and cytokines in allergen-challenged rhesus monkeys. Clin Exp Allergy. 2005;35(7):894-906.

17. King M. Experimental models for studying mucociliary clearance. Eur Respir J. 1998;11(1):222-8.
18. Sturm R, Hofmann W, Scheuch G, Sommerer K, Camner P, et al. Particle clearance in human bronchial airways: Comparison of stochastic model predictions with experimental data. Ann Occup Hyg. 2002;46(suppl 1):329-33.
19. Tronde A, Norden B, Jeppsson AB, Brunmark P, Nilsson E, et al. Drug absorption from the isolated perfused rat lung--correlations with drug physico-chemical properties and epithelial permeability. J Drug Target. 2003;11(1):61-74.
20. Trapp S, Horobin RW. A predictive model for the selective accumulation of chemicals in tumor cells. Eur Biophys J. 2005;34(7):959-66.
21. Zheng N, Zhang X, Rosania GR. Effect of phospholipidosis on the cellular pharmacokinetics of chloroquine. J Pharmacol Exp Ther. 2011;336(3):661-71.
22. Weibel ER. Principles and methods for the morphometric study of the lung and other organs. Lab Invest. 1963;12:131-55.
23. Yeh HC, Schum GM, Duggan MT. Anatomic models of the tracheo-bronchial and pulmonary regions of the rat. Anat Rec. 1979;195(3):483-92.
24. Parent RA, ed. Treatise on Pulmonary Toxicology: Comparative biology of the normal lung. Boca Raton: CRC Press; 1992.
25. Ross MH, Pawlina W, eds. Histology: A text and atlas: With correlated cell and molecular biology. Lippincott Williams & Wilkins; 2006.
26. Poulin P, Theil FP. Prediction of pharmacokinetics prior to in vivo studies. II. Generic physiologically based pharmacokinetic models of drug disposition. J Pharm Sci. 2002;91(5):1358-70.
27. Lee HB, Blaufox MD. Blood volume in the rat. J Nucl Med. 1985;26(1):72-6.
28. Zhang X, Zheng N, Zou P, Zhu H, Hinestroza JP, et al. Cells on pores: A simulation-driven analysis of transcellular small molecule transport. Mol Pharm. 2010;7(2):456-67.
29. Lin H, Li H, Cho HJ, Bian S, Roh HJ, et al. Air-liquid interface (ALI) culture of human bronchial epithelial cell monolayers as an in vitro model for airway drug transport studies. J Pharm Sci. 2007;96(2):341-50.
30. Madlova M, Bosquillon C, Asker D, Dolezal P, Forbes B. In-vitro respiratory drug absorption models possess nominal functional P-glycoprotein activity. J Pharm Pharmacol. 2009;61(3):293-301.
31. Steimer A, Haltner E, Lehr CM. Cell culture models of the respiratory tract relevant to pulmonary drug delivery. J Aerosol Med. 2005;18(2):137-82.
32. Gray TE, Guzman K, Davis CW, Abdullah LH, Nettesheim P. Mucociliary differentiation of serially passaged normal human tracheobronchial epithelial cells. Am J Respir Cell Mol Biol. 1996;14(1):104-12.
33. Lee MK, Yoo JW, Lin H, Kim YS, Kim DD, et al. Air-liquid interface culture of serially passaged human nasal epithelial cell monolayer for in vitro drug transport studies. Drug Deliv. 2005;12(5):305-11.
34. Yoo JW, Kim YS, Lee SH, Lee MK, Roh HJ, et al. Serially passaged human nasal epithelial cell monolayer for in vitro drug transport studies. Pharm Res. 2003;20(10):1690-6.

35. Serkova NJ, Van Rheen Z, Tobias M, Pitzer JE, Wilkinson JE, et al. Utility of magnetic resonance imaging and nuclear magnetic resonance-based metabolomics for quantification of inflammatory lung injury. Am J Physiol Lung Cell Mol Physiol. 2008;295(1):L152-61.
36. Prince GA, Porter DD. Cryostat microtomy of lung tissue in an expanded state. Stain Technol. 1975;50(1):43-5.
37. Rodgers T, Leahy D, Rowland M. Physiologically based pharmacokinetic modeling 1: predicting the tissue distribution of moderate-to-strong bases. J Pharm Sci. 2005;94(6):1259-76.
38. Cohen MD, Zelikoff JT, Schlesinger RB, eds. Pulmonary immunotoxicology: Springer; 2000.
39. Patton JS, Byron PR. Inhaling medicines: delivering drugs to the body through the lungs. Nat Rev Drug Discov. 2007;6(1):67-74.
40. Tronde A. Pulmonary Drug Absorption: In vitro and in vivo investigations of drug absorption across the lung barrier and its relation to drug physicochemical properties: Uppsala University; 2002.
41. Brewis RL, Corrin B, Geddes DM, Gibson GJ, eds. Respiratory Medicine. Second ed. London: WB Saunders Company Ltd.; 1995.
42. LiCalsi C, Christensen T, Bennett JV, Phillips E, Witham C. Dry powder inhalation as a potential delivery method for vaccines. Vaccine. 1999;17(13-14):1796-1803.
43. Niven RW. Delivery of biotherapeutics by inhalation aerosol. Crit Rev Ther Drug Carrier Syst. 1995;12(2-3):151-231.
44. Macheras P, Iliadis A. Modeling in biopharma-ceutics, pharmacokinetics, and pharmacodynamics: homogeneous and heterogeneous approaches. New York: Springer; 2006.
45. Derendorf H, Lesko LJ, Chaikin P, Colburn WA, Lee P, et al. Pharmacokinetic/ pharmacodynamic modeling in drug research and development. J Clin Pharmacol. 2000;40(12):1399-418.
46. Burton ME. Applied pharmacokinetics and pharmacodynamics: principles of therapeutic drug monitoring. Baltimore: Lippincott Williams & Wilkins; 2005.
47. Van't Veen A, Gommers D, Verbrugge SJ, Wollmer P, Mouton JW, et al. Lung clearance of intratracheally instilled 99mTc-tobramycin using pulmonary surfactant as vehicle. Br J Pharmacol. 1999;126(5):1091-6.
48. Sakagami M, Omidi Y, Campbell L, Kandalaft LE, Morris CJ, et al. Expression and transport functionality of FcRn within rat alveolar epithelium: A study in primary cell culture and in the isolated perfused lung. Pharm Res. 2006;23(2):270-9.

Chapter 5

The Extracellular Microenvironment Explains Variations in Passive Drug Transport across Different Airway Epithelial Cell Types

5.1 Background

Variations in the extracellular microenvironment are known to impact the molecular transport across the epithelial cells. Interstitial fluid phase and extracellular matrix (ECM) as components of extracellular microenvironment are controlled by physiological interactions including biochemical factors such as signaling molecules, growth factors, mucus (1, 2) and physical factors such as collagens (3-5).

In the airway, mucociliary clearance influences drug penetrations into the epithelial cell linings, controlled by ciliary movements and mucus secretions (2). Normally, the airway surface layer (ASL) is composed of ~98% water, 1% salt, and 1% proteins by weight, including the high molecular weight mucins which determine the viscoelastic properties of the mucus layers. Proper hydration and thickness or volume of ASL is controlled by a balance between ion secretion and ion absorption (6, 7). Diffusion barriers with unstirred water layers on cell surface have been claimed as impairing the drug permeability, especially for lipophilic drug compounds. There is much evidence

indicating that the variations in the aqueous barriers tend to arise due to experimental conditions such as stirring speeds or apparatus designs (8-10).

The ECM variations also contribute to controlling cell structures and morphologies and accordingly, biochemical interactions and drug transport (11-13). In the transwell apparatus for *in vitro* drug transport studies, pore size or density and tortuosity of the porous membrane (14, 15), and coating materials on the membrane affect the variations in ECM (16-18). The different cell areas exposed to drug molecules in different regions along the airways also affect the varied transport and retention of the molecules in the target sites. For example, differentiated NHBE (primary, normal human bronchial epithelial) cells have shown to grow in transwell inserts as multilayers (19). Different cell areas in bottom or top cell layers resulted in varied exposures to molecular probes (MTR or Hoe) according to the physicochemical properties of drug molecules as shown in Chapter 4.

5.2 Rationale and Significance

The mechanism-based cellular pharmacokinetic model (1CellPK) has demonstrated its usefulness to predict the cell permeability based on the physicochemical properties of the drug molecules and cell physiological parameters (20-22). By using parameter optimization algorithm, the model could help distinguish key parameters contributing drug transport phenomena. The varied ranges of cell physiological parameters (*i.e.*, area or volume of the cell, area or volume of subcellular organelles, pH and electrical membrane potential) are determined, based on the relevant literatures, the established 1CellPK model, and the microscopic imaging examination. Input parameters

related to the physicochemical properties of drug molecules would be based on the calculations of pK_a and logP values.

Calu-3 cells have been widely used as the representative airway cell model of the drug transport assays (23, 24), but primary cells, NHBE might be more physiologically relevant to the lung than the Calu-3 originated from cancer. However, in the transport assays from NHBE cells, the multilayer formation could vary the drug exposures in different cell layers (19), making the data interpretation difficult. Generally, advantageous to cell-to-cell interactions, mixed co-culture methods have been used to establish *in vitro* working models in various fields (25-27). Therefore, mixed co-cultures of NHBE and Calu-3 cells at an optimal ratio might provide cell monolayer conditions of NHBE and could be used to calculate drug transport/cellular uptake in NHBE. Integrations of drug transport assays using co-cultures of airway epithelial cells and the computational modeling could help dissect the various factors affecting mass transport and explain the effects of the extracellular microenvironment (presented as unstirred water layers) on drug transport.

5.3 Abstract

We sought to identify key variables in cellular architecture and physiology that might explain observed differences in the passive transport properties of small molecule drugs across different airway epithelial cell types. Propranolol (PR) was selected as a weakly basic, model compound to compare the transport properties of primary (NHBE) *vs.* tumor-derived (Calu-3) cells. Differentiated on Transwell™ inserts, the architecture of pure *vs.* mixed cell co-cultures was studied with confocal microscopy followed by

quantitative morphometric analysis. Cellular pharmacokinetic modeling was used to identify parameters that differentially affect PR uptake and transport across these two cell types. Pure Calu-3 and NHBE cells possessed different structural and functional properties. Nevertheless, mixed Calu-3 and NHBE cell co-cultures differentiated as stable cell monolayers. After measuring the total mass of PR, the fractional areas covered by Calu-3 and NHBE cells allowed deconvoluting the transport properties of each cell type. Based on the apparent thickness of the unstirred, cell surface aqueous layer, local differences in extracellular microenvironment explained the measured variations in passive PR uptake and permeation between Calu-3 and NHBE cells. Mixed cell co-cultures can be used to compare the local effects of the extracellular microenvironment on drug uptake and transport across two epithelial cell types.

5.4 Introduction

Measurements of small molecule transport across epithelial cell monolayers in tissue culture are routinely performed in pharmaceutical research laboratories to predict the absorption properties of drug candidates, with applications ranging from drug development to regulation. For gastrointestinal drug absorption, Caco-2 or Madin-Darby Canine Kidney (MDCK) cells have been widely used to measure permeability of oral drugs using *in vitro* assay systems. When cultured on porous membrane supports, the ability of these cells to form a monolayer with tight junctions enables reproducible and biorelevant measurements of drug transport and metabolism. *In vitro* transcellular permeability measured using these cell culture models shows good correlation with *in vivo* intestinal permeability measured in animals or humans (28, 29).

Calu-3 cells (American Type Culture Collection, ATCC HTB-55) are a sub-bronchial adenocarcinoma epithelial cell line derived from a human malignant pleural effusion (30). To assay the transport properties of inhaled drugs, Calu-3 cells are most widely used due to their low cost, simple culture conditions and reproducible assay results. Calu-3 cells can be grown on porous supports on which they form a polarized cell monolayer with constant thickness (24, 31-33). These cells can be also cultured under an air-liquid interface (ALI) in the absence of cell culture media in the apical side, mimicking the environment in the intact lung. When differentiated in ALI conditions, Calu-3 cells form tight junctions, secrete mucus on their surface and undergo ciliogenesis (34). These cells are also used to study the dissolution-absorption kinetics of drug powder formulations (35-37). In addition, Calu-3 cells are used to study active transport mechanisms influencing drug absorption, metabolism and efflux (38, 39) and for *in vitro-in vivo* correlation studies involving permeation of passively or actively transported drug molecules in the airways (24, 40).

As an alternative to Calu-3 cells, primary normal human bronchial epithelial (NHBE) cells can be obtained from different locations of the lungs of human cadavers (41). NHBE cells are considered more physiologically relevant because they do not have the transformed phenotype of Calu-3 cells (42, 43). However, unlike Calu-3 cells, NHBE cells are difficult to propagate and mucociliary differentiation becomes significantly impaired after three sub-cultures. Variations in cell culture media composition also influence the differentiated phenotype of NHBE cells (32, 39, 44). Like Calu-3 cells, NHBE cells can be cultured under ALI conditions (45, 46) but they form multilayers of

variable thickness and cellular composition which complicate interpretation of drug uptake and permeability measurements.

Here, to identify specific structural and functional features that might be responsible for differences in the transport properties of NHBE and Calu-3 cell monolayers, we established a specialized *in vitro* assay system. Since NHBE cells tend to differentiate into multilayers, NHBE cells were mixed with Calu-3 cells in various ratios and cultured on a polyester membrane in Transwell™ inserts under ALI conditions. After establishing cell monolayer integrity and tight junction formation, the 3D architectures of the cells differentiated on Transwell™ insert system were investigated using confocal 3D microscopy. By measuring the transport properties of PR across a pure Calu-3 cell monolayer and based on the cell numbers and areas occupied by NHBE and Calu-3 cells in mixed cell monolayers, we calculated the transport properties of PR across individual NHBE cells. In turn, by fitting the data with a cellular pharmacokinetic model, parameter optimization and sensitivity analysis led to the identification of key structural and functional variables that explain the observed differences in PR uptake and transport kinetics across these two cell types.

5.5 Materials and Methods

Materials. Hank's balanced salt solution (HBSS buffer, pH 7.4, 10mM HEPES, 25mM D-glucose) was prepared with chemicals obtained from Fisher Scientific, Inc. (Pittsburgh, PA). NHBE cells (Clonetics™; normal human bronchial epithelial cells; passage #1), bronchial epithelial basal medium (BEBM) and the associated bullet kit including

subculture reagents were from Lonza (Walkersville, MD). Dulbecco's Modified Eagle Medium: Nutrient Mixture F-12 (DMEM:F12) was from Invitrogen (Carlsbad, CA). Lucifer Yellow CH dipotassium salt (MW: 521.57) was from Sigma-Aldrich (St. Louis, MO). MitoTracker® Red CMXRos (M7512), Hoechst 33342 (H3570), LysoTracker® Green DND-26 (L7526), and Alexa Fluor® 488 phalloidin (A12379) were from Molecular Probes, Invitrogen. Transwell™ inserts with polyester membranes (area: 0.33 cm^2, pore size: 0.4 μm) were from Corning Co. (Lowell, MA). Nunc® Lab-Tek® I-chamber slides were used for the microscopic examination of cells. Propranolol, atenolol, anhydrous ethyl acetate, acetonitrile (LC/MS grade) and formic acid were from Sigma-Aldrich. Metabolite standards (4-hydroxypropranolol and N-desisopropyl propranolol) were from Alsachim (Strasbourg, France). Water purified with a Milli-Q water system (Bedford, MA) was used for LC/MS analyses.

Cell culture. Calu-3 cells obtained from American Type Culture Collection (ATCC) (Manassas, VA) were cultured in 75 cm^2 flasks (37°C in a 95 % air/5 % CO_2) in media containing a 1/1 mixture of DMEM:F12 containing 2 mM L-glutamine, high glucose, 1% (v/v) non-essential amino acids, 1% (v/v) penicillin-streptomycin, and 10 % FBS. Culture media was changed every second day until cells were confluent. At that time, Calu-3 cells were subjected to trypsin and sub-cultured at a 1:3 ratio.

NHBE cells (passage #1) were thawed according to the manufacturer's instruction and grown in a 75 cm^2 flask (500 cells/cm^2 at 37°C, 5% CO_2) until they were 70-80% confluent (46). NHBE cells were maintained in the growth medium (BEGM) of serum-free BEBM supplemented with the growth factors in the bullet kit (human recombinant epidermal growth factor, insulin, transferrin, hydrocortisone, triiodothyronine,

epinephrine, retinoic acid, gentamycin / amphotericin-B and bovine pituitary extract (35 mg/ml)).

Air-liquid interface (ALI) cultures on inserts. For transport experiments and confocal image analyses, Calu-3 cells (passage 26-36) were seeded at 5×10^5 cells/cm^2 on the porous membranes (area: 0.33 cm^2) of Transwell™ inserts in 24-well plates. They were maintained in culture media in apical and basolateral sides (37°C, 5% CO_2). After an overnight incubation, polyester membranes were examined using an inverted Nikon TE2000 microscope to ascertain cell attachment and viability. For ALI conditions, the apical media was aspirated and the basolateral media was replaced with fresh media. The apical sides of the inserts were washed with HBSS buffer (pH 7.4) to remove unattached cells. Media in the basolateral sides of the inserts were replaced with fresh media every day while cells were maintained (37°C, 5% CO_2). Transepithelial electrical resistance (TEER) measurements were made to assess the integrity of the intercellular junctions as previously described (37).

NHBE cells (passage #2; 2.5×10^5 cells/cm^2) were seeded on Transwell™ inserts in 24-well plates with differentiation media. Mixed media (1/1) of BEBM and DMEM:F12 supplemented with 8 growth factors (the same ingredients in the BEGM preparation) except for bovine pituitary extract was used as differentiation media for NHBE cells on the inserts (45, 46). To achieve ALI conditions, the media in the apical chamber was removed by aspiration 24 h after cells were plated on the inserts and differentiation media in the basolateral side was replaced every day during which cells were maintained (37°C, 5% CO_2).

For the mixed cell co-cultures, Calu-3 and NHBE cell suspensions were mixed in differentiation media at various ratios (see Table C1 in the Appendix C). Since the cell doubling times are different for these two cell-types, the optimal cell seeding densities in pure culture were considered in the mixed conditions. To monitor culture conditions, functional assays by measuring TEER and lucifer yellow (LY) permeability were periodically conducted as previously described (37). Cytometric analyses by confocal microscopy were also periodically performed.

Confocal fluorescence microscopy and 3D reconstructions. Mixed solution (240 μl) of three different dye molecules (80 μl of each dye, 1 μM MitoTracker® Red (MTR), 10 μg/ml Hoechst 33342 (Hoe) and 2.5 μM LysoTracker® Green (LTG) in HBSS) were added to the apical side of inserts with cells in the presence of buffer (600 μl) in the basolateral chamber. After a 30 min incubation (37°C, 5%), the cell-containing inserts were put on a chamber slide (Lab-Tek). Images were acquired across the z-axis with using 1 μm intervals by a confocal microscope at a different fluorescent channel (UV (364 nm), Argon laser (488 nm), Helium neon 1 laser (543 nm)). A Zeiss LSM 510-META laser scanning confocal microscope (Carl Zeiss Inc., Thornwood, NJ) with a 60 × water immersion objective was used for scanning the insert through the z-axis. Three dimensional (3D) reconstructions of image stacks were performed using the microscope's built-in software package. Additionally, cell-to-cell junction formation between Calu-3 and NHBE cells were also analyzed by confocal microscopy after actin staining with 5 U/ml Alexa Fluor® 488 phalloidin (46).

Morphometric analysis of cell monolayer architecture. Confocal Z-stack images of the cells on the inserts under ALI conditions were analyzed using MetaMorph image

analysis software (Molecular Devices, Sunnyvale, CA) as previously described (47). Briefly, after background subtraction, regions around each cell were manually drawn using the "Trace region" tool. Region area and integrated intensity of MTR or LTG corresponding to each region were measured using the "Region measurement" function. Assuming the shape of a cell as a polyhedron, cell volume was calculated by summing the segmented cell areas (polygonal area) along the z-axis based on 1 μm spacing between sequential images according to Simpson's rule for integrations (47). Based on the measured areas and calculated cell volumes, cell population distribution histograms were generated and plotted with MATLAB R2010b. A normal mixture statistical model with probability density function in MATLAB was used to estimate the fraction of the mixed cell population in each image that was occupied by Calu-3 or NHBE cells.

Assessment of PR metabolism. Confluent cells were harvested using trypsin and the isolated cell suspension (10^7 cells in 1 ml) was incubated with PR (50 or 100 μM) by shaking (37°C, 5% CO_2) for 4 h. After incubation, the cell suspension was centrifuged (1,300 × g, 5 min, 4°C). The supernatant was collected and the cell pellets were washed with cold DPBS twice by centrifugation. In preparation for LC/MS analysis, cell pellets were extracted with cold methanol. For PR metabolite detection, confluent cells in 75 cm^2 flasks were incubated with PR (50 or 100 μM) for 4 h. Cells were isolated by trypsin and centrifuged (200 × g, 5 min, 4°C). Then, the supernatant was collected and cell pellets were washed twice with cold DPBS (15 ml). Cells were extracted with cold methanol. All the samples were stored at -80°C.

PR transport experiments. Transport experiments were performed using Calu-3 cells, NHBE cells or the mixed cell cultures (1/1 Calu-3/NHBE ratios) on inserts in both

directions (apical-to-basolateral (AP→BL) and basolateral-to-apical (BL→AP)) after 8 days in culture under ALI conditions. For the assays, cells on the inserts were washed and left to equilibrate in HBSS at 37°C for 30 min. For AP→BL transport assays, 110 µl of PR in HBSS buffer (5, 10, 20, 50, 80, or 100 µM) was added into the apical side of the inserts, with 600 µl of HBSS buffer without PR in the basolateral side. For BL→AP transport assays, 600 µl of PR in HBSS was added to the basolateral side, and 110 µl of PR-free HBSS buffer was added to the apical side. Plates with inserts were incubated (37°C, 5% CO_2) while on a shaking platform and samples were collected from the receiver side at various time points until 4 h and a single sample was acquired from the donor side at 4 h. After transport experiments, cells on the inserts were washed twice with cold DPBS and detached with trypsin. The isolated cells were counted and after centrifugation (1,300 × g for 5 min), the cell pellets were lysed with cold methanol and sonication (10 min) and were incubated on ice. The methanol in the cell lysis supernatant was evaporated by Savant DNA SpeedVac Concentrator (Thermo Scientific) for 50 min and then reconstituted with HBSS. PR concentrations in the samples from transport studies were quantified with LC/MS.

LC/MS analysis. Stock solutions (500 µM) of PR, atenolol (internal standard; IS) or standard metabolites of PR (4-OHP and N-DIP) were prepared in methanol. They were diluted with acetonitrile:water (1:1) with 0.1 % formic acid (mobile phase) to generate standard solutions of 0.005, 0.01, 0.05, 0.1, 0.5, and 1 µM. Internal standard was prepared by diluting the stock atenolol to yield a final concentration of 5 µM in acetonitrile:water (1:1) with 0.1 % formic acid. Twenty µl of IS solution in mobile phase was added to each standard solution (230 µl) in acetonitrile:water (1:1) with 0.1 % formic

acid. The mixtures were vortexed and filtered (0.22 μm). The solutions were transferred to vials for LC/MS.

Standards or samples from transport studies were diluted with water to which atenolol (5μM) was added. The solutions were alkalinized with ammonium hydroxide (25%) to a pH 8-10. The solutions were extracted with 3 ml of anhydrous ethyl acetate (EtOAc), vortexted, then centrifuged (200 × g, 5 min, 4°C) to separate the solvent layers. The EtOAc layers were transferred to tube and evaporated in a SpeedVac Concentrator for 50 min. The dried residues were reconstituted with 250 μl of mobile phase solvent (acetonitrile:water (1:1) with 0.1 % formic acid). After filtering (0.22 μm syringe filter), samples (5 μl) were injected into LC/MS.

Three different batches of standards at six concentrations were prepared for intraday and interday validation on three consecutive days. Precision was evaluated as the relative standard deviation of the mean (% CV). For intraday and interday validations, CV values at each concentration level (0.01, 0.05, 0.1, 0.5, and 1 μM) yielded less than 15 % (< 20 % CV at LLOQ (lower limit of quantification)). Three replicates of unextracted and extracted standards were evaluated for extraction efficiency (% recovery). The extraction efficiency was determined by dividing the peak area of compound in the extracted sample by the peak area in the unextracted sample. Standard curves for the calibration were determined using linear least-squares regression analysis based on the peak area of PR normalized by the extraction efficiency of the IS.

The LC/MS analysis was conducted using Shimadzu HPLC system coupled to a Shimadzu 2010A mass spectrometer equipped with electrospray ionization (ESI) source. The system was operated by LC/MS solution Ver. 3 software. Quantitative analysis was

accomplished on an XTerra MS C18 column (5 µm, 2.1 x 50 mm; Waters Co.). The mobile phases were 0.1% formic acid in purified water (mobile A) and 0.1% formic acid in acetonitrile (mobile B). The gradient of mobile B was 5% (0-5 min), increased to 70% at 10 min and to 80% at 12 min, then held at isocratic 80% B for 3 min, and then immediately returned to 5% for re-equilibration. Flow rate was set at 0.2 mL/min. The LC/MS was operated at positive ESI with a detector voltage of 1.5 kV, the nebulizing N_2 gas flow of 1.2 ml/min, CDL temperature of 250°C and heat block of 200 °C. The m/z ratios for propranolol and atenolol are 260.30 and 267.10, respectively. SIM and full scan mode was used to detect specific ions and possible fragments.

Mass transport and cellular uptake data analysis. By using the transported PR mass measured in pure Calu-3 monolayer and in mixed Calu-3/NHBE cell monolayer (1/1 ratio) and the fraction of each cell population in the mixed cell monolayer that were directly measured in the distribution analyses of the confocal images, transported PR mass per NHBE cell at each time point was readily calculated with equation 1.

$$T_{Mass\_total} = T_{Mass(Calu-3)} \times f_{(Calu-3)} \times C_{no} + T_{Mass(NHBE)} \times f_{(NHBE)} \times C_{no} \quad (1)$$

Where T_{Mass_total} is total transported mass of PR in the mixed cell monolayer at each time point; T_{Mass} is the transported PR mass per a Calu-3 or NHBE cell at each time point; f is the fraction of cell population (Calu-3 or NHBE) in the mixed cell monolayer and, C_{no} is total cell numbers in the mixed cell monolayer.

Similarly, intracellular mass of PR in the NHBE cell monolayer was calculated using equation 2.

$$C_{Mass\_total} = C_{Mass(Calu-3)} \times f_{(Calu-3)} \times C_{no} + C_{Mass(NHBE)} \times f_{(NHBE)} \times C_{no} \quad (2)$$

Where C_{Mass_total} is total cell mass of PR in the mixed cell monolayer; C_{Mass} is the intracellular PR mass per a Calu-3 or NHBE cell. Masses of PR were calculated with molecule numbers to help determine the number of drug molecules that are transported or trapped inside the cells.

The rate of PR transcellular mass transport (*dM/dt*) in the NHBE cell monolayer was estimated by using the rate of PR mass transport in the Calu-3 monolayer and the mixed cell monolayer and also the fraction of each cell population in the mixed cell monolayer from the distribution analyses of the confocal images in equation 3.

$$\frac{dM}{dt}_{(Mix)} = \frac{dM}{dt}_{(Calu\text{–}3)} \times f_{(Calu\text{–}3)} + \frac{dM}{dt}_{(NHBE)} \times f_{(NHBE)} \quad (3)$$

The transcellular permeability coefficient (P_{eff}) for the NHBE cell monolayer was calculated using equations 3 and 4

$$P_{eff} = \frac{\frac{dM}{dt}}{Area \cdot C_D} \quad (4)$$

Where *dM/dt* is mass changes in the receiver side per time; *Area* is the insert area (0.33 cm^2); and C_D is PR concentration at donor side.

Statistical analyses were performed using GraphPad Prism 5.03 (GraphPad Software; LaJolla, CA). Data were analyzed by either an unpaired Student's t-test or a one-way analysis of variance (ANOVA; $\alpha = 0.05$) as appropriate. For data analyzed by ANOVA, a Tukey's multiple comparison test was used if needed. In all cases, a *p*-value $\leq$ 0.05 was considered statistically significant.

Mathematical model of cellular pharmacokinetics. A biophysical compartmental model of passive small molecule transport across single cells (20) was adapted to model the cellular pharmacokinetics of PR transport across lung epithelial cells. This model uses coupled sets of ordinary differential equations to simulate drug transport between 8

different compartments: apical; apical unstirred water layer; cytosol; mitochondria; lysosomes; porous membrane; basolateral unstirred water layer; and, basolateral compartments. According to the model, the passive mass transport of PR is driven by the concentration gradients of PR between adjacent compartments. PR ionization is modeled with the Henderson-Hasselbalch equation, as a weakly basic molecule existing as neutral or protonated species in instantaneous equilibrium determined by the local pH and lipid fractions of each compartment. Membrane permeability across each lipid bilayer was estimated based on the physicochemical properties of PR: 1) pK_a (the dissociation constant of the protonated functional group); 2) log P_n (the logarithm of lipid/water partitioning coefficient of neutral forms of PR); and, 3) log P_d (the logarithm of lipid/water partitioning coefficient of ionized forms of PR). The net fluxes (J) of passive diffusion in a unit area of neutral and ionized forms of PR were expressed using Fick's equation and the Nernst-Plank equation, respectively (see online supplement). Liposomal partition coefficients for neutral and ionized forms of PR were calculated with the empirical equations (20).

To capture the effect of the local cell surface microenvironment on PR transport, we included an unstirred water layer in the apical and basolateral side of the cell surface. The aqueous diffusion coefficient (D_w) of PR was estimated from the empirical equation (equation 5) (48) using the molecular weight of PR (MW: 259.3 g/mole). The aqueous permeability across the unstirred water layers (P_a and P_b for the apical and basolateral side, respectively) was calculated with D_w and the layer thicknesses (H_{aq} or H_{bq}) (equation 6).

$$\log D_w = -4.113 - 0.4609 \log MW \tag{5}$$

$$P_{a/b} = \frac{D_w}{H_{aq/bq}} \quad (6)$$

PR concentrations (μM) in each compartment were calculated over time using MATLAB R2010b ODE solver (see Appendix C). PR mass was calculated by multiplying concentration to volume of each compartment, after converting mass units using Avogadro's number (6.022×10^{23} molecules/mol) and PR's molecular weight.

Parameter optimization and sensitivity analysis. Input parameters in the model were optimized using a physiologically-relevant, experimentally-determined range of values. For each parameter, subscripts a, c, m, l, M, b, aq, and bq, respectively correspond to the following compartments: apical, cytosol, mitochondria, lysosome, porous membrane, basolateral, apical unstirred water layer, and basolateral unstirred water layer. Physiological parameters varied in the optimizations were: 1) membrane electrical potentials (Ea, E_m, E_l, E_b); 2) pH (pH_a, pH_c, pH_m, pH_l, pH_b); 3) lipid fractions (L_c, L_m, L_l) of each compartment; and, 4) the thicknesses of the apical or basolateral unstirred water layers (H_{aq}, H_{bq}). It is assumed that pH in the apical unstirred water layer is same as pH in the apical compartment and pH in the membrane pores and basolateral unstirred water layer is the same as pH in the basolateral compartment. The thicknesses of apical or basolateral unstirred water layer (H_{aq} or H_{bq}) were varied within the range of reported measurements (49). Histological parameters that were varied were: 1) cell surface areas (A_a, A_{aq}, A_{bq}, A_b, A_m, A_l), and, 2) cell volumes (V_c, V_m, V_l). Surface areas in unstirred water layers (A_{aq} and A_{bq}) were varied within the ranges of minimal cross-sectional area of a Calu-3 and maximal area of a NHBE cell. Apical membrane surface area (A_a) was varied between the minimal area of Calu-3 and the maximal area of NHBE multiplied by 50 considering that there may be villi or cilia on the apical membrane (50). Basolateral

membrane surface area (A_b) was varied within the total area of pores per cell and the maximal area in basolateral unstirred water layer (A_{bq}). Cytosolic volume (V_c) was varied with the minimum cell volume of a Calu-3 and the maximum of NHBE cell measured in quantitative imagings. Other parameters were kept fixed including: 1) physicochemical properties of propranolol, pK_a, log P_n and log P_d calculated with Chemaxon software; 2) mitochondrial and lysosomal area and volume (A_m, A_l, V_m and V_l) (20). The thickness of the porous membrane (H_M) was fixed as 10 μm according to the manufacturer's instructions and volume of solution inside the pores per cell (V_{bM}) was calculated by total area of pores per cell (A_{bM}) and thickness of membrane (H_M). Initial starting values for PR were used as input to model specific experiments (5, 10, 20, 50, 80, or 100 μM). The volume of apical or basolateral compartments (V_{at} and V_{bt}) was also used as input from specific experiments, as well as the number of cells. Apical or basolateral volume per cell was calculated with dividing V_a or V_b by the total number of cells measured in each insert.

Range of parameter values tested was chosen to capture the range of physiological, histological, and experimental conditions. For high initial PR concentrations (50, 80 or 100 μM), the experimental data from the transport studies for both directions (AP→BL; BL→AP) were used for optimizations. In the algorithm of parameter optimizations, the bounded minimum search function *fminsearchbnd* (available at www. matlabcentral.com, developed by J. D'Errico) with a cost function was used to find the 19 optimal parameters to produce good data fits. The criterion for the optimization was to find the parameter sets which provided the solution to predict the transported and intracellular mass of PR for Calu-3 or NHBE cells with the lowest optimization cost (minimized objective function)

and that were consistent with measured cellular physiological and architectural parameters through 15000 times of iterations as maximum. This process was performed with 100 random starting values of each parameter within the ranges as well as 3 starting value sets including mean values and the lower and upper boundaries in the range of each parameter.

Parameter sensitivity tests for transported mass and intracellular mass of PR in both directions of transport (AP→BL; BL→AP) were performed with the optimized parameters of Calu-3 or NHBE cell at 50 μM (initial PR concentration) for 1h transport. In these tests, each of 19 parameters (A_a, A_{aq}, A_{bq}, A_b, V_c, H_{aq}, H_{bq}, Ea, E_m, E_l, E_b, pH_a, pH_c, pH_m, pH_l, pH_b, L_c, L_m, and L_l) was varied with a uniform distribution within the range used for the parameter optimization process when the other parameters were fixed as optimized with the lowest cost in Calu-3 or NHBE cell.

5.6 Results

5.6.1 Calu-3 and NHBE Cells in Mixed Co-Culture Exhibited a Range of Phenotypes.

First, we assessed the differentiation status of Calu-3, NHBE and mixed cell co-culture systems by assaying the tightness of intercellular junctions using TEER measurements (Figure 1). In pure Calu-3 cell cultures, TEER values increased during the first four days of culture. After four days of cultures, TEER values plateaued at 350 $\Omega \cdot cm^2$, which is a typical TEER value for confluent Calu-3 monolayers with tight junctions (45). Between day 7 and day 15, TEER values remained constant (Figure 1a). In contrast, TEER values of primary NHBE cells in ALI condition increased at a faster rate and plateaued at a higher TEER value than the Calu-3 cells, reaching 1041 ± 34.9 $\Omega \cdot cm^2$ on day 14 (Figure 1b). In Calu-3/NHBE cell co-cultures plated at a ratio of 99/1, 9/1, and 1/1, TEER values were similar to those of pure Calu-3 cell monolayers (Figure 1c). However, when the ratio of Calu-3 to NHBE cells was 1/9 or 1/99, the TEER values were similar to those of the primary NHBE cell cultures.

Next, the tightness of intercellular junctions was independently confirmed using LY as a cell impermeant, paracellular transport probe (Table 1). There were no differences among the P_{eff} values of LY in the Calu-3, NHBE or mixed cell cultures (ratios = 99/1, 9/1, 1/1, 1/9, or 1/99) in AP$\rightarrow$BL and BL$\rightarrow$AP directions ($p > 0.05$). Interestingly, the paracellular transport properties and TEER of Calu-3/NHBE cells co-cultured at a ratio ≥1/1 also resembled that of pure Calu-3 monolayer cultures, and varied according to the cells' monolayer *vs.* multilayer organization.

5.6.2 Mixed Cell Cultures of 1/1 Calu-3 and NHBE Formed Stable Cell Monolayers.

Next, we used confocal fluorescent microscopy followed by quantitative image analysis to establish the 3D architecture of the differentiated cells (Figure 2a) (see Appendix C; Figure C1 and C2). Calu-3/NHBE mixed cell co-cultures showed a typical pattern of actin filament staining at intercellular junctions (Figure 2b). Mixed cell co-cultures with cells of Calu-3/NHBE ratios ≥1/1 formed cell monolayers, similar to pure Calu-3 cell cultures. However, co-cultures with cells of Calu-3/NHBE ratios of <1/9 formed cell multilayers, like pure NHBE cell cultures. The mono- *vs.* multi-layer organization paralleled the observed differences in TEER values.

Quantitative image analysis also revealed a large difference in the volume of Calu-3 and NHBE cells (Figure 3a). Accordingly, cell volume measurements could be used to distinguish Calu-3 from NHBE cells in mixed cell cultures. Mixed cell co-cultures plated at 99/1, 9/1, or 1/1 (Calu-3/NHBE ratios ≥1/1) exhibited a bimodal distribution of cellular volumes (Figure 3b). The volumes of these two cell subpopulations corresponded to the volumes of the pure Calu-3 and NHBE cells, while the relative ratios corresponded to the approximate plating ratios (Figure 3a). In the case of the mixed cell co-cultured multilayer (those plated at a Calu-3/NHBE ratio <1/1), the bottom and top layers were separately analyzed (Figure 3c). A bimodal distribution of cell volumes was observed in the layer of cells closest to the membrane (bottom layer), while unimodal distribution was observed in the top layer of cells (Figure 3c). The volumes of the bottom layer corresponded to the volumes of Calu-3 and NHBE cells while the volume of the top, outer layer corresponded to a pure NHBE cell population.

Most importantly, in 1/1 co-cultures, Calu-3 cells completely suppressed multilayer formation by NHBE cells, forming stable monolayers.

5.6.3 Passive Transport Explains PR Permeation across Calu-3/NHBE Mixed Co-Cultures.

Next, we used PR as a model transport probe (51). In both NHBE and Calu-3 cells, no PR metabolites were formed when cells were incubated with PR (Figure 4), consistent with a previous study (41). The transport properties of PR were compared in Calu-3 and NHBE cells, in the mixed 1/1 Calu-3/NHBE cell monolayers (Figure 5). PR transport was concentration dependent in both AP→BL (Figure 5a and b) and BL→AP directions (Figure 5c and d) in both Calu-3 and NHBE cells. Computer simulations of passive PR transport behavior in both Calu-3 and NHBE cells yielded close fits to the data. Transport rate of PR across a NHBE cell was 1.5 fold greater than across Calu-3 cells in both directions (AP→BL; BL→AP) across all concentrations tested.

In 1/1 Calu-3/NHBE monolayer co-cultures, the bidirectional transport ratio of Calu-3 cells ($P_{eff,\ AP\rightarrow BL}$ /$P_{eff,\ BL\rightarrow AP}$) was 0.85, and was constant for different PR concentrations. Similarly, the bidirectional transport ratio of NHBE cells ($P_{eff,\ AP\rightarrow BL}$ /$P_{eff,\ BL\rightarrow AP}$) was 0.88 as constant for different PR concentrations. This was consistent with a predominantly passive transport mechanism. Comparing the effective permeability values of Calu-3 *vs.* NHBE in monolayer co-cultures, P_{eff} in NHBE was 1.7-fold larger than that in Calu-3 in all tested PR concentrations, for both AP→BL and BL→AP transport, respectively (p-value < 0.0001 by ANOVA).

5.6.4 Passive Transport Explains PR Accumulation Kinetics in Calu-3 and NHBE Cells.

The intracellular accumulation of PR was also measured in mixed Calu-3 and NHBE cell monolayers (Figure 6). During the transport studies, the intracellular mass of PR was analyzed at each time point for the Calu-3 and NHBE cells, and the cell accumulation of PR was fitted well using the cellular pharmacokinetic model. For fitting the data, parameter optimization was performed to minimize the absolute difference between calculated and experimental values (transported PR mass and the intracellular mass). The measurements indicate that intracellular mass accumulation of PR in NHBE cells was about 2-fold greater than in Calu-3 cells, both in AP→BL (Figure 6a and b) and BL→AP directions (Figure 6c and d) at 4 h.

5.6.5 Variations in Apparent, Unstirred Water Layer Thickness Explain Transport Differences.

With the cellular pharmacokinetic model, parameter optimization and sensitivity tests were carried out to identify the individual parameters that exerted the greatest impact on drug transport and intracellular accumulation, within the range of measured cell physiological and architectural parameters (Table 2). Parameter sensitivity tests showed that only a few parameters (A_b, H_{aq}, H_{bq}, E_m, pH_m, and L_m) individually affected transport or intracellular accumulation by >1.5–fold when they were varied within a physiologically-relevant range of values. Based on the results (Table 3, and Figure C3 in the Appendix C), the apparent, unstirred water layer thickness (H_{bq}) on the basolateral side of the cells was the individual parameter with the greatest effect on transport/intracellular accumulation in both directions (AP→BL; BL→AP). Based on

parameter sensitivity results and the goodness of fits, H_{bq} in Calu-3 was 4–fold larger than that in NHBE (Table 2). Variations in the cell surface area (A_{aq} or A_{bq}) or cell volume (V_c) showed little effect on the transported mass and intracellular accumulation for both directions in NHBE or Calu-3 (Table 3). Variations of all other physiological parameters, except for thickness of apical and basolateral unstirred water layers and the basolateral area $A_{b,}$ exerted a relatively minor effect on transport or uptake (Table 3 and Figure C3). However, A_b variation alone was not sufficient to explain observed kinetic differences of PR transport and uptake in Calu-3 or NHBE cells. We also found that total intracellular PR mass was sensitive to changes in mitochondrial pH (pH_m), electrical potential (E_m), and lipid fraction (L_m), which is consistent with PR's tendency to accumulate in mitochondria. However, the rate of PR transport across the cells was not sensitive to variations in these parameters. Only the apparent thickness of the basolateral unstirred water layer (H_{bq}) was necessary and sufficient for explaining the differences in PR transport and uptake across these two airway epithelial cell types.

5.7 Discussion

In this study, we combined an innovative *in vitro* cell-based assay system with an *in silico* cellular pharmacokinetic modeling approach to identify key parameters that can explain differences in the absorption and transport properties of PR in two types of airway epithelial cells. Remarkably, we found that the apparent thickness of the unstirred water layer exerted the most significant effect on the transport properties of Calu-3 and NHBE cells. This apparent, unstirred water layer thickness is an empirical variable that captures a large number of factors such as viscosity, convection, ciliary motility, and

macromolecular crowding, which can affect differences in the local, passive diffusive properties of PR in the layer of fluid immediately above and below the surface of each cell. Thus, differences in PR accumulation and permeation between Calu-3 and NHBE likely result from cell type-dependent, local differences in the extracellular, surface microenvironment.

Previously, the role of apparent unstirred water layer on cellular transport has been mostly considered in the context of drug permeability studies across intestinal epithelial cells (49, 52, 53). This unstirred water layer thickness is not a physical parameter that is directly measured, but rather it is an empirical variable that is determined by fitting the transport data with a mathematical model. In previous experiments, the unstirred water layer thickness has appeared as a highly variable parameter, affected by local differences in stirring speed, buffer volume, and the geometrical design of the assay apparatus (48, 49, 54). Hence, it has been previously considered as a real, hydrodynamic parameter that can dramatically affect the measured permeability of passively diffusing compounds (55).

Of noteworthy significance, in our 1/1 Calu-3/NHBE cell co-cultures, the stirring conditions between Calu-3 and NHBE cells were nearly identical since the cells are randomly dispersed. Therefore, we expected the actual thickness of the unstirred water layer above Calu-3 and NHBE cells in co-culture to be similar. Therefore, the reason that fitted H_{aq} and H_{bq} values appear different is most likely the result of variations in the local extracellular microenvironment surrounding NHBE *vs.* Calu-3 cells, which affect the passive diffusion of PR in the immediate vicinity of the cell surface. Mechanistically, there are many known cell physiological variables that can explain differences the

passive diffusion of PR on the surface of Calu-3 *vs.* NHBE cells. Under the ALI-conditioned cultures, lung epithelial cells secret mucus which coats the extracellular, apical side of the cells in culture (32, 56). Depending on the part of the airway from which NHBE cells were obtained, the expression levels of different classes of mucin (*i.e.*, MUC2, MUC5AC, and MUC5B) and the cell surface pattern of mucin secretion can be quite variable (57, 58). The culture environment of NHBE cells, including the extracellular matrix and the medium's composition, exert a major influence on mucus secretion (58, 59). In addition, Calu-3 and NHBE cells possess different ion regulatory mechanisms including differences in Cl^- channel and Ca^{2+}-activated potassium channel function (60, 61). These differences could potentially affect the hydration, viscosity and thickness of the mucus layer on the cell surface.

Perhaps more importantly, Calu-3 and NHBE cells possess motile cilia on their surface, which is the main reason why the unstirred water layer on airway epithelial cells has to be considered as "apparent". Calu-3 and NHBE cells exhibit differences in the expression and location of ciliary markers (α-, β-, γ-Tubulin) (57, 62). Calu-3 show diffused immunostaining patterns with higher mRNA levels of β-tubulin compared with NHBE cells which show localized tubulin staining patterns on the cell surface with low or intermediate mRNA expression levels (57). Previous transmission electron microscopic analyses indicate that the morphology of cilia is different in Calu-3 *vs.* NHBE cells (50). Accordingly, variations in cell surface area, viscosity and ciliary motility could also lead to differences in convection around the cell which is reflected in the different fitted H_{aq} and H_{bq} values.

Previous investigations of the transport properties of small molecules across different types of airway epithelial cells have focused on the effects of active transporters (*i.e.*, P-glycoprotein). NHBE and Calu-3 cells exhibit significant differences in transporter expression which has been linked to differences in the effective permeability of small molecules (44, 63). However, these past studies have largely relied on measurements performed across NHBE cell multilayers differentiated on porous membranes. Arguably, the 1/1 Calu-3/NHBE cell co-culture system elaborated in this study, combined with cellular pharmacokinetic analysis and mathematical modeling/optimization approach, could offer a more accurate way to measure the cellular permeation of both passively and actively transported molecules across NHBE cells. Previously, we studied the staining pattern of MTR in NHBE cell multilayers on Transwell™ inserts by confocal microscopic analyses (19). We observed MTR accumulation was largely restricted to the solvent exposed, upper layer of cells. This is consistent with the local microenvironment in NHBE cell multilayers exerting a significant influence on the observed cellular transport behavior.

To summarize, a Calu-3/NHBE mixed cell co-culture model was developed to suppress cell multilayers formed by NHBE cells differentiated in ALI conditions. Based on the differences in morphology between Calu-3 and NHBE, the relative areas occupied by these two cell types in the mixed co-cultures allowed calculating the differential contribution of NHBE *vs.* Calu-3 cells to the transport properties of the monolayer. Differences in the transport and uptake of a passive transport probe, coupled to cellular pharmacokinetics analyses suggest that variations in the local microenvironment account for the observed differences in PR transport properties.

5.8 Conclusions

For inhaled drug development, *in vitro* cell-based assays can be used to measure the uptake and transport properties of small molecules across airway epithelial cells, to identify drugs that are substrates of active transport mechanisms affecting drug permeability, and to assay the dissolution-absorption behavior of inhaled drug formulations which is important for regulatory purposes (44, 64). From the trachea and bronchi to the most distal airways and alveoli, the thickness, viscosity and flow properties of the airway liquid lining vary by orders of magnitude. Furthermore, the local composition of the extracellular matrix and the airway liquid lining surrounding epithelial cells also vary greatly under normal physiological conditions, and may vary even more under pathological conditions. While the effect of the airway cell surface microenvironment on the absorption properties of inhaled drugs in the lungs would ultimately need to be studied *in vivo*, our results are significant because they demonstrate how differences in the cellular uptake and transport properties of small molecules can be studied in relation to local differences in the extracellular microenvironment, using co-cultures of normal and transformed airway epithelial cells differentiated *in vitro*.

5.9 Acknowledgements

This study was supported by NIH grant R01GM078200 (G. R. Rosania). K. A. Min was supported by the Warner Lambert/Parke Davis Fellowship, University of Michigan College of Pharmacy and the Rackham Pre-doctoral Fellowship. The authors

would like to acknowledge and thank the staff of the University of Michigan Microscopy and Image Analysis Laboratory for their technical assistance.

5.10 Tables

Table 5-1. Lucifer Yellow (LY) permeability (P_{eff}) measurements in Calu-3, NHBE, and Mixed cells with different mixed ratios on day 8 of ALI cultures

P_{eff} ($\times 10^{-7}$ cm/sec)	Calu-3	NHBE	Mixed cells (Calu-3/NHBE)				
			99/1	9/1	1/1	1/9	1/99
AP→BL	0.78 (0.29) [a]	0.68 (0.16)	0.77 (0.19)	0.73 (0.23)	0.67 (0.17)	0.71 (0.08)	0.62 (0.03)
BL→AP	0.84 (0.10)	0.78 (0.30)	0.88 (0.10)	0.74 (0.29)	0.81 (0.11)	0.81 (0.05)	0.75 (0.09)

[a] Standard deviations (S.D.) are displayed in the parenthesis under the average values (N=3).

Table 5-2. Optimized parameters for Calu-3 or NHBE cells, and the range of starting values used for the optimization process.

Optimized parameter	Calu-3 [a]	NHBE [a]	LB [b]	UB [b]
Area (μm^2)				
A_a	2.48E+04	2.48E+04	79	2.69E+04
A_{aq}	198	154	79	538
A_{bq}	262	197	79	538
A_b	6.91	7.05	0.84	538
Unstirred water layer thickness (μm)				
H_{aq}	495	217	1.00E-03	500
H_{bq}	52.5	13.2	1.00E-03	500
Cell volume (μm^3)				
V_c	2707	6971	1239	8483
Membrane electrical potential (V)				
E_a	-0.0065	-0.0140	-0.0143	-0.0043
E_l	0.0102	0.0150	0.005	0.015
E_m	-0.1727	-0.1717	-0.21	-0.11
E_b	0.0069	0.0070	0.0069	0.0169
pH				
pH_a	7.8	7.8	6.0	7.8
pH_c	7.0	7.1	7.0	7.8
pH_l	5.6	4.9	4.8	6.0
pH_m	7.8	7.7	7.7	8.2
pH_b	7.0	7.1	7.0	7.8
Lipid fraction				
L_c	0.08	0.08	0.05	0.15
L_m	0.08	0.15	0.05	0.15
L_l	0.07	0.07	0.05	0.15

[a] Optimized parameters with the predictions of the lowest errors for Calu-3 or NHBE
[b] LB (lower boundary) or UB (upper boundary) of ranges within which each parameter is varied for optimizations.

Table 5-3. Parameter sensitivity analysis results using the Calu-3 and NHBE cell models.

Optimized parameter	Fold changes of Mass Transported [a]				Fold changes of Mass Uptake [a]			
	Calu-3 (A→B)	Calu-3 (B→A)	NHBE (A→B)	NHBE (B→A)	Calu-3 (A→B)	Calu-3 (B→A)	NHBE (A→B)	NHBE (B→A)
A_a	1.1	1.1	1.1	1.1	1.0	1.1	1.0	1.1
A_{aq}	1.4	1.3	1.4	1.2	1.2	1.2	1.1	1.4
A_{bq}	1.0	1.0	1.0	1.0	1.0	1.0	1.0	1.0
A_b	25.9(↑)[d]	42.3(↑)	19.6(↑)	33.4(↑)	7.3(↓)[e]	30.3(↑)	6.9(↓)	25.3(↑)
H_{aq}	1.5(↓)[c]	1.5(↓)	1.8(↓)	1.6(↓)	1.1	1.2	1.1	1.3
H_{bq}	8.5(↓)	11.7(↓)	9.0(↓)	12.3(↓)	1.6(↑)[b]	10.2(↓)	1.5(↑)	11.3(↓)
V_c	1.1	1.1	1.1	1.1	1.4	1.3	1.2	1.2
E_a	1.2	1.1	1.1	1.2	1.2	1.2	1.1	1.2
E_l	1.0	1.0	1.0	1.0	1.0	1.0	1.0	1.0
E_m	1.2	1.2	1.3	1.2	1.8(↓)	1.7(↓)	1.6(↓)	1.6(↓)
E_b	1.2	1.1	1.2	1.2	1.1	1.1	1.1	1.2
pH_a	1.1	1.1	1.1	1.1	1.1	1.2	1.1	1.2
pH_c	1.0	1.0	1.0	1.0	1.1	1.1	1.1	1.1
pH_l	1.0	1.0	1.0	1.0	1.0	1.0	1.0	1.0
pH_m	1.2	1.2	1.3	1.2	1.8(↓)	1.8(↓)	1.7(↓)	1.6(↓)
pH_b	1.1	1.1	1.0	1.1	1.0	1.1	1.0	1.1
L_c	1.1	1.0	1.1	1.1	1.1	1.1	1.2	1.2
L_m	1.3	1.2	1.3	1.2	1.9(↑)	1.8(↑)	1.7(↑)	1.7(↑)
L_l	1.0	1.0	1.0	1.0	1.0	1.0	1.0	1.0

[a] Fold changes of mass transported or uptake of PR (maximal change divided by minimal change) by each parameter varied within the range (Table II) as other parameters were fixed as optimized for Calu-3 or NHBE.

[b] Upward arrows indicate the increase by more than 1.5-fold in mass transported or uptake as the varied parameter increases.

[c] Downward arrows indicate the decrease by more than 1.5-fold in mass transported or uptake as the varied parameter increases.

[d] Red bold upward arrows indicate the increase by more than 5-fold in mass transported or uptake as the varied parameter increases.

[e] Red bold downward arrows indicate the decrease by more than 5-fold in mass transported or uptake as the varied parameter increases.

5.11 Figures

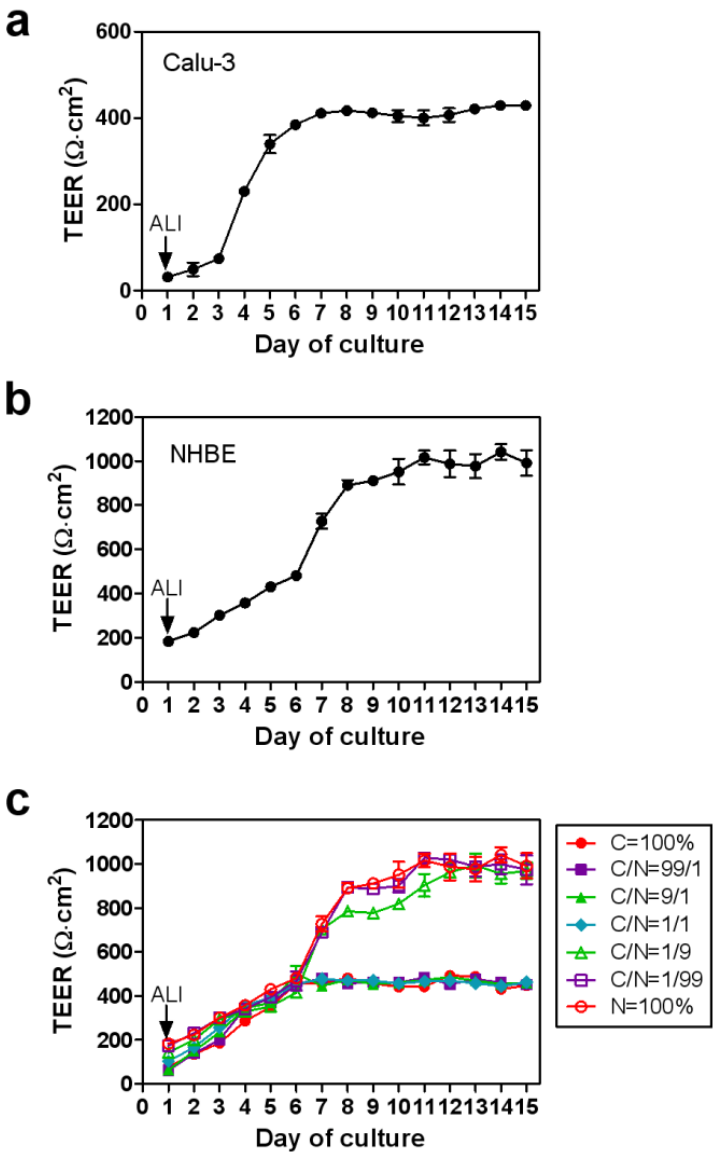

Figure 5-1. Mixed cell cultures exhibited a variety of properties similar to those of pure Calu-3 and NHBE cells depending on the relative ratio of the two cell types.

(**a**) TEER measurements of cells plated on inserts were made as the cells differentiated under ALI conditions. (**a**) Calu-3 cells showed increased TEER values as cells differentiated. (**b**) NHBE cells in differentiation medium had higher TEER values than Calu-3 cells. Mixed cells with various ratios of Calu-3 (C)/NHBE cells (N) exhibited TEER values between those of NHBE and Calu-3 cells.

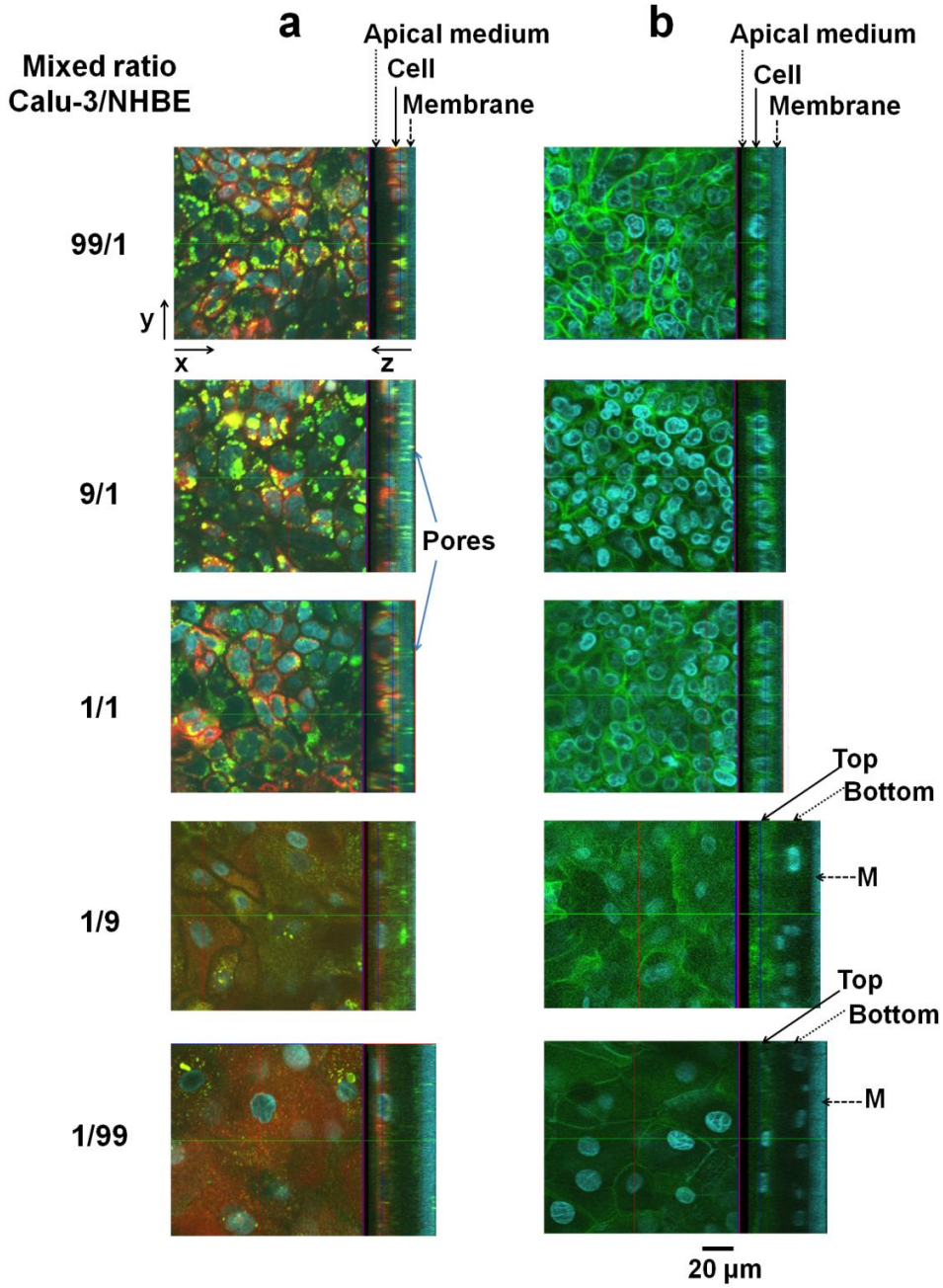

Figure 5-2. Confocal 3D image analyses of the mixed cell cultures confirmed TEER values of the monolayer or multilayer architecture of airway epithelial cells.

Images were acquired on day 8 under ALI conditions. (**a**) Mixed cells on the inserts were incubated for 30 min (37°C, 5% CO_2) with dye mixtures containing Hoe, MTR, and LTG staining cell nuclei, mitochondria, and lysosomes. Zeiss LSM confocal microscopy was used for the examination with z-axis scanning. Two dimensional images in xy planes

show cell nuclei (blue), mitochondria (red), and lysosomes (green) and cell architecture on the insert are shown in yz planes with the arrows indicating “apical medium”, “cell”, and “membrane”. (**b**) Development of tight junctions in cell-to-cell contacts was examined for the mixed cell cultures on day 8 in ALI condition. Actin filaments in the cells grown on the inserts were stained with Alexa Fluor® 488 phalloidin (green) and cell nuclei stained with Hoe (blue). For the mixed cells (Calu-3/NHBE = 99/1), the vertical arrows represent “apical medium”, “cell layers”, and “porous membrane”. As shown in the yz planes, the mixed cells with more NHBE cells (Calu-3/NHBE = 1/9 or 1/99) formed multilayers with varied thickness of layers. The arrows point to the top cell layer, bottom cell layer and porous membrane support.

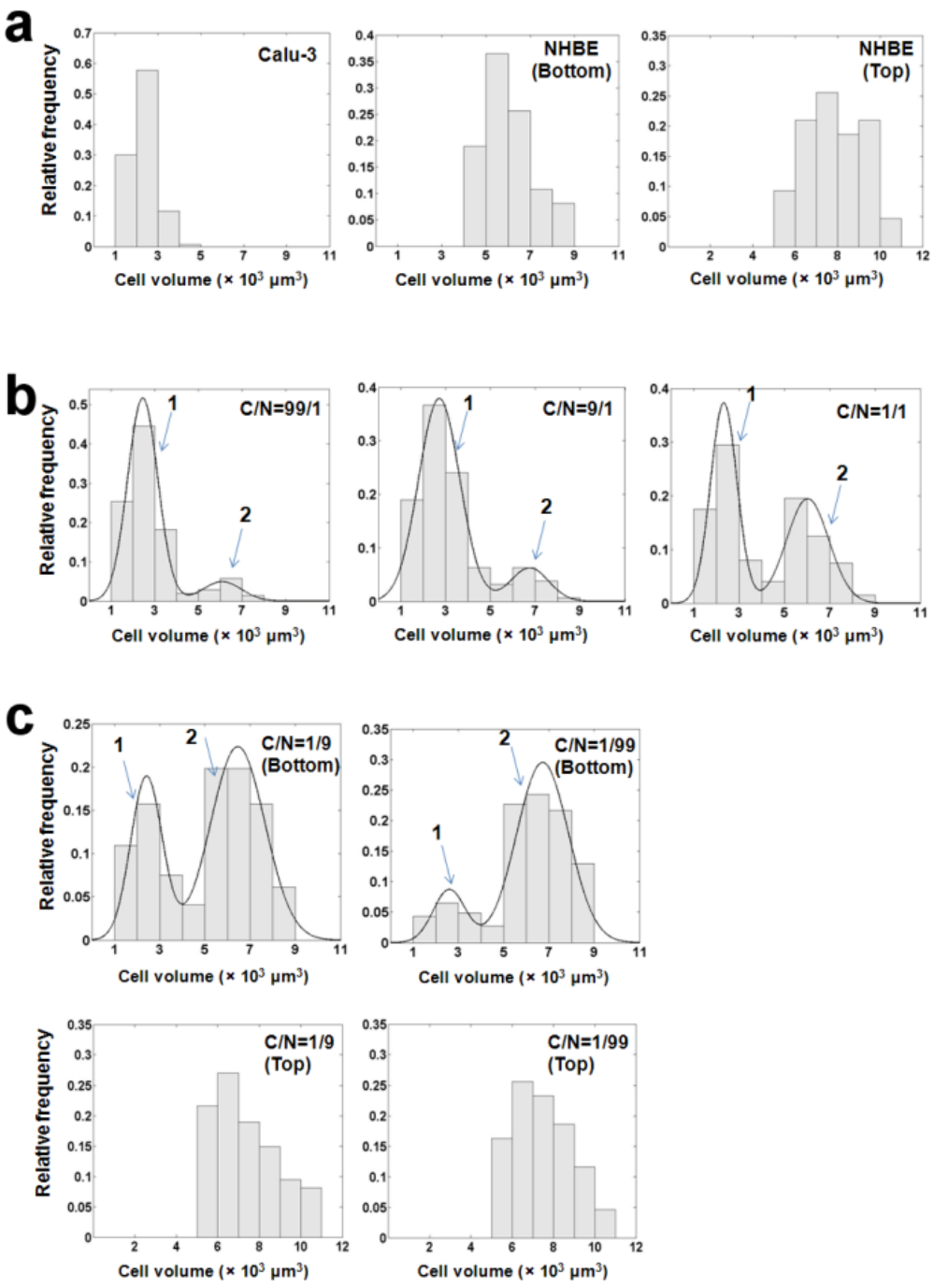

Figure 5-3. The fraction of Calu-3 and NHBE cells in cell populations consisting of pure (**a**) Calu-3 and NHBE cultures and mixed cell cultures (**b, c**) were estimated by fitting the distribution of cell volumes in the mixed cell population using a normal mixture statistical model.

Cell volume (μm^3) was calculated by Metamorph in the confocal 3D images and was used as a representative cytometric parameter to evaluate the distribution profiles in the pure and mixed cell populations. All the mixed cell cultures (Calu-3/NHBE = (**b**) 99/1, 9/1, 1/1, (**c**) 1/9, and 1/99) showed bimodal distributions with two distinct cell populations as indicated with the blue arrows (group 1 and 2). For the multilayers in the mixed cell cultures with more NHBE cells (Calu-3/NHBE= 1/9 or 1/99), the bottom cell layers and top cells were separately analyzed. As shown in (**c**), bottom cell layers consisted of two cell populations while top cells showed unimodal distribution, reflecting one cell-type in the top layer.

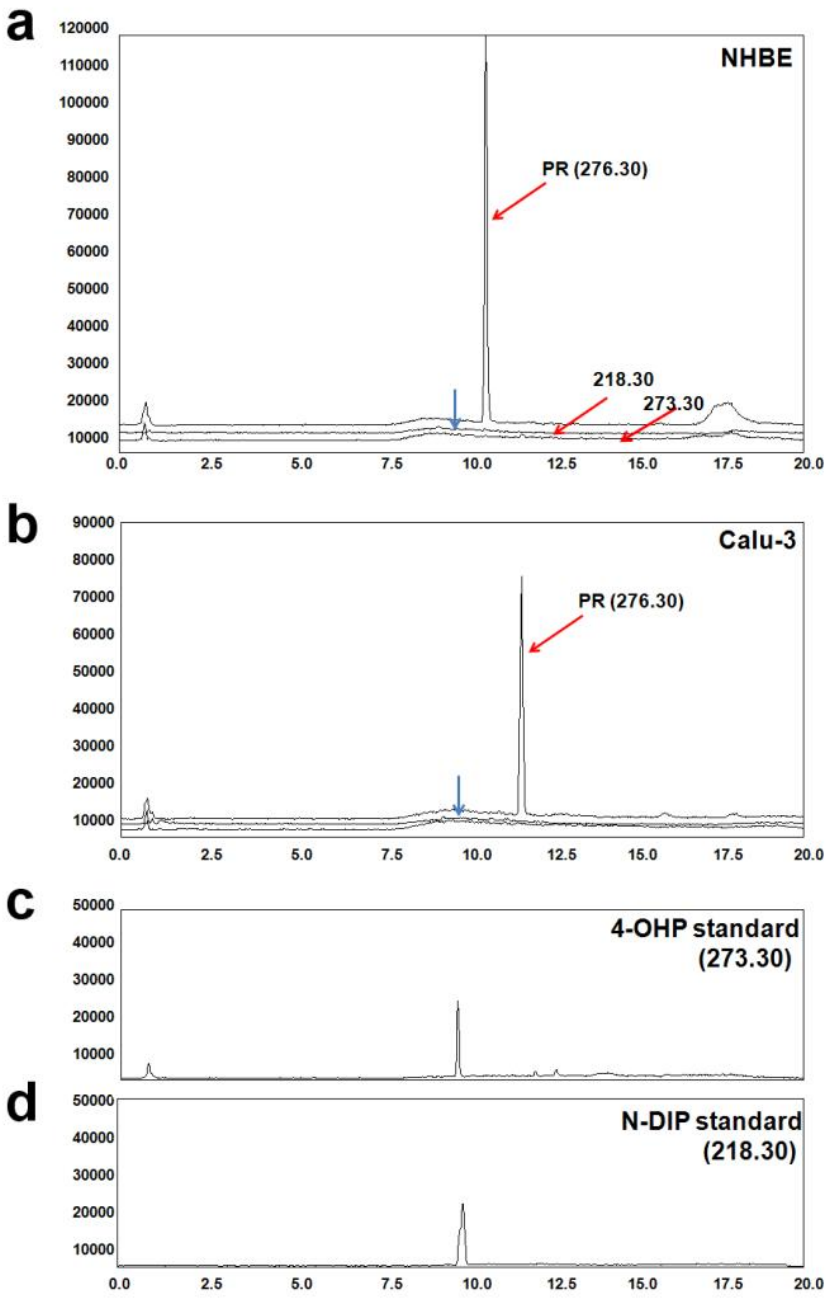

Figure 5-4. PR is not metabolized to any significant extent in NHBE or Calu-3 cells based on LC/MS ion chromatograms.

After adding PR to cells (10^7 cells in ml) in suspension, the cells were lysed and the samples were prepared for LC/MS. In NHBE (**a**) or Calu-3 (**b**) cells, PR (m/z: 276.30) eluted at 11 min as indicated with red arrows in the chromatogram. However, there was no metabolite peak (blue arrow at 9 min) in the chromatogram of cell lysate. (**c, d**) In a positive control experiment, pure PR metabolite standards could be readily detected. The

metabolite standards, (**c**) 4-OHP (4-hydroxypropranolol) or (**d**) N-DIP (N-desisopropyl propranolol) showed peaks at 9 min with m/z 273.30 and 218.30, respectively.

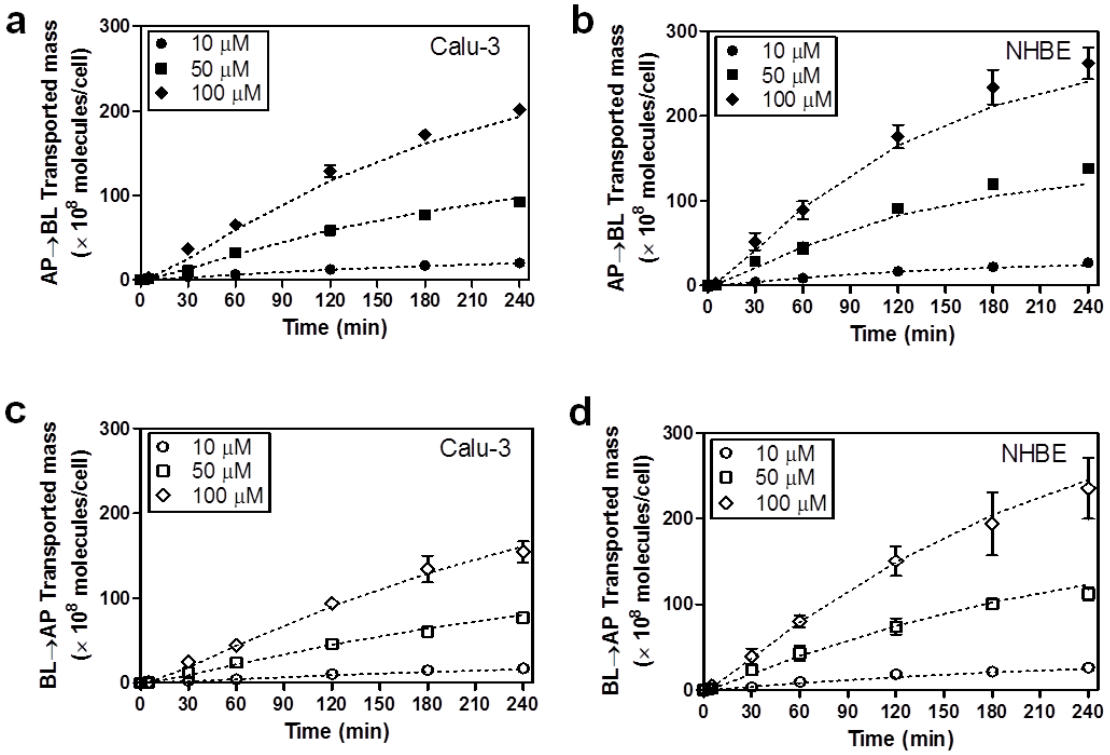

Figure 5-5. In 1/1 mixed cell monolayer co-cultures, the individual Calu-3 cells (**a, c**) exhibited lower PR mass transport rates as compared to the corresponding NHBE cells (**b, d**).

Bidirectional transport studies were performed with the Calu-3 monolayers (N = 3) or mixed cell monolayers (1/1) (N = 3) on the Transwell™ inserts. Representative results obtained with three different initial PR concentrations (10, 50, and 100 μM) are displayed in the plots. The transported mass (molecules/cell) of PR in a Calu-3 or NHBE cell was plotted as function of incubation time. It is noted that the kinetics in the AP→BL direction (**a, b**) are similar to kinetics in the BL→AP direction (**c, d**), consistent with a passive transport mechanism. Fitted curves correspond to the calculated mass transport kinetics in both directions, based on the optimized, cellular pharmacokinetic model.

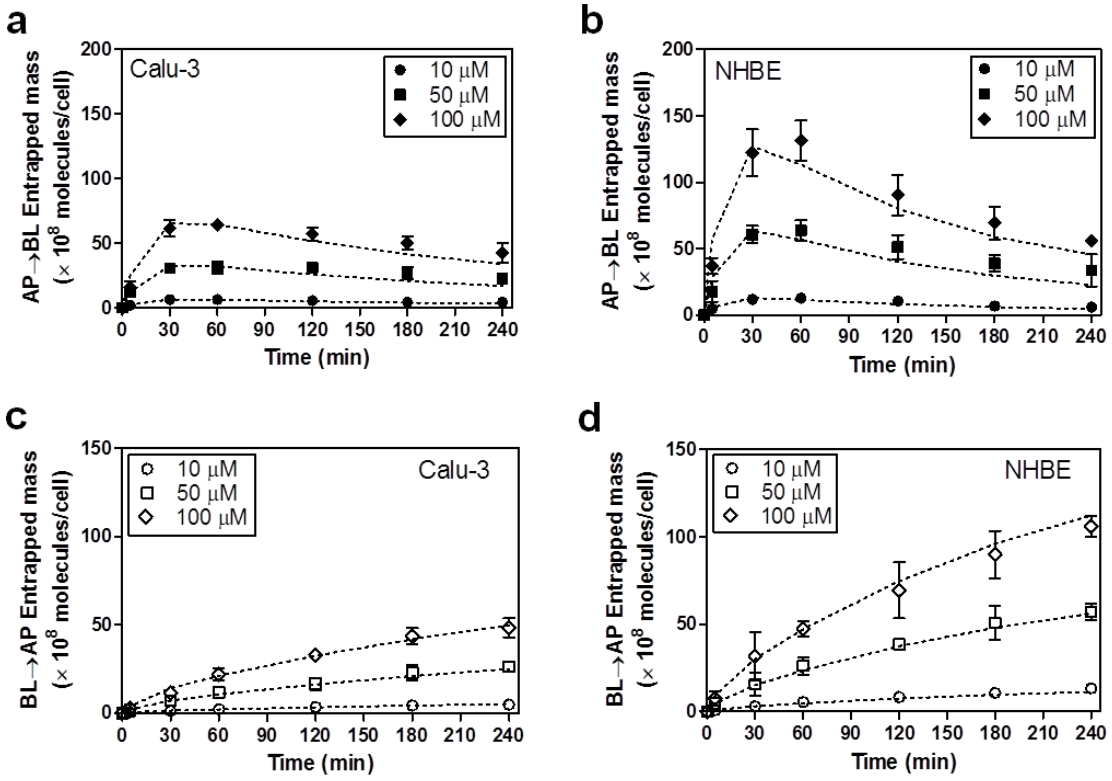

Figure 5-6. In 1/1 mixed cell co-cultures, the measured intracellular uptake of PR in the individual Calu-3 cells (**a, c**) was less than that of individual NHBE cells (**b, d**).

(**a**) Based on transport experiments in the AP→BL (**a, b**) or BL→AP (**c, d**) directions, the intracellular PR mass (molecules/cell) in a Calu-3 or NHBE cell was analyzed over time. For the PR uptake measurements, cells were collected from the inserts by trypsin digestion at each time point (0, 5, 30, 60, 120, 180, and 240 min) after the transport studies and lysed in cold methanol by 10 min-sonication and incubation in the ice. Cell lysis in buffer was subjected to the extraction process for LC/MS analysis. The plots show representative results using three different initial PR concentrations (10, 50, and 100 μM). Fitted curves correspond to the calculated PR mass uptake kinetics, based on the optimized, cellular pharmacokinetic model.

5.12 Supporting Information Available

Supporting information is available in the Appendix C.

5.13 References

1. Chambers LA, Rollins BM, Tarran R. Liquid movement across the surface epithelium of large airways. Respiratory physiology & neurobiology. 2007;159(3):256-70.
2. Davis CW, Lazarowski E. Coupling of airway ciliary activity and mucin secretion to mechanical stresses by purinergic signaling. Respiratory physiology & neurobiology. 2008;163(1):208-13.
3. Byron A, Humphries JD, Humphries MJ. Defining the extracellular matrix using proteomics. International Journal of Experimental Pathology. 2013.
4. Hynes RO. The extracellular matrix: not just pretty fibrils. Science. 2009;326(5957):1216-9.
5. Eerenstein W, Kalev L, Niesen L, Palstra TTM, Hibma T. Magneto-resistance and superparamagnetism in magnetite films on MgO and MgAl2O4. Journal of Magnetism and Magnetic Materials. 2003;258:73-6.
6. Garcia GJ, Boucher RC, Elston TC. Biophysical Model of Ion Transport across Human Respiratory Epithelia Allows Quantification of Ion Permeabilities. Biophysical Journal. 2013;104(3):716-26.
7. Song Y, Verkman A. Aquaporin-5 dependent fluid secretion in airway submucosal glands. Journal of Biological Chemistry. 2001;276(44):41288-92.
8. Adson A, Burton PS, Raub TJ, Barsuhn CL, Audus KL, Ho NF. Passive diffusion of weak organic electrolytes across Caco-2 cell monolayers: Uncoupling the contributions of hydrodynamic, transcellular, and paracellular barriers. J Pharm Sci-Us. 1995;84(10):1197-204.
9. Everitt C, Redwood W, Haydon D. Problem of boundary layers in the exchange diffusion of water across bimolecular lipid membranes. Journal of theoretical biology. 1969;22(1):20-32.
10. Khanvilkar K, Donovan MD, Flanagan DR. Drug transfer through mucus. Adv Drug Deliver Rev. 2001;48(2):173-93.
11. Buck CA, Horwitz AF. Cell surface receptors for extracellular matrix molecules. Annu Rev Cell Biol. 1987;3:179-205.
12. Akiyama SK, Nagata K, Yamada KM. Cell surface receptors for extracellular matrix components. Biochim Biophys Acta. 1990;1031(1):91-110.
13. Geiger B, Yamada KM. Molecular architecture and function of matrix adhesions. Cold Spring Harbor Perspectives in Biology. 2011;3(5).
14. Adson A, Raub TJ, Burton PS, Barsuhn CL, Hilgers AR, Ho NF, et al. Quantitative approaches to delineate paracellular diffusion in cultured epithelial cell monolayers. J Pharm Sci-Us. 1994;83(11):1529-36.
15. Zhang X, Zheng N, Zou P, Zhu H, Hinestroza JP, Rosania GR. Cells on pores: a simulation-driven analysis of transcellular small molecule transport. Molecular Pharmaceutics. 2010;7(2):456-67.
16. Ho NF, Raub TJ, Burton PS, Barsuhn CL, Adson A, Audus KL, et al. Quantitative approaches to delineate passive transport mechanisms in cell culture monolayers. Transport Processes in Pharmaceutical Systems. 2000:219-316.

17. Bishop WP, Wen JT. Regulation of Caco-2 cell proliferation by basolateral membrane epidermal growth factor receptors. American Journal of Physiology-Gastrointestinal and Liver Physiology. 1994;267(5):G892-G900.
18. Sanders MA, Basson MD. Collagen IV regulates Caco-2 migration and ERK activation via α1β1-and α2β1-integrin-dependent Src kinase activation. American Journal of Physiology-Gastrointestinal and Liver Physiology. 2004;286(4):G547-G57.
19. Yu JY, Zheng N, Mane G, Min KA, Hinestroza JP, Zhu H, et al. A cell-based computational modeling approach for developing site-directed molecular probes. Plos Comput Biol. 2012;8(2):e1002378.
20. Zhang X, Shedden K, Rosania GR. A cell-based molecular transport simulator for pharmacokinetic prediction and cheminformatic exploration. Mol Pharm. 2006;3(6):704-16.
21. Yu J-y, Rosania GR. Cell-based multiscale computational modeling of small molecule absorption and retention in the lungs. Pharmaceut Res. 2010;27(3):457-67.
22. Zheng N, Zhang X, Rosania GR. Effect of phospholipidosis on the cellular pharmacokinetics of chloroquine. J Pharmacol Exp Ther. 2011;336(3):661-71.
23. Forbes B. Human airway epithelial cell lines for< i> in vitro</i> drug transport and metabolism studies. Pharmaceutical science & technology today. 2000;3(1):18-27.
24. Mathias NR, Timoszyk J, Stetsko PI, Megill JR, Smith RL, Wall DA. Permeability characteristics of calu-3 human bronchial epithelial cells: in vitro-in vivo correlation to predict lung absorption in rats. Journal of Drug Targeting. 2002;10(1):31-40.
25. Bhatia S, Balis U, Yarmush M, Toner M. Effect of cell–cell interactions in preservation of cellular phenotype: cocultivation of hepatocytes and nonparenchymal cells. The FASEB Journal. 1999;13(14):1883-900.
26. Bhatia S, Balis U, Yarmush M, Toner M. Microfabrication of Hepatocyte/Fibroblast Co-cultures: Role of Homotypic Cell Interactions. Biotechnology progress. 1998;14(3):378-87.
27. Narayan PJ, Gibbons HM, Mee EW, Faull RL, Dragunow M. High throughput quantification of cells with complex morphology in mixed cultures. Journal of neuroscience methods. 2007;164(2):339-49.
28. Yamashita S, Furubayashi T, Kataoka M, Sakane T, Sezaki H, Tokuda H. Optimized conditions for prediction of intestinal drug permeability using Caco-2 cells. Eur J Pharm Sci. 2000;10(3):195-204.
29. Irvine JD, Takahashi L, Lockhart K, Cheong J, Tolan JW, Selick HE, *et al.* MDCK (Madin-Darby canine kidney) cells: A tool for membrane permeability screening. J Pharm Sci. 1999;88(1):28-33.
30. Fogh J, Fogh JM, Orfeo T. One hundred and twenty-seven cultured human tumor cell lines producing tumors in nude mice. J Natl Cancer Inst. 1977;59(1):221-6.
31. Gruenert DC, Finkbeiner WE, Widdicombe JH. Culture and transformation of human airway epithelial cells. Am J Physiol-Lung C. 1995;268(3):L347-L60.

32. Forbes II. Human airway epithelial cell lines for *in vitro* drug transport and metabolism studies. Pharm Sci Technolo Today. 2000;3(1):18-27.
33. Wan H, Winton HL, Soeller C, Stewart GA, Thompson PJ, Gruenert DC, *et al.* Tight junction properties of the immortalized human bronchial epithelial cell lines Calu-3 and 16HBE14o-. Eur Respir J. 2000;15(6):1058-68.
34. Grainger CI, Greenwell LL, Lockley DJ, Martin GP, Forbes B. Culture of Calu-3 cells at the air interface provides a representative model of the airway epithelial barrier. Pharm Res. 2006;23(7):1482-90.
35. Grainger CI, Saunders M, Buttini F, Telford R, Merolla LL, Martin GP, *et al.* Critical characteristics for corticosteroid solution metered dose inhaler bioequivalence. Mol Pharm. 2012;9(3):563-9.
36. Patton JS, Brain JD, Davies LA, Fiegel J, Gumbleton M, Kim KJ, *et al.* The particle has landed-Characterizing the fate of inhaled pharmaceuticals. J Aerosol Med Pulm Drug Deliv. 2010;23 Suppl 2:S71-87.
37. Suresh MV, Wagner MC, Rosania GR, Stringer KA, Min KA, Risler L, *et al.* Pulmonary administration of a water-soluble curcumin complex reduces severity of acute lung injury. Am J Respir Cell Mol Biol. 2012;47(3):280-7.
38. Florea BI, Cassara ML, Junginger HE, Borchard G. Drug transport and metabolism characteristics of the human airway epithelial cell line Calu-3. J Control Release. 2003;87(1-3):131-8.
39. Foster KA, Avery ML, Yazdanian M, Audus KL. Characterization of the Calu-3 cell line as a tool to screen pulmonary drug delivery. Int J Pharm. 2000;208(1-2):1-11.
40. Tronde A, Norden B, Marchner H, Wendel AK, Lennernas H, Bengtsson UH. Pulmonary absorption rate and bioavailability of drugs *in vivo* in rats: structure-absorption relationships and physicochemical profiling of inhaled drugs. J Pharm Sci. 2003;92(6):1216-33.
41. Ehrhardt C, Forbes B, Kim K-J. *In vitro* models of the tracheo-bronchial epithelium. In: Ehrhardt C, Kim K-J, editors. Drug absorption studies. New York: Springer US; 2008. p. 235-57.
42. Forrest IA, Murphy DM, Ward C, Jones D, Johnson GE, Archer L, *et al.* Primary airway epithelial cell culture from lung transplant recipients. Eur Respir J. 2005;26(6):1080-5.
43. Mathias NR, Kim KJ, Lee VHL. Targeted drug delivery to the respiratory tract: Solute permeability of air-interface cultured rabbit tracheal epithelial cell monolayers. J Drug Targeting. 1996;4(2):79-86.
44. Sporty JL, Horalkova L, Ehrhardt C. *In vitro* cell culture models for the assessment of pulmonary drug disposition. Expert Opin Drug Metab Toxicol. 2008;4(4):333-45.
45. Madlova M, Bosquillon C, Asker D, Dolezal P, Forbes B. *In-vitro* respiratory drug absorption models possess nominal functional P-glycoprotein activity. J Pharm Pharmacol. 2009;61(3):293-301.
46. Lin H, Li H, Cho HJ, Bian S, Roh HJ, Lee MK, *et al.* Air-liquid interface (ALI) culture of human bronchial epithelial cell monolayers as an *in vitro* model for airway drug transport studies. J Pharm Sci. 2007;96(2):341-50.

47. Frixione E, Lagunes R, Ruiz L, Urban M, Porter RM. Actin cytoskeleton role in the structural response of epithelial (MDCK) cells to low extracellular Ca^{2+}. J Muscle Res Cell M. 2001;22(3):229-42.
48. Avdeef A, Nielsen PE, Tsinman O. PAMPA-a drug absorption *in vitro* model: 11. Matching the *in vivo* unstirred water layer thickness by individual-well stirring in microtitre plates. Eur J Pharm Sci. 2004;22(5):365-74.
49. Korjamo T, Heikkinen AT, Waltari P, Monkkonen J. The asymmetry of the unstirred water layer in permeability experiments. Pharm Res. 2008;25(7):1714-22.
50. Berube K, Prytherch Z, Job C, Hughes T. Human primary bronchial lung cell constructs: the new respiratory models. Toxicology. 2010;278(3):311-8.
51. Upthagrove AL, Nelson WL. Importance of amine pKa and distribution coefficient in the metabolism of fluorinated propranolol derivatives. Preparation, identification of metabolite regioisomers, and metabolism by CYP2D6. Drug Metab Dispos. 2001;29(11):1377-88.
52. Fagerholm U, Lennernas H. Experimental estimation of the effective unstirred water layer thickness in the human jejunum, and its importance in oral drug absorption. Eur J Pharm Sci. 1995;3(5):247-53.
53. Hidalgo IJ, Hillgren KM, Grass GM, Borchardt RT. Characterization of the unstirred water layer in Caco-2 cell monolayers using a novel diffusion apparatus. Pharm Res. 1991;8(2):222-7.
54. Youdim KA, Avdeef A, Abbott NJ. *In vitro* trans-monolayer permeability calculations: often forgotten assumptions. Drug Discovery Today. 2003;8(21):997-1003.
55. Taub ME, Kristensen L, Frokjaer S. Optimized conditions for MDCK permeability and turbidimetric solubility studies using compounds representative of BCS classes I-IV. Eur J Pharm Sci. 2002;15(4):331-40.
56. Matsui H, Randell SH, Peretti SW, Davis CW, Boucher RC. Coordinated clearance of periciliary liquid and mucus from airway surfaces. J Clin Invest. 1998;102(6):1125-31.
57. Stewart CE, Torr EE, Mohd Jamili NH, Bosquillon C, Sayers I. Evaluation of differentiated human bronchial epithelial cell culture systems for asthma research. J Allergy (Cairo). 2012;2012:943982.
58. Huang TW, Chan YH, Cheng PW, Young YH, Lou PJ, Young TH. Increased mucociliary differentiation of human respiratory epithelial cells on hyaluronan-derivative membranes. Acta Biomater. 2010;6(3):1191-9.
59. Guzman K, Gray TE, Yoon JH, Nettesheim P. Quantitation of mucin RNA by PCR reveals induction of both MUC2 and MUC5AC mRNA levels by retinoids. Am J Physiol-Lung C. 1996;271(6):L1023-L8.
60. Szkotak AJ, Man SF, Duszyk M. The role of the basolateral outwardly rectifying chloride channel in human airway epithelial anion secretion. Am J Respir Cell Mol Biol. 2003;29(6):710-20.
61. Wang D, Sun Y, Zhang W, Huang P. Apical adenosine regulates basolateral Ca^{2+}-activated potassium channels in human airway Calu-3 epithelial cells. Am J Physiol Cell Physiol. 2008;294(6):C1443-53.

62. Lehmann M, Noack D, Wood M, Perego M, Knaus UG. Lung epithelial injury by B. anthracis lethal toxin is caused by MKK-dependent loss of cytoskeletal integrity. PLoS One. 2009;4(3).
63. Hamilton KO, Backstrom G, Yazdanian MA, Audus KL. P-glycoprotein efflux pump expression and activity in Calu-3 cells. J Pharm Sci. 2001;90(5):647-58.
64. H. Eixarch, Haltner-Ukomadu E, Beisswenger C, Bock U. Drug delivery to the lung: permeability and physicochemical characteristics of drugs as the basis for a pulmonary biopharmaceutical classification system (pBCS). J Epithelial Biol Pharmacol. 2010;3:1-14.

Chapter 6

Enhanced Permeability and Efficacy of Curcumin-Cyclodextrin Complex in the Airway *in vitro* and *in vivo* Model

The contents in this Chapter have been published in American Journal of Respiratory Cell and Molecular Biology with titled as "Pulmonary Administration of Water-soluble Curcumin Complex Reduces ALI Severity" (Suresh MV, Wagner MC, Rosania GR, Stringer KA, Min KA, Risler L, Shen DD, Georges GE, Reddy AT, Parkkinen J, Reddy RC. Pulmonary Administration of Water-soluble Curcumin Complex Reduces ALI Severity. *Am J Resp Cell Mol.* 2012; 47(3):280-287). My contribution to this paper was to confirm the effects of complexation with cyclodextrin on the transport/ cellular uptake of curcumin across the human airway epithelial cell line, Calu-3. Data from *in vitro* cell-based permeability assays and microscopic imaging are critical for this study to show more enhanced transport and cell-association of curcumin-cyclodextrin complex (CDC) with lower toxicity than those of curcumin solubilized with co-solvents. My collaborators have performed *in vivo* animal experiments to confirm the tissue permeation of CDC *via* IT instillation and anti-inflammatory and antioxidant effects of CDC in the animal model.

6.1 Background

Turmeric as an Indian spice, derived from the rhizomes of the plant has been used as medicine for treating inflammatory diseases. Curcumin identified by Lampe and Milobedzka in 1910 is the primary active, yellow color constituent of turmeric (the common name for Curcuma longa) (1). Curcumin has been reported to have numerous pharmacological activities such as antioxidant (2), antimicrobial properties (3), and anti-inflammatory activities (4). Despite of its therapeutic potential, use of curcumin as drugs is hampered by the poor pharmacokinetic profiles. Curcumin is a lipophilic polyphenol that is nearly insoluble in water (logP= 4.12; calculated by MarvinView 5.3.2 (ChemAxon Ltd.)), causing low bioavailability (5). Animal studies have shown rapid metabolism with conjugation in the liver, and excretion into the feces of curcumin, resulting in poor systemic bioavailability (6). The pharmacokinetic studies with curcumin in humans, mostly conducted on cancer patients and some in healthy subjects, also showed the issues of the limited bioavailability and metabolism of curcumin. Clinical trials conducted with cancer patients taking oral doses of curcumin daily demonstrated that curcumin was poorly absorbed and serum concentration peaked in 1-2 hours post-dose, declining rapidly (7). Plasma concentration of curcumin was not detectable in the patients taking low doses (< 10 g) (8). Other clinical studies have shown that curcumin was rapidly cleared and subsequently conjugated in the GI tract and liver (9). Because of the limited therapeutic applications of curcumin by its rapid plasma clearance and metabolism, a lot of research has been devoted to investigate the ways to increase systemic bioavailability of curcumin by complexing agents.

Cyclodextrins (CDs) are cone-shaped cyclic oligosaccharides with a hydrophilic outer surface and a hydrophobic central cavity. Hydroxypropyl CD derivatives of β- and γ-CD (HP-β-CD, HP-γ-CD) have been of pharmaceutical interest because of the safety and efficiency for enhancing solubility of lipophilic drugs. There are more than 30 different pharmaceutical products containing CDs in the market worldwide. In the pharmaceutical products, CDs have been used as complexing agents to increase the aqueous solubility and stability of lipophilic drugs, and ultimately to increase the bioavailability of drugs (10). Most trials to increase curcumin solubility with CDs aimed to develop intravenous or oral delivery curcumin agents, but achieved moderate systemic bioavailability because of metabolism of curcumin. Therefore, development of CD-curcumin complex for pulmonary diseases is promising for pulmonary drug delivery.

6.2 Rationale and Significance

It is quite challenging for drug molecules to go through the biological membrane for being delivered into the drug-acting site. Although there are specialized transport systems in the plasma membranes, most drugs should permeate the membranes by passive diffusion as described in the Fick's diffusion law (equation 1): J is the net drug flux through a membrane; P, the membrane permeability of drug; and C, the aqueous drug concentration.

$$J = P \cdot C \qquad (1)$$

The membrane permeability, P is defined as the equation 2, where D is the diffusion coefficient of drug within the cell membrane; K, the partition coefficient of drug from the aqueous phase into membrane; and h, the effective thickness of the membrane.

$$P = \frac{D \cdot K}{h} \qquad (2)$$

Equations 1 and 2 indicate that for successful drug transport through the cell membrane, the drug molecule must have sufficient aqueous solubility (a high C value) as well as sufficient lipophilicity to be able to partition from the extracellular aqueous phase into the lipophilic membrane (high K value). Adjacent to the cell membrane surface is an unstirred water layer that acts as a diffusion barrier for rapidly permeated drugs with high lipophilicy. The thickness of this diffusion barrier and its significance in the overall barrier function of the epithelial cell depend on the physicochemical properties of the drug molecule. For the lipophilic drugs, diffusion through the water layer becomes the rate-limiting step in the absorption process.

There is much published evidence that hydrophilic CDs may enhance drug delivery through biological membranes without affecting their barrier function at optimal concentrations (11-13). These observations indicate that under normal conditions, neither the free hydrophilic CDs nor their drug complexes are able to permeate lipophilic biological membranes. The chemical structure of CDs (the large number of hydrogen donors and acceptors), large molecular weight (≥ 1,000 Da) and very low octanol/water partition coefficient (logP ≤ -3) are all characteristics of CDs that do not readily permeate biological membranes (10). Based on the reports, it has been suggested that CDs enhance drug delivery through biological membranes by increasing the availability of dissolved drug molecules in the aqueous layer in the vicinity to the lipophilic membrane surface (11, 14). According to the quasi-equilibrium model proposed by A. Dahan *et al.*, CDs solubilize the water-insoluble drug molecules in an aqueous vehicle and enhance the drug permeation through an aqueous diffusion layer on the cell surface by decreasing the

thickness of unstirred water layers (15). CDs can only act as drug penetration enhancers when permeation through the unstirred water layer contributes to the overall barrier function of the cell membrane (P_{aq} (aqueous permeability) $\leq$ P_m (membrane permeability)). Since the excessive amount of CDs is more than is needed to dissolve the drug, it will hamper drug permeation through the membrane (15, 16). It is of utmost importance to optimize CD concentrations in the complex formulations. Appropriate settings of *in vitro* cell model and *in vivo* model are important to test the optimal CD-drug formulations. Acute lung injury (ALI) is known as a pulmonary disease with high mortality and no effective treatment. With the high potential therapeutic activity of curcumin, the study of curcumin formulations in the cell cultures, lung tissues, and animal model has high impacts on the lung complications with inflammation including ALI.

Many studies have indicated that curcumin might have anti-inflammatory effects by modulating signal transduction processes related to inflammatory responses. Curcumin is known to be involved in the suppression of nuclear factor-kappa B (NF-κB) activation (17), resulting in COX-2 and iNOS inhibition and inhibiting the inflammatory process and tumorigenesis (18). Based on the relevant importance of CD-curcumin complexes as promising drugs, herein, we focused on the *in vitro* transport studies of CD-curcumin complexes using the Calu-3, the representative airway epithelial cell model to investigate the enhancing effects of CDs on transcellular transport and cellular uptake of curcumin. In addition to our cell-based permeability studies, our collaborators examined the therapeutic effects of CD-curcumin complexes in the lung inflammatory model.

6.3 Abstract

Local or systemic inflammation can result in acute lung injury (ALI) and is associated with capillary leakage, reduced lung compliance, and hypoxemia. Curcumin, a plant-derived polyphenolic compound, exhibits potent anti-inflammatory properties, but its poor solubility and limited oral bioavailability reduce its therapeutic potential. A novel curcumin formulation (CDC) was developed by complexing the compound with hydroxypropyl γ-cyclodextrin (CD). This results in greatly enhanced water solubility and stability that facilitates direct pulmonary delivery. *In vitro* studies demonstrated that CDC increased curcumin association with and transport across Calu-3 human airway epithelial cell monolayers compared to uncomplexed curcumin solubilized using DMSO or ethanol. Importantly, Calu-3 cell monolayer integrity was preserved after CDC exposure, while it was disrupted by equivalent uncomplexed curcumin solutions. We then tested whether direct delivery of CDC to the lung would reduce severity of ALI in a murine model. Fluorescence microscopic examination revealed association of curcumin with cells throughout the lung. Administration of CDC following LPS attenuated multiple markers of inflammation and injury, including pulmonary edema and neutrophils in bronchoalveolar lavage (BAL) fluid and lung. CDC also reduced oxidant stress in the lungs and activation of the pro-inflammatory transcription factor NF-κB. These results demonstrate the efficacy of CDC in a murine model of lung inflammation and injury and support the feasibility of developing a lung-targeted curcumin-based therapy for the treatment of patients with ALI.

6.4 Introduction

Acute lung injury (ALI) can result from a variety of pulmonary and extra-pulmonary insults and is characterized by capillary leakage with resulting pulmonary edema and hypoxemia (19). In the early acute phase, ALI exhibits severe neutrophil-rich alveolar inflammation (20) and associated oxidant stress (21). The result is epithelial and endothelial injury that increases permeability and impairs fluid clearance. Mortality remains high and there is no effective pharmacotherapy (22). Novel therapies for ALI are therefore urgently needed.

Curcumin, a polyphenolic compound from the rhizome of the *Curcuma longa* plant commonly known as turmeric, has been shown to exhibit a number of beneficial effects (23) that are exerted through a wide variety of signaling pathways (24-27). These effects include potent anti-inflammatory and antioxidant activities. Although use of curcumin appears potentially attractive in a number of disease states, clinical applications have been restricted because of its limited water solubility and oral bioavailability make it difficult to achieve therapeutically useful concentrations. For example, Garcea *et al.* found plasma concentrations only in the low nanomolar range following oral doses of 450 to 3,600 mg/d for 1 week (28). Others have similarly observed very low or undetectable plasma concentrations following doses up to 8 g/d or 12 g as a single dose (29, 30). Oral bioavailability of curcumin is similarly limited in the mouse, with plasma concentrations in the low nanomolar range following daily doses of 300 mg/kg by oral gavage (31).

We have recently developed a stable, water-soluble formulation of curcumin (CDC) in which the compound is complexed with hydroxyalkyl-substituted γ-

cyclodextrin (32). This formulation can be administered in ways not feasible with free curcumin, including delivery directly to the lung. Direct pulmonary administration is particularly attractive for lung diseases such as ALI because it bypasses the systemic circulation, thus reducing the potential for both metabolic breakdown and unwanted systemic effects. This route of administration also directly targets the drug to the site of therapeutic action. Direct pulmonary delivery is further supported by the canine pharmacokinetic study reported here, which demonstrates rapid plasma elimination of curcumin following intravenous (IV) CDC administration. However, it is possible that complexation of curcumin with cyclodextrins may alter the activity of the compound and impair cell penetration. We therefore tested the ability of CDC to penetrate and permeate human airway-derived epithelial cells, and determined whether intratracheally (IT) instilled CDC reduced inflammation and injury in a murine model of ALI induced by lipopolysaccharide (LPS).

6.5 Materials and Methods

Cell Culture. Cell culture methods are described in the Appendix D.

Curcumin Transport across the Calu-3 Cell Monolayer. A more detailed description of these methods is provided in the Appendix D.

Evaluation of Cell-associated Curcumin. Methods for qualitative and quantitative determination of curcumin associated with Calu-3 cells are described in the Appendix D. Cell-associated curcumin was detected with the FITC channel of an epifluorescence microscope, as previously described (33-35).

Animals. Male C57BL/6 mice at 6-8 wk of age were obtained from Jackson Laboratories (Bar Harbor, ME). Beagles were purchased from commercial kennels and raised at the Fred Hutchinson Cancer Research Center (FHCRC). All experimental animal care and treatments followed the guidelines established by the University of Michigan, Atlanta VA Medical Center, and FHCRC Committees on Use and Care of Animals.

LPS and Curcumin Administration. Mice were anesthetized with 50 mg/kg ketamine and 5 mg/kg xylazine, administered via intraperitoneal injection. A tracheotomy was performed and mice were injected IT with 50 μg/50 μl of *E. coli* LPS O111:B4 (Sigma-Aldrich; St. Louis, MO) or vehicle (PBS). Two hours later they received 30 μg/50 μl of curcumin as CDC or vehicle (CD).

Bronchoalveolar Lavage (BAL) Fluid Protein and Cell Count. BAL fluid was collected by flushing 3 × 1 ml of PBS into the lung via the tracheal cannula. The BAL fluid was centrifuged at 500 × g, 4°C for 5 min. The supernatant was analyzed for total protein using the BCA Protein Assay Kit (Pierce; Rockford, IL). Pelleted cells were then resuspended in 1 ml of PBS. Total cell number was counted by hemocytometer and a differential cell count was performed by cytospin staining with Diff-Quik (Scientific Products; McGaw Park, IL).

Nuclear Protein Preparation and NF-κB (p65) Transcription Factor Assay. Nuclear protein from lung tissue was isolated using a nuclear protein extraction kit (Cayman Chemical; Ann Arbor, MI). NF-κB activity was measured using the ELISA-based NF-κB (p65) Transcription Factor Assay kit (Cayman Chemical).

Wet:Dry Weight Ratio and Lung Histology. These methods are described in the Appendix D.

Measurement of Oxidant Stress. H_2O_2 production in lung tissue was determined using the Amplex Red Hydrogen Peroxide Assay Kit (Molecular Probes; Eugene, OR) according to the manufacturer's direction. The fluorescence intensity of samples and standards was measured in a plate reader (PerkinElmer; Waltham, MA) with an excitation at 560 nm and emission at 590 nm. The concentrations of nitrite/nitrate and malondialdehyde (MDA) in lung homogenates were measured using commercially available colorimetric assay kits (Cayman Chemical), according to the manufacturer's instruction.

Statistical Analysis. Data are presented as means ± SD. For the sample analyses, Tukey's multiple comparison test was used following ANOVA using GraphPad Prism 5.03 (GraphPad Software; LaJolla, CA). *P* values < 0.05 were considered statistically significant.

6.6 Results

6.6.1 Curcumin Association with and Transport by Human Lung Epithelial Cells

The local absorption, tissue distribution and intracellular accumulation of drug molecules can be a critical determinant of drug efficacy. The epithelial lining of the lung serves as a barrier preventing the absorption of inhaled substances, thus potentially blocking the ability of inhaled drugs to reach the underlying endothelial cells and

interstitial spaces where inflammatory cells can accumulate. The ability of epithelial cells to take up and transport curcumin *in vitro* was therefore used to assess whether the CDC formulation may be adequate as an ALI treatment. For this purpose, we used a standard human lung epithelial cell line, Calu-3 cells, grown in an air-liquid interface system that resembles the natural conditions in the lungs (36). Both apical-to-basolateral (AP→BL) and basolateral-to-apical (BL→AP) transport of CDC solutions in HBSS transport buffer were examined over a range of therapeutically relevant concentrations (0 – 200 μM). For comparison, we conducted similar studies using a standard, commercially available curcumin diluted from stock solutions prepared in DMSO (DMSO-C) or ethanol (EtOH-C). We found that with CDC formulations at 200 μM, curcumin was transported across intact cell monolayers at rates as high as 22×10^{-5} nmol/sec. At the equivalent curcumin concentration, DMSO-C or EtOH-C showed slightly higher mass transport rates (Figure 1A) but cell monolayers were disrupted (see below). Observed curcumin mass transport rates were concentration-dependent and were higher in the AP→BL than the BL→AP transport direction.

The cellular permeability coefficient (P_{eff}), a parameter describing mass transport rate normalized by donor initial concentration and monolayer area, for the AP→BL direction was maximal at 50 μM and appeared to decrease with increasing curcumin concentrations in the donor compartment, suggesting a complex transport pathway (Figure 1B, top). P_{eff} in the BL→AP direction was much lower than in the AP→BL direction (Figure 1B, bottom), consistent with a cellular mechanism selectively facilitating passage of curcumin in the AP→BL direction. P_{eff} in the BL→AP direction was relatively constant at different donor drug concentrations with no evidence of

saturation. P_{eff} for CDC was greater than that for either DMSO-C or EtOH-C at 50 μM in the AP→BL direction and at both concentrations in the BL→AP direction.

In all studies, Lucifer Yellow (LY) transport was also measured. As a hydrophilic, membrane impermeant compound (MW 457), LY is commonly used as a marker for paracellular transport (37). The calculated P_{eff} of LY was very low ($P_{eff,\ AP\rightarrow BL}$: 8.21×10^{-8} cm/sec ($\pm2.99\times10^{-8}$), $P_{eff,\ BL\rightarrow AP}$: 4.69×10^{-8} cm/sec ($\pm2.72\times10^{-8}$)), thus confirming integrity of the cellular monolayers for the transport experiments. In addition, monolayer integrity before and after transport studies was independently established by measurement of TEER. TEER values were unchanged in 50 μM CDC in the AP→BL direction, and in 50 and 100 μM CDC in the BL→AP direction, although TEER decreased slightly with increasing curcumin concentration. The 200 μM (donor) concentrations of DMSO-C and EtOH-C decreased TEER values from 422±6 to 176 ±12 $\Omega\cdot cm^2$ and from 418±3 to 152±9 $\Omega\cdot cm^2$, respectively, in the AP→BL direction, suggesting disruption of monolayer integrity. In 200 μM CDC, TEER values changed from 423±5 to 351 ±13 $\Omega\cdot cm^2$. Nevertheless, TEER values remained >350 $\Omega\cdot cm^2$, consistent with preservation of monolayer integrity.

We next assessed the extent to which Calu-3 cells accumulated curcumin in the CD solutions. First, inserts were examined with the 10 × objective of a fluorescence microscope following incubation with the nucleus-specific molecular probe Hoechst 33342 (10 μg/ml). Cell-associated curcumin was detected in the FITC channel and nuclei were visualized in the DAPI channel. Microscopic examination showed concentration-dependent cell association of curcumin, which was greater following exposure on the apical side than on the basolateral side (Figure 2A). Our methods cannot determine

whether this cell association represents extracellular attachment or intracellular uptake, although we find it is not removed by rinsing.

To quantify cell-associated curcumin, additional Calu-3 cell monolayers on inserts were incubated for 90 min with 1% Triton X-100 and the mass of curcumin extracted from the cell monolayers was measured. This value was normalized by the number of cells on the membranes (detached by trypsinization) and plotted as cell-associated mass per cell (Figure 2B, C). Cell-associated curcumin mass increased in proportion to the extracellular curcumin concentration under all conditions examined (Figure 2B). Significantly greater curcumin mass was observed following apical exposure to CDC than to DMSO-C or EtOH-C, but curcumin mass associated with cells from the basolateral compartment was nearly similar under all conditions tested (Figure 2B, C).

Because absorption of inhaled drug formulations involves a transient drug exposure, the tightness of cell-to-cell contacts as measured by the TEER value is a key, highly sensitive indicator of epithelial barrier function. Since exposure to DMSO-C or EtOH-C concentrations $\geq$ 100 μM led to significant changes in TEER values after transport, we assessed the effect of CDC, DMSO-C, and EtOH-C on cell monolayer integrity using microscopy over the course of the transport studies. Following CDC exposure, microscopic analysis revealed no evidence of cell-cell separation or detachment under any condition (Figure 2A). With DMSO-C or EtOH-C, however, evidence of cell rounding and cell-cell disruption appeared at 100 μM and was prominent at the 200 μM level for AP $\rightarrow$BL transport. Cell monolayer integrity was compromised at 200 μM for BL$\rightarrow$AP transport whether the initial solvent was DMSO or ethanol (Figure 2A).

6.6.2 Pharmacokinetics and Toxicology Following Systemic CDC Administration

CDC was administered IV to beagle dogs at doses as high as 10 mg/kg twice daily for 14 days, with no adverse effects being observed in any dog (Supplemental Material; Appendix D). Pharmacokinetics of curcumin was also assessed. Both curcumin and its principle metabolite, tetrahydrocurcumin, disappeared rapidly and plasma concentrations were undetectable after 30 min. After repeated daily administration, tetrahydrocurcumin sulfate became a major metabolite, peaking at 30 min and largely disappearing by 60 min. This rapid plasma clearance of curcumin following systemic CDC administration supports our choice of pulmonary administration for further *in vivo* studies.

6.6.3 Curcumin Deposition in the Lungs

To test the efficacy of pulmonary CDC delivery in a relevant animal model of ALI, we extended our *in vitro* studies by determining the extent of curcumin accumulation on or in lung cells following intratracheal CDC administration. One hour after intratracheal administration of CDC (Figure 3, bottom) or vehicle (Figure 3, top) the lungs were removed, fixed, and sectioned. Sections were examined by light microscopy and by fluorescence microscopy at curcumin-specific emission and detection wavelengths. Some intrinsic autofluorescence was observed at these wavelengths, but fluorescence was much brighter following curcumin administration and was prominent throughout most of the lung. These observations support successful delivery to cellular targets in this organ.

6.6.4 Inhibition of LPS-induced Lung Inflammation and Injury by CDC Administration

Since our data demonstrated that the potent anti-inflammatory agent curcumin is extensively taken up by cells throughout the lung following CDC administration, we proceeded to test whether CDC could inhibit lung inflammation induced by LPS, a well-characterized murine model of ALI. LPS was administered IT to mice, followed by CDC (30 μg) or vehicle 2 hours later. The CDC dose was based on preliminary dose response studies (data not shown). Four hours after the CDC dose, BAL fluid was collected and the lungs were prepared for microscopic examination of lung injury. Both cell counts (Figure 4A, left) and microscopy (Figure 4B) showed notably fewer cells in BAL fluid from CDC-treated than from vehicle-treated mice. Furthermore, whereas a majority of the cells in BAL fluid of vehicle-treated mice were inflammation-related neutrophils, this proportion was markedly reduced following CDC treatment (Figure 4A, right).

Activation of specific transcription factors, notably NF-κB, and consequent production of pro-inflammatory cytokines and other molecules is a prominent feature of inflammation. We next tested whether reduced inflammation is reflected in downregulation of NF-κB activity. Nuclear protein was isolated from the lungs of mice treated with LPS and CDC or vehicle and NF-κ B activity was determined. The increase in activity following LPS treatment was significantly reduced by CDC (Figure 4C). Inflammation and activation of NF-κB upregulates production of reactive oxygen species and thus oxidant stress. Measured markers of LPS-induced oxidant stress (H_2O_2 production, nitrite/nitrate concentration, and malonaldehyde as a measure of lipid peroxidation) were also attenuated by CDC treatment (Figure 4C).

To further assess the ability of CDC to inhibit LPS-induced lung injury, we measured the amount of protein in the BAL fluid. Protein was significantly increased by LPS, but this increase was largely blocked by CDC treatment (Figure 5A). We also examined changes in the ratio of wet:dry weight in lung tissue, a quantitative measure of vascular permeability and resulting edema (38). We found that LPS treatment produced significant increases in the wet:dry weight ratio and CDC attenuated this increase (Figure 5A). Histopathological examination of H&E-stained lung tissue also showed reductions in inflammatory markers following CDC treatment (Figure 5B).

6.7 Discussion

Clinical use of curcumin has been limited by its low solubility and poor oral bioavailability. Delivery by inhalation for treatment of pulmonary disease likewise appears infeasible, since the organic solvents in which it must be dissolved are toxic to the lung. To overcome these drug delivery obstacles, we developed a new formulation of curcumin in which it is complexed with hydroxypropyl ether derivatives of cyclodextrin (CD). This formulation of curcumin is stable, highly water-soluble, bioavailable, and easily produced (32, 39, 40). This permits administration by either the IV or inhalation routes at doses that have been shown to elicit anti-inflammatory effects. However, preliminary studies in beagle dogs (Supplemental Material; Appendix D) showed that CDC is rapidly cleared from the circulation following IV administration. Furthermore, oral bioavailability of curcumin is low due to metabolism in the intestine (41), which would presumably affect oral CDC as well. These limitations make inhalation a viable

route of administration for CDC, particularly for the targeted treatment of inflammatory lung disease.

In this study we delivered CDC IT to ensure that the dose was delivered to the lungs. Pulmonary delivery of a nebulized preparation via the oropharyngeal cavity may be more directly relevant to human use, but in rodents (obligate nose breathers) most of the drug deposits in the nasal passages and upper respiratory tract (42). Therefore, intratracheal administration is the preferred method for proof-of-concept studies in which accurate dosage is required.

One major advantage of the CDC formulation is ease of preparation. Curcumin is dissolved at high pH, hydroxypropyl-γ-cyclodextrin is added at a slight molar excess, and after a brief period of agitation the solution is neutralized. Previous attempts to solubilize curcumin with cyclodextrin or its derivatives did not use elevated pH (39). These formulations required large molar excesses of cyclodextrin and achieved much lower concentrations of solubilized curcumin. As previously reported (32), the CDC formulation is also much more stable in solution than those formulations. A wide variety of other methods also have been used to improve curcumin solubility. These include micro- and nano-emulsions, liposomes, several types of encapsulated nanoparticles, and self-microemulsifying drug delivery systems, as well as surfactants and solvents (40). Many of these formulations have exhibited a degree of success in preclinical studies (43). However, all of these approaches involve more complex procedures than those used to prepare CDC and many produce smaller incremental improvements in curcumin solubility (40). Furthermore, since these formulations were developed for IV use or with

the goal of improving oral bioavailability, their suitability for pulmonary delivery remains unclear.

Our present studies show that curcumin transport is promoted by CDC in lung epithelial cells *in vitro* and by lung tissues *in vivo*. The Calu-3 cell line is a well-established cell model for the quantitative evaluation of mechanisms and pharmacokinetics (*e.g.,* drug absorption, toxicity) of formulations of lung-targeted or inhaled molecules and has been used to characterize *in vitro-in vivo* associations for various drug molecules (44-47). Our findings of increased curcumin association with Calu-3 cells agrees with previous reports indicating that CD formulations promote uptake of highly insoluble drugs in other *in vitro* cell models (32). Cyclodextrins have been previously tested in nebulized, inhaled drug formulations, with some reports indicating that CDs enhance pulmonary penetration (48-50). For these experiments, Calu-3 cell monolayers have been used as a standard reference cell line for establishing the transport properties of drug formulations (13, 50, 51). However, previous reports indicated that CDs promoted delivery, not by directly enhancing permeability or cell association, but by acting as a reservoir for drug and promoting its dispersion (52-54). Since CDs are cell impermeant (48, 52, 53), it is plausible that curcumin-CD complexes might inhibit the intracellular uptake of curcumin. Nevertheless, our *in vitro* and *in vivo* experiments demonstrated that CD increased the amount of delivered and cell-associated curcumin and its transcellular permeability, with an associated enhancement of efficacy in experimental ALI.

The CD-enhanced delivery of curcumin to lung cells, together with the well-known anti-inflammatory and antioxidant effects of curcumin (23), led us to test the

ability of CDC to reduce inflammation in a murine model of ALI. ALI is associated with influx of inflammatory cells, especially neutrophils, into the lungs, and we found that CDC administration following induction of ALI significantly reduced both total cell and neutrophil count. In addition, CDC downregulated activity of the pro-inflammatory transcription factor NF-κB and reduced oxidant stress. This finding provides *in vivo* confirmation of previous *in vitro* observations that CDC reduces NF-κB activity more effectively than uncomplexed curcumin (32). In other settings, curcumin has been shown to downregulate the activity of not only NF-κB but also the pro-inflammatory transcription factors AP-1 (55) and HIF-1α (56). Production of pro-inflammatory cytokines, and thus subsequent inflammatory changes, are largely dependent on activation of these transcription factors, so the decreased NF-κB activity provides a molecular mechanism for the observed decrease in inflammatory markers.

To our knowledge, there has been no previous demonstration that any curcumin formulation can effectively treat established ALI, although several previous studies have shown that curcumin can at least partially prevent ALI when administered prior to the triggering event. In an LPS-induced model of ALI, Lian *et al.* found that intravenous curcumin dissolved in DMSO administered to rats 30 min prior to LPS reduced ALI severity (57). Olszanecki *et al.* administered curcumin intraperitoneally 2 hours before intraperitoneal LPS (58). They found that curcumin pretreatment decreased sequestration of leukocytes by the lung, and presented evidence that this was mediated by induction of heme oxygenase-1. We also found that administration of intraperitoneal, but not oral, curcumin reduced the severity of inflammation following bleomycin-induced lung injury (31).

Interestingly, in Calu-3 cells we observed that epithelial cell monolayer integrity was intact after transient exposures to CDC concentrations up to 200 μM, although monolayer integrity was visibly disrupted with lower doses of DMSO-C or EtOH-C. Given that the epithelial cell barrier is dependent on monolayer integrity, CDC appears to be safer than the DMSO or ethanol solutions commonly used to solubilize curcumin. Perhaps most importantly, preliminary toxicological studies of CDC in dogs similarly provided no evidence of adverse effects following doses up to 20 mg/kg-d for 14 days (Supplemental Material; Appendix D).

Ours appears to be the first study of any curcumin formulation administered directly to the pulmonary system. Although we did not systematically investigate the toxicology of IT-delivered CDC, no drug-attributable toxicity was apparent in physiological parameters or on histopathological examination even when the CDC concentration was increased to 600 μM (data not shown). Human studies of curcumin have revealed no adverse effects other than diarrhea following very high oral doses (30). By contrast, adverse effects are frequent with commonly used systemic anti-inflammatory agents. In ALI and acute respiratory distress syndrome (ARDS), results with systemic anti-inflammatory agents have been disappointing. Methylprednisolone in ARDS (59), as well as ketoconazole (60) and lisofylline (61) in mixed ALI/ARDS patient populations, have all proven ineffective. This ineffectiveness may reflect the adverse effects of these drugs, including interference with wound healing. Significantly, dysfunctional wound healing is thought to be a major pathophysiological factor in late-stage ARDS, and methylprednisolone appears to decrease survival when started more than 14 days after disease onset (59). Curcumin, by contrast, has been shown to promote

wound healing (23). Both the greater safety of CDC and its delivery directly to the target organ support the possibility that CDC may prove effective where other anti-inflammatory agents have not.

ALI remains a disease with high mortality and no effective treatment. Our results indicate that direct lung delivery of CDC is safe and effective in a murine model of ALI and its effectiveness may be attributable to its association with the lung epithelium. The attractiveness of CDC is further increased by the ease and simplicity with which it can be produced. These promising early results support the potential of CDC as a possible therapy for human ALI and other inflammatory lung diseases.

6.8 Acknowledgements

This work was supported by National Institutes of Health grants AI079539 (R.C.R.), HL093196 (R.C.R.), and GM078200 (G.R.R.).

6.9 Figures

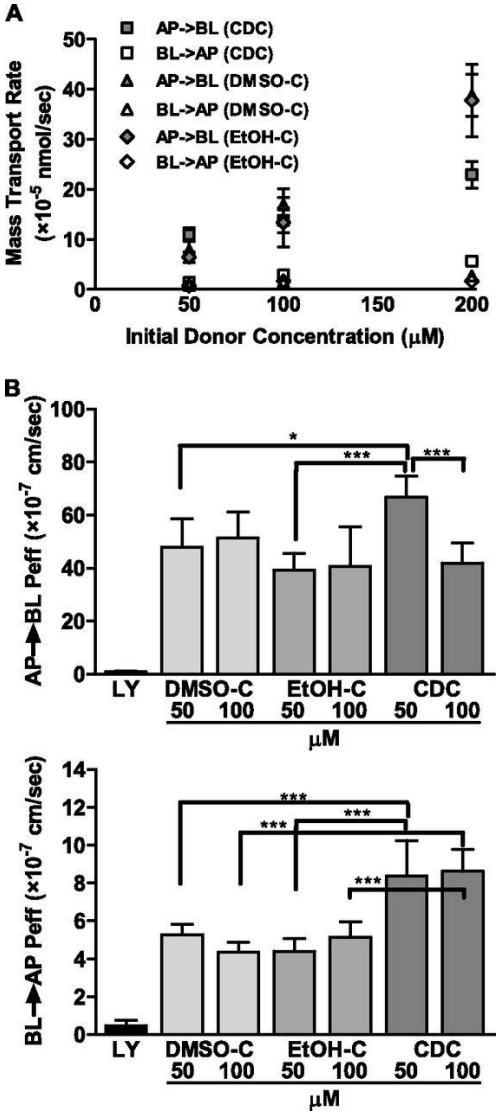

Figure 6-1. CDC promotes curcumin transport across lung epithelial cells.

Calu-3 cell monolayers were grown on Transwell inserts. CDC, DMSO-C, EtOH-C, or LY was added to HBSS transport buffer in either the apical (AP) or basolateral (BL) compartment. The contralateral compartment was sampled at intervals and curcumin or LY concentrations were measured by fluorescence using a plate reader set to 485 nm (EX)/540 nm (EM). (A) Mass transport rate as a function of initial donor concentration of CDC, DMSO-C, or EtOH-C for the AP→BL and BL→AP directions. (B) The P_{eff} for the AP→BL (top) or BL→AP (bottom) directions of LY (paracellular marker, 1 mM), DMSO-C, EtOH-C, and CDC as a function of initial donor concentration. $n = 6$; $^{*}P < 0.05$; $^{***}P < 0.001$.

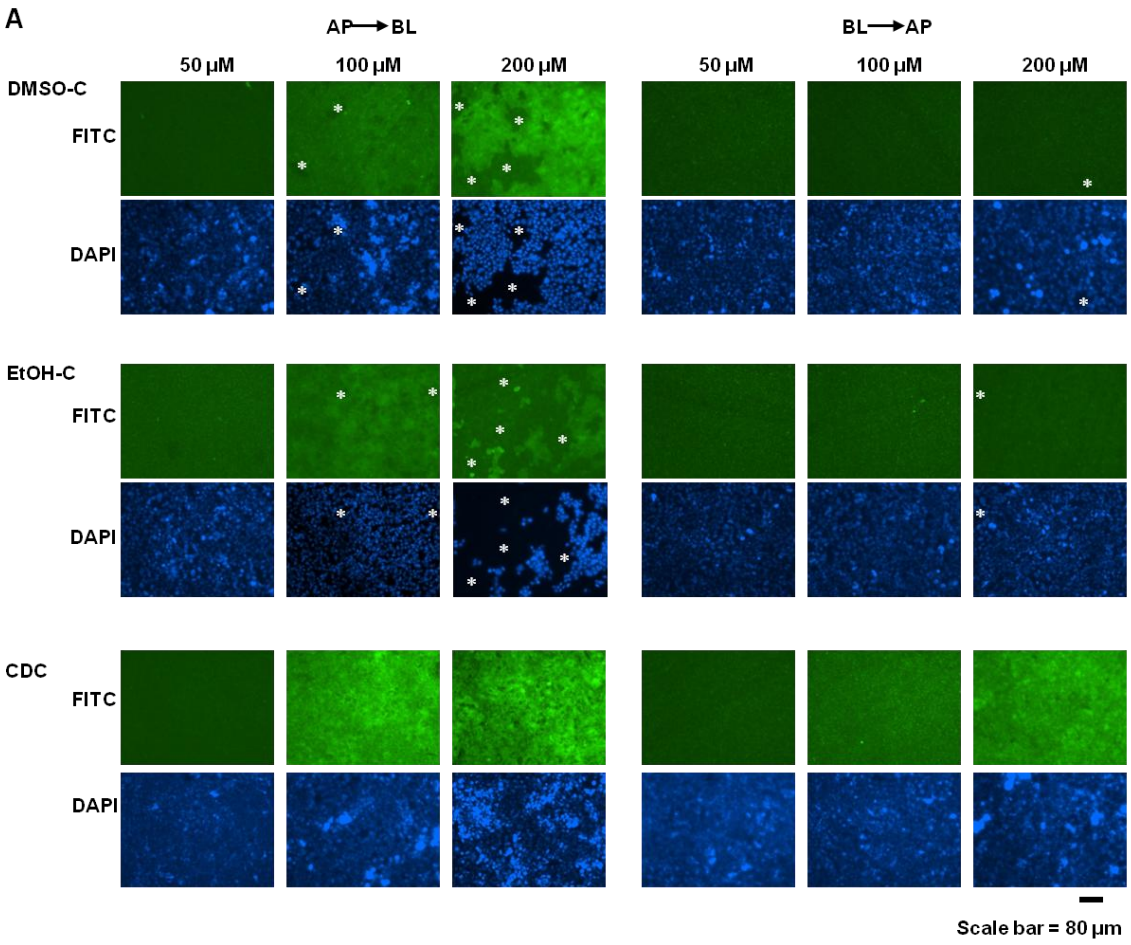
A
AP→BL
BL→AP
50 μM
100 μM
200 μM
50 μM
100 μM
200 μM
DMSO-C
FITC
DAPI
EtOH-C
FITC
DAPI
CDC
FITC
DAPI
Scale bar = 80 μm

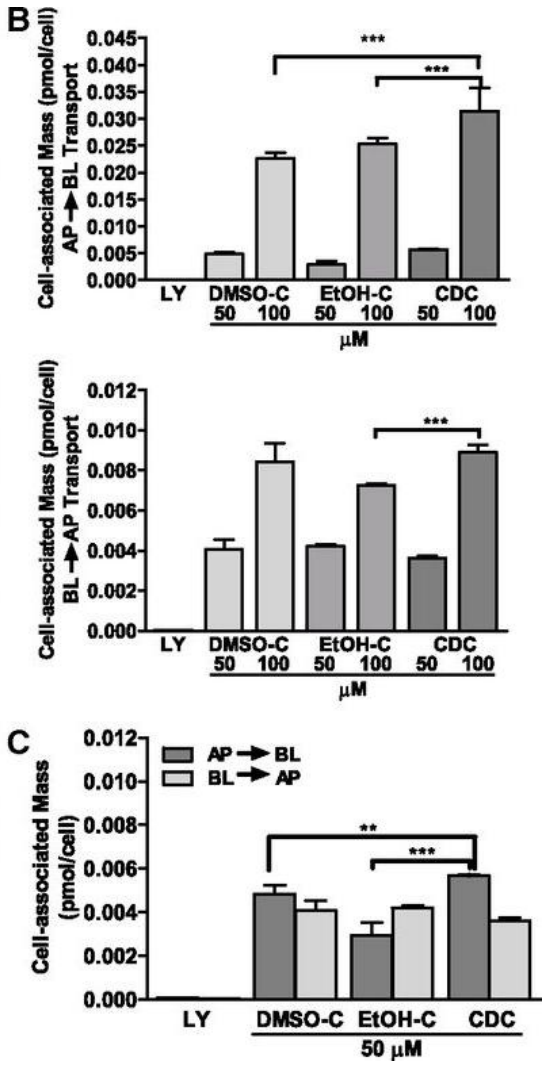

Figure 6-2. CDC promotes curcumin association with lung epithelial cells.

Calu-3 cell monolayers on Transwell inserts were exposed to CDC, DMSO-C, or EtOH-C in either the apical (AP→BL) or basolateral (BL→AP) compartments for 180 min with shaking at 37ºC in a 5% CO_2 incubator. (A) The inserts were then washed and incubated for another 30 min with the nucleus-specific dye Hoechst 33342 (10 μg/ml) in the apical compartment and dye-free HBSS transport buffer in the basolateral compartment. The cell monolayers were examined with a Nikon TE 2000 fluorescence microscope (10 × objective). Curcumin was visualized in the FITC channel and nuclei in the DAPI channel. Regions where cells have detached or monolayer integrity is visibly compromised are indicated with an asterisk. Scale bar of 80 μm is displayed below . Representative images are shown from 3 independent experiments. (B, C) Following exposure, the cells were washed and cell-associated curcumin extracted with 1% Triton X-100. Extracted curcumin was quantitated (mass per cell) by fluorescence using a plate reader. Amounts of the paracellular marker LY are also shown. (B) Cell-associated curcumin as a function of initial donor concentration for AP→BL (top) and BL→AP (bottom) transport. (C)

Cell-associated curcumin as a function of transport direction at 50 μM. $n = 6$; $^{**}P < 0.01$; $^{***}P < 0.001$.

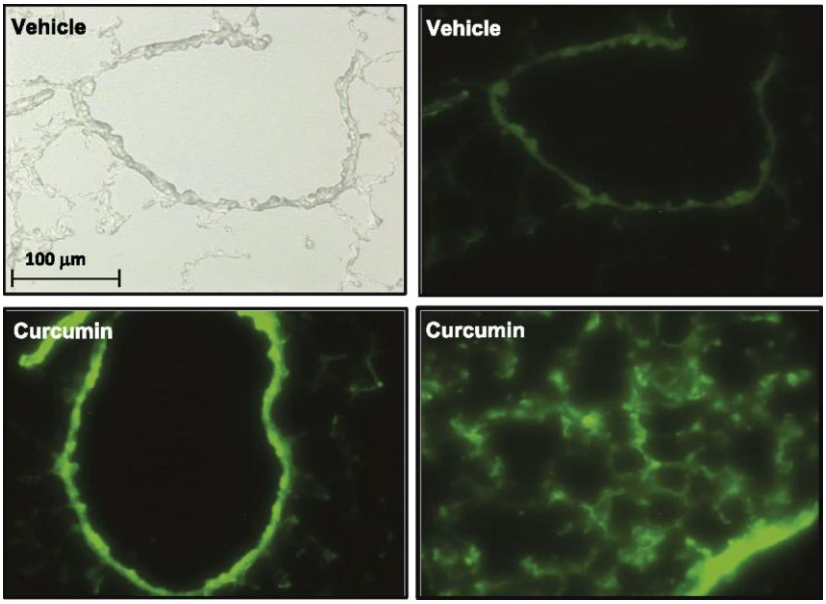

Figure 6-3. CDC fluorescence is associated with lung cells *in vivo*.

C57BL/6 mice received CDC (30 μg) or vehicle intratracheally. One hour later the lungs were embedded in O.C.T. compound, frozen and sectioned. Sections were examined by light (top left) or fluorescence microscopy with curcumin visualized in the FITC channel. The bottom right image shows lung parenchyma; other images are cross-sections of airways. Representative images shown from 3 independent experiments.

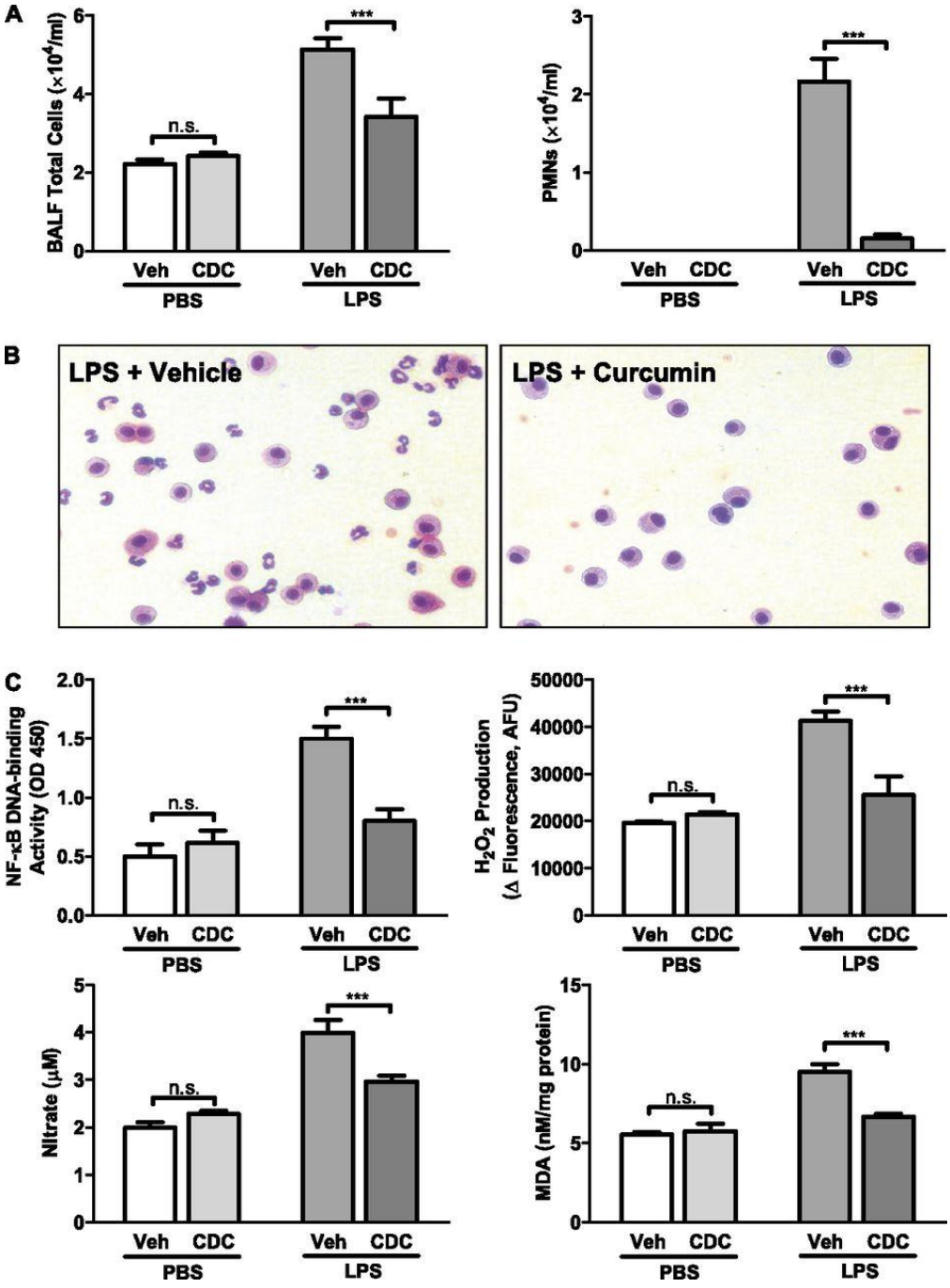

Figure 6-4. CDC reduces LPS-induced lung inflammation.

ALI was induced by intratracheal administration of LPS (50 μg). CDC (30 μg) or vehicle (CD) was administered two hours later. BAL fluid was collected and lung excised after 4 hours. (A) BAL fluid was centrifuged at 500 × *g* for 5 min. Pelleted cells were washed and cellular content of the resuspended pellet was determined by cytospin. (B) Cells from BAL fluid were stained with Diff-Quick and examined microscopically. (C) Nuclear protein was isolated from lungs and NF-κB activity was determined using an ELISA-based assay kit (top left). Lung tissue was homogenized and oxidant stress was assessed

by measuring H_2O_2 production (top right), nitrite/nitrate (bottom left), and malonaldehyde (bottom right) using commercially available kits. n = 16-18 mice/group; ***$P < 0.001$.

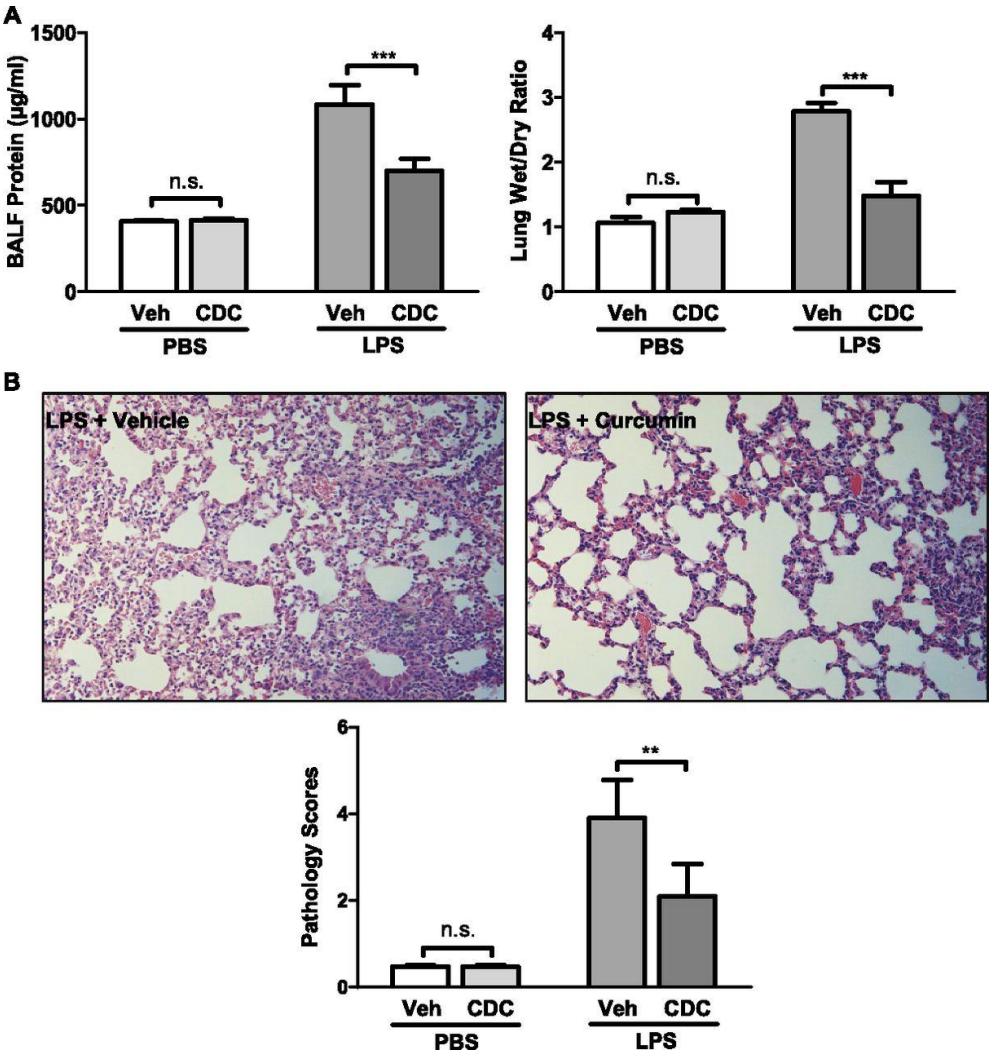

Figure 6-5. CDC attenuates lung injury and edema following LPS administration.

ALI was induced by intratracheal administration of LPS (50 µg). CDC (30 µg) or vehicle (CD) was administered two hours later and BAL fluid was collected after 4 hours. (A) Cells in BAL fluid were pelleted by centrifugation, after which protein content of the supernatant was determined as a marker of lung injury (left). After BAL fluid was collected the superior lobe of the left lung was excised and immediately weighed. It was then dried in a 60°C incubator for 24 hours and weighed again. The ratio of wet:dry weight was determined as an index of edema (right). (B) Lungs were fixed, sectioned, and stained with hematoxylin and eosin. Representative sections were then examined microscopically (top). The degree of injury (pathology score) was scored according to the following scale: no injury = 1; injury to 25% of the field = 2; injury to 50% of the field = 3; injury to 75% of the field = 4; diffuse injury = 5; (bottom). n = 16-18 mice/group; $^{**}P < 0.01$; $^{***}P < 0.001$.

6.10 Supporting Information Available

This material is published in *American Journal of Respiratory Cell and Molecular Biology* and supporting information (experimental methods and results with figures) is available in the Appendix D**.**

6.11 References

1. Araujo C, Leon L. Biological activities of Curcuma longa L. Memórias do Instituto Oswaldo Cruz. 2001;96(5):723-8.
2. Unchern S, editor. Curcumin: Promising antioxidant. 24 Congress on Science and Technology of Thailand, Bangkok (Thailand), 19-21 Oct 1998; 1998.
3. De R, Kundu P, Swarnakar S, Ramamurthy T, Chowdhury A, Nair GB, et al. Antimicrobial activity of curcumin against Helicobacter pylori isolates from India and during infections in mice. Antimicrobial agents and chemotherapy. 2009;53(4):1592-7.
4. Chainani-Wu N. Safety and anti-inflammatory activity of curcumin: a component of tumeric (Curcuma longa). The Journal of Alternative & Complementary Medicine. 2003;9(1):161-8.
5. Anand P, Kunnumakkara AB, Newman RA, Aggarwal BB. Bioavailability of curcumin: problems and promises. Molecular Pharmaceutics. 2007;4(6):807-18.
6. Ireson C, Orr S, Jones DJ, Verschoyle R, Lim C-K, Luo J-L, et al. Characterization of metabolites of the chemopreventive agent curcumin in human and rat hepatocytes and in the rat in vivo, and evaluation of their ability to inhibit phorbol ester-induced prostaglandin E2 production. Cancer Research. 2001;61(3):1058-64.
7. Cheng A-L, Hsu C-H, Lin J-K, Hsu M-M, Ho Y-F, Shen T-S, et al. Phase I clinical trial of curcumin, a chemopreventive agent, in patients with high-risk or pre-malignant lesions. Anticancer research. 2001;21(4B):2895.
8. Sharma RA, Euden SA, Platton SL, Cooke DN, Shafayat A, Hewitt HR, et al. Phase I Clinical Trial of Oral Curcumin Biomarkers of Systemic Activity and Compliance. Clinical Cancer Research. 2004;10(20):6847-54.
9. Vareed SK, Kakarala M, Ruffin MT, Crowell JA, Normolle DP, Djuric Z, et al. Pharmacokinetics of curcumin conjugate metabolites in healthy human subjects. Cancer Epidemiology Biomarkers & Prevention. 2008;17(6):1411-7.
10. Loftsson T, Brewster ME. Pharmaceutical applications of cyclodextrins: effects on drug permeation through biological membranes. Journal of Pharmacy and Pharmacology. 2011;63(9):1119-35.
11. Sinha V, Bindra S, Kumria R, Nanda A. Cyclodextrins as skin-penetration enhancers. Pharmaceutical technology. 2003;27(3):120-38.
12. Haeberlin B, Gengenbacher T, Meinzer A, Fricker G. Cyclodextrins—Useful excipients for oral peptide administration? Int J Pharmaceut. 1996;137(1):103-10.
13. Matilainen L, Toropainen T, Vihola H, Hirvonen J, Jarvinen T, Jarho P, et al. In vitro toxicity and permeation of cyclodextrins in Calu-3 cells. J Control Release. 2008;126(1):10-6.
14. Loftsson T, Masson M. Cyclodextrins in topical drug formulations: theory and practice. Int J Pharmaceut. 2001;225(1):15-30.
15. Dahan A, Miller JM, Hoffman A, Amidon GE, Amidon GL. The solubility–permeability interplay in using cyclodextrins as pharmaceutical solubilizers:

Mechanistic modeling and application to progesterone. J Pharm Sci-Us. 2010;99(6):2739-49.
16. Loftsson T, Sigfússon S, Sigurdsson H, Másson M. The effects of cyclodextrins on topical delivery of hydrocortisone: the aqueous diffusion layer. STP pharma sciences. 2003;13(2):125-31.
17. Plummer SM, Holloway KA, Manson MM, Munks RJ, Kaptein A, Farrow S, et al. Inhibition of cyclo-oxygenase 2 expression in colon cells by the chemopreventive agent curcumin involves inhibition of NF-kB activation via the NIK/IKK signalling complex. Oncogene. 1999;18(44):6013-20.
18. Aggarwal BB, Kumar A, Bharti AC. Anticancer potential of curcumin: preclinical and clinical studies. Anticancer Res. 2003;23(1A):363-98.
19. Matuschak GM, Lechner AJ. Acute lung injury and the acute respiratory distress syndrome: Pathophysiology and treatment. Mo Med. 2010;107(4):252-8.
20. Matute-Bello G, Frevert CW, Martin TR. Animal models of acute lung injury. Am J Physiol Lung Cell Mol Physiol. 2008;295(3):L379-99.
21. Ward PA. Oxidative stress: Acute and progressive lung injury. Ann N Y Acad Sci. 2010;1203:53-9.
22. Bosma KJ, Taneja R, Lewis JF. Pharmacotherapy for prevention and treatment of acute respiratory distress syndrome: Current and experimental approaches. Drugs. 2010;70(10):1255-82.
23. Maheshwari RK, Singh AK, Gaddipati J, Srimal RC. Multiple biological activities of curcumin: A short review. Life Sci. 2006;78(18):2081-7.
24. Chen Y-R, Tan T-H. Inhibition of the c-jun n-terminal kinase (jnk) signaling pathway by curcumin. Oncogene. 1998;17(2):173-8.
25. Gaedeke J, Noble NA, Border WA. Curcumin blocks multiple sites of the tgf-b signaling cascade in renal cells. Kidney Int. 2004;66(1):112-20.
26. Hu M, Du Q, Vancurova I, Lin X, Miller EJ, Simms HH, Wang P. Proapoptotic effect of curcumin on human neutrophils: Activation of the p38 mitogen-activated protein kinase pathway. Crit Care Med. 2005;33(11):2571-8.
27. Zhou Y, Zheng S, Lin J, Zhang QJ, Chen A. The interruption of the pdgf and egf signaling pathways by curcumin stimulates gene expression of pparg in rat activated hepatic stellate cell in vitro. Lab Invest. 2007;87(5):488-98.
28. Garcea G, Jones DJ, Singh R, Dennison AR, Farmer PB, Sharma RA, Steward WP, Gescher AJ, Berry DP. Detection of curcumin and its metabolites in hepatic tissue and portal blood of patients following oral administration. Br J Cancer. 2004;90(5):1011-5.
29. Jurenka JS. Anti-inflammatory properties of curcumin, a major constituent of curcuma longa: A review of preclinical and clinical research. Altern Med Rev. 2009;14(2):141-53.
30. Sharma RA, Gescher AJ, Steward WP. Curcumin: The story so far. Eur J Cancer. 2005;41(13):1955-68.
31. Smith MR, Gangireddy SR, Narala VR, Hogaboam CM, Standiford TJ, Christensen PJ, Kondapi AK, Reddy RC. Curcumin inhibits fibrosis-related effects in ipf fibroblasts and in mice following bleomycin-induced lung injury. Am J Physiol Lung Cell Mol Physiol. 2010;298(5):L616-25.

32. Yadav VR, Prasad S, Kannappan R, Ravindran J, Chaturvedi MM, Vaahtera L, Parkkinen J, Aggarwal BB. Cyclodextrin-complexed curcumin exhibits anti-inflammatory and antiproliferative activities superior to those of curcumin through higher cellular uptake. Biochem Pharmacol. 2010;80(7):1021-32.
33. Bisht S, Feldmann G, Soni S, Ravi R, Karikar C, Maitra A. Polymeric nanoparticle-encapsulated curcumin ("nanocurcumin"): A novel strategy for human cancer therapy. J Nanobiotechnology. 2007;5:3.
34. Schiborr C, Eckert GP, Rimbach G, Frank J. A validated method for the quantification of curcumin in plasma and brain tissue by fast narrow-bore high-performance liquid chromatography with fluorescence detection. Anal Bioanal Chem. 2010;397(5):1917-25.
35. Mohorko N, Repovs G, Popovic M, Kovacs GG, Bresjanac M. Curcumin labeling of neuronal fibrillar tau inclusions in human brain samples. J Neuropathol Exp Neurol. 2010;69(4):405-14.
36. Foster KA, Avery ML, Yazdanian M, Audus KL. Characterization of the calu-3 cell line as a tool to screen pulmonary drug delivery. Int J Pharm. 2000;208(1-2):1-11.
37. Lacombe O, Woodley J, Solleux C, Delbos JM, Boursier-Neyret C, Houin G. Localisation of drug permeability along the rat small intestine, using markers of the paracellular, transcellular and some transporter routes. Eur J Pharm Sci. 2004;23(4-5):385-91.
38. Wang Y, Phelan SA, Manevich Y, Feinstein SI, Fisher AB. Transgenic Mice Overexpressing Peroxiredoxin 6 Show Increased Resistance to Lung Injury in Hyperoxia. Am J Respir Cell Mol Biol. 2006:34(4):481-6.
39. Tonnesen HH, Masson M, Loftsson T. Studies of curcumin and curcuminoids. Xxvii. Cyclodextrin complexation: Solubility, chemical and photochemical stability. Int J Pharm. 2002;244(1-2):127-35.
40. Kumar A, Ahuja A, Ali J, Baboota S. Conundrum and therapeutic potential of curcumin in drug delivery. Crit Rev Ther Drug Carrier Syst. 2010;27(4):279-312.
41. Shoba G, Joy D, Joseph T, Majeed M, Rajendran R, Srinivas PS. Influence of piperine on the pharmacokinetics of curcumin in animals and human volunteers. Planta Med. 1998;64(4):353-6.
42. Southam DS, Dolovich M, O'Byrne PM, Inman MD. Distribution of intranasal instillations in mice: Effects of volume, time, body position, and anesthesia. Am J Physiol Lung Cell Mol Physiol. 2002;282(4):L833-9.
43. Bisht S, Maitra A. Systemic delivery of curcumin: 21st century solutions for an ancient conundrum. Curr Drug Discov Technol. 2009;6(3):192-9.
44. Forbes B. Human airway epithelial cell lines for in vitro drug transport and metabolism studies. Pharm Sci Technolo Today. 2000;3(1):18-27.
45. Mathia NR, Timoszyk J, Stetsko PI, Megill JR, Smith RL, Wall DA. Permeability characteristics of calu-3 human bronchial epithelial cells: In vitro-in vivo correlation to predict lung absorption in rats. J Drug Target. 2002;10(1):31-40.
46. Tronde A, Norden B, Marchner H, Wendel AK, Lennernas H, Bengtsson UH. Pulmonary absorption rate and bioavailability of drugs in vivo in rats: Structure-

absorption relationships and physicochemical profiling of inhaled drugs. J Pharm Sci. 2003;92(6):1216-33.
47. Ehrhardt C, Fiegel J, Fuchs S, Abu-Dahab R, Schaefer UF, Hanes J, Lehr CM. Drug absorption by the respiratory mucosa: Cell culture models and particulate drug carriers. J Aerosol Med. 2002;15(2):131-9.
48. Uekama K, Hirayama F, Irie T. Cyclodextrin drug carrier systems. Chem Rev. 1998;98(5):2045-76.
49. Loftsson T, Jarho P, Masson M, Jarvinen T. Cyclodextrins in drug delivery. Expert Opin Drug Deliv. 2005;2(2):335-51.
50. Tewes F, Brillault J, Couet W, Olivier JC. Formulation of rifampicin-cyclodextrin complexes for lung nebulization. J Control Release. 2008;129(2):93-9.
51. Salem LB, Bosquillon C, Dailey LA, Delattre L, Martin GP, Evrard B, Forbes B. Sparing methylation of beta-cyclodextrin mitigates cytotoxicity and permeability induction in respiratory epithelial cell layers in vitro. J Control Release. 2009;136(2):110-6.
52. Arima H, Yunomae K, Miyake K, Irie T, Hirayama F, Uekama K. Comparative studies of the enhancing effects of cyclodextrins on the solubility and oral bioavailability of tacrolimus in rats. J Pharm Sci. 2001;90(6):690-701.
53. Davis ME, Brewster ME. Cyclodextrin-based pharmaceutics: Past, present and future. Nat Rev Drug Discov. 2004;3(12):1023-35.
54. Nagarsenker MS, Meshram RN, Ramprakash G. Solid dispersion of hydroxypropyl beta-cyclodextrin and ketorolac: Enhancement of in-vitro dissolution rates, improvement in anti-inflammatory activity and reduction in ulcerogenicity in rats. J Pharm Pharmacol. 2000;52(8):949-56.
55. Huang TS, Lee SC, Lin JK. Suppression of c-jun/ap-1 activation by an inhibitor of tumor promotion in mouse fibroblast cells. Proc Natl Acad Sci U S A. 1991;88(12):5292-6.
56. Bae MK, Kim SH, Jeong JW, Lee YM, Kim HS, Kim SR, Yun I, Bae SK, Kim KW. Curcumin inhibits hypoxia-induced angiogenesis via down-regulation of hif-1. Oncol Rep. 2006;15(6):1557-62.
57. Lian Q, Li X, Shang Y, Yao S, Ma L, Jin S. Protective effect of curcumin on endotoxin-induced acute lung injury in rats. J Huazhong Univ Sci Technolog Med Sci. 2006;26(6):678-81.
58. Olszanecki R, Gebska A, Korbut R. The role of haem oxygenase-1 in the decrease of endothelial intercellular adhesion molecule-1 expression by curcumin. Basic Clin Pharmacol Toxicol. 2007;101(6):411-5.
59. Steinberg KP, Hudson LD, Goodman RB, Hough CL, Lanken PN, Hyzy R, Thompson BT, Ancukiewicz M. Efficacy and safety of corticosteroids for persistent acute respiratory distress syndrome. N Engl J Med. 2006;354(16):1671-84.
60. Ketoconazole for early treatment of acute lung injury and acute respiratory distress syndrome: A randomized controlled trial. The ards network. JAMA. 2000;283(15):1995-2002.

61. Randomized, placebo-controlled trial of lisofylline for early treatment of acute lung injury and acute respiratory distress syndrome. Crit Care Med. 2002;30(1):1-6.

Chapter 7

Final Discussion

7.1 Overview of Results

This thesis has elucidated the effects of local interactions between extracellular microenvironment and molecules ranging from small molecules to nanoparticles on molecule transport across the cell barriers. Results have shown that the extracellular microenvironment significantly contributes to transcellular transport. The influences of local extracellular interactions on drug transport were reflected i) as differences in the accumulation of nanoparticle aggregates on the cell surface under the pulsed *vs.* constant *vs.* no magnetic field; ii) as exposed cell surface area-related differences in small molecule uptake or transport; or, iii) as variations in the apparent thickness of diffusion boundary layers on the cell surface. In order to investigate underlying mechanisms of *in vitro* cell-based drug transport data in the presence of multi-components, we have used microscopic imaging, mechanism-based cellular pharmacokinetic model (1CellPK), and relevant *in vivo* model.

In Chapter 2 and 3, cell-based transport assays using MDCK cell monolayer in the Transwell® inserts have indicated that heparin-coated magnetic iron oxide nanoparticles (MNPs) form particle aggregates proportionally to initial particle concentrations on the

cell surface in the presence of a constant magnetic field. Although MNPs were stable in the physiological medium with high serum concentrations, extensive particle aggregations were shown at high starting MNP concentrations under the constant magnetic field. Sizes of particle aggregates induced by magnetic field in the high serum-containing medium did not limit MNP transport across the porous membrane with 3 μm-sized pores in the absence of cell barriers. However, in the presence of a cell monolayer on the membrane, diffusion of the particles across the cells appeared to be limited by accumulation of particle aggregates at the cell or membrane surface. These results were more highlighted by microscopic imaging studies including transmitted light microscopy with high magnifications, TEM, and confocal fluorescent microscopy in Chapter 3. Those imaging results provided insights about the mechanism underlying particle transport across cell barriers under different magnetic field conditions. In contrast to the accumulations of large MNP aggregates on cell surface or membrane under the constant magnetic field, the propensity of forming large particle aggregates after interaction of MNPs with the cell surface at high particle concentrations was reduced by the pulsed magnetic field. These studies confirmed that in the presence of cells, the differential application of external magnetic fields significantly affects the extents of particle aggregations, endocytic uptakes, MNP retention on the cell surface, and MNP transport across the cells and pores.

In Chapter 4, small molecular probes, MitoTracker® Red (MTR) and Hoechst ®33342 (Hoe) have shown different local retention and transport in airway *vs.* alveoli. Such behaviors depended on their physicochemical properties including acid association constant (pK_a) and lipophilicity (logP) and also on the regional variations of cell surface

properties along the airway to alveoli. The *in vitro* transport assays with NHBE cell multilayers on inserts indicated that most of the probes were retained in the vicinity of the administered sites (intracellular retentions limited in top cell layers). Simulated results in the alveoli and MDCK cells on porous supports have also shown that these probes were retained intracellularly by transcellular dye concentration gradient in both apical-to-basolateral and lateral directions. Meanwhile, *in vivo* lung studies have shown closely paralleled results to *in silico* predictions, in that MTR (hydrophilic cation) was retained in the airway by local intratracheal (IT) administration whereas Hoe distributed in both the airway and alveoli after intravenous (IV) or IT administration. High, local intracellular retention of the probes were confirmed by *in vitro* results. However, *in silico* model showed a better prediction for *in vivo* situation along the airway to alveoli in the context of small molecular transport and retention after local administration. This might result from *in silico* model constructions with the three-dimensional organization and physiological parameters of *in vivo* conditions.

In Chapter 5, integration of quantitative drug transport assays with mixed co-cultures and 1CellPK model showed that the variations in the extracellular microenvironment of Calu-3 *vs.* NHBE might lead to differences in drug transport/uptake measurements from these cell-types. Results of parameter optimizations in computational modeling suggested that unstirred water layers on the cell surface was the key factor affecting transcellular transport and cellular uptake of drug molecules in *in vitro* transport assay system. The thickness of the diffusion boundary layer is a complex parameter reflecting various underlining interactions between the molecules and the cell surface including diffusivity, drug binding, electrostatic interactions, ciliary convection, pH or

viscosity on the cell surface, and so on. Based on the simulations, the only major difference in Calu-3 *vs.* NHBE was the thicknesses of diffusion boundary layers, which suggested that extracellular microenvironments in different cell types might affect the passive transport of drug molecules across the cells. As differentiated as monolayers on the inserts, Calu-3 cells proved to be more relevant than NHBE for assaying the drug absorption in the airway.

In Chapter 6, as water-soluble complexation carriers, hydroxypropyl-γ-cyclodextrins (HP-γ-CDs) were used to develop curcumin-CD complex (CDC) formulations to improve bioavailability *via* inhaled route. While organic co-solvents (*e.g.*, DMSO, ethanol) showed toxicity (*i.e.,* compromised cell monolayers) at the doses needed to dissolve curcumin at high concentrations, CDC has shown low toxicity and high efficiency of cellular uptake and permeability across the Calu-3 cells and lung tissues. These studies demonstrated the relevance between *in vitro* assays with the Calu-3 and *in vivo* airway experiments in terms of permeation and cell-association of curcumin in the presence of CDs. CDC has also proved high anti-inflammatory and antioxidant effects for acute lung injury in the murine model. CDC administration significantly reduced total neutrophil counts in the animal model of acute lung injury. It was also confirmed that CDC downregulated activity of the pro-inflammatory transcription factor (NF-κB) and reduced oxidant stress more efficiently than uncomplexed curcumin.

7.2 Interpretation of Results

In the studies about transcellular targeting of magnetic iron oxide nanoparticles (MNPs) in Chapters 2 and 3, quantitative analyses with microscopic imaging showed the

formation of large particle aggregations on the cell surface and membrane pores, inhibiting cell penetration of particles when the particles were exposed to the constant magnetic field. While the large particle aggregates formed by constant magnetic field sterically hindered endocytic particle uptake, MNPs subjected to the pulsed magnetic field showed size ranges that can be endocytosed, resulting in the enhanced cell penetration and minimized retentions on the cell surface. Under the constant magnetic field, in the absence of cells, MNPs at high initial concentrations showed visible particle aggregates with rapid changes in particle concentrations with the time only at a close distance from the magnet (<3 mm), but at the level of transwell insert (≥4 mm), the MNP concentration was changed slowly with no detectable particle aggregates. These results suggest that it was the level of cell layers on the inserts that magnetic force can sufficiently pull down MNPs with magnetically induced particle aggregations with smaller sizes than the resolution limit of the magnifications of imaging (≤250 nm). Particle aggregations on the cell surface might occur faster than cellular uptake under the constant magnetic field. Magnetically induced particle aggregates formed by pre-exposures of MNPs to the constant or pulsed magnetic field before being added into the cells did not affect transcellular transport/uptake in the absence of magnetic field. These results suggest that the external magnetic field mostly influences the manner in which MNPs interact with the cells and other particles when the particles are in contact with the cell surface.

In Chapter 4, two small molecular probes, MTR and Hoe showed different local retention in the airway after local administration (IT). The results indicated that distribution of different molecules in various regions of the lung depends on the

lipophilicity and ionization properties of the molecules and could be affected by the route of administration, histology or circulatory parameters in the airway or alveoli. Parameter sensitivity analysis results from an *in silico* model enabled us to interpret the different behaviors of molecular retention found in two small molecules. The results indicated that mitochondrial uptake might be a critical histological component in determining high MTR (hydrophilic cation) exposures after IT administration. After IT administration, MTR would be traversed through the lumen of the airway into the interstitium, and then rapidly absorbed by the mitochondria in the epithelial cells by the highly negative membrane potential of the mitochondrial inner membrane. By this property of mitochondrial membrane, MTR would be slowly released into the systemic circulation. In the alveoli, the surface areas of apical and basolateral membrane are larger than those in the airway, and therefore MTR absorption in the alveoli and release into the circulation are facilitated with less MTR accumulation inside the mitochondria. Compared to behaviors of MTR, Hoe showed no significant differences in local retentions in the airways *vs.* alveoli because the molecules exist as neutral forms at physiological pH and easily diffused across the membranes. When administered *via* IV route, the distribution of molecules between blood and tissue is mostly determined by the partition of molecules between blood and tissue, which could be affected by cellular compositions or densities in tissue. Therefore, after IV administration, both Hoe and MTR showed partitioning more into alveoli than the airways. Underlying mechanisms of different molecular retentions in local regions of the lung could be differences of cellular organized structures or varying cell areas exposed to drug molecules in the airway *vs.* alveoli.

In Chapter 5, the integrated approach of *in vitro* cell-based assay system using co-cultures and an *in silico* cellular pharmacokinetic modeling was used to identify key parameters that can explain the observed differences in the absorption and transport properties of propranolol in two types of airway epithelial cells (Calu-3 *vs.* NHBE). In the 1/1 Calu-3/NHBE cell co-cultures, the stirring conditions in Calu-3 and NHBE cells could be nearly identical because the cells are randomly dispersed. Therefore, the thickness of the unstirred water layer on the cell surface should be similar for both Calu-3 and NHBE cells in co-culture. However, parameter optimization and sensitivity tests from the *in silico* model indicated that differences in the apparent thickness of the unstirred water layer significantly affected the transport properties of Calu-3 and NHBE cells. The apparent unstirred water barriers could be factors combining various cell type-dependent components related to local differences in the extracellular, surface microenvironment (*e.g.,* viscosity, convection, ciliary motility, and macromolecular crowding, *etc*). Therefore, the reason that the thicknesses of unstirred water layers appeared different for Calu-3 *vs.* NHBE cells could be because of the variations in the extracellular microenvironment surrounding the cells, and these local microenvironment differences might affect the passive transport of propranolol in the vicinity of the cell surface of Calu-3 *vs.* NHBE.

In the relation to the studies in Chapter 6, previous reports indicated that CDs promoted drug delivery, not by directly enhancing drug permeation or cell-association, but by acting as a reservoir for drug molecules to promote drug dispersion (1, 2). At optimal CD concentrations, CDs might help to overcome unstirred water barriers on the cell surface and promote permeation of curcumin. Since CDs are cell impermeant (2, 3)

and in most cases, unable to enhance drug permeation through a lipophilic membrane barrier, it is plausible that curcumin-CD complexes might inhibit the intracellular uptake of curcumin. Nevertheless, our *in vitro* transport data from the Calu-3 cells, and *in vivo* experiments performed by our collaborators demonstrated that CDs increased the amount of delivered and cell-associated curcumin and its transcellular permeability, with an associated enhancement of efficacy in the diseased animal model. These results might be related to the physical properties of drug-CD inclusion complexes. CDs can form inclusion complexes with lipophilic drugs by incorporating drug molecules into the central, hydrophobic cavity. The driving forces leading to the inclusion complex formation include release of water molecules from the cavity, van der Waals, hydrophobic or electrostatic interaction, hydrogen bonding, and charge-transfer interaction (4, 5). All the relatively weak forces allow free drug molecules in solution to be in rapid equilibrium with drug molecules within the cavity of CDs (6). Excessive amount of CDs could inhibit free drug permeation through the membrane. Therefore, our results indicate that contents of CDs in our CDC formulations might be optimal for compromising extracellular microenvironment at donor side and promoting free curcumin permeation into the cells.

7.3 Alternative Interpretations

In Chapters 2 and 3, MNP formulations have shown different particle behaviors on the cell surface according to a constant *vs.* pulsed magnetic field. Under a constant magnetic field, due to steric hindrance, large particle aggregates cannot be endocytosed, resulting in increasing MNPs accumulation at the cell surface. In contrast, under a pulsed

magnetic field, MNP transport across the cell monolayers was maximized by effectively concentrating MNPs at the cell surface with less aggregate formation. Our studies in this thesis and other studies using *in vitro* cell-based transport assays suggest that the local extracellular microenvironment on the cell surface could influence the transport of molecules. There have been reports about the effects of static aqueous barriers on the cell surface on the diffusion of nanoparticle formulations across the cell membranes (39-41). The mucus layers of intestinal or airway epithelial cells can affect the passive transport of these particles (42). The concentration gradient in the diffusion boundary layers could be varied by extracellular factors such as magnetic fields (43, 44) or ultrasound shockwaves (45). Under constant magnetic fields, the particles could densely accumulate immediately above the cell surface. Despite a dramatic concentration gradient in the vicinity of the cell surface caused by the external magnetic field, our studies imply that particle transport is prohibited by the large particle aggregations which cannot be endocytosed. In a sharp contrast, under the pulsed magnetic field, particles rather remained well dispersed in the aqueous layers with formation of only small particle aggregates in the vicinity of the cell surface, resulting in enhanced cell penetration of particles.

In Chapter 4, it was suggested that as the underlying mechanism, differences of cellular organized structures with varied cell areas exposed to drug molecules along upper and lower lung might result in different local deposition and absorption of small molecular probe, MTR. Structural features such as collagens (21, 22) as well as cellular components such as smooth muscle or macrophage cells in ECM (23, 24) show variations along the lung, possibly exerting influences on lung absorption/distribution. Moreover, huge variations in airway surface liquid (ASL) on the epithelial cells along the airway to

the alveoli could be important extracellular factors to be considered to alter drug absorption in contact with the cell surface (25). In addition to mucus layers in ASL, viscosity of watery periciliary sol (PCL) around the cilia can affect ciliary movements (26), providing variations in mucociliary clearance (27), which can influence drug deposition/absorption. Thickness and compositions of surface lining liquid are controlled by mucus secretions, ion channels or aquaporins (28-30) and these interactions play important role to determine characteristics of diffusion water barriers on the cell surface. There have been numerous reports that drug transport and distribution could be greatly affected by the variations in drug diffusivity across the diffusion barriers on the airway tissues (25).

In Chapter 5, simulation results suggested different local extracellular microenvironment in two different airway cells might influence the passive diffusion of propranolol across the cells. Physiological differences in mucus secretions (31-34) and ion regulatory mechanism (35, 36) in these cell-types might influence hydration, viscosity and thickness of the mucus layer on the cell surface and accordingly, affect the differences in local microenvironment surrounding the Calu-3 and NHBE cells. There are reports about the different morphology of cilia (37) and ciliary motility (33, 38) in Calu-3 *vs.* NHBE cells. Considering mucociliary clearance is controlled by combinations of mucus secretions and ciliary beats, variations in viscosity and cell surface area could result in differences in convection around the cell, providing differences in the apparent diffusion water barriers as shown in the model.

For the results of Chapter 6, very low permeability of CDs measured from the Calu-3 cell monolayers (~7×10^{-8} cm/sec for CDs with MW. 972-1297 Da) in a previous

report also support that complex with CDs may have difficulty to go across the cell membrane (7). In the report, when compared with the permeability of paracellular markers, CD permeability values in the Calu-3 were higher than those of dextrans of MW. 4-20 kDa ($0.1\text{-}0.6\times10^{-8}$ cm/sec), but on the same order of magnitudes as Lucifer yellow (MW. 479 Da; 4.3×10^{-8} cm/sec) and Na-fluorescein (MW. 376 Da, 14.7×10^{-8} cm/sec). Extractions of lipids or cholesterols from the cell membrane are reported as the mechanism of cytotoxicity by γ-CDs or HP-CDs at high doses (≥ 50 mM) (8-11). With the doses of γ-CDs used in the transport studies, the membrane integrity of the Calu-3 has not been changed before and after the transport studies of CDs, evidenced by TEER or LDH assays (7). This strongly suggests that the hydrophilic CDs or drug-CD inclusion complexes cannot be transported transcellulary but rather possibly *via* paracellular pathway. However, the possibility cannot be excluded that drug inclusion complexes with CDs can go across the cells by receptor-mediated transcytosis (12).

In Chapter 6, cell permeability results of CDC formulations in the Calu-3 cell monolayers have interestingly shown that CDC formulations at higher initial CDC concentrations displayed lower permeability than those at 50 μM whereas the cell-associated CDC masses at higher initial concentrations were much higher than those at 50 μM. Curcumin is known as a non-substrate, but an inhibitor for active transporters, ATP-binding cassette (ABC) (*e.g.,* P-glycoprotein (P-gp), multi-drug resistance associated protein families (MRPs) or breast cancer resistance protein (BCRP)) and SLC transporters (*e.g.,* organic anionic transporters (OATs)) (13, 14). Calu-3 cells are known to express low levels of phase II enzymes (i.e., glutathione or glucuronide, or sulfate conjugation enzymes) (15) which are major metabolizing enzymes of curcumin.

Considering the current limited knowledge about curcumin's accumulation inside the cells, the phenomenon of differential curcumin masses associated with the Calu-3 cells according to the initial curcumin concentrations might be involved in other pathways than passive diffusion, active transport, or metabolism. Mechanistic studies related to drug sequestration inside the cells have reported various pathways such as ion trappings, phospholipidosis, or multi-lamellar body (MLB) formations, *etc.*, which could limit the final drug solubility in the aqueous phase in cells or suborganelles (16-20).

7.4 Future Directions

Consistent with other works in *in vitro* cell-based permeability measurements, our studies indicate that the local interaction of molecules with the extracellular microenvironment could be a rate limiting step for drug permeation and cellular uptake thereby impeding efficient drug delivery to target sites. As an apparent barrier, the diffusion boundary layers could be formed not only by experimental setup of transport assays (*e.g.*, stirring conditions) as other studies reported, but also by various factors related to extracellular microenvironment of different cell-types. Mucus secretions, ciliary functions, pH variations, or ion compositions can all control each other, resulting in different local environment on the epithelial cell surface.

Moreover, external magnetic forces have shown spatiotemporal effects in determining transcellular transport, cellular uptake and retention on the cell surface of magnetic iron oxide nanoparticles. The regional differences in cell areas or ECM environment as shown in the studies with MTR *vs.* Hoe in upper or lower airways could affect the drug exposure and retention in locally administered sites. Drug solubilizing

agents such as CDs can control the thickness of unstirred water layers. The interactions among the extracellular factors could make the real transcellular permeability of drugs measurements over- or under-estimated.

Therefore, in order to make *in vitro*, cell-based permeability assay data applicable to high throughput screenings with a variety of drug-like molecules in a more accurate way, integrated methodologies should be established by considering multiple components of extracellular factors. Our quantitative analysis with mass balance and imaging can help to elucidate how the transcellular drug transport/distribution could be affected by the manner in which the extracellular factors are changed. The studies about molecular transport pathways under the effects of extracellular interactions could guide the drug development process to the downstream drug delivery applications. In addition to our approach presented herein, it could be helpful to substantiate mechanistic cell-based pharmacokinetic model with multiple components including extracellular and intracellular factors based on hypotheses. Additionally, more specific microscopic imaging and biochemical assays can help ascertain the different extracellular factors which might be correlated with varied drug transport/uptake. The extracellular factors should be also studied in relation to the molecular targeting and distribution for different drug formulations (*i.e.,* ion states, sizes, surface chemistry) and produced batches. Those assay system should reflect physiological structures of organs/tissues and apparent barriers for molecular transport. To include multiple components related to the key factors into the cell-based pharmacokinetic model can facilitate appropriate hypothesis-driven model predictions to enable insightful interpretation about the data obtained from cell-based permeability assays with various drug-like molecules.

7.5 Overarching Conclusions

On the basis of the findings presented in this thesis, it is suggested that factors related to extracellular microenvironment should be considered when seeking to interpret cell permeability data in the presence of multi-components in a more accurate manner. In our studies we elucidated the effects of extracellular interactions on drug transport in the presence of various multi-components, such as external magnetic forces, different exposed cell surface areas, apparent diffusion boundary layers, drug solubilizing agents throughout bulk mass balance assays, in silico modeling, and microscopic imaging. The studies with magnetic nanoparticles (MNPs) (49, 50) have shown that the cellular uptake and transcellular targeting efficiency of MNPs should count for the interactions between particles, external magnetic field, and the cell barriers. The *in vitro* quantitative analysis with microscopic imaging has elucidated how magnetic force should be utilized to tailor the magnetic targeting with less unnecessary depositions of particles on the cell surface. From the integrated *in silico*-to-*in vitro*-to-*in vivo* studies about local drug deposition/absorption of small molecule markers in the airways (48), computational simulations have shown that different cell areas in airway *vs.* alveoli could affect transport and cellular retention of small molecules. Those results warrant investigation on the effects of structural and physicochemical components in the cell microenvironment along airways to alveoli in local lung distribution/absorption of inhaled drug molecules or biomarkers. In the *in vitro* airway cell models (Calu-3/NHBE), our studies have shown the impact of differences in extracellular microenvironment surrounding the cells on drug transport and cellular uptake. Considering the physiological conditions *in vivo* with

varied extracellular matrix or fluidic phase, the interpretation of *in vitro* cell-based permeability data should be linked with the extracellular microenvironment components. Understanding the role of CD interaction with aqueous barriers on the cell surface supports the concept of delivering curcumin-CD complex *via* inhalation which has been confirmed as a non-toxic, efficient method for acute lung injury treatment in the *in vitro* transport assays and relevant animal studies (46, 47). Ultimately, in order to use *in vitro* cell-based permeability assays for testing a variety of drug formulations accurately, it is important to account for the extracellular microenvironment as essential factors upon drug transport/distribution.

7.6 References

1. Arima H, Yunomae K, Miyake K, Irie T, Hirayama F, Uekama K. Comparative studies of the enhancing effects of cyclodextrins on the solubility and oral bioavailability of tacrolimus in rats. J Pharm Sci. 2001;90(6):690-701.
2. Davis ME, Brewster ME. Cyclodextrin-based pharmaceutics: past, present and future. Nat Rev Drug Discov. 2004;3(12):1023-35.
3. Uekama K, Hirayama F, Irie T. Cyclodextrin Drug Carrier Systems. Chem Rev. 1998;98(5):2045-76.
4. Loftsson T, Brewster ME. Pharmaceutical applications of cyclodextrins. 1. Drug solubilization and stabilization. J Pharm Sci-Us. 1996;85(10):1017-25.
5. Liu L, Guo Q-X. The driving forces in the inclusion complexation of cyclodextrins. Journal of Inclusion Phenomena and Macrocyclic Chemistry. 2002;42(1):1-14.
6. Stella VJ, Rajewski RA. Cyclodextrins: their future in drug formulation and delivery. Pharmaceut Res. 1997;14(5):556-67.
7. Matilainen L, Toropainen T, Vihola H, Hirvonen J, Jarvinen T, Jarho P, et al. In vitro toxicity and permeation of cyclodextrins in Calu-3 cells. J Control Release. 2008;126(1):10-6.
8. Irie T, Otagiri M, Sunada M, Uekama K, Ohtani Y, Yamada Y, et al. Cyclodextrin-induced hemolysis and shape changes of human erythrocytes in vitro. J Pharmacobiodyn. 1982;5(9):741-4.
9. Miyazawa I, Ueda H, Nagase H, Endo T, Kobayashi S, Nagai T. Physicochemical properties and inclusion complex formation of δ-cyclodextrin. Eur J Pharm Sci. 1995;3(3):153-62.
10. Irie T, Uekama K. Pharmaceutical applications of cyclodextrins. III. Toxicological issues and safety evaluation. J Pharm Sci-Us. 1997;86(2):147-62.
11. Laza-Knoerr A, Gref R, Couvreur P. Cyclodextrins for drug delivery. Journal of Drug Targeting. 2010;18(9):645-56.
12. Agüeros M, Espuelas S, Esparza I, Calleja P, Peñuelas I, Ponchel G, et al. Cyclodextrin-poly (anhydride) nanoparticles as new vehicles for oral drug delivery. Expert Opin Drug Del. 2011;8(6):721-34.
13. Li Y, Lu J, W Paxton J. The Role of ABC and SLC Transporters in the Pharmacokinetics of Dietary and Herbal Phytochemicals and their Interactions with Xenobiotics. Current drug metabolism. 2012;13(5):624-39.
14. Li Y, Paxton JW. The effects of flavonoids on the ABC transporters: consequences for the pharmacokinetics of substrate drugs. Expert Opin Drug Met. 2013;(0):1-19.
15. Ehrhardt C, Forbes B, Kim K-J. In vitro models of the tracheo-bronchial epithelium. Drug Absorption Studies. 2008:235-57.
16. Reasor MJ, Kacew S. Drug-induced phospholipidosis: are there functional consequences? Experimental Biology and Medicine. 2001;226(9):825-30.
17. Zheng N, Zhang X, Rosania GR. Effect of phospholipidosis on the cellular pharmacokinetics of chloroquine. J Pharmacol Exp Ther. 2011;336(3):661-71.

18. Lajoie P, Guay G, Dennis JW, Nabi IR. The lipid composition of autophagic vacuoles regulates expression of multilamellar bodies. Journal of cell science. 2005;118(9):1991-2003.
19. Gruenberg J, Stenmark H. The biogenesis of multivesicular endosomes. Nature Reviews Molecular Cell Biology. 2004;5(4):317-23.
20. Rajendran L, Knölker H-J, Simons K. Subcellular targeting strategies for drug design and delivery. Nature reviews Drug discovery. 2010;9(1):29-42.
21. Aplin J, Hughes R. Complex carbohydrates of the extracellular matrix structures, interactions and biological roles. Biochimica et biophysica acta. 1982;694(4):375.
22. Olsen CE, Isakson BE, Seedorf GJ, Lubman RL, Boitano S. Extracellular matrix-driven alveolar epithelial cell differentiation in vitro. Experimental lung research. 2005;31(5):461-82.
23. Sannes PL. Structural and functional relationships between type II pneumocytes and components of extracellular matrices. Experimental lung research. 1991;17(4):639-59.
24. Tam A, Wadsworth S, Dorscheid D, Man SP, Sin DD. The airway epithelium: more than just a structural barrier. Therapeutic advances in respiratory disease. 2011;5(4):255-73.
25. Khanvilkar K, Donovan MD, Flanagan DR. Drug transfer through mucus. Adv Drug Deliver Rev. 2001;48(2):173-93.
26. Widdicombe J. Regulation of the depth and composition of airway surface liquid. J Anat. 2002;201(4):313-8.
27. Matsui H, Randell SH, Peretti SW, Davis CW, Boucher RC. Coordinated clearance of periciliary liquid and mucus from airway surfaces. Journal of Clinical Investigation. 1998;102(6):1125.
28. Herschlag G, Garcia GJ, Button B, Tarran R, Lindley B, Reinhardt B, et al. A mechanochemical model for auto-regulation of lung airway surface layer volume. Journal of theoretical biology. 2013.
29. Song Y, Verkman A. Aquaporin-5 dependent fluid secretion in airway submucosal glands. Journal of Biological Chemistry. 2001;276(44):41288-92.
30. Tarran R, Trout L, Donaldson SH, Boucher RC. Soluble mediators, not cilia, determine airway surface liquid volume in normal and cystic fibrosis superficial airway epithelia. The Journal of general physiology. 2006;127(5):591-604.
31. Matsui H, Randell SH, Peretti SW, Davis CW, Boucher RC. Coordinated clearance of periciliary liquid and mucus from airway surfaces. J Clin Invest. 1998;102(6):1125-31.
32. Forbes II. Human airway epithelial cell lines for in vitro drug transport and metabolism studies. Pharm Sci Technolo Today. 2000;3(1):18-27.
33. Stewart CE, Torr EE, Mohd Jamili NH, Bosquillon C, Sayers I. Evaluation of differentiated human bronchial epithelial cell culture systems for asthma research. J Allergy (Cairo). 2012;2012:943982.
34. Huang TW, Chan YH, Cheng PW, Young YH, Lou PJ, Young TH. Increased mucociliary differentiation of human respiratory epithelial cells on hyaluronan-derivative membranes. Acta Biomater. 2010;6(3):1191-9.
35. Szkotak AJ, Man SF, Duszyk M. The role of the basolateral outwardly rectifying chloride channel in human airway epithelial anion secretion. Am J Respir Cell Mol Biol. 2003;29(6):710-20.

36. Wang D, Sun Y, Zhang W, Huang P. Apical adenosine regulates basolateral Ca2+-activated potassium channels in human airway Calu-3 epithelial cells. Am J Physiol Cell Physiol. 2008;294(6):C1443-53.
37. Berube K, Prytherch Z, Job C, Hughes T. Human primary bronchial lung cell constructs: the new respiratory models. Toxicology. 2010;278(3):311-8.
38. Lehmann M, Noack D, Wood M, Perego M, Knaus UG. Lung Epithelial Injury by B-Anthracis Lethal Toxin Is Caused by MKK-Dependent Loss of Cytoskeletal Integrity. PLoS One. 2009;4(3).
39. Elder A, Vidyasagar S, DeLouise L. Physicochemical factors that affect metal and metal oxide nanoparticle passage across epithelial barriers. Wiley Interdisciplinary Reviews: Nanomedicine and Nanobiotechnology. 2009;1(4):434-50.
40. Ferrati S, Streiff AK, Srinivasan S, Alexander JF, Bhargava N, Peters AM, et al. Mass Transport via Cellular Barriers and Endocytosis. Intracellular Delivery. 2011:3-55.
41. Pack CG, Song MR, Lee EJ, Hiroshima M, Byun KH, Kim JS, et al. Microenvironments and different nanoparticle dynamics in living cells revealed by a standard nanoparticle. Journal of Controlled Release. 2012.
42. Ahmed A, KS Yadav H, V Lakshmi S, VN Namburi B, G Shivakumar H. Mucoadhesive Nanoparticulate System for Oral Drug Delivery: A Review. Current Drug Therapy. 2012;7(1):42-55.
43. Teeguarden JG, Hinderliter PM, Orr G, Thrall BD, Pounds JG. Particokinetics in vitro: dosimetry considerations for in vitro nanoparticle toxicity assessments. Toxicological Sciences. 2007;95(2):300-12.
44. Chorny M, Fishbein I, Forbes S, Alferiev I. Magnetic nanoparticles for targeted vascular delivery. IUBMB life. 2011;63(8):613-20.
45. Yang X. Nano-and Microparticle-based Imaging of Cardiovascular Interventions: Overview1. Radiology. 2007;243(2):340-7.
46. Dahan A, Miller JM, Hoffman A, Amidon GE, Amidon GL. The solubility–permeability interplay in using cyclodextrins as pharmaceutical solubilizers: Mechanistic modeling and application to progesterone. J Pharm Sci-Us. 2010;99(6):2739-49.
47. Suresh M, Wagner M, Rosania G, Stringer K, Min K, Risler L, et al. Pulmonary Administration of Water-soluble Curcumin Complex Reduces ALI Severity. Am J Resp Cell Mol. 2012.
48. Yu J-y, Zheng N, Mane G, Min KA, Hinestroza JP, Zhu H, et al. A Cell-based Computational Modeling Approach for Developing Site-Directed Molecular Probes. Plos Comput Biol. 2012;8(2):e1002378.
49. Min KA, Yu F, Yang VC, Zhang X, Rosania GR. Transcellular Transport of Heparin-coated Magnetic Iron Oxide Nanoparticles (Hep-MION) Under the Influence of an Applied Magnetic Field. Pharmaceutics. 2010;2(2):119-35.
50. Min KA, Shin MC, Yu F, Yang M, David AE, Yang VC, et al. Pulsed Magnetic Field Improves the Transport of Iron Oxide Nanoparticles through Cell Barriers. ACS Nano. 2013.

Appendices

Appendix A

Supporting Information in Chapter 3

Supplemental experimental methods and results

1. Physicochemical characterizations of Hep-MNPs preparation. Hydrodynamic sizes and zeta potential values of MNPs showed no significant changes during the incubation time (0 or 5 h) in water or in buffer containing 10 % fetal bovine serum (FBS) (Figure A1). Zeta potential measurements showed the changes in the surface charge of MNPs in the serum-containing buffer, relative to the water (-36 (± 1.1) mV in water; -14.2 (± 2.3) mV in buffer with serum). This might be because of serum protein adsorptions on the nanoparticles (1, 2). However, the presence of serum in the buffer during the 90 min transport experiments may not affect the stability of the particles since little changes are shown in the size and also in zeta potential during the incubation with 10 % FBS.

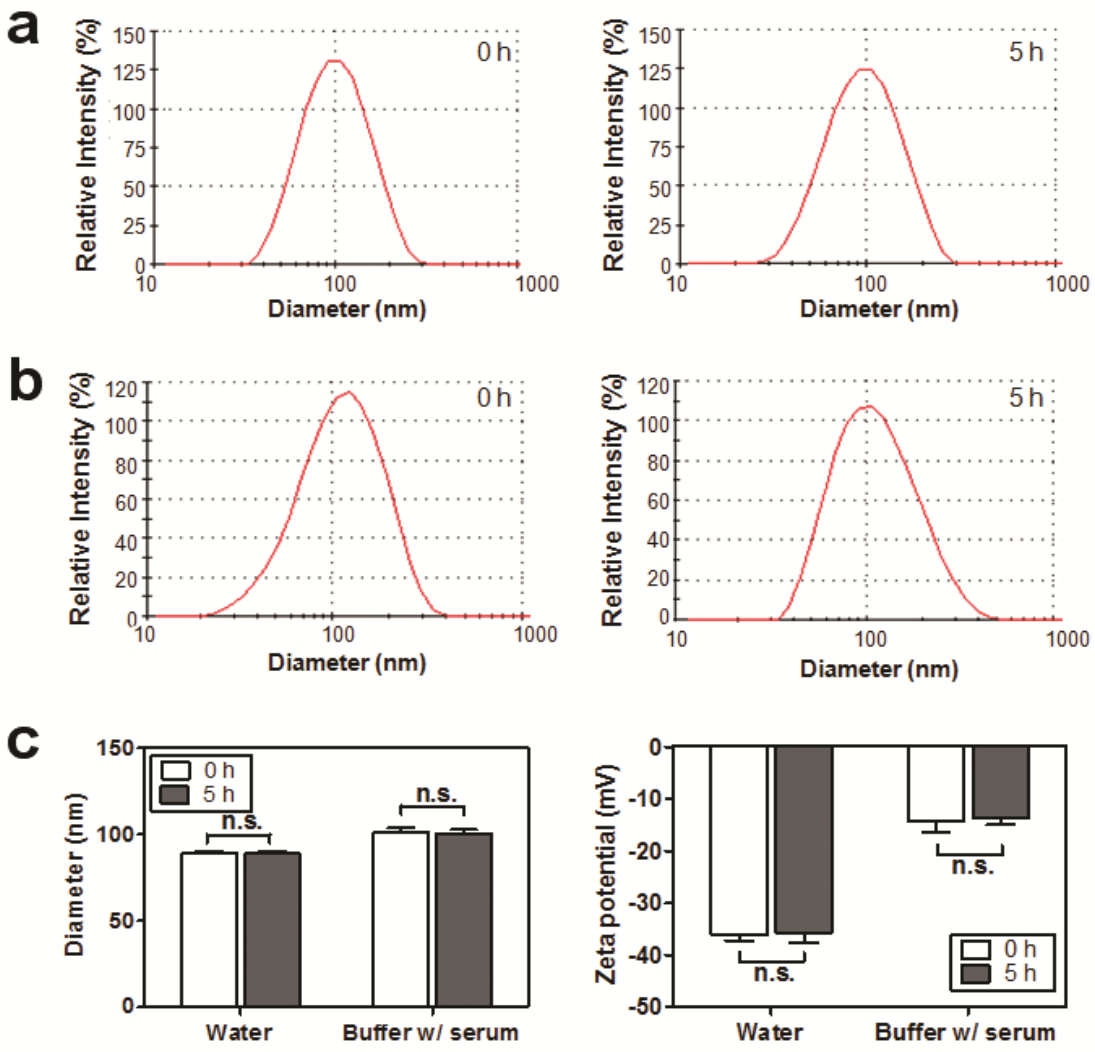

Figure A1. Stability of Hep-MNPs in physiological buffers.

Size distribution profiles of MNPs in (a) water or (b) HBSS buffer with 10 % FBS after incubation at 37°C for 0 and 5 h. (c) Size (nm) and Zeta potential (mV) measurements (mean ± SD, N = 3) of MNPs in water or HBSS with 10 % FBS after incubation at 37°C for 0 and 5 h.

2. A Constant Magnetic Field Visibly Promoted Accumulation of MNPs on Cell Monolayers. After transport studies under a constant magnetic field at different initial MNPs concentrations, the inserts were examined under the bright field microscope. As shown in Figure A2a, particle aggregates accumulated on the cell monolayers were visible

as brown patches and the accumulations of particle aggregates appeared greater as the concentration of MNP was increased. To confirm this observation, the microscopic images were subjected to quantitative analyses. The area covered by brown clusters of particle aggregates on the surface of cell monolayers was measured (Figure A2b).

As previously reported (3), an external magnetic field promoted mass transport of MNPs across cell monolayers with transport kinetics of particles dependent on the initial particle concentrations. Paradoxically, mass transport rates decreased as MNP concentration in the donor compartment was increased. In the absence of magnetic field, there was no significant difference in apical to basolateral transport of particles, in various initial donor concentrations of MNPs (Figure A3). Under constant magnetic field conditions at high MNP concentration (0.412 mg Fe/ml), the rate of transport into the basolateral compartment over time (0.63 ng Fe/sec (± 0.05)) was less than that at the lower MNP concentration (0.258 mg Fe/ml) (1.15 ng Fe/sec (± 0.11)).

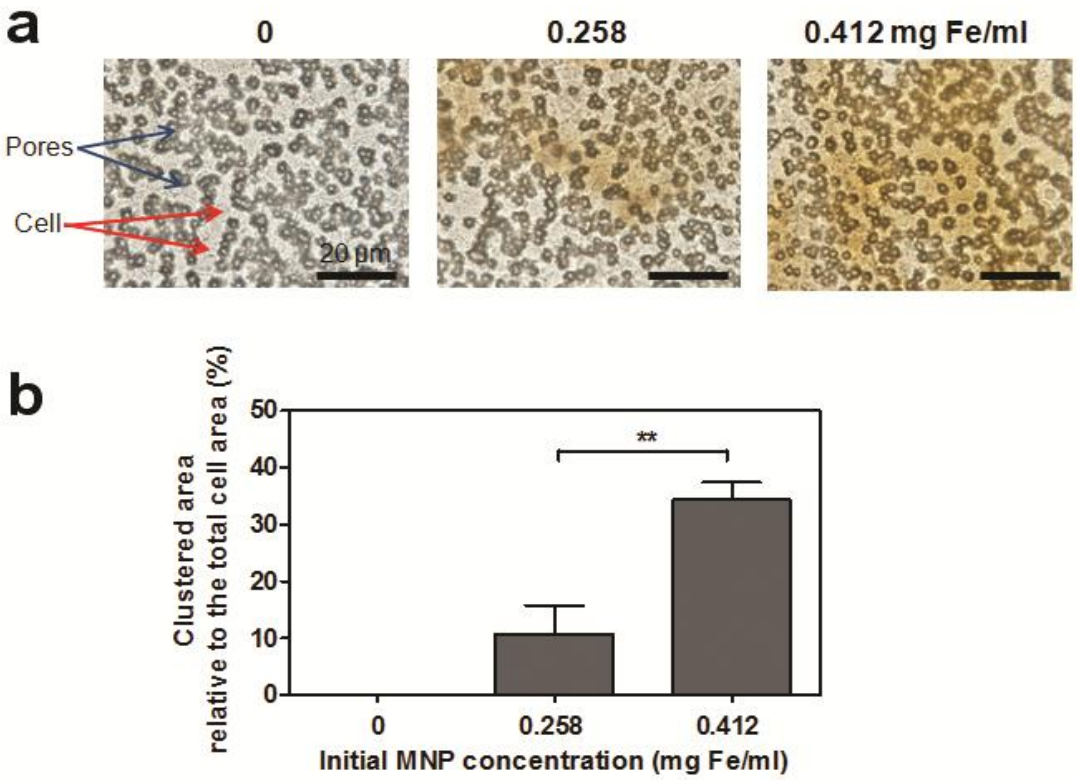

Figure A2. Microscopic images revealed visible, brown MNP aggregates covering the apical surface of cell monolayers after transport studies.

(a) After a 90 min transport experiment, the cells on the insert were examined under bright field optics of Olympus BX-51 upright light microscope (100 × objectives). MNP aggregates covering the surface of the cell monolayer at 0.258 and 0.412 mg Fe/ml were visible as brown patches. No such brown patches were visible before the experiments, or in negative control inserts without MNPs. Pores on the PET membrane of inserts (pore size: 3 µm) and MDCK cells are indicated in the images with the blue and red arrows in the bright field image of the negative control. Scale bar is 20 µm. (b) Area covered by brown particle aggregates relative to the cell monolayer area (%) at the end of a 90 min transport experiment was compared for different initial apical concentrations of MNP suspension (N = 5) by unpaired t-test ($\alpha = 0.05$).

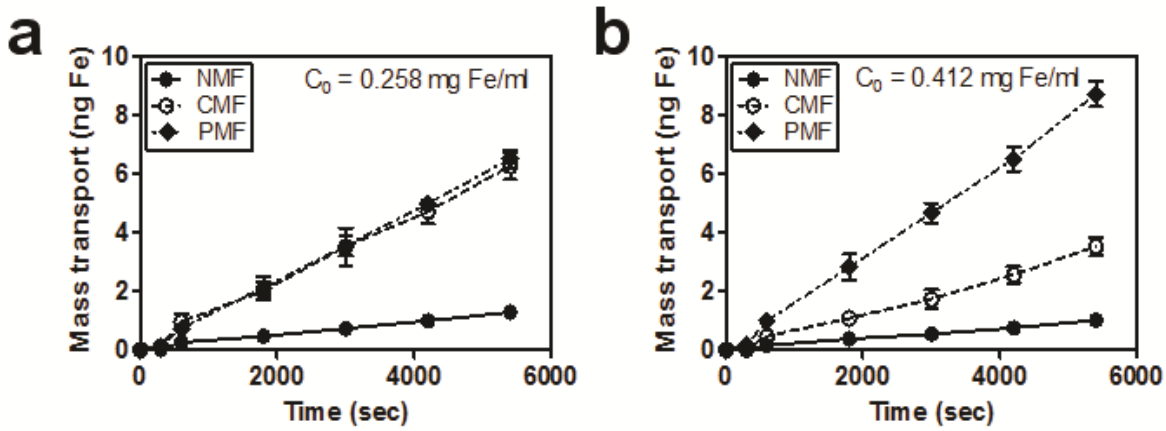

Figure A3. Mass transport of MNPs across MDCK cells in Transwell™ insert was assessed as a function of time for different initial MNP concentration in the presence or absence of the magnetic field (NMF means "no magnet", CMF "constant magnetic field", and PMF "pulsed magnetic field"; N = 3) ((a) 0.258 mg Fe/ml; (b) 0.412 mg Fe/ml).

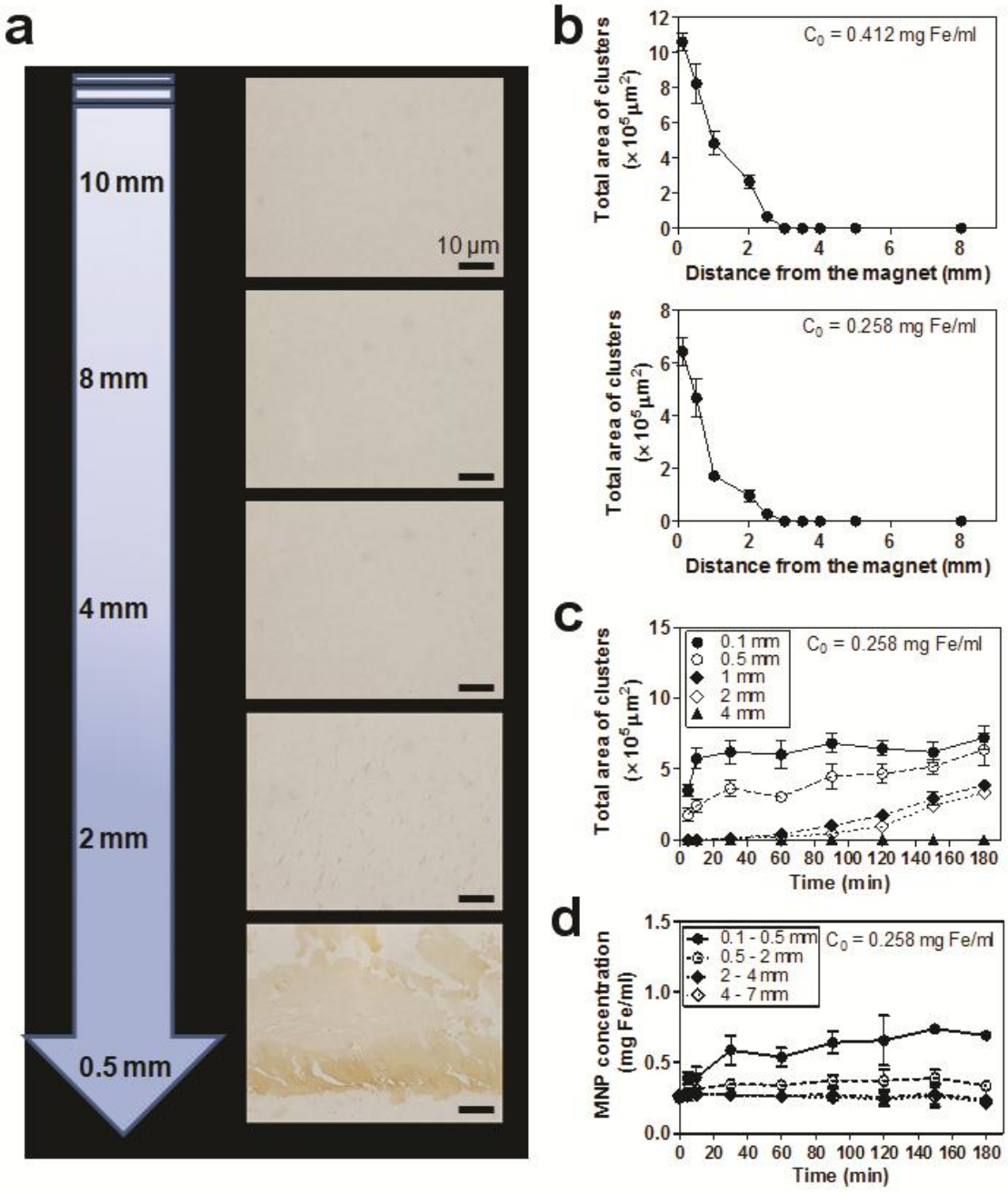

Figure A4. Microscopic examination of magnetically-induced aggregates of MNPs in suspension according to the distance from the magnet.

(a) MNPs within 2 mm from the magnet showed apparent aggregates with the sizes detectable by at 1000 × magnification with an Olympus BX-51 upright light microscope (scale bar = 10 µm). Bright field images of MNPs at high concentration (0.412 mg Fe/ml) at different distances from the magnet surface, at 3 h. (b) Total sizes (area; μm^2) of clusters of particle aggregates measured at 3 h is displayed according to the distance from the magnet between 0.1 and 8 mm for different initial MNP concentrations (0.412 or 0.258 mg

Fe/ml). At lower initial MNP concentration (0.258 mg Fe/ml), (c) Total sizes (area; μm^2) of clusters of particle aggregates measured from the bright field images of particle suspension within 4 mm (0.1, 0.5, 1, 2, and 4 mm) from the magnet is displayed as a function of time (5-180 min) under the magnetic field. (d) MNP concentration changes at each segment in the tube (0.1-0.5, 0.5-2, 2-4, and 4-7 mm from the magnet) are plotted as a function of time (5–180 min) under the external magnetic field (0.258 mg Fe/ml).

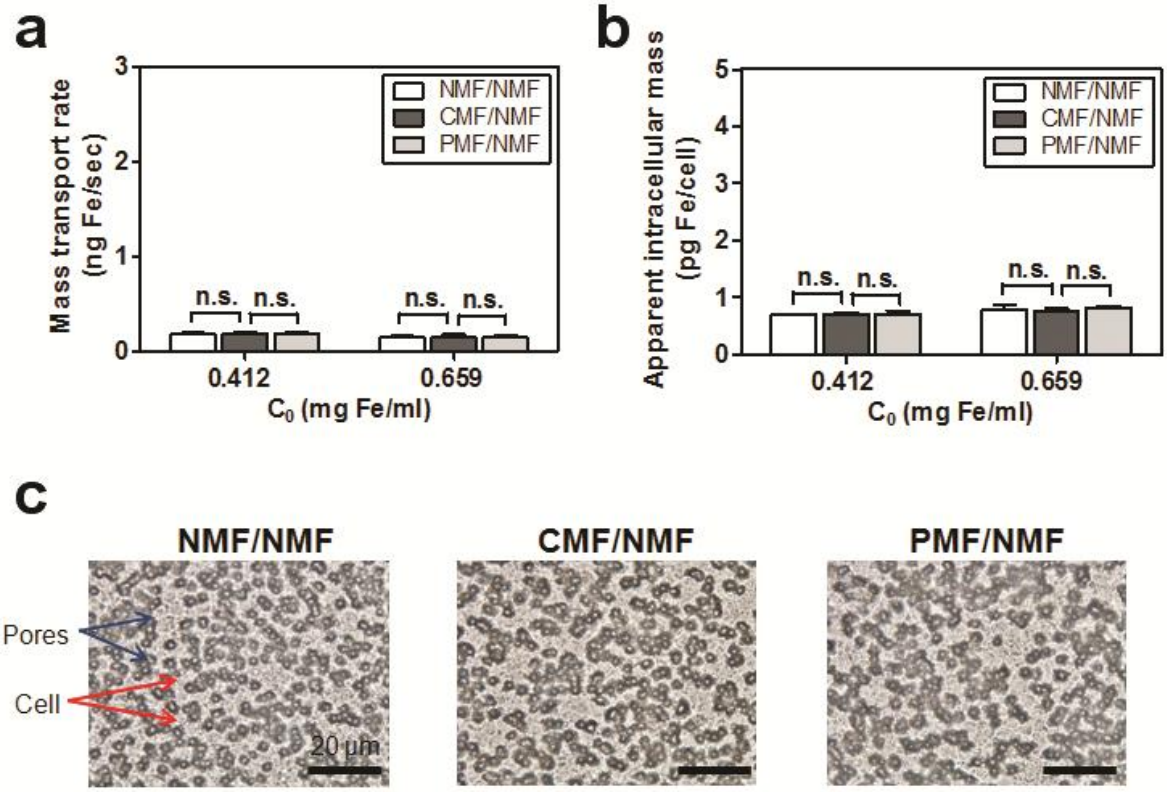

Figure A5. Mass transport of MNPs across MDCK cell monolayers was not affected by pre-exposure of MNPs to various magnetic field conditions.

NMF/NMF corresponds to "the cell experiments under no magnetic field (NMF) with MNPs pretreated with no magnetic field (NMF)"; CMF/NMF means "the experiments with MNPs pretreated with a constant magnetic field (CMF)"; and, PMF/NMF is "the experiments with MNPs pretreated with a pulsed magnetic field (PMF)" (N = 3). (a) Mass transport rates of pretreated MNPs and (b) apparent intracellular masses of MNPs per cell, after a 90 min transport, for different initial MNP concentrations (C_0: 0.412 or 0.659 mg Fe/ml) under no magnetic field conditions. (c) Microscopic images of cells after transport studies in the absence of magnetic field with MNPs pretreated with different magnetic

fields. Scale bars (20 μm) are presented in the images. For statistical analysis, one-way ANOVA test was used with Tukey's multiple comparison tests ($\alpha = 0.05$).

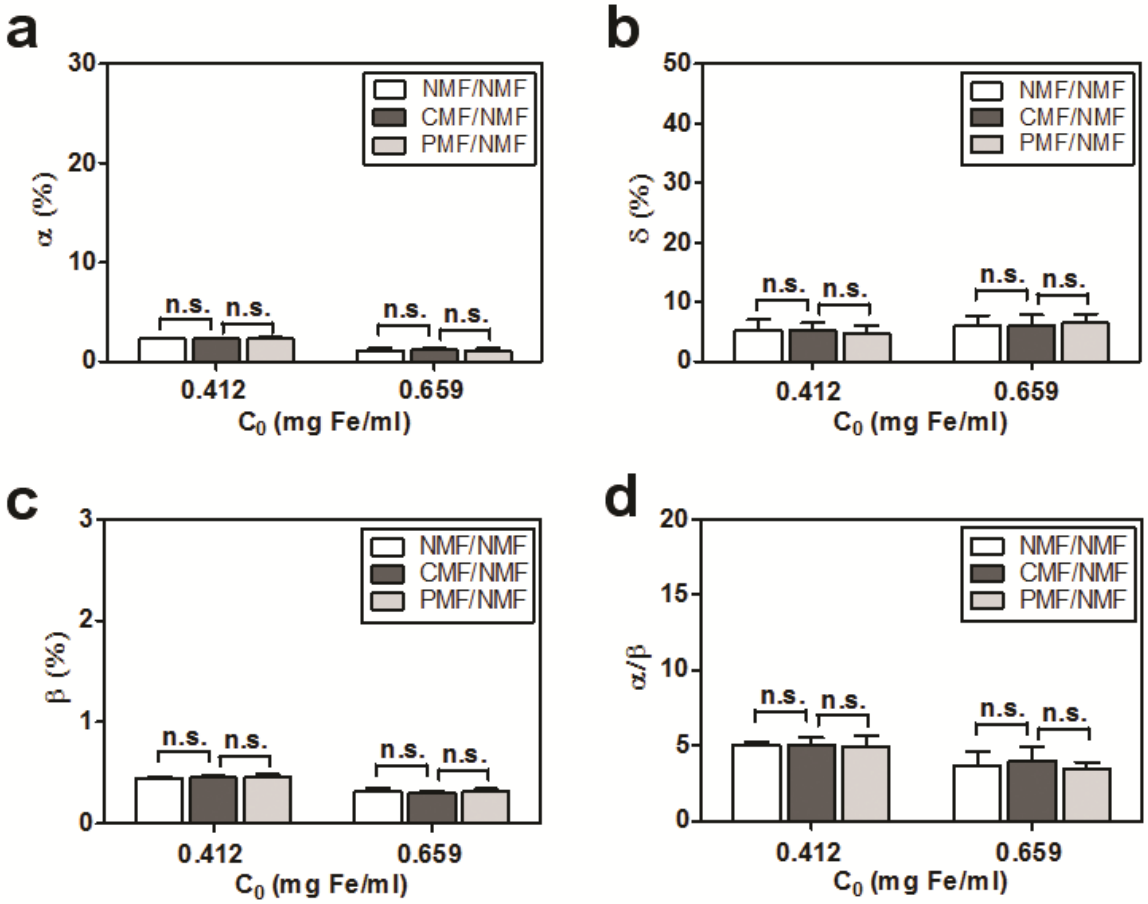

Figure A6. Mass balance analysis after transport experiments in the absence of magnet with MNPs pre-exposed to different magnetic field conditions.

Transport experiments were performed at 0.412 or 0.659 mg Fe/ml (C_0) and data were subjected to mass balance analysis (equations 1-5). (a) Apical-to-basolateral transported fraction of MNPs, α (%); (b) fraction of particles bound to the cell surface, δ (%); (c) fraction of particles inside the cells, β (%). (d) Ratio (α/β) is depicted at 0.412 or 0.659 mg Fe/ml under various magnetic field conditions for MNP pretreatments (NMF/NMF, CMF/NMF, or PMF/NMF). Statistical analysis was performed using one-way ANOVA with Tukey's multiple comparison tests ($\alpha = 0.05$).

Supplemental References

1. Chithrani, B. D.; Ghazani, A. A.; Chan, W. C. W. Determining the size and shape dependence of gold nanoparticle uptake into mammalian cells. Nano Lett. 2006;6(4): 662-8.
2. Chung, Y. I.; Kim, J. C.; Kim, Y. H.; Tae, G.; Lee, S. Y.; Kim, K.; Kwon, I. C. The effect of surface functionalization of PLGA nanoparticles by heparin- or chitosan-conjugated pluronic on tumor targeting. J Controlled Release. 2010;143(3):374-82.
3. Min, K. A.; Yu, F.; Yang, V. C.; Zhang, X.; Rosania, G. R. Transcellular transport of heparin-coated magnetic iron oxide nanoparticles (Hep-MION) under the influence of an applied magnetic field. Pharmaceutics. 2010;2(2):119-35.

Appendix B

Supporting Information in Chapter 4

Matlab Codes of the *in silico* model are available in online supporting information in the published paper (Yu J-y, Zheng N, Mane G, Min KA, Hinestroza JP, Zhu H, Stringer KA, Rosania GR. A Cell-based Computational Modeling Approach for Developing Site-Directed Molecular Probes. *PLoS Comput Biol.* 2012;8(2):e1002378)

Parameters and Sensitivity Analysis (*in silico* Model)

Table B1. Constant Parameters in the Model

Symbol	Value	Unit	Description
T	310.15	K	Body temperature
R	8.314	J / mol / K	Universal gas Constant
F	96485.3415	sA / mol	Faraday constant

Parameter abbreviations in Supplementary Tables below: L indicates the volumetric fraction of lipids (dimensionless), G indicates the activity coefficient γ (dimensionless), A indicates the surface area of the membrane (unit: m^2), *V* indicates the

volume of the corresponding compartment (unit: m^3). E indicates the membrane potential (unit: V), pH indicates the pH values in corresponding compartment (dimensionless). Ro indicates the volumetric percentage of organelles in cellular compartments (dimensionless). The subscripts *aEp* indicates the apical side of epithelial cells, *cEp* indicates the cytosol of epithelial, *imEp* indicates the macrophage/immune cells on the surface of epithelium, *int* indicates the interstitium, *imInt* indicates the immune cells in the interstitium, *sm* indicates the smooth muscle, *cEd* indicates the cytosol of endothelium, *p* indicates the plasma.

Table B2. Parameter values and sensitivity analysis of AUC (mg/ml*min) for alveoli

Para -meter	Default	Low	High	Mean	SD	CV	Trend
LaEp	0.95	0.05	0.95	0.06148	0.01861	0.3027	+
LimEp	0.05	0.005	0.5	0.09819	0.001462	0.01489	+
LcEp	0.05	0.005	0.5	0.09709	0.000794	0.008183	+
Lint	0	0.005	0.5	0.09702	0.00055	0.005668	+
LimInt	0.05	0.005	0.5	0.09621	5.61E-05	0.000583	+
LcEd	0.05	0.005	0.5	0.09863	0.001656	0.0168	+
Lp	0	0.005	0.5	0.09612	6.08E-12	6.33E-11	-
GaEpN	1	0.5	1.5	0.09677	0.005074	0.05243	-
GaEpD	1	0.5	1.5	0.1017	0.02376	0.2336	-
GimEpN	1.23	0.5	1.5	0.09614	1.45E-05	0.000151	-
GimEpD	0.74	0.5	1.5	0.09569	0.000605	0.006326	-
GcEpN	1.23	0.5	1.5	0.09613	7.49E-06	7.79E-05	-
GcEpD	0.74	0.5	1.5	0.09589	0.000346	0.003612	-
GintN	1	0.5	1.5	0.09612	6.30E-07	6.55E-06	-
GintD	1	0.5	1.5	0.09615	0.000236	0.002452	-
GimIntN	1.23	0.5	1.5	0.09612	6.24E-07	6.50E-06	-
GimIntD	0.74	0.5	1.5	0.0961	2.73E-05	0.000284	-
GcEdN	1.23	0.5	1.5	0.09613	1.86E-05	0.000194	-
GcEdD	0.74	0.5	1.5	0.09553	0.000717	0.007507	-
GpN	1	0.5	1.5	0.09612	6.88E-13	7.16E-12	+
GpD	1	0.5	1.5	0.09612	1.12E-11	1.17E-10	+

AaEp	0.387	0.0387	3.87	0.06819	0.04024	0.5901	-
Aabp	0.387	0.0387	3.87	0.09149	0.01539	0.1682	-
AimEp	0.0042	0.00042	0.042	0.101	0.003111	0.0308	+
AimInt	0.00042	0.000042	0.0042	0.09612	1.32E-09	1.37E-08	+
AbEd	0.452	0.0452	4.52	0.09261	0.008726	0.09422	-
AaEd	0.452	0.0452	4.52	0.09281	0.01073	0.1156	-
ASL	5	0.5	50	0.1065	0.01065	0.1001	+
Vint	2.68E-07	2.68E-08	2.68E-06	0.07264	0.01426	0.1963	-
Ro	0.1	0.01	0.5	0.09777	0.001412	0.01444	+
pHaEp	7.4	4	9	0.09607	0.003608	0.03756	+
pHimEp	7	4	9	0.09593	0.001094	0.01141	-
pHcEp	7	4	9	0.09889	0.005637	0.057	+
pHint	7	4	9	0.1004	0.008185	0.08152	+
pHimInt	7	4	9	0.09612	4.42E-05	0.00046	-
pHcEd	7	4	9	0.09596	0.002246	0.02341	-
PHp	7.4	4	9	0.09612	1.28E-11	1.33E-10	-
EbEd	-0.06	-0.12	0	0.09933	0.01645	0.1656	+
EaEd	-0.06	-0.12	0	0.09759	0.009574	0.0981	-
EimInt	-0.06	-0.12	0	0.09616	0.000112	0.001164	-
EimEp	-0.06	-0.12	0	0.09388	8.63E-05	0.000919	+
EbEp	0.0119	0	0.12	0.07161	0.01334	0.1863	-
EaEp	-0.0093	-0.12	0	0.04605	0.02446	0.1311	+

Table B3. Parameter values and sensitivity analysis of AUC (mg/ml*min) for airways

Para -meter	Default	Low	High	Mean	SD	CV	Trend
LaEp	0.2	0.05	0.95	8.555	0.8889	0.1039	+
LcEp	0.05	0.005	0.5	7.83	0.3157	0.04032	+
Lint	0	0.005	0.5	7.509	0.03813	0.005078	+
LimInt	0.05	0.005	0.5	7.452	0.003692	0.000495	+
Lsm	0.05	0.005	0.5	9.912	1.706	0.1721	+
LcEd	0.05	0.005	0.5	7.47	0.01523	0.002039	+
Lp	0	0.005	0.5	7.447	1.18E-08	1.58E-09	-
GaEpN	1	0.5	1.5	7.453	0.05194	0.006969	-
GaEpD	1	0.5	1.5	7.54	0.3954	0.05243	-
GcEpN	1.23	0.5	1.5	7.449	0.002974	0.000399	-
GcEpD	0.74	0.5	1.5	7.357	0.1376	0.01871	-
GintN	1	0.5	1.5	7.447	4.36E-05	5.85E-06	-
GintD	1	0.5	1.5	7.449	0.01635	0.002195	-
GimIntN	1.23	0.5	1.5	7.447	4.11E-05	5.52E-06	-
GimIntD	0.74	0.5	1.5	7.446	0.001797	0.000241	-
GsmN	1.23	0.5	1.5	7.461	0.01669	0.002237	-
GsmD	0.74	0.5	1.5	6.921	0.7033	0.1016	-
GcEdN	1.23	0.5	1.5	7.447	0.000171	2.30E-05	-
GcEdD	0.74	0.5	1.5	7.441	0.006594	0.000886	-
GpN	1	0.5	1.5	7.447	8.91E-09	1.20E-09	-

GpD	1	0.5	1.5	7.447	1.99E-08	2.67E-09	-
AaEp	1.08E-02	2.70E-03	4.32E-02	7.291	3.757	0.5153	-
AimInt	1.08E+04	1.08E-05	1.08E-03	7.447	8.62E-08	1.16E-08	+
Asm	2.16E-02	2.16E-03	2.16E-01	15.18	4.173	0.2749	+
AbEd	2.16E-03	5.40E-04	8.64E-03	7.152	1.164	0.1627	-
AaEd	2.16E-03	5.40E-04	8.64E-03	7.116	1.149	0.1614	-
ASL	15	1.5	150	4.889	1.849	0.3781	-
VcEp	7.20E-08	7.20E-09	7.20E-07	5.656	1.082	0.1912	-
Vint	1.08E-08	1.08E-09	1.08E-07	6.774	0.4348	0.06419	-
Vsm	4.70E-08	4.70E-09	4.70E-07	15.56	4.529	0.2911	+
pHaEp	7.4	4	9	7.448	0.1056	0.01418	-
pHcEp	7.0	4	9	7.409	0.07615	0.01028	-
pHint	7.0	4	9	7.805	0.6839	0.08762	+
pHsm	7.0	4	9	7.309	2.272	0.3109	-
pHimInt	7.0	4	9	7.446	0.002912	0.000391	-
pHcEd	7.0	4	9	7.445	0.02066	0.002775	-
pHp	7.4	4	9	7.447	3.19E-08	4.28E-09	-
EbEd	-0.06	-0.12	0	8.59	0.5854	0.06815	+
EaEd	-0.06	-0.12	0	7.79	0.2234	0.02868	-
Esm	-0.06	-0.12	0	10.46	6.49	0.6205	-
EimInt	-0.06	-0.12	0	7.449	0.007372	0.00099	-
EbEp	0.0119	0	0.12	6.296	0.6186	0.09824	-
EaEp	-0.0093	-0.12	0	6.958	0.3514	0.05051	+
Ro	0.1	0.01	0.5	10.44	2.555	0.2448	+

Table B4. Parameter values and sensitivity analysis of T_{SS} (min) for alveoli

Para -meter	Default	Low	high	Mean	SD	CV	Trend
LaEp	0.95	0.05	0.95	1.795	0.6543	0.3645	+
LimEp	0.05	0.05	0.5	3.297	0.1911	0.05796	+
LcEp	0.05	0.005	0.5	3.021	0.01608	0.005323	+
Lint	0	0.005	0.5	2.992	0.006055	0.002024	-
LimInt	0.05	0.005	0.5	3.016	0.01673	0.005546	+
LcEd	0.05	0.005	0.5	2.912	0.05801	0.01992	-
Lp	0	0.005	0.5	2.998	0.004398	0.001467	-
GaEpN	1	0.5	1.5	3.038	0.1957	0.06441	-
GaEpD	1	0.5	1.5	3.335	0.8703	0.261	-
GimEpN	1.23	0.5	1.5	3.002	0.002848	0.000949	-
GimEpD	0.74	0.5	1.5	2.97	0.05358	0.01804	-
GcEpN	1.23	0.5	1.5	3.001	0.001427	0.000476	+
GcEpD	0.74	0.5	1.5	2.994	0.007105	0.002373	-
GintN	1	0.5	1.5	3.001	0.001191	0.000397	+
GintD	1	0.5	1.5	2.997	0.004986	0.001664	+
GimIntN	1.23	0.5	1.5	2.999	0.002187	0.000729	+
GimIntD	0.74	0.5	1.5	2.998	0.004614	0.001539	-
GcEdN	1.23	0.5	1.5	2.998	0.004602	0.001535	+

GcEdD	0.74	0.5	1.5	3.024	0.03149	0.01041	+
GpN	1	0.5	1.5	3.001	0.00178	0.000593	-
GpD	1	0.5	1.5	2.998	0.004921	0.001641	-
AaEp	0.387	0.0387	3.87	3.259	0.725	0.2225	+
AbEp	0.387	0.0387	3.87	2.924	0.3595	0.1229	-
AimEp	0.0042	0.00042	0.042	2.956	0.03784	0.0128	-
AimInt	0.00042	4.19E-05	0.004192	2.997	0.009786	0.003266	-
AbEd	0.452	0.0452	4.52	2.7	0.2743	0.1016	-
AaEd	0.452	0.0452	4.52	2.774	0.3023	0.109	-
ASL	5	0.5	50	15.3	9.311	0.6087	+
Vint	2.68E-07	2.68E-08	2.68E-06	2.983	0.009908	0.003322	-
EaEp	-0.0093	-0.12	0	1.162	0.08901	0.07661	+
EbEp	0.0119	0	0.12	1.651	0.0762	0.04614	-
EimEp	-0.06	-0.12	0	3.147	0.293	0.09308	-
EimInt	-0.06	-0.12	0	3.007	0.01809	0.006017	-
EbEd	-0.06	-0.12	0	3.338	1.073	0.3214	+
EaEd	-0.06	-0.12	0	3.119	0.3052	0.09785	-
pHaEp	7.4	4	9	2.998	0.09591	0.03199	+
pHimEp	7	4	9	2.977	0.08239	0.02767	-
pHcEp	7	4	9	3.138	0.2374	0.07565	+
pHint	7	4	9	3.226	0.3662	0.1135	+
pHimInt	7	4	9	2.998	0.004545	0.001516	-
pHcEd	7	4	9	3.063	0.1185	0.03868	+
pHp	7.4	4	9	2.997	0.005152	0.001719	-
Ro	0.1	0.01	0.5	2.921	0.06519	0.02232	-

Table B5. Parameter values and sensitivity analysis of T_{SS} (min) for airways

Para -meter	default	low	High	Mean	SD	CV	Trend
LaEp	0.2	0.05	0.95	34.37	3.208	0.09334	+
LcEp	0.05	0.005	0.5	32.61	1.097	0.03365	+
Lint	0	0.005	0.5	31.26	0.1733	0.005542	+
LimInt	0.05	0.005	0.5	30.99	0.05303	0.001711	-
Lsm	0.05	0.005	0.5	41.89	7.162	0.171	+
LcEd	0.05	0.005	0.5	31	0.05826	0.001879	-
Lp	0	0.005	0.5	30.96	0.0523	0.001689	+
GaEpN	1	0.5	1.5	31	0.1873	0.006043	-
GaEpD	1	0.5	1.5	31.48	1.314	0.04172	-
GcEpN	1.23	0.5	1.5	30.93	0.03826	0.001237	+
GcEpD	0.74	0.5	1.5	30.65	0.4926	0.01607	-
GintN	1	0.5	1.5	30.93	0.02438	0.000788	-
GintD	1	0.5	1.5	30.99	0.09294	0.002999	-
GimIntN	1.23	0.5	1.5	30.92	0.03475	0.001124	+
GimIntD	0.74	0.5	1.5	30.97	0.04729	0.001527	-

GsmN	1.23	0.5	1.5	31.03	0.1006	0.003242	-
GsmD	0.74	0.5	1.5	28.41	3.055	0.1075	-
GcEdN	1.23	0.5	1.5	30.95	0.04532	0.001465	-
GcEdD	0.74	0.5	1.5	30.95	0.04737	0.00153	+
GpN	1	0.5	1.5	30.93	0.02644	0.000855	+
GpD	1	0.5	1.5	30.97	0.05493	0.001774	-
AaEp	1.08E-02	2.70E-03	4.32E-02	31.08	10.23	0.3292	-
AimInt	1.08E+04	1.08E-05	1.08E-03	30.96	0.04623	0.001493	-
Asm	2.16E-02	2.16E-03	2.16E-01	124.4	66.76	0.5367	-
AbEd	2.16E-03	5.40E-04	8.64E-03	22.11	9.556	0.4322	-
AaEd	2.16E-03	5.40E-04	8.64E-03	22.8	10.32	0.4529	-
ASL	15	1.5	150	50.52	15.21	0.301	+
VcEp	7.20E-08	7.20E-09	7.20E-07	45.77	10.24	0.2237	+
Vint	1.08E-08	1.08E-09	1.08E-07	32.05	0.7181	0.02241	+
Vsm	4.70E-08	4.70E-09	4.70E-07	124.4	66.76	0.5367	+
EaEp	-0.0093	-0.12	0	28.33	1.249	0.04409	+
EbEp	0.0119	0	0.12	26.38	2.277	0.08634	-
Esm	-0.06	-0.12	0	40.18	26.64	0.6632	-
EimInt	-0.06	-0.12	0	30.99	0.06302	0.002034	-
EbEd	-0.06	-0.12	0	47.79	3.545	0.07418	+
EaEd	-0.06	-0.12	0	34.99	1.05	0.03001	-
pHaEp	7.4	4	9	30.98	0.2709	0.008745	-
pHcEp	7	4	9	30.79	0.2611	0.008477	-
pHint	7	4	9	32.87	3.068	0.09333	+
pHimInt	7	4	9	30.95	0.05372	0.001736	+

pHcEd	7	4	9	30.94	0.05553	0.001795	-
pHp	7.4	4	9	30.97	0.06052	0.001954	+
Ro	0.1	0.01	0.5	51.29	17.51	0.3415	+

Table B6. Parameter values and sensitivity analysis of mass deposition for alveoli (mass fraction in lungs)

Para-meter	Default	low	high	Mean	SD	CV	Trend
LaEp	0.95	0.05	0.95	0.8867	0.02451	0.02764	+
LimEp	0.05	0.005	0.5	0.9215	0.000416	0.000452	+
LcEp	0.05	0.005	0.5	0.9215	0.000432	0.000469	+
Lint	0	0.005	0.5	0.9222	0.001027	0.001114	+
LimInt	0.05	0.005	0.5	0.921	9.63E-05	0.000105	+
LcEd	0.05	0.005	0.5	0.9276	0.004776	0.005148	+
Lp	0	0.005	0.5	0.8295	0.05402	0.06512	-
GaEpN	1	0.5	1.5	0.9153	0.003549	0.003877	-
GaEpD	1	0.5	1.5	0.9181	0.01396	0.01521	-
GimEpN	1.23	0.5	1.5	0.9147	4.31E-06	4.71E-06	-
GimEpD	0.74	0.5	1.5	0.9146	0.000202	0.00022	-

GcEpN	1.23	0.5	1.5	0.9147	4.96E-06	5.43E-06	-
GcEpD	0.74	0.5	1.5	0.9146	0.000211	0.000231	-
GintN	1	0.5	1.5	0.9147	1.22E-05	1.34E-05	-
GintD	1	0.5	1.5	0.9149	0.000565	0.000618	-
GimIntN	1.23	0.5	1.5	0.9147	9.48E-07	1.04E-06	-
GimIntD	0.74	0.5	1.5	0.9147	3.95E-05	4.32E-05	-
GcEdN	1.23	0.5	1.5	0.9148	6.31E-05	6.89E-05	-
GcEdD	0.74	0.5	1.5	0.9133	0.002762	0.003024	-
GpN	1	0.5	1.5	0.9147	1.79E-09	1.95E-09	+
GpD	1	0.5	1.5	0.9097	0.02491	0.02738	+
AaEp	0.387	0.0387	3.87	0.9279	0.02019	0.02176	+
AbEp	0.387	0.0387	3.87	0.9208	2.48E-15	2.70E-15	-
AimEp	0.0042	0.00042	0.042	0.9242	0.002247	0.002431	+
AimInt	0.00042	4.19E-05	0.004192	0.9208	2.61E-15	2.83E-15	-
AbEd	0.452	0.0452	4.52	0.9511	0.01806	0.01899	+
AaEd	0.452	0.0452	4.52	0.9208	2.30E-15	2.50E-15	+
ASL	5	0.5	50	0.9693	0.02505	0.02584	+
Vint	2.68E-07	2.68E-08	2.68E-06	0.9266	0.004073	0.004395	+
EaEp	-0.0093	-0.12	0	0.7143	0.1568	0.2196	+
EbEp	0.0119	0	0.12	0.8432	0.05729	0.06795	-
EimEp	-0.06	-0.12	0	0.921	0.00079	0.000858	-
EimInt	-0.06	-0.12	0	0.9209	0.000192	0.000209	-
EbEd	-0.06	-0.12	0	0.9152	0.05026	0.05491	+
EaEd	-0.06	-0.12	0	0.8826	0.09135	0.1035	-
pHaEp	7.4	4	9	0.9213	0.002439	0.002647	+

pHimEp	7	4	9	0.9207	0.000335	0.000364	-
pHcEp	7	4	9	0.9246	0.006427	0.006951	+
pHint	7	4	9	0.9279	0.01363	0.01469	+
pHimInt	7	4	9	0.9208	6.61E-05	7.18E-05	-
pHcEd	7	4	9	0.9169	0.008666	0.009452	-
pHp	7.4	4	9	0.9284	0.01869	0.02013	+
Ro	0.1	0.01	0.5	0.9302	0.008617	0.009263	+

Table B7. Parameter and sensitivity analysis of mass deposition for airways (mass fraction in lungs)

Para-meter	Default	low	high	Mean	SD	CV	Trend
LaEp	0.2	0.05	0.95	0.08661	0.006106	0.0705	+
LcEp	0.05	0.005	0.5	0.08279	0.002397	0.02896	+
Lint	0	0.005	0.5	0.07976	0.000444	0.00556	+
Lsm	0.05	0.005	0.5	0.1035	0.01537	0.1485	+
LimInt	0.05	0.005	0.5	0.07923	3.87E-05	0.000489	+
LcEd	0.05	0.005	0.5	0.07966	0.000349	0.004382	+
Lp	0	0.005	0.5	0.03946	0.001595	0.04042	-
GaEpN	1	0.5	1.5	0.07924	0.000363	0.004582	-
GaEpD	1	0.5	1.5	0.08016	0.002608	0.03254	-

GcEpN	1.23	0.5	1.5	0.07919	2.40E-05	0.000303	-
GcEpD	0.74	0.5	1.5	0.07833	0.001	0.01277	-
GintN	1	0.5	1.5	0.07917	6.29E-06	7.94E-05	-
GintD	1	0.5	1.5	0.07929	0.00027	0.003408	-
GsmN	1.23	0.5	1.5	0.07936	0.000182	0.002295	-
GsmD	0.74	0.5	1.5	0.07293	0.007359	0.1009	-
GimIntN	1.23	0.5	1.5	0.07917	4.28E-07	5.40E-06	-
GimIntD	0.74	0.5	1.5	0.07916	1.75E-05	0.000221	-
GcEdN	1.23	0.5	1.5	0.07917	3.46E-06	4.36E-05	-
GcEdD	0.74	0.5	1.5	0.07904	0.00013	0.00165	-
GpN	1	0.5	1.5	0.07913	0.000155	0.001964	+
GpD	1	0.5	1.5	0.07391	0.002036	0.02755	+
AaEp	1.08E-02	2.70E-03	4.32E-02	0.08063	0.00408	0.0506	+
AimInt	1.08E+04	1.08E-05	1.08E-03	0.07945	0.000201	0.002525	+
Asm	2.16E-02	2.16E-03	2.16E-01	0.2206	0.1051	0.4766	+
AbEd	2.16E-03	5.40E-04	8.64E-03	0.07947	0.000445	0.005597	+
AaEd	2.16E-03	5.40E-04	8.64E-03	0.0833	0.002652	0.03184	+
Vint	1.08E-08	1.08E-09	1.08E-07	0.08255	0.00229	0.02774	+
EaEp	-0.0093	-0.12	0	0.07357	0.002812	0.03823	+
EbEp	0.0119	0	0.12	0.0688	0.005865	0.08524	-
Esm	-0.06	-0.12	0	0.09275	0.06086	0.6562	-
EimInt	-0.06	-0.12	0	0.0792	8.91E-05	0.001125	-
EbEd	-0.06	-0.12	0	0.1321	0.01128	0.08541	+
EaEd	-0.06	-0.12	0	0.0943	0.007571	0.08028	-
pHaEp	7.4	4	9	0.07907	0.00068	0.008595	-

pHcEp	7	4	9	0.07879	0.000626	0.007948	-
pHint	7	4	9	0.08395	0.007481	0.08911	+
pHsm	7	4	9	0.07023	0.02485	0.3538	-
pHimInt	7	4	9	0.07916	3.29E-05	0.000416	-
pHcEd	7	4	9	0.07901	0.000458	0.005797	-
pHp	7.4	4	9	0.09632	0.003901	0.0405	+
Ro	0.1	0.01	0.5	0.119	0.03917	0.3292	+

Appendix C

Supporting Information in Chapter 5

I. Supporting information with experimental results and equations

1. Morphological Examination of Pure Calu-3 or NHBE Cultures under Air-Liquid Interfaced (ALI) Conditions.

Throughout the days of ALI cultures, the Calu-3 or NHBE cells in the inserts were examined by confocal microscopy. On day 3, Calu-3 cells had imperfect cell intactness with sparse cuboidal shaped-cells on the membrane as shown in yz planes (Figure C1a). After day 6, columnar cells became compact with the neighboring cells. In contrast, the differentiated NHBE cells showed multilayer formation from day 3 with various cell layer thicknesses (Figure C1b). Moreover, cell morphologies were different in the top and bottom cell layers of NHBE. Cells in the bottom layers of NHBE were cuboidal and columnar shape whereas the top layer consisted of squamous cells.

In the imaging analyses by Metamorph, Calu-3 cells showed consistency in cell area with the averages of 188.2 μm^2 (± 37.3, S.D.), 173.8 μm^2 (± 45.5) and179.9 μm^2 (± 36.9)

on day 6, 8, and 10, respectively (Figure C2a). But, there was statistically significant difference in cell area on day 3 from other days ($P < 0.0001$), having the average, 255.9 μm^2 (± 58.1). This difference in cell area could be explained by cell height of the Calu-3 cells in different days. On day 3, the cells had 7.5 μm of cell height in average (± 1.12) whereas cell height were 11.6 μm (± 2.61), 12.3 μm (± 2.02) and 11.1 μm (± 1.44) on day 6, 8, and 10. As the cells became compact with the neighboring cells, there would be more columnar cells with larger cell height and smaller cell area. Especially, on day 8, the cells had largest cell heights with 11 μm as a 25 % percentile and 16 μm as a 75 % percentile. The cells on day 6 had 25 % and 75 % percentiles with 10 and 16 μm, similar to day 8, but containing more cuboidal cells. Cell volume of Calu-3 cells showed no differences on day 6, 8, and 10 except for day 3.

On the other hand, NHBE cells were analyzed for the cells in top (T) or bottom (B) layers (Figure C2b). For the cell area, bottom cells had almost the same cell area on day 3, 6, 8, and 10 while top cell area on day 6, 8 and 10 was different from that on day 3 and bigger than the bottom cell area. Cell heights in bottom layers reflect mixed cell shapes of cuboidal and columnar cells, ranging from 6 to 13 μm. Top layers had smaller cell heights with 7.77 μm (± 0.99), 6.42 μm (± 1.30) and 6.65 μm (± 1.44) on average on day 6, 8 and 10. Bottom cells in NHBE on day 3 had smaller cell volume than those in different days ($P<0.01$), reflecting that NHBE on day3 might not be fully differentiated, yet. Cell volume of bottom cells on day 6, day 8 and 10 were 5570 μm^3 (± 1042), 6005 μm^3 (± 1103) and 5682 μm^3 (± 1241), but those of top cells were larger with 8083 μm^3 (± 1364), 7721 μm^3 (± 1288) and 8379 μm^3 (± 1448) on average. The morphological

parameters are consistent with the cell morphologies in the confocal images, showing that NHBE bottom cells are more cuboidal and columnar and top cells squamous.

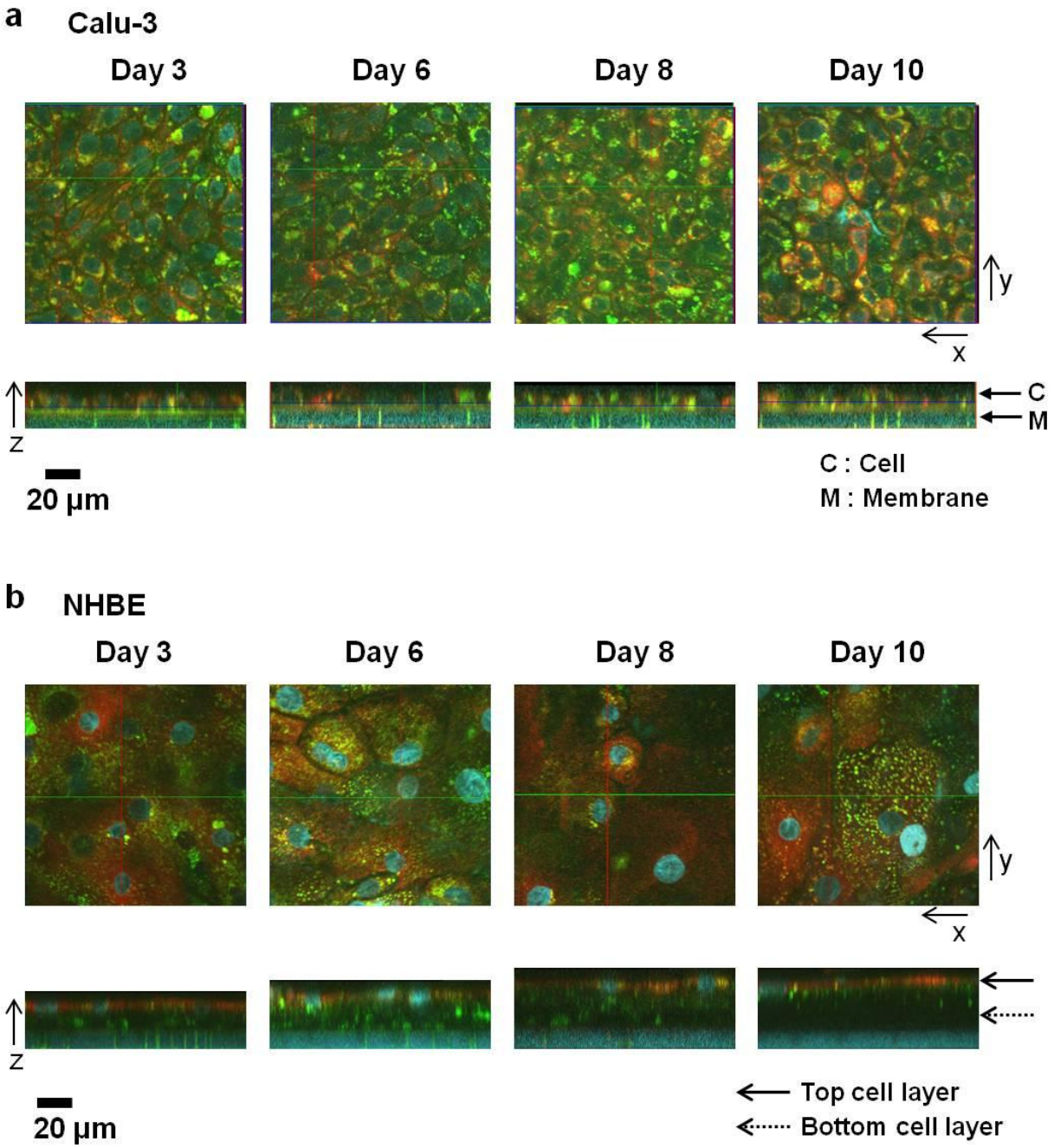

Figure C1. Cytometric examination in the Calu-3 or NHBE cells under Confocal microscopy.

(**a**) Calu-3 or (**b**) NHBE cells were grown on the porous PET (polyester) membrane (area: 0.33 cm^2, pore size: 0.4 μm) in the Transwell inserts under ALI condition. In different days of the cultures (day 3, 6, 8, and 10), the cells in the inserts were washed with HBSS buffer twice and then, incubated with the mixed dye solutions including MTR,

Hoe, and LTG. The cell suborganelles (mitochondria (red), cell nuclei (blue), and lysosomes (green)) were visualized in xy and also yz planes. Cell architectures in the inserts are apparently shown in yz planes with the indications of the arrows for the cells (C) and the membrane (M). The scale bars are placed under the images as 20 μm.

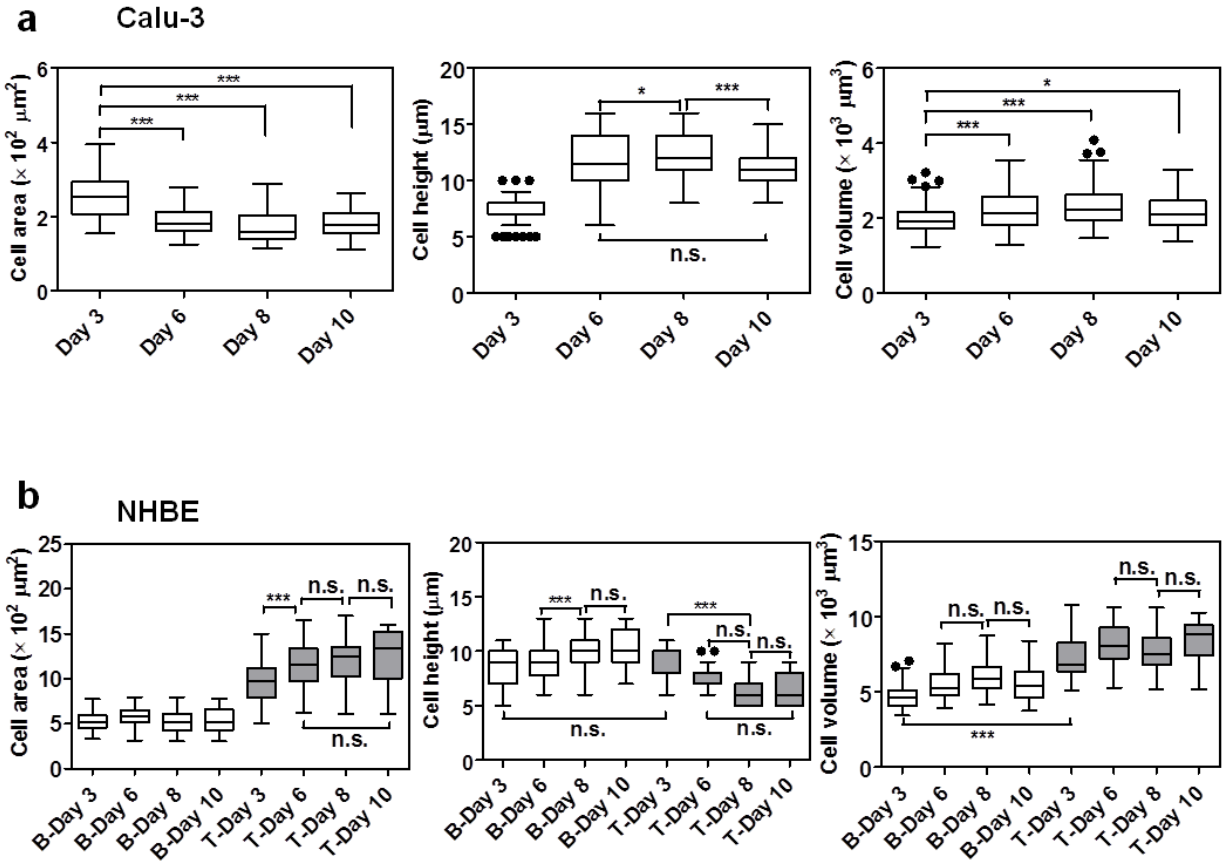

Figure C2. Variations in the morphological parameters of Calu-3 or NHBE cells on different days of ALI cultures.

(**a, b**) Cell area, height, and volume on day 3, 6, 8, and 10 are displayed for the (**a**) Calu-3 or (**b**) NHBE cells after image analyses by Metamorph. Data are presented as mean ± SD. Box-whisker plots showing median and interquartile range with whisker ends were depicted after the post-hoc multiple mean comparison (Tukey's test, $p < 0.05$). Statistical analyses were performed with Tukey's multiple comparison test with the 5 % significance level. (**a**) Calu-3 cells showed variations in the cell area, height, and volume through the ALI cultures. On day 3, cell area, height, and cell volume was statistically significant differences from the other days of cultures ($p<0.001$). Calu-3 cells developed

more columnar cells on day 6 and 8 than day 3 or 10 from the comparison of cell heights. Cell volume was consistent from day 6 until day 10. (**b**) In the NHBE cell multilayers in differentiation medium, bottom (B) and top (T) cell layers showed differences in cell area, height, and volume throughout the cultures. n.s.=not significant, *$P < 0.05$, **$P < 0.001$, ***$P < 0.0001$.

2. Mixed Cell Co-Cultures of Calu-3 and NHBE Cells

Cell seeding densities were 5×10^5 cells/cm^2 (16.5×10^5 cells/ml) for Calu-3 cells and 2.5×10^5 cells/cm^2 (8.25×10^5 cells/ml) for NHBE cells. As summarized in Table C1, for 99:1 (C:N = Calu-3:NHBE) ratio, 99 μl of Calu-3 cell suspension (16.5×10^5 cells/ml) was mixed with 1 μl of NHBE cell suspension (8.25×10^5 cells/ml) to make 100 μl of the mixed cell suspension. For 9:1, 1:1, 1:9, and 1:99 (C:N), cell suspensions were mixed with 90 μl of Calu-3 and 10 μl of NHBE for 9:1, 50 μl of Calu-3 and 50 μl of NHBE for 1:1, 10 μl of Calu-3 and 90 μl of NHBE for 1:9, 1 μl of Calu-3 and 99 μl of NHBE for 1:99. Therefore, the mixed volume ratios (99:1, 9:1, 1:1, 1:9 and 1:99) were corresponded to mixed cell number ratios (99:1, 95:5, 67:33, 18:82 and 2:98).

Table C1. Cell plating ratios of Calu-3 and NHBE cells for mixed cell co-cultures.

	Mixed cells (Calu-3: NHBE)				
Volume ratio (v/v)	99:1	9:1	1:1	1:9	1:99
Cell number ratio	99:1	95:5	67:33	18:82	2:98
Calu-3 suspension (μl)	99	90	50	10	1
NHBE suspension (μl)	1	10	50	90	99

3. Parameter Sensitivity Analysis

Table C2. Ranges of the input parameters for optimization for Calu-3 and NHBE in a monolayer.

Parameters (units)	Values or range
[a]pKa	9.67
[a]logPn	2.58
[a]logPd	-0.66
A_insert (cm^2)	0.33
[b]A_a (μm^2)	[79, 538×50]
[b]A_aq (μm^2)	[79, 538]
[b]A_bq (μm^2)	[79, 538]
A_m (μm^2)	314
A_l (μm^2)	314
[b]A_b (μm^2)	[A_pore_cell, 538]
	$\text{A\_pore\_cell} = \frac{\text{Pore density} \times \text{A\_insert}}{\text{Cell numbers}} \times \text{Area of single pore}$
[b]V_c (μm^3)	[1239, 8483]
[c]H_aq (μm)	[10^{-3}, 500]
[c]H_bq (μm)	[10^{-3}, 500]
[d]V_at (ml)	0.11
[d]V_at (ml)	0.6
[e]V_a (ml)	5.5556×10^{-7}
[e]V_b (ml)	3.0303×10^{-6}
V_m (μm^3)	524
V_l (μm^3)	524
L_c	[0.05, 0.15]
L_m	[0.05, 0.15]
L_l	[0.05, 0.15]
E_a (V)	[-0.0143, -0.0043]
E_m (V)	[-0.21, -0.11]
E_l (V)	[0.005, 0.015]
E_b (V)	[0.0069, 0.0169]

pH_a	[6.0, 7.8]
pH_c	[7.0, 7.8]
pH_m	[7.7, 8.2]
pH_l	[4.8, 6.0]
pH_b	[7.0, 7.8]

Electrical potential (E), pH in each compartment, lipid fractions (L) were varied within the range reported by X. Zhang *et al*.(1). Area and volume of mitochondria or lysosomes were fixed with the values reported (1).

a. Physicochemical properties of PR were calculated by Chemaxon software, consistent with other softwares (2).
b. Ranges of apical membrane surface area (A_a), apical or basolateral unstirred water layer surface area (A_aq or A_bq) and cell volume (V_c) were based on the experimental data from the quantitative imaging analyses (Table S1). Lower boundary value is based on the minimum value (surface area or cell volume) of Calu-3 and upper boundary value on the maximum value of NHBE cell in the monolayer condition. Ranges of basolateral membrane surface area (A_b) were determined between total pore area per one cell (A_pore_cell) and maximum surface area of NHBE cell. A_pore_cell was calculated with the equation described using pore density (4×10^6 pores/cm^2 from a manufacture report), area of an insert, cell numbers, and area of single pore (diameter of one pore = 0.4 μm) based on an assumption that a pore is a circle.
c. T. Korjamo, *et al*.(3)
d. Apical and basolateral bulk volume (V_at and V_bt) were fixed with the experimental conditions.
e. Range of apical and basolateral solution volume per cell (V_a and V_b) were determined from the bulk solution volume normalized by cell numbers. Cell density in the insert was fixed as 6×10^5 cells/cm^2 based on the experimental conditions. Cell numbers were calculated from the cell density multiplied by area of insert (A_insert).

a

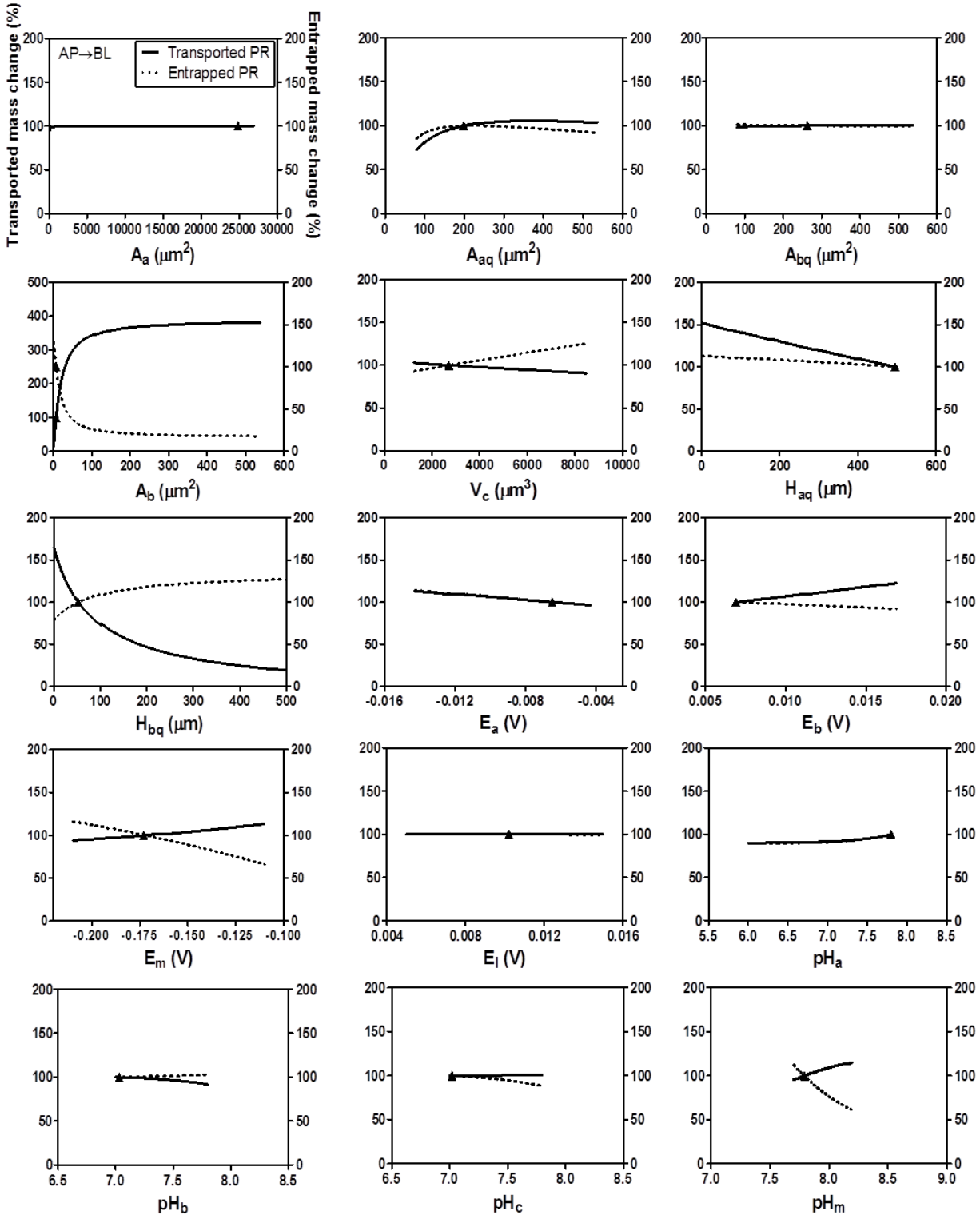
Transported mass change (%)
Entrapped mass change (%)
AP→BL
Transported PR
Entrapped PR
A_a (μm^2)
A_{aq} (μm^2)
A_{bq} (μm^2)
A_b (μm^2)
V_c (μm^3)
H_{aq} (μm)
H_{bq} (μm)
E_a (V)
E_b (V)
E_m (V)
E_l (V)
pH_a
pH_b
pH_c
pH_m

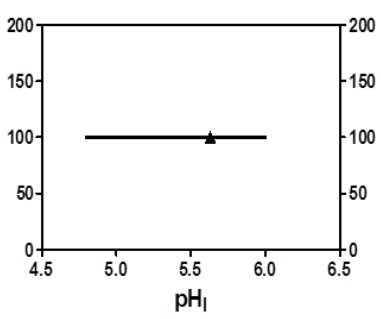
200
150
100
50
0
4.5
5.0
5.5
6.0
6.5
pH_I

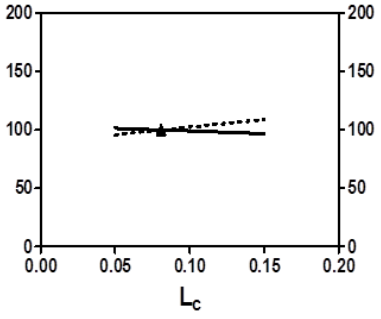
200
150
100
50
0
0.00
0.05
0.10
0.15
0.20
L_c

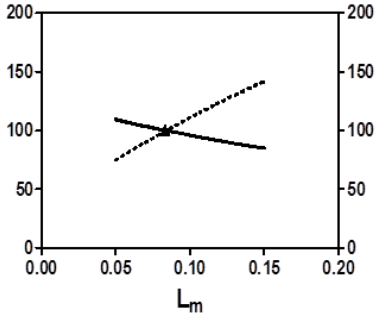
200
150
100
50
0
0.00
0.05
0.10
0.15
0.20
L_m

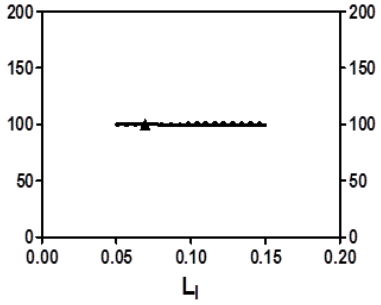
200
150
100
50
0
0.00
0.05
0.10
0.15
0.20
L_I

b

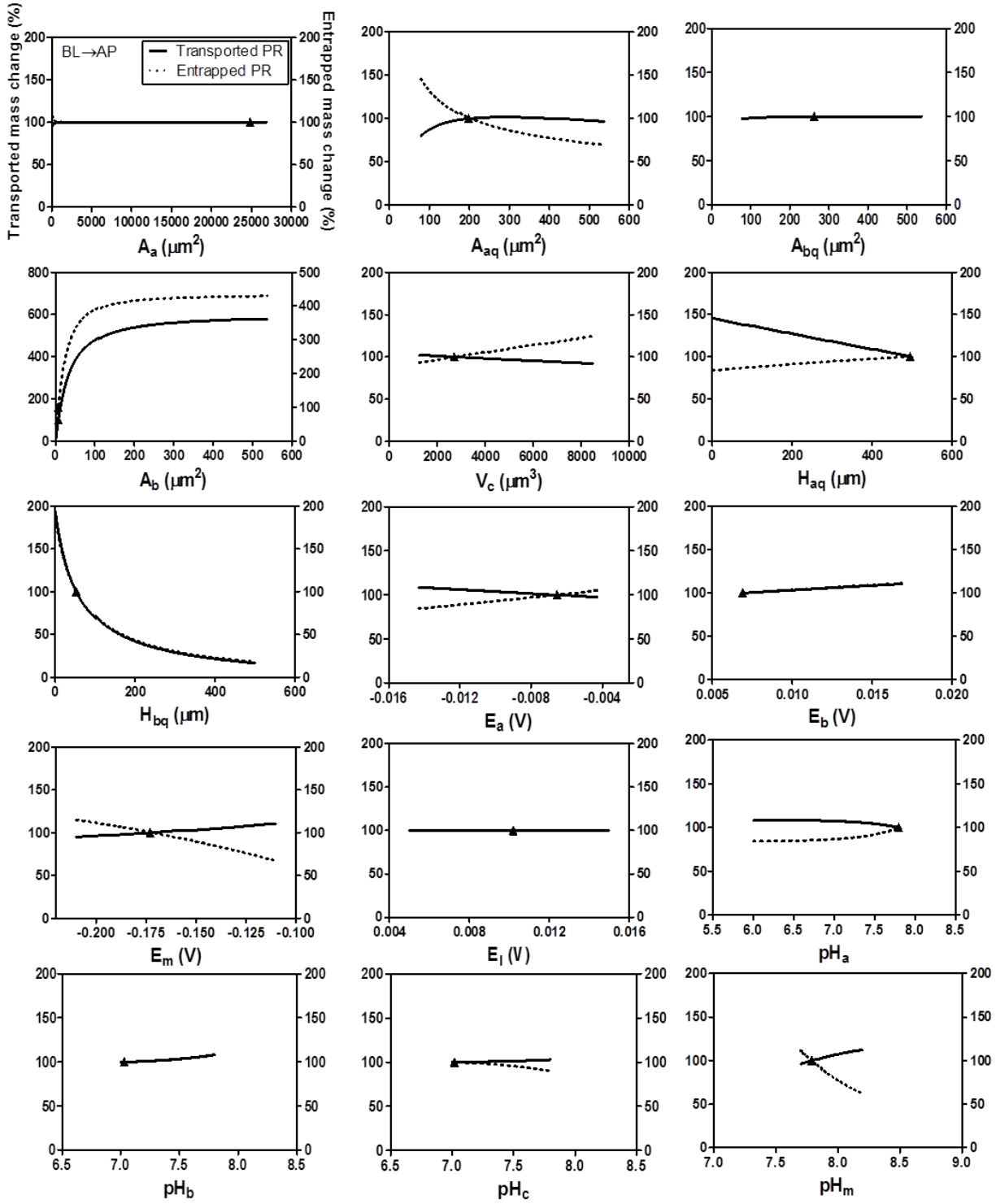
BL→AP
Transported PR
Entrapped PR
Transported mass change (%)
Entrapped mass change (%)
A_a (μm^2)
A_{aq} (μm^2)
A_{bq} (μm^2)
A_b (μm^2)
V_c (μm^3)
H_{aq} (μm)
H_{bq} (μm)
E_a (V)
E_b (V)
E_m (V)
E_l (V)
pH_a
pH_b
pH_c
pH_m

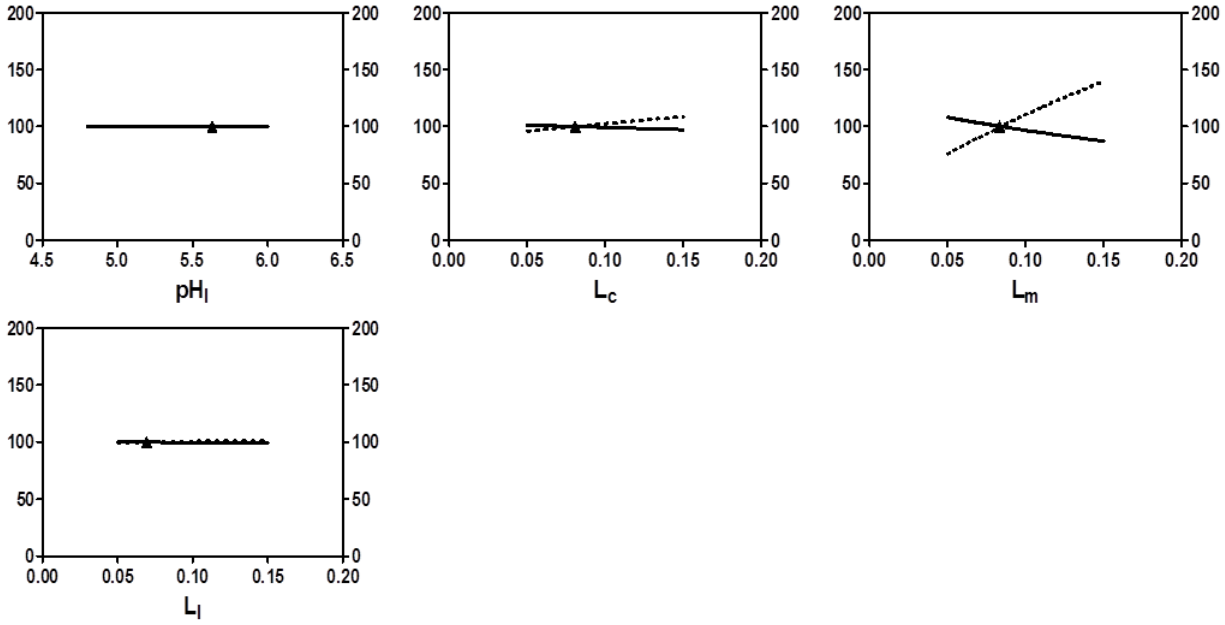

Figure C3. Parameter sensitivity analysis results at 50 μM PR, 1h transport ((**a**) AP→BL; (**b**) BL→AP) in Calu-3 cell model.

For each individual parametric analysis, one parameter was changed and other parameters were fixed with the optimized values in Table C1. Test results are depicted as percentages (%) relative to the values (Transported mass and entrapped mass) at the optimized parameters for Calu-3 (indicated as closed triangle in the plots).

4. Mass Flux Equations across the Compartments in the Model

Mass fluxes per unit area from 1 to 2 compartment ($J_{1,2}$) are expressed with the following equations (S-Eqs. 1-7). The subscripts (a, aq, c, m, l, M, bq, and b) mean apical, apical unstirred water layer, cytosol, mitochondria, lysosomes, basolateral porous membrane, basolateral unstirred water layer, basolateral compartments. Neutral and ionized forms of PR are indicated as n and d.

$$J_{a,aq} = P_a(f_{n,a}C_a - f_{n,aq}C_{aq}) \qquad \text{S-Eq. 1}$$

$$J_{aq,c} = P_n(f_{n,a}C_{aq} - f_{n.c}C_c) + P_d \frac{N_a}{e^{N_a} - 1}(f_{d,a}C_{aq} - f_{d,c}C_c e^{N_a}) \quad \text{S-Eq. 2}$$

$$J_{c,m} = P_n(f_{n,c}C_c - f_{n.m}C_m) + P_d \frac{N_m}{e^{N_m} - 1}(f_{d,c}C_c - f_{d,m}C_m e^{N_m}) \quad \text{S-Eq. 3}$$

$$J_{c,l} = P_n(f_{n,c}C_c - f_{n.l}C_l) + P_d \frac{N_l}{e^{N_l} - 1}(f_{d,c}C_c - f_{d,l}C_l e^{N_l}) \quad \text{S-Eq. 4}$$

$$J_{c,M} = P_n(f_{n,c}C_c - f_{n.M}C_M) + P_d \frac{N_b}{e^{N_b} - 1}(f_{d,c}C_c - f_{d,b}C_b e^{N_b}) \quad \text{S-Eq. 5}$$

$$J_{M,bq} = P_b(f_{n,M}C_M - f_{n,bq}C_{bq}) \quad \text{S-Eq. 6}$$

$$J_{bq,b} = P_b(f_{n,bq}C_{bq} - f_{n,b}C_b) \quad \text{S-Eq. 7}$$

5. Ordinary Differential Equations of Concentrations at 8 Compartments in the Model for Both Directions ((a) AP→BL; (b) BL→AP)

Concentration changes with the time in each compartment are expressed as S-Eqs. 8-15 for AP→BL and S-Eqs. 16-23 for BL→AP transport.

(**a**) AP→BL

$$\frac{dC_a}{dt} = -\frac{A_{aq}}{V_a} J_{a,aq} \quad \text{S-Eq. 8}$$

$$\frac{dC_{aq}}{dt} = \frac{A_{aq}}{V_{aq}} J_{a,aq} - \frac{A_a}{V_{aq}} J_{aq,c} \quad \text{S-Eq. 9}$$

$$\frac{dC_c}{dt} = \frac{A_a}{V_c} J_{aq,c} - \frac{A_m}{V_c} J_{c,m} - \frac{A_l}{V_c} J_{c,l} - \frac{A_b}{V_c} J_{c,M} \quad \text{S-Eq. 10}$$

$$\frac{dC_m}{dt} = \frac{A_m}{V_m} J_{c,m}$$ S-Eq. 11

$$\frac{dC_l}{dt} = \frac{A_l}{V_l} J_{c,l}$$ S-Eq. 12

$$\frac{dC_M}{dt} = \frac{A_b}{V_{bM}} J_{c,M} - \frac{A_{bM}}{V_{bM}} J_{M,bq}$$ S-Eq. 13

$$\frac{dC_{bq}}{dt} = \frac{A_{bM}}{V_{bq}} J_{M,bq} - \frac{A_{bq}}{V_{bq}} J_{bq,b}$$ S-Eq. 14

$$\frac{dC_b}{dt} = \frac{A_{bq}}{V_b} J_{bq,b}$$ S-Eq. 15

(**b**) BL→AP

$$\frac{dC_b}{dt} = -\frac{A_{bq}}{V_b} J_{b,bq}$$ S-Eq. 16

$$\frac{dC_{bq}}{dt} = \frac{A_{bq}}{V_{bq}} J_{b,bq} - \frac{A_{bM}}{V_{bq}} J_{M,c}$$ S-Eq. 17

$$\frac{dC_M}{dt} = \frac{A_{bM}}{V_{bM}} J_{bq,M} - \frac{A_b}{V_{bM}} J_{M,c}$$ S-Eq. 18

$$\frac{dC_c}{dt} = \frac{A_b}{V_c} J_{M,c} - \frac{A_m}{V_c} J_{c,m} - \frac{A_l}{V_c} J_{c,l} - \frac{A_a}{V_c} J_{c,aq}$$ S-Eq. 19

$$\frac{dC_m}{dt} = \frac{A_m}{V_m} J_{c,m}$$ S-Eq. 20

$$\frac{dC_l}{dt} = \frac{A_l}{V_l} J_{c,l}$$ S-Eq. 21

$$\frac{dC_{aq}}{dt} = \frac{A_a}{V_{aq}} J_{c,aq} - \frac{A_{aq}}{V_{aq}} J_{aq,a}$$ S-Eq. 22

$$\frac{dC_a}{dt} = \frac{A_{aq}}{V_a} J_{aq,a}$$ S-Eq. 23

II. Matlab Codes

1. Normal mixture statistical model with probability density function in Matlab.

(A) Code 1-data extraction with CSV files

```
C100=volumefinal2(1:130,1); %Calu-3 only (100 %)
C99=volumefinal2(1:209,2);  %Calu-3:NHBE (C:N) = 99:1
C90=volumefinal2(1:158,3);   % C:N = 9:1 (90:10)
C50=volumefinal2(1:200,4);   % C:N = 1:1 (50:50)
C10B=volumefinal2(1:146,5);  % C:N = 1:9 (10:90) (Bottom layer)
C10T=volumefinal2(1:74,6);   % C:N = 1:9 (10:90) (Top layer)
C1B=volumefinal2(1:185,7);   % C:N = 1:99  (Bottom layer)
C1T=volumefinal2(1:43,8);    % C:N = 1:99  (Top layer)
C0B=volumefinal2(1:74,9);    % NHBE only (Bottom layer)
C0T=volumefinal2(1:43,10);   % NHBE only (Top layer)
Mix_all = [C100;C99;C90;C50;C10B;C10T;C1B;C1T;C0B;C0T];
save('volume');
```

(B) Code 2-bimodal histogram

```
clc
clear
close all
load('volume');
x= C50;    % C:N = 1:1 (50:50)
pdf_normmixture = @(x,p,mu1,mu2,sigma1,sigma2) ...
                    p*normpdf(x,mu1,sigma1) + (1-p)*normpdf(x,mu2,sigma2);
pStart = .5;
muStart = quantile(x,[.25 .75]);
sigmaStart = sqrt(var(x) - .25*diff(muStart).^2);
start = [pStart muStart sigmaStart sigmaStart];

lb = [0 -Inf -Inf 0 0];
ub = [1 Inf Inf Inf Inf];

%paramEsts = mle(x, 'pdf',pdf_normmixture, 'start',start, 'lower',lb, 'upper',ub);
statset('mlecustom');
options = statset('MaxIter',3000, 'MaxFunEvals',3000);
paramEsts = mle(x, 'pdf',pdf_normmixture, 'start',start, 'lower',lb, 'upper',ub, 'options',options);

bins = 1000:1000:11000;
h = bar(bins,histc(x,bins)/(length(x)),'histc');
```

```
set(h,'FaceColor',[.9 .9 .9]);
xgrid = linspace(0,11000,1000);
pdfgrid = 1000*pdf_normmixture(xgrid,paramEsts(1),paramEsts(2),paramEsts(4));
hold on;
plot(xgrid,pdfgrid,'-');
xlabel('Cell volume (um^3)');
ylabel('Relative frequency');
hold off;

trapz(xgrid,pdfgrid)
```

2. Optimization codes for transported mass and entrapped mass of PR, compared to AP→BL or BL→AP transport data in a Calu-3 cell

(A) Scratch sheet with the parameter ranges

```
global P_a P_b  A_m A_l
global A_a A_aq A_b A_bM A_bq V_aq V_a V_c V_bM V_bq V_b V_l V_m H_aq H_bq A_aa
global cell_no H_M D_w i1 pKa z1 F R Temp logPn logPd V_at V_bt
global L_c L_m L_l

% Constant
Temp = 310.15 ;          % Temperature
R = 8.314 ;              % Universal gas constant
F = 96484.56 ;           % Faraday constant

A_insert = 0.33*10^(-4) ;        % Insert area (m^2)
A_l = 314*10^(-12) ;             % Lysosomal membrane surface area (m^2)
A_m = 314*10^(-12) ;             % Mitochondrial membrane surface area (m^2)
H_M = 10*10^(-6);                % Porous membrane thickness (m)
V_l = 524*10^(-18);              % Lysosomal volume (m^3)
V_m = 524*10^(-18);              % Mitochondrial volume (m^3)

% Drug information (propranolol: PR)-ChemAxon calculation including pKa, logPn, and log Pd
pKa1 = 9.67;
logPn = 2.58;
logPd = -0.66;

z1 = 1 ;                 % Electric charge of PR
i1 = sign(z1) ;          % Monovalent base PR (+1)

D_w= 5.9495*10^(-6)*10^(-4) ; % Diffusion coefficient of PR in aqueous phase (m^2/sec)


%%%%%%%%%%%%%%%%%%%%%%%%%%%%%%%%%%%%%%%%%%%%%%%%%%%%%%%%%%%%%%%%%%%%%%%%%%%%%%%
% PARAMETERS TO BE OPTIMIZED [RANGES]
```

```
A_a =[79*10^(-12), 538*10^(-12)*50] ; % Apical membrane surface area (m^2)
A_aq =[79*10^(-12), 538*10^(-12)] ; % Apical unstirred water layer (UWL) surface area (m^2)
A_bq =[79*10^(-12), 538*10^(-12)] ; % Basolateral UWL surface area (m^2)
A_b = [8.3776*10^(-13), 538*10^(-12)] ; % Basolateral membrane surface area (m^2)
H_aq = [1*10^(-9), 500*10^(-6)] ;  % Apical UWL thickness (m)
H_bq = [1*10^(-9), 500*10^(-6)] ;  % Basolateral UWL thickness (m)
V_c = [1239*10^(-18), 8483*10^(-18)];% Cytosolic volume (m^3)

% Membrane potential (units in 'Voltage')
E_a = [-0.0143, -0.0043];  % Apical membrane electrical potential
E_l = [0.005, 0.015];      % Lysosomal membrane electrical potential
E_m = [-0.21, -0.11];      % Mitochondrial membrane electrical potential
E_b = [0.0069, 0.0169];    % Basolateral membrane electrical potential

% pH values
pH_a = [6.0, 7.8];           % pH in apical compartment
pH_c = [7.0, 7.8];           % pH in cytosol
pH_l = [4.8, 6.0];           % pH in lysosomes
pH_m = [7.7, 8.2];           % pH in mitochondria
pH_b = [7.0, 7.8];           % pH in basolateral compartment
%%%%%%%%%%%%%%%%%%%%%%%%%%%%%%%%%%%%%%%%%%%%%%%%%%%%%%%%%%%%%%%%%%%%%%%%%%%%%%%

% Cytoplasm
L_c = [0.05, 0.15];          % Lipid fraction in cytosol


% Mitochondria
L_m = [0.05, 0.15];          % Lipid fraction in mitochondria


% Lysosomes
L_l = [0.05, 0.15];         % Lipid fraction in lysosomes

%%%%%%%%%%%%%%%%%%%%%%%%%%%%%%%%%%%%%%%%%%%%%%%%%%%%%%%%%%%%%%%%%%%%%%%%%%%%%%%

A_bM = A_b;                    % Total Pore area of polyester membrane per cell(m^2)
V_aq = A_aq.*H_aq;             % Apical UWL drug solution volume (m^3)
V_bM = A_bM.*H_M;              % Total pore volume of polyester membrane per cell (um^3)
V_bq = A_bq.*H_bq;             % Basolateral UWL solution volume (m^3)
V_a = 5.5556*10^(-13);         % Apical bulk volume per one cell (m^3)
V_b = 3.0303*10^(-12);         % Basolateral volume per one cell (m^3)
V_at = 0.11*10^(-6) ;          % Apical bulk volume (m^3)
V_bt = 0.6*10^(-6) ;           % Basolateral bulk volume (m^3)
P_a = D_w./H_aq ;              % Aqueous permeability across Apical  UWL (m/sec)
P_b = D_w./H_bq ;              % Aqueous permeability across Basolateral UWL (m/sec)


% Set lower bounds
lb  = [ min(A_a)
min(A_aq)
```

```
min(A_bq)
min(A_b)
min(H_aq)
min(H_bq)
min(V_c)
min(E_a)
min(E_l)
min(E_m)
min(E_b)
min(pH_a)
min(pH_c)
min(pH_l)
min(pH_m)
min(pH_b)
min(L_c)
min(L_m)
min(L_l)
   ];

% Set upper bounds
ub = [ max(A_a)
max(A_aq)
max(A_bq)
max(A_b)
max(H_aq)
max(H_bq)
max(V_c)
max(E_a)
max(E_l)
max(E_m)
max(E_b)
max(pH_a)
max(pH_c)
max(pH_l)
max(pH_m)
max(pH_b)
max(L_c)
max(L_m)
max(L_l)
   ];

ub = ub'; lb = lb';

options = optimset('TolX',1e-4,'MaxFunEvals', 13000,'MaxIter',15000,'Display','iter');
f = @(x)both_opt_loop50(x);

tic;
% Number of parameters
parms = length(ub);

% Create a storage for all parameters (we are doing 50 iterations)
```

```
% and starting parameters
parameter_matrix = zeros(50,parms);
start_matrix = zeros(50,parms);

% Generate list of random numbers to use
perturb = rand(50,parms);

for i = 1:50
   % Display iteration number
   fprintf('Iteration: %d of 50 \n', i);

   % Difference between upper and lower bound
   delta = ub - lb;

   % Randomly generate starting values between upper and lower bounds
   start = lb + perturb(i,:).*delta;
   start_matrix(i,:) = start;

   % Optimize from start parameters
   [both_params,fval,exitflag,output] = fminsearchbnd(f,start,lb,ub,options);

   % Store optimized parameters into matrix
   parameter_matrix(i,:) = both_params;
end
toc;
```

(B) Optimization codes referring to the experimental datasets

```
% % Uncomment this for optimization
function [error] = both_opt_loop50(x)

% Uncomment this for predicted values
% function [output,vals] = both_opt_loop50(x)

global P_a P_b Pn Pd
global Ca_initial Cb_initial fn_a fd_a fn_c fd_c fn_m fd_m fn_l fd_l fn_b fd_b Nd_a Nd_m Nd_l
Nd_b
global A_aq A_b A_bM A_bq V_aq V_a V_c V_bM V_bq V_b V_l V_m H_aq H_bq A_aa A_a
V_at V_bt
global H_M D_w i1 pKa z1 F R Temp logPn logPd logP_nlip logP_dlip logP_n logP_d Is_c
gamman_c gammad_c Is_m gamman_m gammad_m
global L_c L_m L_l


A_a = x(1);         % Apical membrane surface area (m^2)
A_aq = x(2);        % Apical UWL surface area (m^2)
A_bq = x(3) );      % Basolateral UWL surface area (m^2)
A_b = x(4);         % Basolateral membrane surface area (m^2)
```

```
H_aq = x(5);       % Apical UWL thickness (m)
H_bq = x(6);       % Basolateral UWL thickness (m)
V_c = x(7);        % Cytosolic volume (m^3)
E_a = x(8);        % Apical membrane electrical potential (V)
E_l = x(9);        % Lysosomal membrane electrical potential (V)
E_m = x(10);       % mitochondrial membrane electrical potential (V)
E_b = x(11);       % Basolateral membrane electrical potential (V)
pH_a = x(12);      % pH in the apical aqueous phase
pH_c = x(13);      % pH in the cytosol
pH_l = x(14);      % pH in the lysosomes
pH_m = x(15);      % pH in the mitochondria
pH_b = x(16);      % pH in the basolateral aqueous phase
L_c = x(17);       % Lipid fraction in the cytosol
L_m = x(18);       % Lipid fraction in the mitochondria
L_l = x(19);       % Lipid fraction in the lysosomes


A_insert = 0.33*10^(-4) ;          % Insert area (m^2)
A_bM = A_b;                        % Total Pore area of polyester membrane per cell(m^2)
V_aq = A_aq.*H_aq;                 % Apical UWL drug solution volume (m^3)
V_bM = A_bM.*H_M;                  % Total pore volume of polyester membrane per cell (um^3)
V_bq = A_bq.*H_bq;                 % Basolateral UWL solution volume (m^3)
V_a = 5.5556*10^(-13);             % Apical bulk volume per one cell (m^3)
V_b = 3.0303*10^(-12);             % Basolateral volume per one cell (m^3)
V_at = 0.11*10^(-6) ;              % Apical bulk volume (m^3)
V_bt = 0.6*10^(-6) ;               % Basolateral bulk volume (m^3)


% Physicochemical properties of PR
logP_nlip = 0.33*logPn+2.2 ;  % Liposomal logPn
logP_dlip = 0.37*logPd+2 ;    % Liposomal logPd
logP_n = logP_nlip ;
logP_d = logP_dlip ;
Pn = 10^(logP_n-6.7);         % Membrane permeability of neutral species
Pd = 10^(logP_d-6.7);         % Membrane permeability of +1 ionized species
D_w= 5.9495*10^(-6)*10^(-4) ; % Diffusion coefficient of PR in aqueous phase (m^2/sec)
P_a = D_w./H_aq ;             % Aqueous permeability across Apical  UWL (m/sec)
P_b = D_w./H_bq ;             % Aqueous permeability across Basolateral UWL (m/sec)
z1 = 1 ;                      % Electric charge of PR
i1 = sign(z1) ;               % Monovalent base PR (+1)


% Apical compartment-UWL (unstirred water layer)
fn_a = 1 ./ (1 + 10.^(i1.*(pKa-pH_a))) ;
% Ratio of the activity of neutral species and total concentration in apical compartment
fd_a = fn_a .* 10.^(i1.*(pKa-pH_a)) ;
% Ratio of the activity of +1 ion species and total concentration in apical compartment
Nd_a = z1.*E_a.*F./(R.*Temp) ;


% Cytoplasm
```

```
W_c = 1-L_c ;                    % Water fraction in cytosol
Is_c = 0.3 ;                     % Ion strength in cytosol (mole)
gamman_c = 10^(0.3*Is_c) ;       % Activity coefficient of neutral molecules in cytosol
gammad_c = 10^(-0.5*z1*z1*(sqrt(Is_c)/(1+sqrt(Is_c))-0.3*Is_c));
Kn_c = L_c.*1.22.*10.^(logP_n) ;     % Sorption coefficient for neutral species in cytosol
Kd_c = L_c.*1.22.*10.^(logP_d) ;   % Sorption coefficient for +1 ion species in cytosol
an_c = 1 ./ (1 + 10.^(i1.*(pKa-pH_c))) ;% Activity of neutral species in cytosol
ad_c = an_c .* 10.^(i1.*(pKa-pH_c)) ;  % Activity of +1 ion species in cytosol
Dd_c = ad_c ./ an_c ;
fn_c = 1 ./ (W_c./gamman_c + Kn_c./gamman_c + Dd_c.*W_c./gammad_c +
Dd_c.*Kd_c./gammad_c ) ;
fd_c = fn_c .* Dd_c ;% Ratio of the activity of +1 ion species and total concentration in cytosol

% Mitochondria
W_m = 1-L_m ;                    % Water fraction in mitochondria
Is_m = 0.3 ;                     % Ion strength in mitochondria (mole)
gamman_m = 10^(0.3*Is_m) ;  % Activity coefficient of neutral molecules in mitochondria
gammad_m = 10^(-0.5*z1*z1*(sqrt(Is_m)/(1+sqrt(Is_m))-0.3*Is_m));
Nd_m = z1.*E_m.*F./(R.*Temp) ;
Kn_m = L_m.*1.22.*10.^(logP_n) ;     % Sorption coefficient for neutral species in mitochondria
Kd_m = L_m.*1.22.*10.^(logP_d) ;   % Sorption coefficient for +1 ion species in mitochondria
an_m = 1 ./ (1 + 10.^(i1.*(pKa-pH_m))) ;% Activity of neutral species in mitochondria
ad_m = an_m .* 10.^(i1.*(pKa-pH_m)) ;  % Activity of +1 ion species in mitochondria
Dd_m = ad_m ./ an_m ;
fn_m = 1 ./ (W_m./gamman_m + Kn_m./gamman_m + Dd_m.*W_m./gammad_m +
Dd_m.*Kd_m./gammad_m ) ;
fd_m = fn_m .* Dd_m ;% Ratio of the activity of +1 ion species and total concentration in
mitochondria

% Lysosomes
W_l = 1-L_l ;                    % Water fraction in lysosomes
Is_l = 0.3 ;                     % Ion strength in lysosomes (mole)
Nd_l = z1.*E_l.*F./(R.*Temp) ;
gamman_l = 10.^(0.3.*Is_l) ;       % Activity coefficient of neutral molecules in lysosomes
gammad_l = 10.^(-0.5.*z1.*z1.*(sqrt(Is_l)./(1+sqrt(Is_l))-0.3.*Is_l));
Kn_l = L_l.*1.22.*10.^(logP_n) ;     % Sorption coefficient for neutral species in lysosomes
Kd_l = L_l.*1.22.*10.^(logP_d) ;   % Sorption coefficient for +1 ion species in lysosomes
an_l = 1 ./ (1 + 10.^(i1.*(pKa-pH_l))) ;% Activity of neutral species in lysosomes
ad_l = an_l .* 10.^(i1.*(pKa-pH_l)) ;  % Activity of +1 ion species in lysosomes
Dd_l = ad_l ./ an_l ;
fn_l = 1 ./ (W_l./gamman_l + Kn_l./gamman_l + Dd_l.*W_l./gammad_l +
Dd_l.*Kd_l./gammad_l ) ;
fd_l = fn_l .* Dd_l ;% Ratio of the activity of +1 ion species and total concentration in lysosomes


% Basolateral compartment-UWL (unstirred water layer)
fn_b = 1 ./ (1 + 10.^(i1.*(pKa-pH_b))) ;
% Ratio of the activity of neutral species and total concentration in apical compartment
fd_b = fn_b .* 10.^(i1.*(pKa-pH_b)) ;
% Ratio of the activity of +1 ion species and total concentration in apical compartment
Nd_b = z1.*(-E_b).*F./(R*Temp) ;
```

```
%%%%%%%%%%%%%%%%%%%%%%%%%
% Calculate values at 1hr
% A->B 50 uM
Ca_initial = 50*10^(-3) ;
time = 3600;
Y0 = [Ca_initial,0,0,0,0,0,0,0]';
options = odeset('RelTol',1e-6,'AbsTol',[1e-10 1e-10 1e-10 1e-10 1e-10 1e-10 1e-10 1e-10]);
[T,Y] = ode15s(@AB_ODE_calu3,[0 time],Y0,options);
[a,b] = size(Y);
AB_B_Mass_50_3600 = Y(a,8)*V_b*(6.022*10^(23))*10^(-8); % B_Mass; Transported mass
into basolateral compartment (10^(8)*molecules/cell)
AB_Cell_Mass_50_3600 = (Y(a,3)*V_c+Y(a,4)*V_m+Y(a,5)*V_l)*6.022*10^(23)*10^(-8);   %
Cell_Mass; Total mass in the cell (10^(8)*molecules/cell)

%%%%%%%%%%%%%%%%%%%%%%%%%
% Calculate values at 1hr
% A->B 80 uM
Ca_initial = 80*10^(-3) ;
time = 3600;
Y0 = [Ca_initial,0,0,0,0,0,0,0]';
options = odeset('RelTol',1e-6,'AbsTol',[1e-10 1e-10 1e-10 1e-10 1e-10 1e-10 1e-10 1e-10]);
[T,Y] = ode15s(@AB_ODE_calu3,[0 time],Y0,options);
[a,b] = size(Y);
AB_B_Mass_80_3600 = Y(a,8)*V_b*(6.022*10^(23))*10^(-8); % B_Mass; Transported mass
into basolateral compartment (10^(8)*molecules/cell)
AB_Cell_Mass_80_3600 = (Y(a,3)*V_c+Y(a,4)*V_m+Y(a,5)*V_l)*6.022*10^(23)*10^(-8);   %
Cell_Mass; Total mass in the cell (10^(8)*molecules/cell)

%%%%%%%%%%%%%%%%%%%%%%%%%
% Calculate values at 1hr
% A->B 100 uM
Ca_initial = 100*10^(-3) ;
time = 3600;
Y0 = [Ca_initial,0,0,0,0,0,0,0]';
options = odeset('RelTol',1e-6,'AbsTol',[1e-10 1e-10 1e-10 1e-10 1e-10 1e-10 1e-10 1e-10]);
[T,Y] = ode15s(@AB_ODE_calu3,[0 time],Y0,options);
[a,b] = size(Y);
AB_B_Mass_100_3600 = Y(a,8)*V_b*(6.022*10^(23))*10^(-8); % B_Mass; Transported mass
into basolateral compartment (10^(8)*molecules/cell)
AB_Cell_Mass_100_3600 = (Y(a,3)*V_c+Y(a,4)*V_m+Y(a,5)*V_l)*6.022*10^(23)*10^(-8);
% Cell_Mass; Total mass in the cell (10^(8)*molecules/cell)

%%%%%%%%%%%%%%%%%%%%%%%%%
% Calculate values at 1hr
% B->A 50 uM
Cb_initial = 50*10^(-3) ;
time = 3600;
Y0 = [Cb_initial,0,0,0,0,0,0,0]';
options = odeset('RelTol',1e-6,'AbsTol',[1e-10 1e-10 1e-10 1e-10 1e-10 1e-10 1e-10 1e-10]);
```

```
[T,Y] = ode15s(@BA_ODE_calu3,[0 time],Y0,options);
[a,b] = size(Y);
BA_A_Mass_50_3600 = Y(a,8)*V_a*(6.022*10^(23))*10^(-8); % A_Mass; Transported mass into apical compartment (10^(8)*molecules/cell)
BA_Cell_Mass_50_3600 = (Y(a,4)*V_c+Y(a,5)*V_m+Y(a,6)*V_l)*6.022*10^(23)*10^(-8) ;  % Cell_Mass; Total mass in the cell (10^(8)*molecules/cell)

%%%%%%%%%%%%%%%%%%%%%%%%%
% Calculate values at 1hr
% B->A 80 uM
Cb_initial = 80*10^(-3) ;
time = 3600;
Y0 = [Cb_initial,0,0,0,0,0,0,0]';
options = odeset('RelTol',1e-6,'AbsTol',[1e-10 1e-10 1e-10 1e-10 1e-10 1e-10 1e-10 1e-10]);
[T,Y] = ode15s(@BA_ODE_calu3,[0 time],Y0,options);
[a,b] = size(Y);
BA_A_Mass_80_3600 = Y(a,8)*V_a*(6.022*10^(23))*10^(-8); % A_Mass; Transported mass into apical compartment (10^(8)*molecules/cell)
BA_Cell_Mass_80_3600 = (Y(a,4)*V_c+Y(a,5)*V_m+Y(a,6)*V_l)*6.022*10^(23)*10^(-8) ;  % Cell_Mass; Total mass in the cell (10^(8)*molecules/cell)

%%%%%%%%%%%%%%%%%%%%%%%%%
% Calculate values at 1hr
% B->A 100 uM
Cb_initial = 100*10^(-3) ;
time = 3600;
Y0 = [Cb_initial,0,0,0,0,0,0,0]';
options = odeset('RelTol',1e-6,'AbsTol',[1e-10 1e-10 1e-10 1e-10 1e-10 1e-10 1e-10 1e-10]);
[T,Y] = ode15s(@BA_ODE_calu3,[0 time],Y0,options);
[a,b] = size(Y);
BA_A_Mass_100_3600 = Y(a,8)*V_a*(6.022*10^(23))*10^(-8); % A_Mass; Transported mass into apical compartment (10^(8)*molecules/cell)
BA_Cell_Mass_100_3600 = (Y(a,4)*V_c+Y(a,5)*V_m+Y(a,6)*V_l)*6.022*10^(23)*10^(-8) ;
% Cell_Mass; Total mass in the cell (10^(8)*molecules/cell)

%%%%%%%%%%%%%%%%%%%%%%%%%%%%%%%%%%%%%%%%%
% Calculate values at earlier times
% 50 uM
Ca_initial = 50*10^(-3) ;
Cb_initial = 50*10^(-3) ;

% 5 min
time = 300;
Y0 = [Ca_initial,0,0,0,0,0,0,0]';
options = odeset('RelTol',1e-6,'AbsTol',[1e-10 1e-10 1e-10 1e-10 1e-10 1e-10 1e-10 1e-10]);
[T,Y] = ode15s(@AB_ODE_calu3,[0 time],Y0,options);
[a,b] = size(Y);
AB_B_Mass_50_300 = Y(a,8)*V_b*(6.022*10^(23))*10^(-8); % B_Mass; Transported mass into basolateral compartment (10^(8)*molecules/cell)
AB_Cell_Mass_50_300 = (Y(a,3)*V_c+Y(a,4)*V_m+Y(a,5)*V_l)*6.022*10^(23)*10^(-8);   % Cell_Mass; Total mass in the cell (10^(8)*molecules/cell)
```

```
Y0 = [Cb_initial,0,0,0,0,0,0,0]';
options = odeset('RelTol',1e-6,'AbsTol',[1e-10 1e-10 1e-10 1e-10 1e-10 1e-10 1e-10 1e-10]);
[T,Y] = ode15s(@BA_ODE_calu3,[0 time],Y0,options);
[a,b] = size(Y);
BA_A_Mass_50_300 = Y(a,8)*V_a*(6.022*10^(23))*10^(-8); % A_Mass; Transported mass
into apical compartment (10^(8)*molecules/cell)
BA_Cell_Mass_50_300 = (Y(a,4)*V_c+Y(a,5)*V_m+Y(a,6)*V_l)*6.022*10^(23)*10^(-8) ;  %
Cell_Mass; Total mass in the cell (10^(8)*molecules/cell)

% 30 min
time = 1800;
Y0 = [Ca_initial,0,0,0,0,0,0,0]';
options = odeset('RelTol',1e-6,'AbsTol',[1e-10 1e-10 1e-10 1e-10 1e-10 1e-10 1e-10 1e-10]);
[T,Y] = ode15s(@AB_ODE_calu3,[0 time],Y0,options);
[a,b] = size(Y);
AB_B_Mass_50_1800 = Y(a,8)*V_b*(6.022*10^(23))*10^(-8); % B_Mass; Transported mass
into basolateral compartment (10^(8)*molecules/cell)
AB_Cell_Mass_50_1800 = (Y(a,3)*V_c+Y(a,4)*V_m+Y(a,5)*V_l)*6.022*10^(23)*10^(-8);   %
Cell_Mass; Total mass in the cell (10^(8)*molecules/cell)

Y0 = [Cb_initial,0,0,0,0,0,0,0]';
options = odeset('RelTol',1e-6,'AbsTol',[1e-10 1e-10 1e-10 1e-10 1e-10 1e-10 1e-10 1e-10]);
[T,Y] = ode15s(@BA_ODE_calu3,[0 time],Y0,options);
[a,b] = size(Y);
BA_A_Mass_50_1800 = Y(a,8)*V_a*(6.022*10^(23))*10^(-8); % A_Mass; Transported mass
into apical compartment (10^(8)*molecules/cell)
BA_Cell_Mass_50_1800 = (Y(a,4)*V_c+Y(a,5)*V_m+Y(a,6)*V_l)*6.022*10^(23)*10^(-8) ;  %
Cell_Mass; Total mass in the cell (10^(8)*molecules/cell)

% 2 hrs
time = 7200;
Y0 = [Ca_initial,0,0,0,0,0,0,0]';
options = odeset('RelTol',1e-6,'AbsTol',[1e-10 1e-10 1e-10 1e-10 1e-10 1e-10 1e-10 1e-10]);
[T,Y] = ode15s(@AB_ODE_calu3,[0 time],Y0,options);
[a,b] = size(Y);
AB_B_Mass_50_7200 = Y(a,8)*V_b*(6.022*10^(23))*10^(-8); % B_Mass; Transported mass
into basolateral compartment (10^(8)*molecules/cell)
AB_Cell_Mass_50_7200 = (Y(a,3)*V_c+Y(a,4)*V_m+Y(a,5)*V_l)*6.022*10^(23)*10^(-8);   %
Cell_Mass; Total mass in the cell (10^(8)*molecules/cell)

Y0 = [Cb_initial,0,0,0,0,0,0,0]';
options = odeset('RelTol',1e-6,'AbsTol',[1e-10 1e-10 1e-10 1e-10 1e-10 1e-10 1e-10 1e-10]);
[T,Y] = ode15s(@BA_ODE_calu3,[0 time],Y0,options);
[a,b] = size(Y);
BA_A_Mass_50_7200 = Y(a,8)*V_a*(6.022*10^(23))*10^(-8); % A_Mass; Transported mass
into apical compartment (10^(8)*molecules/cell)
BA_Cell_Mass_50_7200 = (Y(a,4)*V_c+Y(a,5)*V_m+Y(a,6)*V_l)*6.022*10^(23)*10^(-8) ;  %
Cell_Mass; Total mass in the cell (10^(8)*molecules/cell)

% 3 hrs
```

```
time = 10800;
Y0 = [Ca_initial,0,0,0,0,0,0,0]';
options = odeset('RelTol',1e-6,'AbsTol',[1e-10 1e-10 1e-10 1e-10 1e-10 1e-10 1e-10 1e-10]);
[T,Y] = ode15s(@AB_ODE_calu3,[0 time],Y0,options);
[a,b] = size(Y);
AB_B_Mass_50_10800 = Y(a,8)*V_b*(6.022*10^(23))*10^(-8); % B_Mass; Transported mass
into basolateral compartment (10^(8)*molecules/cell)
AB_Cell_Mass_50_10800 = (Y(a,3)*V_c+Y(a,4)*V_m+Y(a,5)*V_l)*6.022*10^(23)*10^(-8);
% Cell_Mass; Total mass in the cell (10^(8)*molecules/cell)

Y0 = [Cb_initial,0,0,0,0,0,0,0]';
options = odeset('RelTol',1e-6,'AbsTol',[1e-10 1e-10 1e-10 1e-10 1e-10 1e-10 1e-10 1e-10]);
[T,Y] = ode15s(@BA_ODE_calu3,[0 time],Y0,options);
[a,b] = size(Y);
BA_A_Mass_50_10800 = Y(a,8)*V_a*(6.022*10^(23))*10^(-8); % A_Mass; Transported mass
into apical compartment (10^(8)*molecules/cell)
BA_Cell_Mass_50_10800 = (Y(a,4)*V_c+Y(a,5)*V_m+Y(a,6)*V_l)*6.022*10^(23)*10^(-8) ;
% Cell_Mass; Total mass in the cell (10^(8)*molecules/cell)

% 4 hrs
time = 14400;
Y0 = [Ca_initial,0,0,0,0,0,0,0]';
options = odeset('RelTol',1e-6,'AbsTol',[1e-10 1e-10 1e-10 1e-10 1e-10 1e-10 1e-10 1e-10]);
[T,Y] = ode15s(@AB_ODE_calu3,[0 time],Y0,options);
[a,b] = size(Y);
AB_B_Mass_50_14400 = Y(a,8)*V_b*(6.022*10^(23))*10^(-8); % B_Mass; Transported mass
into basolateral compartment (10^(8)*molecules/cell)
AB_Cell_Mass_50_14400 = (Y(a,3)*V_c+Y(a,4)*V_m+Y(a,5)*V_l)*6.022*10^(23)*10^(-8);
% Cell_Mass; Total mass in the cell (10^(8)*molecules/cell)

Y0 = [Cb_initial,0,0,0,0,0,0,0]';
options = odeset('RelTol',1e-6,'AbsTol',[1e-10 1e-10 1e-10 1e-10 1e-10 1e-10 1e-10 1e-10]);
[T,Y] = ode15s(@BA_ODE_calu3,[0 time],Y0,options);
[a,b] = size(Y);
BA_A_Mass_50_14400 = Y(a,8)*V_a*(6.022*10^(23))*10^(-8); % A_Mass; Transported mass
into apical compartment (10^(8)*molecules/cell)
BA_Cell_Mass_50_14400 = (Y(a,4)*V_c+Y(a,5)*V_m+Y(a,6)*V_l)*6.022*10^(23)*10^(-8) ;
% Cell_Mass; Total mass in the cell (10^(8)*molecules/cell)


%%%%%%%%%%%%%%%%%%%%%%%%%%%%%%%%%%%%%%%%
% Calculate values at earlier times
% 80 uM
Ca_initial = 80*10^(-3) ;
Cb_initial = 80*10^(-3) ;

% 5 min
time = 300;
Y0 = [Ca_initial,0,0,0,0,0,0,0]';
options = odeset('RelTol',1e-6,'AbsTol',[1e-10 1e-10 1e-10 1e-10 1e-10 1e-10 1e-10 1e-10]);
[T,Y] = ode15s(@AB_ODE_calu3,[0 time],Y0,options);
```

```
[a,b] = size(Y);
AB_B_Mass_80_300 = Y(a,8)*V_b*(6.022*10^(23))*10^(-8); % B_Mass; Transported mass
into basolateral compartment (10^(8)*molecules/cell)
AB_Cell_Mass_80_300 = (Y(a,3)*V_c+Y(a,4)*V_m+Y(a,5)*V_l)*6.022*10^(23)*10^(-8);   %
Cell_Mass; Total mass in the cell (10^(8)*molecules/cell)

Y0 = [Cb_initial,0,0,0,0,0,0,0]';
options = odeset('RelTol',1e-6,'AbsTol',[1e-10 1e-10 1e-10 1e-10 1e-10 1e-10 1e-10 1e-10]);
[T,Y] = ode15s(@BA_ODE_calu3,[0 time],Y0,options);
[a,b] = size(Y);
BA_A_Mass_80_300 = Y(a,8)*V_a*(6.022*10^(23))*10^(-8); % A_Mass; Transported mass
into apical compartment (10^(8)*molecules/cell)
BA_Cell_Mass_80_300 = (Y(a,4)*V_c+Y(a,5)*V_m+Y(a,6)*V_l)*6.022*10^(23)*10^(-8) ;  %
Cell_Mass; Total mass in the cell (10^(8)*molecules/cell)

% 30 min
time = 1800;
Y0 = [Ca_initial,0,0,0,0,0,0,0]';
options = odeset('RelTol',1e-6,'AbsTol',[1e-10 1e-10 1e-10 1e-10 1e-10 1e-10 1e-10 1e-10]);
[T,Y] = ode15s(@AB_ODE_calu3,[0 time],Y0,options);
[a,b] = size(Y);
AB_B_Mass_80_1800 = Y(a,8)*V_b*(6.022*10^(23))*10^(-8); % B_Mass; Transported mass
into basolateral compartment (10^(8)*molecules/cell)
AB_Cell_Mass_80_1800 = (Y(a,3)*V_c+Y(a,4)*V_m+Y(a,5)*V_l)*6.022*10^(23)*10^(-8);   %
Cell_Mass; Total mass in the cell (10^(8)*molecules/cell)

Y0 = [Cb_initial,0,0,0,0,0,0,0]';
options = odeset('RelTol',1e-6,'AbsTol',[1e-10 1e-10 1e-10 1e-10 1e-10 1e-10 1e-10 1e-10]);
[T,Y] = ode15s(@BA_ODE_calu3,[0 time],Y0,options);
[a,b] = size(Y);
BA_A_Mass_80_1800 = Y(a,8)*V_a*(6.022*10^(23))*10^(-8); % A_Mass; Transported mass
into apical compartment (10^(8)*molecules/cell)
BA_Cell_Mass_80_1800 = (Y(a,4)*V_c+Y(a,5)*V_m+Y(a,6)*V_l)*6.022*10^(23)*10^(-8) ;  %
Cell_Mass; Total mass in the cell (10^(8)*molecules/cell)

% 2 hrs
time = 7200;
Y0 = [Ca_initial,0,0,0,0,0,0,0]';
options = odeset('RelTol',1e-6,'AbsTol',[1e-10 1e-10 1e-10 1e-10 1e-10 1e-10 1e-10 1e-10]);
[T,Y] = ode15s(@AB_ODE_calu3,[0 time],Y0,options);
[a,b] = size(Y);
AB_B_Mass_80_7200 = Y(a,8)*V_b*(6.022*10^(23))*10^(-8); % B_Mass; Transported mass
into basolateral compartment (10^(8)*molecules/cell)
AB_Cell_Mass_80_7200 = (Y(a,3)*V_c+Y(a,4)*V_m+Y(a,5)*V_l)*6.022*10^(23)*10^(-8);   %
Cell_Mass; Total mass in the cell (10^(8)*molecules/cell)

Y0 = [Cb_initial,0,0,0,0,0,0,0]';
options = odeset('RelTol',1e-6,'AbsTol',[1e-10 1e-10 1e-10 1e-10 1e-10 1e-10 1e-10 1e-10]);
[T,Y] = ode15s(@BA_ODE_calu3,[0 time],Y0,options);
[a,b] = size(Y);
```

```
BA_A_Mass_80_7200 = Y(a,8)*V_a*(6.022*10^(23))*10^(-8); % A_Mass; Transported mass into apical compartment (10^(8)*molecules/cell)
BA_Cell_Mass_80_7200 = (Y(a,4)*V_c+Y(a,5)*V_m+Y(a,6)*V_l)*6.022*10^(23)*10^(-8) ;  % Cell_Mass; Total mass in the cell (10^(8)*molecules/cell)

% 3 hrs
time = 10800;
Y0 = [Ca_initial,0,0,0,0,0,0,0]';
options = odeset('RelTol',1e-6,'AbsTol',[1e-10 1e-10 1e-10 1e-10 1e-10 1e-10 1e-10 1e-10]);
[T,Y] = ode15s(@AB_ODE_calu3,[0 time],Y0,options);
[a,b] = size(Y);
AB_B_Mass_80_10800 = Y(a,8)*V_b*(6.022*10^(23))*10^(-8); % B_Mass; Transported mass into basolateral compartment (10^(8)*molecules/cell)
AB_Cell_Mass_80_10800 = (Y(a,3)*V_c+Y(a,4)*V_m+Y(a,5)*V_l)*6.022*10^(23)*10^(-8);
% Cell_Mass; Total mass in the cell (10^(8)*molecules/cell)

Y0 = [Cb_initial,0,0,0,0,0,0,0]';
options = odeset('RelTol',1e-6,'AbsTol',[1e-10 1e-10 1e-10 1e-10 1e-10 1e-10 1e-10 1e-10]);
[T,Y] = ode15s(@BA_ODE_calu3,[0 time],Y0,options);
[a,b] = size(Y);
BA_A_Mass_80_10800 = Y(a,8)*V_a*(6.022*10^(23))*10^(-8); % A_Mass; Transported mass into apical compartment (10^(8)*molecules/cell)
BA_Cell_Mass_80_10800 = (Y(a,4)*V_c+Y(a,5)*V_m+Y(a,6)*V_l)*6.022*10^(23)*10^(-8) ;
% Cell_Mass; Total mass in the cell (10^(8)*molecules/cell)

% 4 hrs
time = 14400;
Y0 = [Ca_initial,0,0,0,0,0,0,0]';
options = odeset('RelTol',1e-6,'AbsTol',[1e-10 1e-10 1e-10 1e-10 1e-10 1e-10 1e-10 1e-10]);
[T,Y] = ode15s(@AB_ODE_calu3,[0 time],Y0,options);
[a,b] = size(Y);
AB_B_Mass_80_14400 = Y(a,8)*V_b*(6.022*10^(23))*10^(-8); % B_Mass; Transported mass into basolateral compartment (10^(8)*molecules/cell)
AB_Cell_Mass_80_14400 = (Y(a,3)*V_c+Y(a,4)*V_m+Y(a,5)*V_l)*6.022*10^(23)*10^(-8);
% Cell_Mass; Total mass in the cell (10^(8)*molecules/cell)

Y0 = [Cb_initial,0,0,0,0,0,0,0]';
options = odeset('RelTol',1e-6,'AbsTol',[1e-10 1e-10 1e-10 1e-10 1e-10 1e-10 1e-10 1e-10]);
[T,Y] = ode15s(@BA_ODE_calu3,[0 time],Y0,options);
[a,b] = size(Y);
BA_A_Mass_80_14400 = Y(a,8)*V_a*(6.022*10^(23))*10^(-8); % A_Mass; Transported mass into apical compartment (10^(8)*molecules/cell)
BA_Cell_Mass_80_14400 = (Y(a,4)*V_c+Y(a,5)*V_m+Y(a,6)*V_l)*6.022*10^(23)*10^(-8) ;
% Cell_Mass; Total mass in the cell (10^(8)*molecules/cell)

%%%%%%%%%%%%%%%%%%%%%%%%%%%%%%%%%%%%%%%%
% Calculate values at earlier times
% 100 uM
Ca_initial = 100*10^(-3) ;
Cb_initial = 100*10^(-3) ;
```

```
% 5 min
time = 300;
Y0 = [Ca_initial,0,0,0,0,0,0,0]';
options = odeset('RelTol',1e-6,'AbsTol',[1e-10 1e-10 1e-10 1e-10 1e-10 1e-10 1e-10 1e-10]);
[T,Y] = ode15s(@AB_ODE_calu3,[0 time],Y0,options);
[a,b] = size(Y);
AB_B_Mass_100_300 = Y(a,8)*V_b*(6.022*10^(23))*10^(-8); % B_Mass; Transported mass
into basolateral compartment (10^(8)*molecules/cell)
AB_Cell_Mass_100_300 = (Y(a,3)*V_c+Y(a,4)*V_m+Y(a,5)*V_l)*6.022*10^(23)*10^(-8);   %
Cell_Mass; Total mass in the cell (10^(8)*molecules/cell)

Y0 = [Cb_initial,0,0,0,0,0,0,0]';
options = odeset('RelTol',1e-6,'AbsTol',[1e-10 1e-10 1e-10 1e-10 1e-10 1e-10 1e-10 1e-10]);
[T,Y] = ode15s(@BA_ODE_calu3,[0 time],Y0,options);
[a,b] = size(Y);
BA_A_Mass_100_300 = Y(a,8)*V_a*(6.022*10^(23))*10^(-8); % A_Mass; Transported mass
into apical compartment (10^(8)*molecules/cell)
BA_Cell_Mass_100_300 = (Y(a,4)*V_c+Y(a,5)*V_m+Y(a,6)*V_l)*6.022*10^(23)*10^(-8) ;  %
Cell_Mass; Total mass in the cell (10^(8)*molecules/cell)

% 30 min
time = 1800;
Y0 = [Ca_initial,0,0,0,0,0,0,0]';
options = odeset('RelTol',1e-6,'AbsTol',[1e-10 1e-10 1e-10 1e-10 1e-10 1e-10 1e-10 1e-10]);
[T,Y] = ode15s(@AB_ODE_calu3,[0 time],Y0,options);
[a,b] = size(Y);
AB_B_Mass_100_1800 = Y(a,8)*V_b*(6.022*10^(23))*10^(-8); % B_Mass; Transported mass
into basolateral compartment (10^(8)*molecules/cell)
AB_Cell_Mass_100_1800 = (Y(a,3)*V_c+Y(a,4)*V_m+Y(a,5)*V_l)*6.022*10^(23)*10^(-8);
% Cell_Mass; Total mass in the cell (10^(8)*molecules/cell)

Y0 = [Cb_initial,0,0,0,0,0,0,0]';
options = odeset('RelTol',1e-6,'AbsTol',[1e-10 1e-10 1e-10 1e-10 1e-10 1e-10 1e-10 1e-10]);
[T,Y] = ode15s(@BA_ODE_calu3,[0 time],Y0,options);
[a,b] = size(Y);
BA_A_Mass_100_1800 = Y(a,8)*V_a*(6.022*10^(23))*10^(-8); % A_Mass; Transported mass
into apical compartment (10^(8)*molecules/cell)
BA_Cell_Mass_100_1800 = (Y(a,4)*V_c+Y(a,5)*V_m+Y(a,6)*V_l)*6.022*10^(23)*10^(-8) ;
% Cell_Mass; Total mass in the cell (10^(8)*molecules/cell)

% 2 hrs
time = 7200;
Y0 = [Ca_initial,0,0,0,0,0,0,0]';
options = odeset('RelTol',1e-6,'AbsTol',[1e-10 1e-10 1e-10 1e-10 1e-10 1e-10 1e-10 1e-10]);
[T,Y] = ode15s(@AB_ODE_calu3,[0 time],Y0,options);
[a,b] = size(Y);
AB_B_Mass_100_7200 = Y(a,8)*V_b*(6.022*10^(23))*10^(-8); % B_Mass; Transported mass
into basolateral compartment (10^(8)*molecules/cell)
AB_Cell_Mass_100_7200 = (Y(a,3)*V_c+Y(a,4)*V_m+Y(a,5)*V_l)*6.022*10^(23)*10^(-8);
% Cell_Mass; Total mass in the cell (10^(8)*molecules/cell)
```

```
Y0 = [Cb_initial,0,0,0,0,0,0,0]';
options = odeset('RelTol',1e-6,'AbsTol',[1e-10 1e-10 1e-10 1e-10 1e-10 1e-10 1e-10 1e-10]);
[T,Y] = ode15s(@BA_ODE_calu3,[0 time],Y0,options);
[a,b] = size(Y);
BA_A_Mass_100_7200 = Y(a,8)*V_a*(6.022*10^(23))*10^(-8); % A_Mass; Transported mass into apical compartment (10^(8)*molecules/cell)
BA_Cell_Mass_100_7200 = (Y(a,4)*V_c+Y(a,5)*V_m+Y(a,6)*V_l)*6.022*10^(23)*10^(-8) ; % Cell_Mass; Total mass in the cell (10^(8)*molecules/cell)

% 3 hrs
time = 10800;
Y0 = [Ca_initial,0,0,0,0,0,0,0]';
options = odeset('RelTol',1e-6,'AbsTol',[1e-10 1e-10 1e-10 1e-10 1e-10 1e-10 1e-10 1e-10]);
[T,Y] = ode15s(@AB_ODE_calu3,[0 time],Y0,options);
[a,b] = size(Y);
AB_B_Mass_100_10800 = Y(a,8)*V_b*(6.022*10^(23))*10^(-8); % B_Mass; Transported mass into basolateral compartment (10^(8)*molecules/cell)
AB_Cell_Mass_100_10800 = (Y(a,3)*V_c+Y(a,4)*V_m+Y(a,5)*V_l)*6.022*10^(23)*10^(-8); % Cell_Mass; Total mass in the cell (10^(8)*molecules/cell)

Y0 = [Cb_initial,0,0,0,0,0,0,0]';
options = odeset('RelTol',1e-6,'AbsTol',[1e-10 1e-10 1e-10 1e-10 1e-10 1e-10 1e-10 1e-10]);
[T,Y] = ode15s(@BA_ODE_calu3,[0 time],Y0,options);
[a,b] = size(Y);
BA_A_Mass_100_10800 = Y(a,8)*V_a*(6.022*10^(23))*10^(-8); % A_Mass; Transported mass into apical compartment (10^(8)*molecules/cell)
BA_Cell_Mass_100_10800 = (Y(a,4)*V_c+Y(a,5)*V_m+Y(a,6)*V_l)*6.022*10^(23)*10^(-8) ; % Cell_Mass; Total mass in the cell (10^(8)*molecules/cell)

% 4 hrs
time = 14400;
Y0 = [Ca_initial,0,0,0,0,0,0,0]';
options = odeset('RelTol',1e-6,'AbsTol',[1e-10 1e-10 1e-10 1e-10 1e-10 1e-10 1e-10 1e-10]);
[T,Y] = ode15s(@AB_ODE_calu3,[0 time],Y0,options);
[a,b] = size(Y);
AB_B_Mass_100_14400 = Y(a,8)*V_b*(6.022*10^(23))*10^(-8); % B_Mass; Transported mass into basolateral compartment (10^(8)*molecules/cell)
AB_Cell_Mass_100_14400 = (Y(a,3)*V_c+Y(a,4)*V_m+Y(a,5)*V_l)*6.022*10^(23)*10^(-8); % Cell_Mass; Total mass in the cell (10^(8)*molecules/cell)

Y0 = [Cb_initial,0,0,0,0,0,0,0]';
options = odeset('RelTol',1e-6,'AbsTol',[1e-10 1e-10 1e-10 1e-10 1e-10 1e-10 1e-10 1e-10]);
[T,Y] = ode15s(@BA_ODE_calu3,[0 time],Y0,options);
[a,b] = size(Y);
BA_A_Mass_100_14400 = Y(a,8)*V_a*(6.022*10^(23))*10^(-8); % A_Mass; Transported mass into apical compartment (10^(8)*molecules/cell)
BA_Cell_Mass_100_14400 = (Y(a,4)*V_c+Y(a,5)*V_m+Y(a,6)*V_l)*6.022*10^(23)*10^(-8) ; % Cell_Mass; Total mass in the cell (10^(8)*molecules/cell)
```

```
%%%%%%%%%%%%%%%%%%%%%%%%%%%%%%%%%%%%%%%%%%%%%%%
Difference between experimental and computed values
% 1hr
AB_B_Mass_diff_50_3600 = AB_B_Mass_50_3600 - 32.15250956 ;
AB_Cell_Mass_diff_50_3600 = AB_Cell_Mass_50_3600 - 31.20945095 ;

AB_B_Mass_diff_80_3600 = AB_B_Mass_80_3600 - 47.35812345 ;
AB_Cell_Mass_diff_80_3600 = AB_Cell_Mass_80_3600 - 49.33859458;

AB_B_Mass_diff_100_3600 = AB_B_Mass_100_3600 - 65.19429019;
AB_Cell_Mass_diff_100_3600 = AB_Cell_Mass_100_3600 - 64.18510841;

BA_A_Mass_diff_50_3600 = BA_A_Mass_50_3600 - 26.20161338;
BA_Cell_Mass_diff_50_3600 = BA_Cell_Mass_50_3600 - 11.72180907;

BA_A_Mass_diff_80_3600 = BA_A_Mass_80_3600 - 39.88242415;
BA_Cell_Mass_diff_80_3600 = BA_Cell_Mass_80_3600 - 15.76947323;

BA_A_Mass_diff_100_3600 = BA_A_Mass_100_3600 - 46.11545795;
BA_Cell_Mass_diff_100_3600 = BA_Cell_Mass_100_3600 - 21.99010373;
%%%% 50 µM
% 5 min
AB_B_Mass_50_300_diff = AB_B_Mass_50_300 - 0.969117509;
AB_Cell_Mass_50_300_diff = AB_Cell_Mass_50_300 - 12.37596164;
BA_A_Mass_50_300_diff = BA_A_Mass_50_300 - 0.842895843;
BA_Cell_Mass_50_300_diff = BA_Cell_Mass_50_300 - 1.844748098;

% 30 min
AB_B_Mass_50_1800_diff = AB_B_Mass_50_1800 - 10.61214012;
AB_Cell_Mass_50_1800_diff = AB_Cell_Mass_50_1800 - 30.84245203;
BA_A_Mass_50_1800_diff = BA_A_Mass_50_1800 - 12.10320143;
BA_Cell_Mass_50_1800_diff = BA_Cell_Mass_50_1800 - 7.112220621;

% 2 hrs
AB_B_Mass_50_7200_diff = AB_B_Mass_50_7200 - 58.42266383;
AB_Cell_Mass_50_7200_diff = AB_Cell_Mass_50_7200 - 31.12401425;
BA_A_Mass_50_7200_diff = BA_A_Mass_50_7200 - 45.18937094;
BA_Cell_Mass_50_7200_diff = BA_Cell_Mass_50_7200 - 16.6414177;

% 3 hrs
AB_B_Mass_50_10800_diff = AB_B_Mass_50_10800 - 76.7141117;
AB_Cell_Mass_50_10800_diff = AB_Cell_Mass_50_10800 - 26.6327297;
BA_A_Mass_50_10800_diff = BA_A_Mass_50_10800 - 59.62174259;
BA_Cell_Mass_50_10800_diff = BA_Cell_Mass_50_10800 - 23.07379961;

% 4 hrs
AB_B_Mass_50_14400_diff = AB_B_Mass_50_14400 - 92.42209746;
AB_Cell_Mass_50_14400_diff = AB_Cell_Mass_50_14400 - 22.6119983;
BA_A_Mass_50_14400_diff = BA_A_Mass_50_14400 - 75.82636275;
BA_Cell_Mass_50_14400_diff = BA_Cell_Mass_50_14400  - 26.25161103;
```

```
%%%% 80 μM
% 5 min
AB_B_Mass_80_300_diff = AB_B_Mass_80_300 - 1.820344932;
AB_Cell_Mass_80_300_diff = AB_Cell_Mass_80_300 - 12.66937956;
BA_A_Mass_80_300_diff = BA_A_Mass_80_300 - 0.908292458;
BA_Cell_Mass_80_300_diff = BA_Cell_Mass_80_300 - 2.180409069;

% 30 min
AB_B_Mass_80_1800_diff = AB_B_Mass_80_1800 - 22.5945941;
AB_Cell_Mass_80_1800_diff = AB_Cell_Mass_80_1800 - 46.24205291;
BA_A_Mass_80_1800_diff = BA_A_Mass_80_1800 - 21.992041;
BA_Cell_Mass_80_1800_diff = BA_Cell_Mass_80_1800 - 8.774684366;

% 2 hrs
AB_B_Mass_80_7200_diff = AB_B_Mass_80_7200 - 94.44153539;
AB_Cell_Mass_80_7200_diff = AB_Cell_Mass_80_7200 - 45.07849815;
BA_A_Mass_80_7200_diff = BA_A_Mass_80_7200 - 71.96354791;
BA_Cell_Mass_80_7200_diff = BA_Cell_Mass_80_7200 - 23.57431084;

% 3 hrs
AB_B_Mass_80_10800_diff = AB_B_Mass_80_10800 - 117.5475687;
AB_Cell_Mass_80_10800_diff = AB_Cell_Mass_80_10800 - 40.67163343;
BA_A_Mass_80_10800_diff = BA_A_Mass_80_10800 - 96.25445138;
BA_Cell_Mass_80_10800_diff = BA_Cell_Mass_80_10800 - 33.20531379;

% 4 hrs
AB_B_Mass_80_14400_diff = AB_B_Mass_80_14400 - 135.5581845;
AB_Cell_Mass_80_14400_diff = AB_Cell_Mass_80_14400 - 32.47366182;
BA_A_Mass_80_14400_diff = BA_A_Mass_80_14400 - 116.9264128;
BA_Cell_Mass_80_14400_diff = BA_Cell_Mass_80_14400  - 37.04182578;

%%%% 100 μM
% 5 min
AB_B_Mass_100_300_diff = AB_B_Mass_100_300 - 2.664796946;
AB_Cell_Mass_100_300_diff = AB_Cell_Mass_100_300 - 15.92450307;
BA_A_Mass_100_300_diff = BA_A_Mass_100_300 - 1.330710493;
BA_Cell_Mass_100_300_diff = BA_Cell_Mass_100_300 - 2.701248607;

% 30 min
AB_B_Mass_100_1800_diff = AB_B_Mass_100_1800 - 36.12988319;
AB_Cell_Mass_100_1800_diff = AB_Cell_Mass_100_1800 - 61.43209652;
BA_A_Mass_100_1800_diff = BA_A_Mass_100_1800 - 24.81072879;
BA_Cell_Mass_100_1800_diff = BA_Cell_Mass_100_1800 - 11.47499634;

% 2 hrs
AB_B_Mass_100_7200_diff = AB_B_Mass_100_7200 - 128.3837255;
AB_Cell_Mass_100_7200_diff = AB_Cell_Mass_100_7200 - 57.15623065;
BA_A_Mass_100_7200_diff = BA_A_Mass_100_7200 - 91.83800916;
BA_Cell_Mass_100_7200_diff = BA_Cell_Mass_100_7200 - 32.9503378;

% 3 hrs
```

```
AB_B_Mass_100_10800_diff = AB_B_Mass_100_10800 - 171.6498537;
AB_Cell_Mass_100_10800_diff = AB_Cell_Mass_100_10800 - 50.10439357;
BA_A_Mass_100_10800_diff = BA_A_Mass_100_10800 - 132.2810831;
BA_Cell_Mass_100_10800_diff = BA_Cell_Mass_100_10800 - 43.57213126;

% 4 hrs
AB_B_Mass_100_14400_diff = AB_B_Mass_100_14400 - 201.3615209;
AB_Cell_Mass_100_14400_diff = AB_Cell_Mass_100_14400 - 42.46135248;
BA_A_Mass_100_14400_diff = BA_A_Mass_100_14400 - 152.4031399;
BA_Cell_Mass_100_14400_diff = BA_Cell_Mass_100_14400  - 48.43424381;



% Cost function for optimization
error = abs(AB_B_Mass_diff_50_3600) + abs(AB_Cell_Mass_diff_50_3600) ...
   + abs(AB_B_Mass_diff_80_3600) + abs(AB_Cell_Mass_diff_80_3600) ...
   + abs(AB_B_Mass_diff_100_3600) + abs(AB_Cell_Mass_diff_100_3600) ...
   + abs(BA_A_Mass_diff_50_3600) + abs(BA_Cell_Mass_diff_50_3600) ...
   + abs(BA_A_Mass_diff_80_3600) + abs(BA_Cell_Mass_diff_80_3600) ...
   + abs(BA_A_Mass_diff_100_3600) + abs(BA_Cell_Mass_diff_100_3600) ...
   + abs(AB_B_Mass_50_300_diff) +  abs(AB_Cell_Mass_50_300_diff) ...
   + abs(BA_A_Mass_50_300_diff) +  abs(BA_Cell_Mass_50_300_diff) ...
   + abs(AB_B_Mass_50_1800_diff) +  abs(AB_Cell_Mass_50_1800_diff) ...
   + abs(BA_A_Mass_50_1800_diff) +  abs(BA_Cell_Mass_50_1800_diff) ...
   + abs(AB_B_Mass_50_7200_diff) +  abs(AB_Cell_Mass_50_7200_diff) ...
   + abs(BA_A_Mass_50_7200_diff) +  abs(BA_Cell_Mass_50_7200_diff) ...
   + abs(AB_B_Mass_50_10800_diff) +  abs(AB_Cell_Mass_50_10800_diff) ...
   + abs(BA_A_Mass_50_10800_diff) +  abs(BA_Cell_Mass_50_10800_diff) ...
   + abs(AB_B_Mass_50_14400_diff) +  abs(AB_Cell_Mass_50_14400_diff) ...
   + abs(BA_A_Mass_50_14400_diff) +  abs(BA_Cell_Mass_50_14400_diff) ...
   + abs(AB_B_Mass_80_300_diff) +  abs(AB_Cell_Mass_80_300_diff) ...
   + abs(BA_A_Mass_80_300_diff) +  abs(BA_Cell_Mass_80_300_diff) ...
   + abs(AB_B_Mass_80_1800_diff) +  abs(AB_Cell_Mass_80_1800_diff) ...
   + abs(BA_A_Mass_80_1800_diff) +  abs(BA_Cell_Mass_80_1800_diff) ...
   + abs(AB_B_Mass_80_7200_diff) +  abs(AB_Cell_Mass_80_7200_diff) ...
   + abs(BA_A_Mass_80_7200_diff) +  abs(BA_Cell_Mass_80_7200_diff) ...
   + abs(AB_B_Mass_80_10800_diff) +  abs(AB_Cell_Mass_80_10800_diff) ...
   + abs(BA_A_Mass_80_10800_diff) +  abs(BA_Cell_Mass_80_10800_diff) ...
   + abs(AB_B_Mass_80_14400_diff) +  abs(AB_Cell_Mass_80_14400_diff) ...
   + abs(BA_A_Mass_80_14400_diff) +  abs(BA_Cell_Mass_80_14400_diff) ...
   + abs(AB_B_Mass_100_300_diff) +  abs(AB_Cell_Mass_100_300_diff) ...
   + abs(BA_A_Mass_100_300_diff) +  abs(BA_Cell_Mass_100_300_diff) ...
   + abs(AB_B_Mass_100_1800_diff) +  abs(AB_Cell_Mass_100_1800_diff) ...
   + abs(BA_A_Mass_100_1800_diff) +  abs(BA_Cell_Mass_100_1800_diff) ...
   + abs(AB_B_Mass_100_7200_diff) +  abs(AB_Cell_Mass_100_7200_diff) ...
   + abs(BA_A_Mass_100_7200_diff) +  abs(BA_Cell_Mass_100_7200_diff) ...
   + abs(AB_B_Mass_100_10800_diff) +  abs(AB_Cell_Mass_100_10800_diff) ...
   + abs(BA_A_Mass_100_10800_diff) +  abs(BA_Cell_Mass_100_10800_diff) ...
   + abs(AB_B_Mass_100_14400_diff) +  abs(AB_Cell_Mass_100_14400_diff) ...
   + abs(BA_A_Mass_100_14400_diff) +  abs(BA_Cell_Mass_100_14400_diff);
```

```
% vals = [AB_B_Mass_50_3600
%     AB_Cell_Mass_50_3600
%     AB_B_Mass_80_3600
%     AB_Cell_Mass_80_3600
%     AB_B_Mass_100_3600
%     AB_Cell_Mass_100_3600
%     BA_A_Mass_50_3600
%     BA_Cell_Mass_50_3600
%     BA_A_Mass_80_3600
%     BA_Cell_Mass_80_3600
%     BA_A_Mass_100_3600
%     BA_Cell_Mass_100_3600
%     AB_B_Mass_50_300
%     AB_Cell_Mass_50_300
%     BA_A_Mass_50_300
%     BA_Cell_Mass_50_300
%     AB_B_Mass_50_1800
%     AB_Cell_Mass_50_1800
%     BA_A_Mass_50_1800
%     BA_Cell_Mass_50_1800
%     AB_B_Mass_50_7200
%     AB_Cell_Mass_50_7200
%     BA_A_Mass_50_7200
%     BA_Cell_Mass_50_7200
%     AB_B_Mass_50_10800
%     AB_Cell_Mass_50_10800
%     BA_A_Mass_50_10800
%     BA_Cell_Mass_50_10800
%     AB_B_Mass_50_14400
%     AB_Cell_Mass_50_14400
%     BA_A_Mass_50_14400
%     BA_Cell_Mass_50_14400
%     AB_B_Mass_80_300
%     AB_Cell_Mass_80_300
%     BA_A_Mass_80_300
%     BA_Cell_Mass_80_300
%     AB_B_Mass_80_1800
%     AB_Cell_Mass_80_1800
%     BA_A_Mass_80_1800
%     BA_Cell_Mass_80_1800
%     AB_B_Mass_80_7200
%     AB_Cell_Mass_80_7200
%     BA_A_Mass_80_7200
%     BA_Cell_Mass_80_7200
%     AB_B_Mass_80_10800
%     AB_Cell_Mass_80_10800
%     BA_A_Mass_80_10800
%     BA_Cell_Mass_80_10800
%     AB_B_Mass_80_14400
%     AB_Cell_Mass_80_14400
%     BA_A_Mass_80_14400
```

```
%     BA_Cell_Mass_80_14400
%     AB_B_Mass_100_300
%     AB_Cell_Mass_100_300
%     BA_A_Mass_100_300
%     BA_Cell_Mass_100_300
%     AB_B_Mass_100_1800
%     AB_Cell_Mass_100_1800
%     BA_A_Mass_100_1800
%     BA_Cell_Mass_100_1800
%     AB_B_Mass_100_7200
%     AB_Cell_Mass_100_7200
%     BA_A_Mass_100_7200
%     BA_Cell_Mass_100_7200
%     AB_B_Mass_100_10800
%     AB_Cell_Mass_100_10800
%     BA_A_Mass_100_10800
%     BA_Cell_Mass_100_10800
%     AB_B_Mass_100_14400
%     AB_Cell_Mass_100_14400
%     BA_A_Mass_100_14400
%     BA_Cell_Mass_100_14400];
```

(C) Matlab ODE solver for AP→BL transport in a Calu-3 cell

```
function [dC] = AB_ODE_calu3(T,Y)
global P_a P_b Pn Pd
global fn_a fd_a fn_c fd_c fn_m fd_m fn_l fd_l fn_b fd_b Nd_a Nd_m Nd_l Nd_b
global A_a A_aq A_b A_bM A_bq A_l A_m V_aq V_c V_bM V_bq V_b V_l V_m V_a


   % Conc(1) :Apical concentration;
   % Conc(2) : Apical UWL concentration ;
   % Conc(3) : Cytosolic concentration ;
   % Conc(4) : Mitochondrial concentration;
   % Conc(5) : Lysosomal concentration;
   % Conc(6) : Basolateral polyester membrane concentration;
   % Conc(7) : Basolateral UWL concentration;
   % Conc(8) : Basolateral concentration;


 Ja_aq = P_a*(Y(1)-Y(2));
 Jaq_c = Pn*(fn_a*Y(2)-fn_c*Y(3))+Pd*Nd_a*(fd_a*Y(2)-fd_c*Y(3)*exp(Nd_a))/(exp(Nd_a)-
1);
 Jc_m = Pn*(fn_c*Y(3)-fn_m*Y(4))+Pd*Nd_m*(fd_c*Y(3)-
fd_m*Y(4)*exp(Nd_m))/(exp(Nd_m)-1);
 Jc_l = Pn*(fn_c*Y(3)-fn_l*Y(5))+Pd*Nd_l*(fd_c*Y(3)-fd_l*Y(5)*exp(Nd_l))/(exp(Nd_l)-1);
 Jc_M = Pn*(fn_c*Y(3)-fn_b*Y(6))+Pd*Nd_b*(fd_c*Y(3)-fd_b*Y(6)*exp(Nd_b))/(exp(Nd_b)-
1);
 JM_bq = P_b*(Y(6)-Y(7));
```

```
Jbq_b = P_b*(Y(7)-Y(8));

dC(1) = -A_aq*Ja_aq/V_a ;
dC(2) = A_aq*Ja_aq/V_aq-A_a*Jaq_c/V_aq ;
dC(3) = A_a*Jaq_c/V_c-A_m*Jc_m/V_c-A_l*Jc_l/V_c-A_b*Jc_M/V_c;
dC(4) = A_m*Jc_m/V_m;
dC(5) = A_l*Jc_l/V_l;
dC(6) = A_b*Jc_M/V_bM-A_bM*JM_bq/V_bM;
dC(7) = A_bM*JM_bq/V_bq-A_bq*Jbq_b/V_bq;
dC(8) = A_bq*Jbq_b/V_b;


   dC = [dC(1), dC(2), dC(3), dC(4), dC(5), dC(6), dC(7), dC(8)]
```

(D) Matlab ODE solver for BL→AP transport in a Calu-3 cell

```
function [dC] = BA_ODE_calu3(T,Y)
global P_a P_b Pn Pd
global fn_a fd_a fn_c fd_c fn_m fd_m fn_l fd_l fn_b fd_b Nd_a Nd_m Nd_l Nd_b
global A_a A_aq A_b A_bM A_bq A_l A_m V_aq V_c V_bM V_bq V_a V_l V_m V_b


   % C(1) : Basolateral concentration;
   % C(2) : Basolateral UWL concentration;
   % C(3) : Basolateral polyester membrane concentration;
   % C(4) : Cytosolic concentration;
   % C(5) : Mitochondrial concentration ;
   % C(6) : Lysosomal concentration ;
   % C(7) : Apical UWL concentration;
   % C(8) : Apical concentration;


 Jb_bq = P_b*(Y(1)-Y(2));
 Jbq_M = P_b*(Y(2)-Y(3));
 JM_c = Pn*(fn_b*Y(3)-fn_c*Y(4))+Pd*Nd_b*(fd_b*Y(3)-fd_c*Y(4)*exp(Nd_b))/(exp(Nd_b)-
1);
 Jc_m = Pn*(fn_c*Y(4)-fn_m*Y(5))+Pd*Nd_m*(fd_c*Y(4)-
fd_m*Y(5)*exp(Nd_m))/(exp(Nd_m)-1);
 Jc_l = Pn*(fn_c*Y(4)-fn_l*Y(6))+Pd*Nd_l*(fd_c*Y(4)-fd1_l*Y(6)*exp(Nd_l))/(exp(Nd_l)-1);
 Jc_aq = Pn*(fn_c*Y(4)-fn_a*Y(7))+Pd*Nd_a*(fd_c*Y(4)-fd_a*Y(7)*exp(Nd_a))/(exp(Nd_a)-
1);
 Jaq_a = P_a*(Y(7)-Y(8));

 dC(1) = -A_bq*Jb_bq/V_b ;
 dC(2) = A_bq*Jb_bq/V_bq-A_bM*Jbq_M/V_bq;
 dC(3) = A_bM*Jbq_M/V_bM-A_b*JM_c/V_bM;
 dC(4) = A_b*JM_c/V_c-A_m*Jc_m/V_c-A_l*Jc_l/V_c-A_a*Jc_aq/V_c;
 dC(5) = A_m*Jc_m/V_m;
```

```
dC(6) = A_l*Jc_l/V_l;
dC(7) = A_a*Jc_aq/V_aq-A_aq*Jaq_a/V_aq ;
dC(8) = A_aq*Jaq_a/V_a;


  dC = [dC(1), dC(2), dC(3), dC(4), dC(5), dC(6), dC(7), dC(8)]
```

Supplemental References

1. Zhang X, Zheng N, Zou P, Zhu H, Hinestroza JP, Rosania GR. Cells on pores: a simulation-driven analysis of transcellular small molecule transport. Mol Pharm. 2010;7(2):456-67.
2. Flieger J. Application of perfluorinated acids as ion-pairing reagents for reversed-phase chromatography and retention-hydrophobicity relationships studies of selected beta-blockers. J Chromatogr A. 2010;1217(4):540-9.
3. Korjamo T, Heikkinen AT, Waltari P, Monkkonen J. The asymmetry of the unstirred water layer in permeability experiments. Pharm Res. 2008;25(7):1714-22.

Appendix D

Supporting Information in Chapter 6

Supplemental Methods

Cell Culture

Calu-3 cells were obtained from American Type Culture Collection (ATCC; Manassas, VA) and cultured in a 1:1 mixture of Dulbecco's Modified Eagle Medium and nutrient mixture F12 (DMEM:F12) with 1% (v/v) non-essential amino acids, 1% (v/v) penicillin-streptomycin and 10% fetal bovine serum (FBS). Cultures were maintained at 37°C in a humidified incubator with 95% air/5% CO2. For the transport experiments, Calu-3 cells (passage 26-36) were seeded at 5×10^5 cells/cm^2 on Transwell inserts with polyester membranes (area, 0.33 μm^2; pore size, 0.4 μm) (Corning Life Sciences; Lowell, MA). An air-liquid interface culture (ALC) was then created by aspirating the medium in the apical compartment after overnight culture. The apical side of the membrane was washed with HBSS to remove unattached cells and the medium in the basolateral compartment was replaced with fresh medium.

Investigational Curcumin Formulation

Hydroxypropyl-γ-cyclodextrin was dissolved to a concentration of 112 g/l in 0.18 mol/l sodium hydroxide solution. Curcumin (Curcumin C3 Complex; Sabinsa Corporation) was

added to a concentration of 15 g/l. The solution was agitated and after complete dissolution of curcumin the pH was adjusted to pH 6.0 with a mixture of hydrochloric and citric acids. The solution was sterile filtered and filled aseptically into sterile vials, then capped and sealed. The recovered CDC solution contained 12 g/l curcumin and 93 g/l cyclodextrin in 20 mM sodium citrate, 100 mM NaCl solution. Endotoxin content was less than 1.8 IU/ml as measured by the Limulus amebocyte lysate gel clot method. The CDC solution was stored at 2-8°C protected from light. The cyclodextrin vehicle was prepared in the same way but without the addition of curcumin.

Curcumin Transport across the Calu-3 Cell Monolayer

On day 6 of ALC culture, the medium in the basolateral compartment was removed and the apical and basolateral sides of the cell monolayers on the membrane inserts were washed twice with an HBSS transport buffer (HBSS with 10 mM HEPES and 25 mM D-glucose, pH 7.4). The Calu-3 cell monolayers on the polyester membranes were then pre-equilibrated with HBSS transport buffer in the apical and basolateral compartments for 20 min at 37°C. The integrity of the cell monolayers was examined by transepithelial electrical resistance (TEER) measurements using the Millicell ERS (Millipore; Billerica, MA). The TEER values of the cell monolayers were corrected by subtracting the blank TEER values without the cells in the inserts and the TEER values ($\Omega \cdot cm^2$) for the 24-well inserts were obtained by using the area of the membranes (0.33 μm^2). Cell monolayers with TEER values ~ 350 $\Omega \cdot cm^2$ were used for the Lucifer Yellow (LY) and curcumin transport experiments. LY permeability served as a further check on integrity of the cell monolayers. LY (1 mM in HBSS transport buffer) was added to the donor

compartment and apical-to-basolateral (AP→BL) or basolateral-to-apical (BL→AP) transport was measured during 180 min incubation on rocking platform shakers at 37°C in a 5% CO2 incubator. LY in the samples and the standard was measured by a plate reader (BioTEK; Winooski, VT) set for 485 nm (excitation)/540 nm (emission).

For CDC transport experiments, CDC stock solutions were diluted with HBSS transport buffer to concentrations of 50, 100, and 200 μM (donor concentrations). Curcumin solution at each concentration was added to the donor compartment (apical for AP→BL; basolateral for BL→AP transport) with the corresponding curcumin-free HBSS buffer in the receiver compartment. Cells were incubated for 180 min with shaking and samples were collected from the receiver compartment at 0, 5, 10, 30, 60, 90, 120, 150, and 180 min. Samples were also collected from the donor compartment at 180 min. The donor and receiver sides of the inserts were washed twice with HBSS transport buffer and these washings were also included in the mass calculations. Fluorescence of curcumin in the standard and sample solutions was measured in 96-well optical bottom plates using a plate reader (BioTEK Synergy) at 485 nm (EX)/540 nm (EM). For AP→BL or BL→AP transport, the transcellular permeability coefficient, P_{eff} (cm/sec) was calculated by dividing the AP→BL or BL→AP mass transport rate (dM/dt) by the product of insert area, A (0.33 cm^2) and initial donor concentration of curcumin, C_o, as shown in the following equation:

$$P_{\mathrm{eff}} = \frac{\frac{dM}{dt}}{A \cdot C_o}$$

Following each transport experiment, TEER was measured and the cell monolayers were examined by light contrast inverted microscopy to confirm that integrity of the cell monolayers remained unchanged.

To compare effects on transport and monolayer integrity of the uncomplexed curcumin powder with those of CDC, curcumin stock solutions were prepared by dissolving the uncomplexed curcumin powder in DMSO (DMSO-C) or absolute ethanol (EtOH-C). These stock solutions were then diluted with HBSS transport buffer to make donor solutions and these solutions were used for transport experiments as described.

Cellular Curcumin Binding

After the transport assays, the inserts and attached cells were washed twice with cold HBSS transport buffer to remove unbound curcumin. The cells were then incubated with Hoechst 33342 solution in HBSS in 24-well inserts for 30 min at 37°C in a 5% CO_2 incubator. Media in the apical compartment was 100 µl of 10 µg/ml Hoechst 33342 (Invitrogen; Carlsbad, CA) in HBSS and that in the basolateral compartment was 600 µl of dye-free HBSS transport buffer. Following incubation, the inserts were washed with HBSS transport buffer and examined with the 10 × objective of a Nikon TE2000 fluorescence microscope equipped with a XF93 triple pass filter set (Omega Optical; Brattleboro, VT). Cell-associated curcumin could be detected with the fluorescein isothiocyanate (FITC) channel of the filter set while the nuclei were visualized with the diamidino-2-phenylindole (DAPI) channel. Inserts from all experimental conditions were examined for curcumin association and intactness of the cell monolayers.

Other inserts from each experimental condition were used for quantitative determination of curcumin cell-associated mass. These inserts were incubated with 1% Triton X-100 (100 µl in the apical compartment; 600 µl in the basolateral compartment) for 1.5 hours at 37°C in a 95% air/5% CO_2 incubator. The concentration of curcumin extracted into the Triton X-100 medium was measured with a plate reader at 485 nm (EX)/540 nm (EM) and cell-bound curcumin mass per cell was calculated from the cell numbers counted with a hemocytometer following detachment by trypsinization.

Wet:Dry Weight Ratio

The superior lobe of the right lung was excised and the wet weight was recorded. The tissue was then placed in an incubator at 60°C for 24 hours, after which the dry weight was recorded and the ratio of wet to dry weight was calculated.

Lung Histology

For general morphology, sections from formalin-fixed, paraffin-embedded lung tissues were stained with hematoxylin and eosin. For fluorescence analysis, lung tissues were infused with a solution of 50% Tissue-Tek optimum cutting temperature (O.C.T.) compound (Sakura; Torrance, CA) and 50% PBS. The lungs were then frozen and sectioned.

Canine Toxicology and Pharmacokinetics

CDC (34.8 mM in physiological saline) was administered intravenously (IV) to beagle dogs (n = 1/group) at doses of 1 or 4 mg/kg daily or at a dose of 10 mg/kg twice a day. Dosing was continued for 14 days. The first dose was infused over the course of 5 min,

subsequent doses over the course of 3 min. On days 1, 7, and 14 blood was drawn at specified intervals following infusion and concentrations of curcumin and its metabolites were determined by mass spectrometry. Blood for a complete cell count and determination of clinical chemistry parameters was drawn on days 2, 7, and 14. Two to four hours after the last infusion the animals were sacrificed and an autopsy was performed.

Supplemental Results

In Vivo Pharmacokinetics of Curcumin and its Metabolites

Preliminary studies on IV curcumin pharmacokinetics were conducted in beagle dogs. The CDC formulation was given at doses of 1 mg/kg and 4 mg/kg once daily and at 10 mg/kg twice daily for 14 days. Serial blood samples were drawn in EDTA anticoagulant before and 5 min, 15 min, 30 min, 60 min, 2 and 4 hours following the morning dose on days 1, 7 and 14. Blood samples were kept on ice bath and plasma was separated within 20 min. Plasma concentrations of curcumin and its major circulating metabolites, tetrahydrocurcumin and tetrahydrocurcumin sulfate, were analyzed by liquid chromatography-mass spectrometry (LC-MS).

Briefly, 200 µl of dog plasma was combined with 50 µl methanol, 1 ml of 1M ammonium acetate pH 5, 3 ml of 90% ethyl acetate/10% propanol, and 20 µl of internal standard (1 ng/µl in methanol) in a 13 × 100 mm glass tube. Tubes were capped and shaken for 30 minutes, then centrifuged at 1500 × g for 10 minutes. The organic layer

was transferred to clean 12 × 75 mm glass tubes and evaporated to dryness under nitrogen, then reconstituted in 50 µl methanol. Two-µl aliquots of each sample were injected onto an LC-MS. Chromatography was performed on an Agilent 1100 Series HPLC system equipped with a Zorbax SB-C18 column (150 × 2.1 mm i.d., 5 µm particle size). The mobile phase consisting of 1 mM ammonium acetate, pH 4.5 (A) and acetonitrile (B) was pumped at a flow rate of 0.3 ml/min according to the following gradient: 75% A and 25% B (0 min) → 45% A and 55% B (5 min) → 30% A and 70% B (7.5 min) and stopped at 15 min; there was a post-run equilibration of 4 min. Detection of the analytes was performed on an Agilent G1956B Series or G1946B MSD run in negative electrospray ionization (ESI-) mode, with a drying gas temperature of 350°C and flow rate of 12 l/min, and a nebulizer pressure of 35 psi. Ions monitored included m/z 253 (chrysin, IS), m/z 367 (curcumin), m/z 371 (tetrahydrocurcumin), m/z 467 (tetrahydrocurcumin sulfate), and m/z 543 (curcumin glucuronide) (1). The fragmentor was optimized to 120 V (for curcumin) and 160 V (for chrysin), while the capillary voltage was optimized to 3600 V. Curcumin glucuronide was synthesized enzymatically from curcumin and UDP-glucuronide by using rat liver microsomes and curcumin sulphate and THC sulphate were synthesized as described before (1).

No changes in the kinetics of plasma curcumin or its major metabolite, tetrahydrocurcumin, were observed over the 2 weeks of daily curcumin treatment; hence the mean plasma concentration-time data collected on days 1, 7 and 14 are presented. The half-life of curcumin in beagle dogs following IV CDC infusion was approximately 7 min independent of dose (Figure D1). The metabolite tetrahydrocurcumin (THC) appeared almost immediately after infusion of curcumin, then declined at a rate similar to

that of the parent compound (Figure D1). Little or no THC sulfate was detectable on day 1, but a prominent mass ion peak appeared at 30 min after infusion on days 7 and 14 (Figure D2). On day 14 this compound was the major curcumin metabolite present at times ≥ 15 min following infusion (Figure D3).

These results indicate that curcumin is rapidly cleared from the bloodstream following IV administration of CDC. This calls into question the feasibility of systemic CDC administration in pulmonary therapy.

Toxicology

Complete blood cell count and clinical chemistry parameters including biomarkers of muscle/heart, liver, kidney and pancreas function (Table D1) were determined on days 0 (prior to initial CDC administration) and 13. Autopsy was carried out 2-4 hours after the last injection. Histopathological examination of tissue biopsies was carried out by a veterinary pathologist. Biopsies were taken from buccal mucosa, esophagus, small intestine, large intestine, heart, lung, liver, gall bladder, pancreas, kidney, urinary bladder, testicle/ovary, skeletal muscle and bone marrow, including a smear from bone marrow.

No adverse effects were observed in any dog. Hematologic and clinical chemistry parameters were normal throughout dosing, except that blood glucose levels were slightly below the reference range both before and during treatment (Table D1). No abnormalities were observed at autopsy except a parasitic lung infection believed to have been present prior to the study. No curcumin was detected in tissue samples. Systemically administered CDC thus appears safe in this small preclinical study, supporting the expectation of safety following delivery directly to the lung in pulmonary disease.

Table D1. Laboratory Parameters of Dogs Receiving Different Dosages of CDC. Values are shown before (Day 0) and after (Day 13) administration of CDC at the indicated daily doses for 14 days. 20 mg/kg was given as two daily infusions.

		1 mg/kg		4 mg/kg		20 mg/kg		Reference
		Day 0	Day 13	Day 0	Day 13	Day 0	Day 13	values
WBC	/dl	7700	7470	7070	7550	7180	10500	
HCT	%	47	46	50	49	47	45	
PLT	/dl	269000	307000	137000	179000	327000	391000	
Poly	%	32	42	55	65	53	66	
ANC	/dl	2464	3137	3888	4907	3805	6930	
Ly	%	52	42	31	22	29	23	
Mo	%	2	6	8	7	10	10	
Eo	%	14	10	6	6	8	1	
Glucose	mg/dl	54	45	58	63	58	51	65-130
BUN	mg/dl	11	18	16	15	17	26	6-29
Crea	mg/dl	0.9	0.9	0.9	0.9	0.8	0.8	0.6-1.6
Na	mEq/l	149	147	149	149	148	149	140-158
K	mEq/l	5.3	5.3	5.1	4.5	4.9	5.2	4.0-5.7
Na/K		28	28		33	30	29	27-40
Cl	mEq/l	108	110	108	108	111	111	100-115
CO_2	mEq/l	26	26	25	23	22	25	18-26
Anion gap		20	16	21	23	20	18	13-25
Ca	mg/dl	10.8	10.8	10.9	11	10.1	10.1	8.0-12.0
P	mg/dl	6.0	6.3	6.4	6.1	3.7	5.3	3.0-7.0
Osmol		294	292	296	294	294	299	270-310
Total prot	g/dl	5.9	5.8	6.5	5.9	6.1	6.5	5.4-7.6
Albumin	g/dl	3.3	3.3	3.6	3.4	3.2	3.4	2.3-4.0
Globulin	g/dl	2.6	2.5	2.9	2.5	2.9	3.1	2.7-4.4
Alb/Glob		1.3	1.3	1.2	1.4	1.1	1.1	0.6-1.2
Bil	mg/dl	0.1	0.1	0.1	0.2	0.1	0.1	0.0-0.5
ALP	U/l	120	102	88	75	49	57	10-84
GGT	U/l	1	0	2	0	0	2	0-10
ALT	U/l	31	31	48	55	42	51	5-65
AST	U/l	48	51	56	56	52	53	16-60
CK	U/l	324	355	319	309	300	331	50-300
Chol	mg/dl	200	183	188	178	143	143	150-275
Amylase	U/l	887	752	588	565	1130	1189	300-1500
Lipase	U/l	288	223	455	299	224	231	0-425

Supplemental Figures

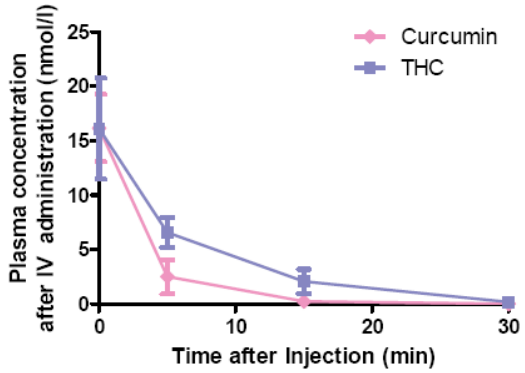

Figure D1 Time Course of Curcumin and Tetrahydrocurcumin (THC) Plasma Concentrations Following Intravenous Administration of CDC.

CDC was administered at a dose of 10 mg/kg and blood was drawn for determination of plasma curcumin and THC concentrations at the indicated intervals following infusion. Values are the mean of measurements on days 1, 7, and 14, as no between-day differences in pharmacokinetics of these compounds was observed.

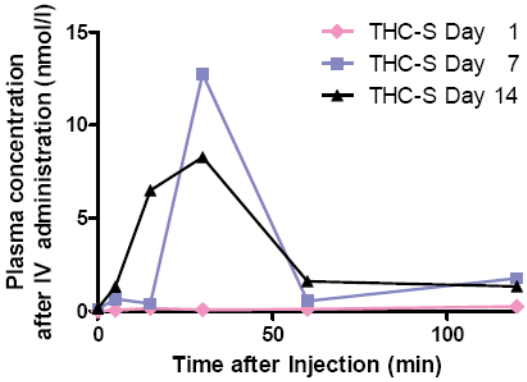

Figure D2 Time Course of Tetrahydrocurcumin Sulfate (THC-S) Plasma Concentration Following CDC Infusion.

Doses of 10 mg/kg were administered intravenously twice daily for 14 days. On days 1, 7, and 14 blood was drawn at indicated intervals following infusion and plasma concentrations of THC-S were determined.

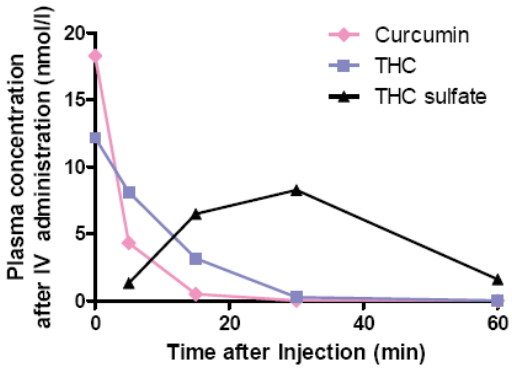

Figure D3 Comparative Plasma Concentration-Time Profile of Curcumin and its Major Circulating Metabolites after Repeated CDC Administration.

CDC (10 mg/kg) was administered intravenously twice daily for 14 days. On day 14, blood was drawn at indicated intervals following infusion and curcumin, THC, and THC-S were determined.

Supplemental Reference

1. Ireson C, Orr S, Jones DJ, Verschoyle R, Lim CK, Luo JL, Howells L, Plummer S, Jukes R, Williams M, Steward WP, and Gescher A. Characterization of metabolites of the chemopreventive agent curcumin in human and rat hepatocytes and in the rat in vivo, and evaluation of their ability to inhibit phorbol ester-induced prostaglandin E2 production. Cancer Res. 2001;61:1058–64.